



THE UNIVERSITY OF BIRMINGHAM

Multiphase contacting in PGM hydrometallurgy

By

Ukachukwu Ibe Oguh

A thesis submitted to
The School of Engineering of
The University of Birmingham
for the degree of

Doctor of Engineering

School of Engineering
Chemical Engineering
The University of Birmingham
Edgbaston
Birmingham B15 2TT
United Kingdom

UNIVERSITY OF
BIRMINGHAM

University of Birmingham Research Archive

e-theses repository

This unpublished thesis/dissertation is copyright of the author and/or third parties. The intellectual property rights of the author or third parties in respect of this work are as defined by The Copyright Designs and Patents Act 1988 or as modified by any successor legislation.

Any use made of information contained in this thesis/dissertation must be in accordance with that legislation and must be properly acknowledged. Further distribution or reproduction in any format is prohibited without the permission of the copyright holder.

Abstract

This thesis describes hydrodynamic studies of the leach and solvent extraction stages of a Platinum Group Metal (*PGM*) hydrometallurgical flowsheet. The studies were motivated by the need to increase *PGM* throughput in Johnson Matthey's *PGM* refining business. In the leach stage, key components in the feed are selectively dissolved using acids in a stirred tank before they are recovered by liquid-liquid (*L-L*) solvent extraction and finally purified. The work described in this thesis tackles four main areas: hydrodynamic studies of *L-L PGM* solvent extraction in both mixer and settler stages, whilst for the leach stage, studies of particle behaviour in gas evolving solid-liquid (*S-L*) reactions and gas-liquid-solid (*GLS*) characterisation by a novel Electrical Resistance Tomography (*ERT*) technique are performed.

In the mixer-settler, the effects of impeller diameter, D , to vessel diameter, T , ratio (D/T), the phase flow ratio, ϕ_c/ϕ_d ; (where ϕ_c is the continuous phase flow fraction and ϕ_d is the dispersed phase flow fraction) and the specific power input, $\bar{\varepsilon}_T$, upon the droplet size distribution in a *L-L* system and their phase separation were investigated. Changing a smaller D/T impeller for a larger D/T impeller at constant P/V and ϕ_c/ϕ_d increased droplet size because the maximum shear rate decreased as a result of increasing ratio of impeller pumping capacity (Q) with tip speed (U_{tip}). Changing a larger ϕ_c/ϕ_d for smaller ϕ_c/ϕ_d at a fixed P/V and D/T impeller increased droplet size because turbulent dampening increased since the average density, $\rho \propto \phi_d$. Meanwhile, Kolmogoroff-Hinze's theory was shown to apply for the measured relationship between $\bar{\varepsilon}_T$ and droplet size.

A settler design criterion, which relates the dispersed phase concentration (C_d) in the dispersion band to the dispersed phase throughput (Q_d/A) agreed with the model by Ryon *et al.* (1959). C_d was significantly dependent on P/V and Q_d/A , whilst the effects of Q_c/Q_d (where Q_c is the continuous phase flowrate and Q_d is the dispersed phase flowrate) and D/T were minimal. Droplet size analysis of the sedimenting region of the dispersion band and dense packed layer revealed a transitional distribution of droplet sizes due to the counteracting effects of droplet sedimentation, hindered settling and droplet-droplet coalescence.

Particle behaviour in gas evolving *S-L* systems were quantified using the Zwietering 'just-suspended' impeller speed (N_{js}) condition in a sponge nickel[®] and sodium hypochlorite system. The presence of gas caused N_{js} to increase, however a coherent relationship between N_{js} in an ungasged and gasged system

could not be easily ascertained. Further work with Positron Emission Particle Tracking (*PEPT*) was advised to quantify the relationship.

A well-known electrical concept called skin effect, which describes how the effective resistance of an electrical conductor varies as the frequency of an alternating current (*AC*) increases and decreases, was used to investigate *GLS* behaviour via a novel *ERT* spectroscopic technique. The process relies on the change in effective resistance of conducting objects with changing *AC* frequency to selectively detect different phases. The concept was initially validated with static phantoms of a stainless steel and plume of gas before being applied to dispersible stainless steel particles and gas. *ERT* spectroscopy showed that two *AC* frequencies (0.3 kHz and 9.6 kHz) could successfully isolate and simultaneously detect the gas and solid phases at a fixed current. By subtracting solids and gas conductivity, the change in solids and gas holdup were obtained.

Dedication

I dedicate this thesis to the Lord and my family. To my dad, Mr Donatus.C. Oguh, who passed away at the end of January 2012, just before I submitted my thesis and to my mum, Mrs Mercy.C.Oguh. You did not just nurture me, but you trained, encouraged and motivated me throughout my life. You both have keenly watched my progress in this field of engineering and have shown patience and selfless love. To my brothers, Chima and Ugo, you encouraged me during moments of despair and discouragement. Finally I dedicate this to the larger Oguh family and Kindred of Obohia, Ahiazu Mbaise, Imo State, Nigeria.

Acknowledgements

I also would like to thank my sponsors *EPSRC*, Dr. Simon Collard of Platinum Group Metals Refining (*PGMR*), Johnson Matthey and my industrial supervisors, Prof. Hugh E. Stitt and Dr. Jonathan F. Hall of Johnson Matthey Technology Centre (*JMTC*), Billingham who made all aspects of this project possible and provided valuable suggestions and comments throughout the research programme.

I want to send a special thanks to Dr. Mark J. Simmons and Prof. Mostafa Barigou of the School of Chemical Engineering, University of Birmingham whose unquestionable experience as academic supervisors gave me the much needed alignment of thought and perspective between academic and industrial requirements of the research programme. I also appreciate the valuable suggestions, comments and encouragement given, as well as the assistance in putting this thesis together.

I am grateful to Dr. Richard Greenwood for being a great Engineering Doctoral co-ordinator and all the staff of the Manufacturing Science Centre in *JMTC*, Billingham and the University of Birmingham.

Table of contents

Abstract.....	1
Dedication.....	4
Acknowledgements.....	5
Table of contents.....	6
List of Figures.....	12
List of Tables.....	18
Nomenclature.....	19
1. Chapter 1: Introduction.....	27
1.1. Hydrometallurgy.....	27
1.2. Sponsoring company and industrial perspective.....	30
1.3. Aims and objectives of the study.....	32
1.4. Scope of investigation and thesis outline.....	33
2. Chapter 2: Hydrodynamic study of an aqueous-organic LIX84-A system agitated by a Rushton Disc Turbine (RDT) in a box mixer.....	36
2.1. Introduction.....	36
2.2. Literature review.....	38
2.2.1. Droplet breakup in turbulent L-L systems.....	38
2.2.2. Droplet size in turbine agitated vessels.....	43
2.2.3. Droplet coalescence in L-L systems.....	45
2.2.4. Droplet size distribution.....	46
2.2.5. Turbines and flow patterns.....	48
2.2.6. Power requirements for low viscosity fluids.....	51

2.2.7.	Pumping capacity and circulation flowrates	52
2.2.8.	Circulation capacity and circulation time	54
2.2.9.	Droplet measurement techniques	55
2.2.9.1.	Direct methods	55
2.2.9.2.	Indirect methods.....	57
2.3.	Conclusion from literature review	61
2.4.	Materials and methods	61
2.4.1.	The phases.....	61
2.4.2.	Mixer-settler design considerations	62
2.4.3.	The Mixer.....	62
2.4.4.	Impeller operating conditions	69
2.4.5.	Achieving the desired dispersion and avoiding phase inversion	71
2.4.6.	Droplet sizing technique	72
2.5.	Results and discussion	74
2.5.1.	The effect of P/V on dispersed phase holdup	74
2.5.2.	The effects of D/T on droplet size and droplet size distribution.....	76
2.5.3.	The effects of ϕ_c/ϕ_d on droplet size.....	86
2.5.4.	The effects of P/V on droplet size.....	93
2.5.5.	We and $\bar{\varepsilon}_T$ as functions of d_{32}	93
2.6.	Conclusion	100
3.	Chapter 3:The study of a settler for the separation of Copper/HCl dispersion in organic LIX 84-A	102
3.1.	Introduction.....	102

3.2.	Literature review	104
3.2.1.	Settlers.....	104
3.2.2.	Droplet coalescence	106
3.2.3.	Coalescence rate.....	107
3.2.4.	Settler scale-up correlations	112
3.2.5.	Coalescence enhancement	113
3.3.	Conclusions from literature review.....	115
3.4.	Materials and methods	115
3.4.1.	Settler	115
3.4.2.	Dispersion measurement technique	116
3.4.3.	Properties of the aqueous and organic phases.....	117
3.5.	Results and discussion	118
3.5.1.	Dense packed region analysis	118
3.5.2.	Droplet size within the sedimenting and transition to the dense packed region in the turbulent mixing regime.....	124
3.5.3.	The effects of D/T on C_a in the vertical plane	128
3.5.4.	The effects of Q_c/Q_d on C_a in the vertical plane	133
3.5.5.	The effects of P/V on the C_a in the vertical plane.....	143
3.5.6.	Factor analysis of the effects of D/T , Q_d , P/V and fixed dispersion band depth on C_a	146
3.5.7.	The effects of Q_d/A on C_a	149
3.6.	Conclusions.....	156
4.	Chapter 4. Hydrodynamics of gas evolving solid – liquid reactions	158

4.1.	Introduction.....	158
4.2.	Literature Review.....	159
4.2.1.	Nickel-Hypochlorite chemical reaction	159
4.2.2.	Gas-Liquid-Solid (GLS) systems.....	160
4.3.	Conclusions from literature review.....	168
4.4.	Materials and Methods.....	168
4.4.1.	Gas evolution rate	169
4.4.2.	Terminal settling velocity	170
4.4.3.	Vessel design, configuration and impeller type.....	170
4.4.4.	Just suspended speed, N_{js} , of gassing and ungassed systems.....	171
4.5.	Results and discussion	171
4.5.1.	The effects of Sponge Nickel [®] and Sodium hypochlorite concentration on gas evolution rate	171
4.5.2.	Particle and gas hold-up in gas evolving reactions.....	173
4.5.3.	Solid phase suspension and settling behaviour in gas evolving reactions	176
4.6.	Conclusions.....	179
5.	Chapter 5. The use of Electrical Resistance Spectro-Tomography for Phase Discrimination in Gas-Liquid-Solid (GLS) mixing.....	180
5.1.	Introduction.....	180
5.2.	Literature Review.....	182
5.2.1.	Electrical based tomography techniques.....	183
5.2.2.	Radiation based tomography techniques	188
5.2.3.	Fundamentals of ERT Spectroscopy.....	198

5.2.4.	Conclusions from literature review.....	201
5.3.	Materials and methods	202
5.3.1.	Limitations of the technique	207
5.4.	Results and discussion	209
5.4.1.	The effects of frequency on the conductivity of the phantom and plume of air in nickel nitrate solution and the circular array ERT vessel.	209
5.4.2.	Study of the effects of frequency on the conductivity of agitated S-L and G-L systems with a linear ERT probe	212
5.4.3.	Agitated GLS system characterised at 9.6 kHz and 0.3 kHz with the linear ERT probe	214
5.5.	Conclusion	232
6.	Chapter 6. Conclusions and future work	235
6.1.	Conclusions.....	235
6.2.	Future work.....	238
	References.....	240
	Appendix.....	266
	Appendix A (i)	266
	Plot of Po versus Re.....	266
	Appendix A (ii).....	266
	Droplet size percentage error	266
	Appendix A(iii).....	267
	Statistical tests for d_{32} versus $\overline{\varepsilon_T}$	267
	Appendix B	270

Turbidity meter calibrations.....	270
Appendix C	271
List of publications	271
Appendix D.....	272
A study of hydrodynamics in gas evolving	272
Appendix E	281
6 th International Symposium on Process Tomography	281
Appendix F.....	297

List of Figures

Chapter 1: Introduction

Figure 1.1. Components of Hydrometallurgical Flowsheets.

Figure 1.2. Schematic of a reacting particle following the shrinking-core mode.

Chapter 2: Hydrodynamic study of an aqueous-organic LIX84-A system agitated by a Rushton Disc Turbine (RDT) in a box mixer

Figure 2.1. (a) Radial flow pattern of (b) Rushton disc turbine (*RDT*).

Figure 2.2. (a) Axial flow pattern of (b) Pitched blade turbine (*PBT*).

Figure 2.3. *CAD* drawing of mixer settler.

Figure 2.4. Mixer settler flow diagram.

Figure 2.5. *RDT* of $D/T = 4/13$.

Figure 2.6. *RDT* of $D/T = 5/13$.

Figure 2.7. *RDT* of $D/T = 6/13$.

Figure 2.8. An image of droplets stabilised by Polyglycerol polyricinoleate solution.

Figure 2.9. Image of droplets captured with the Photron Fastcam SA-5.

Figure 2.10. Organic supernatant layer at P/V of 0.3 kW m^{-3} and D/T of $4/13$.

Figure 2.11. Change in φ_d at 0.3 kW m^{-3} and D/T of $4/13$.

Figure 2.12. Droplet size distribution and cumulative volume percentage as a function of D/T at P/V of (a) 0.3 kW m^{-3} at $\phi_c/\phi_d = 1:1$ (b) 0.9 kW m^{-3} at $\phi_c/\phi_d = 3.5:1$ (c) 2.7 kW m^{-3} at $\phi_c/\phi_d = 3.5:2$.

Figure 2.13. d_{32} as a function of Q for all operating conditions.

Figure 2.14. d_{32} as a function of U_{tip} for all D/T and all ϕ_c/ϕ_d at (a) 0.3 kW m^{-3} (b) 0.9 kW m^{-3} (c) 2.7 kW m^{-3} .

Figure 2.15. d_{32} as a function of ϕ_d for (a) $D/T = 4/13$ (b) $D/T = 5/13$ (c) $D/T = 6/13$.

Figure 2.16. Variation in droplet size distribution with ϕ_c/ϕ_d for (a) $4/13$ at 0.3 kW m^{-3} (b) $5/13$ at 0.9 kW m^{-3} (c) $6/13$ at 2.7 kW m^{-3} .

Figure 2.17. Droplet size images for ϕ_c/ϕ_d of (a) 3.5:1 with $d_{32} = 88 \text{ }\mu\text{m}$ (b) 1:1 with $d_{32} = 116 \text{ }\mu\text{m}$; for $D/T = 4/13$ and $P/V = 0.9 \text{ kW m}^{-3}$ at similar magnifications.

Figure 2.18. Evidence of air entrained at ϕ_c/ϕ_d of 3.5:1 for D/T of 6/13.

Figure 2.19. Evidence of vessel occupied by air.

Figure 2.20. Dimensionless d_{32} as a function of We for all ϕ_c/ϕ_d (a) 1:1 (b) 3.5:2 (c) 3.5:1 at varying D/T .

Figure 2.21. The effects of $\bar{\varepsilon}_T$ on d_{32} for all D/T and ϕ_c/ϕ_d (a) 1:1 (b) 3.5:2 (c) 3.5:1.

Chapter 3: The study of a settler for the separation of Copper/HCl dispersion in organic LIX 84-A.

Figure 3.1. Schematic of a wedge shaped dispersion band.

Figure 3.2. Schematic of a deep layer dispersion band.

Figure 3.3. Batch dispersion decay (Jeelani and Hartland, 1985)

Figure 3.4. Description of sampling process.

Figure 3.5. Normal plot of the effects of the P/V , Q_c/Q_d and D/T .

Figure 3.6. Pareto plot of the standardised effect of each factor.

Figure 3.7. Clear wedge shaped region at the $P/V = 0.3 \text{ kW m}^{-3}$.

Figure 3.8. Emulsified wedge shaped region observed at the $P/V = 0.9 \text{ kW m}^{-3}$.

Figure 3.9. A typical deep layer dispersion band at the $P/V = 2.7 \text{ kW m}^{-3}$.

Figure 3.10. *CVD* illustrating the change in the uniformity of droplet size distribution as P/V was increased.

Figure 3.11. Droplet size distributions of samples withdrawn from the sedimenting region for $D/T = 4/13$, $P/V = 2.7 \text{ kW m}^{-3}$ and $Q_c/Q_d = 1:1$ and $3.5:2$.

Figure 3.12. Droplet size distribution and *CVD* of samples taken from the sedimenting region and transition to the dense packed region for $D/T = 4/13$.

Figure 3.13. C_a as D/T changes for $P/V = 0.9 \text{ kW m}^{-3}$ and Q_c/Q_d of (a) 3.5:1 (b) 3.5:2 (c) 1:1.

Figure 3.14. C_a as D/T changes for $P/V = 2.7 \text{ kW m}^{-3}$ and $Q_c/Q_d =$ (a) 3.5:1 (b) 3.5:2.

Figure 3.15. The effects of D/T on the *CVD* of droplets in the mixer at the $Q_c/Q_d = 3.5:1$ and $P/V =$ (a) 0.9 kW m^{-3} (b) 2.7 kW m^{-3} .

Figure 3.16. C_a as Q_c/Q_d changes for $P/V = 0.9 \text{ kW m}^{-3}$ and $D/T =$ (a) $4/13$ (b) $5/13$ (c) $6/13$.

Figure 3.17. C_a as Q_c/Q_d changes for $P/V = 2.7 \text{ kW m}^{-3}$ and $D/T =$ (a) $4/13$ (b) $5/13$ (c) $6/13$.

Figure 3.18. The effects of Q_c/Q_d on the cumulative volume distribution of droplets and droplet size distribution in the mixer for the $P/V = 0.9 \text{ kW m}^{-3}$ and $D/T =$ (a) $4/13$ (b) $6/13$.

Figure 3.19. C_a as P/V changes using $D/T = 4/13$ and $Q_c/Q_d =$ (a) 1:1 (b) 3.5:2 (c) 3.5:1.

Figure 3.20. Main effects to the C_a in the vertical plane.

Figure 3.21. Interaction of the variables.

Figure 3.22. Pareto plot of the Factors and interactions.

Figure 3.23. The effects of Q_d/A on the C_a along the horizontal plane at $L_s =$ (a) 0 m (b) 0.05 m (c) 0.1 m, for $P/V = 0.9 \text{ kW m}^{-3}$ and $Q_c/Q_d = 1:1$.

Figure 3.24. C_a as a function of Q_d/A for the $D/T = 4/13$ and $Q_c/Q_d = 3.5:2$ and 1:1

agitated with a $P/V = 0.9 \text{ k W m}^{-3}$.

Figure 3.25. The effects of Q_d/A on the dispersed phase C_a along the horizontal plane at (a) 0 m (b) 0.05 m (c) 0.1 m, for $P/V = 2.7 \text{ kW m}^{-3}$ and $Q_c/Q_d = 1:1$.

Figure 3.26. C_a as a function of Q_d/A for the $D/T = 4/13$ and Q_c/Q_d and 1:1.

Chapter 4. Chapter 4. Hydrodynamics of gas evolving solid – liquid reactions.

Figure 4.1. *G-L* flow patterns. (Harnby *et al.*, 1992).

Figure 4.2. Cavity structures observed behind *RDT* blades. (Harnby *et al.*, 1992).

Figure 4.3. Relationship between P_g/P and Fl_g . (Harnby *et al.*, 1992).

Figure 4.4. Gas evolution rate measuring apparatus.

Figure 4.5. The effects of sodium hypochlorite concentration on gas evolution rate.

Figure 4.6. The effects of Ni concentration on gas evolution rate.

Figure 4.7. φ_g and liquid levels associated with particle settling, gas expansion and contraction.

Figure 4.8. Telemetry of φ_g and liquid levels associated with particle settling, gas expansion and contraction.

Figure 4.9. φ_g before ceasing agitation and Level A and as a function of gas evolution rate for 4.74 % (w/v) Ni in 8, 7, 6, 4 and 2 % sodium hypochlorite solutions.

Chapter 5. The use of Electrical Resistance Spectro-Tomography for Phase Discrimination in Gas-Liquid-Solid (GLS) mixing.

Figure 5.1. Adjacent electrode pair strategy for 16 electrodes sensor (Dyakowski *et al.*, 2000).

Figure 5.2. Rotating electrical field measurement strategy with *ECT* (Dyakowski *et al.*, 2000).

Figure 5.3. Multi-frequency excitation conductivity intersections (Hoyle and Nahvi, 2008).

Figure 5.4. The effects of varying the frequency from 20 to 200 kHz on the isolation of banana from cucumber.

Figure 5.5. (a) Flow of charge on the surface of conductor due to self inductance (b) Flow of charge across the entire cross section of a conductor.

Figure 5.6. Linear *ERT* probe with electrode arrangements.

Figure 5.7. An overview of the external and internal electrode arrangements.

Figure 5.8. Schematic of *ERT* with the circular array *ERT* vessel.

Figure 5.9. Rushton disc turbine (*RDT*).

Figure 5.10. Schematic of the linear *ERT* probe arrangement.

Figure 5.11. The effects of agitation on the conductivity and temperature of nickel nitrate solution.

Figure 5.12. The effects of changing frequency on self inductance of the stainless steel phantom.

Figure 5.13. Relative change in conductivity across the plane of the tomogram.

Figure 5.14. The effects of frequency on the mean conductivity of stainless steel phantom and air in nickel nitrate solution.

Figure 5.15. The effects of frequency on the mean conductivity of dispersed stainless steel particles (*S-L*) and air (*G-L*) system.

Figure 5.16. Gas flow regime map for the Rushton turbine (Harnby *et al.*, 1992).

Figure 5.17. Mean conductivity plot of the *GLS* system characterised at 9.6 kHz and 0.3 kHz.

Figure 5.18. Image of *S-L* mixing.

Figure 5.19. Conductivity profile for *S-L* mixing.

Figure 5.20. (i) Normalised conductivity and (ii) Dimensionless conductivity for *S-L* mixing.

Figure 5.21. Tomogram of solids distribution in the vessel at 9.6 kHz.

Figure 5.22. Tomogram of solids distribution in the vessel at 0.3 kHz.

Figure 5.23. Image of *GLS* mixing in region 'c' for $Fl_g \approx 0.029$ and $Fr \approx 1.08$.

Figure 5.24. Conductivity profile for *GLS* mixing in region 'c'.

Figure 5.25. (i) Normalised conductivity and (ii) Dimensionless conductivity for $Fl_g \approx 0.0048$ and $Fr \approx 1.08$.

Figure 5.26. Tomograms of gas and solids distribution in region 'c' at $Fl_g \approx 0.0$ and $Fr \approx 1.08$ at 9.6 kHz.

Figure 5.27. Tomograms of gas and solids distribution in region 'c' at $Fl_g \approx 0.029$ and $Fr \approx 1.08$ at 0.3 kHz.

Figure 5.28. Image of *GLS* system in region 'd' at $Fl_g \approx 0.0386$ and $Fr \approx 0.7$.

Figure 5.29. Conductivity profile for *GLS* mixing in region 'd'.

Figure 5.30. (i) Normalised conductivity and (ii) Dimensionless conductivity for $Fl_g \approx 0.0048$ and $Fr \approx 1.08$.

Figure 5.31. Tomograms of gas and solids distribution in region 'd' at $Fl_g \approx 0.0$.

Figure 5.32. Tomograms of gas and solids distribution in region 'd' at $Fl_g \approx 0.0386$.

Figure 5.33. Image of *GLS* system in region 'e' at $Fl_g \approx 0.058$ and $Fr \approx 0.31$.

Figure 5.34. Conductivity profile for *GLS* mixing in region 'e'.

Figure 5.35. Normalised conductivity and (ii) Dimensionless conductivity for $Fl_g \approx 0.058$ and $Fr \approx 0.31$

Figure 5.36. Collimated conductivity distributions at 9.6 kHz.

Figure 5.37. Collimated conductivity distributions at 0.3 kHz.

List of Tables

Table 2.1. Flowrates

Table 2.2. Impeller operating conditions.

Table 2.3. d_{10} and d_{32} for the various D/T , ϕ_c/ϕ_d and P/V .

Table 2.4. We power law exponents for all P/V , D/T and ϕ_c/ϕ_d .

Table 2.4. $\bar{\varepsilon}_T$ Power law exponents for all P/V , D/T and Q_c/Q_d .

Table 3.1. Physical properties of the phases.

Table 3.2. Factors, levels and variables for the dense packed region.

Table 3.3. Estimated effects and coefficients table.

Table 3.4. Factors, levels and variables along the vertical plane.

Table 3.5. Estimated effects and coefficients for the C_a in the vertical plane.

Table 4.1. Concentrations of Ni and sodium hypochlorite investigated.

Table 4.2. Ni and sodium hypochlorite concentrations investigated.

Table 4.3. Summary of just suspended speed for gassed and ungassed system.

Table 5.1. *GLS* study operating conditions.

Nomenclature

<i>Ir</i>	Iridium
<i>Ni</i>	Nickel
<i>Pt</i>	Platinum
<i>Pd</i>	Palladium
<i>Rh</i>	Rhodium
<i>Ru</i>	Ruthenium
<i>AC</i>	Alternating Current (mA)
<i>BM</i>	Base metal
<i>CARPT</i>	Computer Automated Radioactive Particle Tracking
<i>CAD</i>	Computed aided design
<i>CCD</i>	Charge-coupled device
<i>CFD</i>	Computational Fluid Dynamics
<i>CT</i>	Gamma-ray computed tomography
<i>CuSO₄</i>	Copper sulphate solution
<i>CVD</i>	Cumulative volume distribution
<i>DAS</i>	Data Acquisition System
<i>DC</i>	Direct Current (mA)
<i>ECT</i>	Electrical Capacitance Tomography
<i>EIT</i>	Electrical Impedance Tomography
<i>EngD</i>	Engineering Doctorate
<i>ERT</i>	Electrical Resistance Tomography
<i>G-L</i>	Gas-liquid

<i>GLS</i>	Gas Liquid Solid
<i>GDT</i>	Gamma Densitometry Tomography
<i>HCl</i>	Hydrochloric acid
<i>JM</i>	Johnson Matthey
<i>JMTC</i>	Johnson Matthey Technology Centre
<i>LDV</i>	Laser Doppler Velocimetry
<i>L-L</i>	Liquid-Liquid
<i>NaOH</i>	Sodium Hydroxide
<i>MRI</i>	Magnetic Resonance Imaging.
<i>NTU</i>	Neophelometric turbidity units
<i>PEPT</i>	Positron Emission Particle Tracking
<i>PBT</i>	Pitched blade turbines
<i>PVA</i>	Polyvinyl Acetate
<i>PDA</i>	Phase Doppler Anemometry
<i>PGM</i>	Platinum Group Metals
<i>PGMR</i>	Platinum Group Metals Refinery
<i>PIV</i>	Particle Image Velocimetry
<i>PVA</i>	Polyvinyl Acetate
<i>RDT</i>	Ruston disc turbine
<i>REIT</i>	Resistance Electrical Impedance Tomography
<i>RSP</i>	Relative span
<i>S-L</i>	Solid-Liquid
<i>SLR</i>	Single-lens reflex

UPBT

Up-pumping pitched blade turbines

Greek symbols

σ	Interfacial tension (mN m ⁻¹)
λ_K	Kolmogoroff length scale (m)
ζ	Surface tension (mN m ⁻¹)
ε_T	Specific turbulent energy dissipation rate (W kg ⁻¹)
$\overline{\varepsilon_T}$	Specific power input (W kg ⁻¹)
Γ_m	Torque
η_E	Pumping effectiveness (N_q/P_o)
ϕ_d	Dispersed phase volume fraction
ϕ_*	Dispersed phase holdup in the dense packed region
θ_t	Mixing time (s)
φ_d	Dispersed phase holdup
φ_g	Gas holdup
ρ_c	Density of continuous phase (kg m ⁻³)
ρ_d	Density of dispersed phase (kg m ⁻³)
ρ_m	Density of mixture (kg m ⁻³)
γ_a	Average shear rate (s ⁻¹)
γ_m	Maximum shear rate (s ⁻¹)
u_K	Kolmogoroff velocity scale (m s ⁻¹)
μ_c	Viscosity of continuous phase (kg m ⁻¹ s ⁻¹)

μ_d	Viscosity of dispersed phase ($\text{kg m}^{-1}\text{s}^{-1}$)
μ_m	Viscosity of mixture of dispersed and continuous phase
ν	Kinematic viscosity ($\text{m}^2 \text{s}^{-1}$)
Ω	Ohm
ψ	Coalescence rate (m s^{-1})
ψ_*	Coalescence rate at inflection point (m s^{-1})
<i>Latin</i>	
a	Interfacial area
$c_1- c_4$	Constant
d	Droplet size (m)
d_p	Particle diameter (m)
d_{max}	Maximum attainable droplet size (m)
d_{min}	Minimum droplet size (m)
d_{10}	Arithmetic mean diameter (m)
d_{32}	Sauter mean diameter (m)
d_{50}	Geometric mean diameter (m)
d_{vx}	x % of the total volume of droplets made up of droplets with diameters smaller or equal to x.
g	Gravitation constant (m s^{-2})
h	Dynamic head (m)
j	Imaginary Term
kHz	Kilohertz
mA	Milliamps

mS	Millisiemens
n_i	Total number of droplets
n_b	Number of blades
r	Radius (m)
r_c	Recirculation ratio
r^+	Radial component (m)
rps	Revolutions per second (s^{-1})
s	Standard deviation
s^2	Variance
t_c	Circulation time (s^{-1})
u	Velocity ($m\ s^{-1}$)
u'	Mean fluctuating part of the turbulent decomposition velocity ($m\ s^{-1}$)
v	Volume (m^3)
y	Exponential constant
y_i^*	Unit length at inflection point (m)
% v/v	Volume of aqueous phase per unit volume of dispersion
% vvm	Volume percentage
% w/w	Mass percentage
z	Axial component
A	Horizontal cross sectional area of the settler (m^2)
$A(h_o)$	Energy of adhesion between two colliding droplets ($kg\ m^2\ s^{-2}$)
B	Baffle width (m)

C_a	Concentration of dispersion (% v/v)
C	Constant
C/H	Clearance to height ratio
D	Impeller diameter (m)
D_s	Settler diameter (m)
D_T	Diameter of torque arm (m)
D/T	Impeller diameter to vessel diameter ratio
E_c	Circulation efficiency number
F	Force parameter
F_d	Drag force (N)
Fr	Froude number
F_t	Restraining force (N)
Fl_g	Aeration number
Ga	Galileo number
H	Vessel height (m)
H_d	Steady state dispersion height (m)
H^g	Height of the mixture after gas introduction (m)
H	Height of the mixture before gas introduction (m)
I	Current (mA)
K	Constant
K_{1-7}	Constant
L_s	Settler length (m)
M	Molar content

N	Impeller speed (s^{-1})
N_c	Dimensionless circulation flowrate
N_{CD}	Completely dispersed point (s^{-1})
N_F	Loading point (s^{-1})
N_{fr}	Frequency of forward and reverse rotation (s^{-1})
N_q	Pumping number
N_R	Grossly recirculated state (s^{-1})
N_{sd}	Optimum impeller speed optimum required to maintain a stable dispersion.
N_{js}	Just suspended speed (s^{-1})
N_{jsg}	Just suspended gassed speed (s^{-1})
P	Power (W)
P_g	Gassed power (W)
P_o	Power number
P_m	Instantaneous power consumed (W)
P_{mav}	Time averaged power consumed (W)
P/V	Power input ($W m^{-3}$)
Q	Pumping capacity ($m^3 s^{-1}$)
Q_d	Dispersed phase flowrate ($m^3 hr^{-1}$)
Q_c	Continuous phase flowrate ($m^3 hr^{-1}$)
Q_g	Aeration rate ($m^3 s^{-1}$)
Q_t	Total dispersed and continuous phase volumetric flowrate ($m^3 s^{-1}$)
Q_d/A	Dispersed phase throughput ($m^3 m^{-2} hr^{-1}$)

Q_c/A	Dispersed phase throughput ($\text{m}^3 \text{m}^{-2} \text{hr}^{-1}$)
Q_c/Q_d	Phase flow fraction ratio
Q_f/A	Total feed throughput ($\text{m}^3 \text{m}^{-2} \text{hr}^{-1}$)
R	Resistance term (Ohms)
Re	Reynolds number
S	Constant
T	Vessel diameter (m)
U_g	Superficial rise velocity (m s^{-1})
U_{tip}	Tip speed (m s^{-1})
\bar{U}	Mean velocity of the turbulent decomposition velocity (m s^{-1})
V_t	Terminal settling velocity (m s^{-1})
V	Volume of the liquid (m^3)
V_v	Voltage distribution ($\text{kg.m}^2 \text{A}^{-1} \text{s}^{-1}$)
W	Watt
W_b	Blade width (m)
W_s	Settler width (m)
We	Weber number
We_{crit}	Critical Weber number
X	Reactance term
X_N	Solids to liquid mass percentage.
Z	Impedance

Chapter 1: Introduction

1.1. Hydrometallurgy

Hydrometallurgy is the process of recovering valuable materials from feed sources by the low temperature contact of the feed by an aqueous solution. It is an important part of metallurgical extraction processes especially in base metal (*BM*), rare earth metal and the Platinum Group Metal (*PGM*) refining industries. It enables the treatment of low grade metal sources, which may not be economically viable in methods such as smelting and it is also a widely accepted process because it is compatible with smelting operations (Wadsworth and Pitt, 1980). The hydrometallurgical flowsheet is comprised of a leach stage, solvent extraction stage and a final metal recovery stage as shown in Figure 1.1.

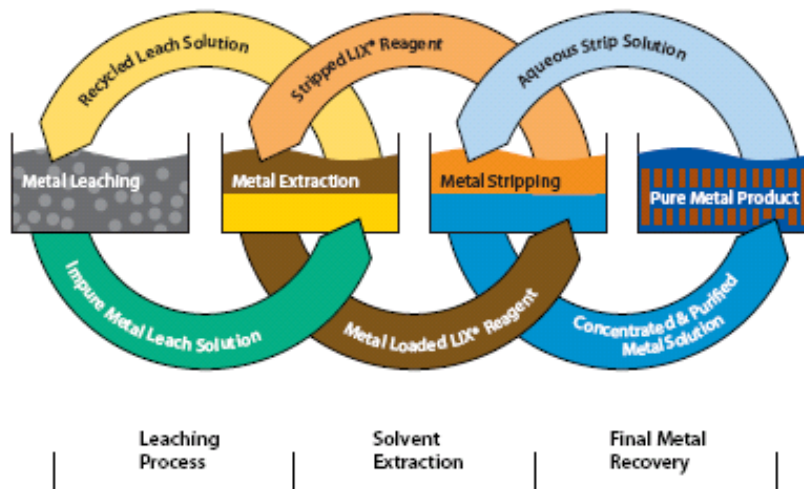


Figure 1.1. Components of Hydrometallurgical Flowsheets.

(www.cognis.com/MCT_Redbook_English.pdf)

The leach stage involves a selective dissolution process whereby valuable or invaluable materials are extracted from a carrier solid into an aqueous solution by suitable lixivants in agitated vessels or confined spaces. In *PGM* refining, the carrier solid is a *BM-PGM* alloy. Lixivants are

reagents such as acids or bases that have a great affinity for the material of interest. During the leach process, *BMs* are dissolved from the alloy in an etching manner by a shrinking-core process (Roman *et al.*, 1974) wherein the reaction occurs on the outer surface of alloys with limited porosity. A sharp reaction interface moves into the solid leaving behind dendrites and an unreacted sponge (Roman *et al.*, 1974). A schematic of the shrinking core process is shown in Figure 1.2. The reaction process is chemical and gas film diffusion controlled, where the balance between the diffusion of the reactant to the particle surface and gas expulsion creates a concentration gradient that limits the rate of reaction.

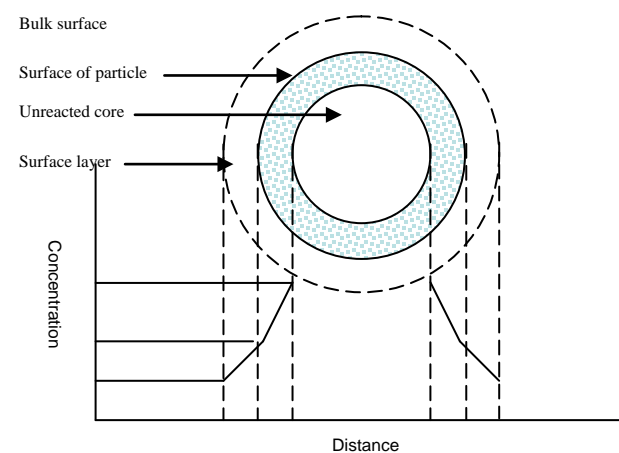


Figure 1.2. Schematic of a reacting particle following the shrinking-core model

Following the leach, solvent extraction is used to selectively recover the metals of interest from the solution. The process is comprised of an extraction and strip stage. In the extraction stage, the solution containing the metal comes into contact with an organic, which contains an extractant. The extractant retrieves the desired metal from the solution. The extractant is a specially designed molecule such as an oxime, amine or organophosphate, which has a high affinity for the metal of interest. After extraction, the metal loaded organic is transferred to a strip stage

where it is contacted with another aqueous phase to recover the metal from the extractant. This stage precedes the final metal recovery stage where precipitation or electrolysis can be used to purify the metal.

On the industrial scale, there are several challenges that must be addressed which are a function of the operating conditions used within each of the unit operations. Agitated vessels are used in the leach stage to disperse solids in liquids, whilst mixer-settlers are used in the solvent extraction stage to contact and separate immiscible liquid-liquid (*L-L*) phases.

Within the agitated vessels used in the leach process, the reaction between the *BM-PGM* alloy and the lixiviant converts a previous solid-liquid (*S-L*) system to a gas-liquid-solid (*GLS*) system because of gas evolution during the reaction process. The presence of gas in *S-L* systems can be problematic for solids suspension. This has been shown by numerous authors, including Warmoeskerken and Smith (1985), Nienow *et al.* (1985) and Bruijn *et al.* (1974). In agitated *GLS* systems, the gas could accumulate in low pressure regions found behind impeller blades, acting as a sink to inertial forces generated by the impeller and leading to solids deposition on the vessel bottom. If this takes place, the leach efficiency will decrease. To improve the efficacy of the leach process under such circumstances, an understanding of the mixing, hydrodynamics and particle behaviour during gas emission is essential.

In solvent extraction, a mixer is initially used to contact the *L-L* phases so that the droplet size distribution necessary for a given extraction rate and residence time is achieved before the contents of the mixer are transferred into the settler. The function of settler is to provide the

necessary residence time for effective phase separation. However, in the design of mixer-settlers, the settler alone constitutes ~ 80 to 90 % of the total unit volume and cost (Eckert, 1989). The operating factors, such as the continuous to dispersed phase flow ratio, Q_c/Q_d (where Q_d and Q_c are the dispersed and continuous phase flowrates), total feed throughput, Q_t/A (where Q_t is the total dispersed and continuous phase flowrate and A is the horizontal cross sectional area of the settler), the continuity and the mixing conditions will significantly alter the settler size, which will subsequently affect metal inventory and equipment footprint. There are correlations in the literature that can be used for settler design; however they are usually unreliable because they require the use of large safety factors (Eckert, 1989), which can lead to an overestimation or underestimation of the settler size. Thus, it is usual practice to conduct laboratory or pilot scale experiments to minimise the errors that could come about before settler design.

In this Engineering Doctorate (*EngD*) Thesis, experiment-based investigative studies are described which have been designed to elucidate the underlying hydrodynamic phenomena which drive the performance of both leach and solvent extraction stages of hydrometallurgical processes, with emphasis placed on the extraction of *PGMs* which is of relevance to the sponsoring company.

1.2. Sponsoring company and industrial perspective

This *EngD* project was sponsored by the Platinum Group Metals Refining (*PGMR*) division of Johnson Matthey (*JM*) located at Brimsdown in Enfield, London and Royston, Hertfordshire, UK. It was carried out at the Johnson Matthey Technology Centre (*JMTC*) at Chilton, Billingham, UK.

JM is a world leader in the marketing, distribution, refining and recycling of *PGMs*. They make an annual operating profit of ~ £170 million in their Precious Metals Products Division alone, which is made up of the Platinum Marketing and Distribution, Noble metals, Catalysts, Chemicals and Refining and Colour Technologies. The profit is obtained primarily in the trading of *PGMs* such as Platinum (*Pt*), Palladium (*Pd*), Ruthenium (*Ru*), Rhodium (*Rh*) and Iridium (*Ir*) as either the refined metals, with selling prices of \$1531, \$656, \$116, \$1589 and \$1085 per ounce (as at December of 2011) or as fabricated products.

Industries with the highest consumption of *PGMs* are the automotive industry driven by autocatalyst manufacturing (~ 9,000,000 ounces of *Pt* and *Pd* annually), chemical industry (~ 4,600,000 of *Pt* and *Pd* annually), the platinum jewellery industry (~ 3,000,000 ounces of *Pt* and *Pd* annually) respectively (as at November of 2011, Platinum Interim Review, 2011).

Generally, in the *PGM* industry:

- The supply of *PGMs* is primarily affected by the ease of extraction and the availability of reserves in the countries of source.
- In the autocatalyst sector the main factor that affects demand is the emissions standards imposed by legislation.
- The prices of metals will also fluctuate due to the risks and uncertainties associated with global demand, supply and commodity prices.

Due to these uncertainties it is important to hasten the flow of metals through the refining circuit to benefit in times of high prices and avoid loss due to the drop in prices. Such benefits are only

achieved by auditing and understanding the chemistry and engineering aspects of each refining unit process to identify and prioritise areas of savings based on financial practicality.

JM employs hydrometallurgical processes in its *PGM* refining circuit wherein gaps in knowledge of gas evolution in the leach and phase disengagement in mixer settlers for solvent extraction were identified. Similarly, fiscal benefits by the reduction of the lead time of these units were identified. This thesis is aimed at optimising these units and improving scientific understanding of these processes for the benefits of both *JM* and the academic community.

1.3. Aims and objectives of the study

This study was carried out to investigate the hydrometallurgical leach and solvent extraction stages of the *PGM* refining process and to advise improvements to enhance process efficiency.

For the *leach stage*:

- A mimic system is used to study particle hydrodynamic behaviour during gas emitting reactions under mixing conditions.
- A novel *GLS* characterisation technique is developed with Electrical Resistance Tomography (*ERT*) that enables gas and solids distribution to be detected and measured in agitated *GLS* systems.

For the *solvent extraction stage*:

- An agitated *L-L* system for *PGM* extraction is investigated using a substitute Copper (*Cu*) aqueous phase solution dispersed in an organic made-up of a kerosene and an oxime (*LIX84-A*). The effects of agitation intensity, P/V (where P and V represent power and volume respectively), Q_c/Q_d and the impeller diameter, D , to vessel diameter, T , ratio on the droplet

size distribution in a mixer are studied to determine the design requirements for a mixer. Then the effect of these factors as well as dispersed phase throughput (Q_d/A) on the dispersion concentration in the settler is investigated to establish the requirements for settler design.

1.4. Scope of investigation and thesis outline

An engineering study of the leach and solvent extraction stages of the refining circuit are thus presented.

In Chapter 1, an introduction to the problem was given to set the background, business case and the aims and objectives of the study. The business case highlighted the problems and business benefit sought from the study.

In Chapter 2, the effects of varying the P/V , Q_c/Q_d and D/T on the droplet size distribution generated in a mixer for a $L-L$ system is presented. An introduction to the problem is initially given, followed by a literature review on droplets including the physics behind droplet breakup, the factors that affect their thermodynamic stability, empirical correlations for droplet size estimation and the droplet size measurement techniques. A detailed materials and methods section is then given before proceeding to the results and discussion. The droplet sizes generated are assessed against theory and fundamental engineering principles in the results and discussions.

In Chapter 3, the effects of the changes in P/V , Q_c/Q_d and D/T within the mixer as well as the Q_d/A on the dispersion concentration in the settler is investigated. The Chapter also starts with an

introduction to the problem, then a literature review on settler operation, dispersion separation and settler scale-up is given before proceeding to the materials and methods used and the results and discussions. Reference is made to the operating conditions in the materials and methods section of the mixer studies because the mixer and settler were combined. In the results section, Minitab[®] was used for factor analysis and quantification of the percentage contribution of each factor to the dispersion concentration. The droplet size distribution at fixed operating conditions that are responsible for the dispersion concentration in the sedimentation layer of the dispersion band are investigated. The change in dispersion concentration in the vertical plane of the settler and the effects of varying the Q_d/A of the settler are also investigated and discussed.

In Chapter 4, the hydrodynamics of spongy solid particles in gas emitting *S-L* reactions is investigated as a mimic to the behaviour of particles found in the leach stage. The study was carried out to understand particle behaviour in gas emitting reactions. An introduction to the problem is initially given, before proceeding to the literature review on *S-L*, gas-liquid (*G-L*) and *GLS* systems to understand the problems faced in multiphase mixing. Then the materials and methods section follows. The experimental techniques used to measure gas evolution rate and gas holdup (ϕ_g) are presented. Then the results obtained are presented and discussed.

In Chapter 5, Electrical Resistance Tomography (*ERT*) is used in a novel approach to characterise an agitated *GLS* system. This study carries on from the problem faced in Chapter 4. The Chapter commences with an introduction to the problem, then a literature review on the techniques that have been used to characterise phase distribution in multiphase systems before proceeding to the materials and methods. In this section the equipment used is detailed whilst in

the results and discussions, the concept behind the *GLS* characterisation technique is demonstrated before being applied to an agitated *GLS* system. Limitations to the technique that were identified are also highlighted.

In Chapter 6, an overall conclusion is given, appraising the objectives set to the findings of the study. The future work is also suggested wherein technologies transfer to the company's processes is advised and gaps in the studies are disclosed for further investigation.

Chapter 2: Hydrodynamic study of an aqueous-organic LIX84-A system agitated by a Rushton Disc Turbine (RDT) in a box mixer

2.1. Introduction

For any defined liquid-liquid ($L-L$) extraction process, the thermodynamic equilibria and extraction rates can be obtained by a set of laboratory-scale experiments. However to scale-up the process, it is important to consider the hydrodynamics of the system, since the rate of mass transfer will depend on the interfacial area of the droplets generated, which can become rate limiting if the desired hydrodynamic requirements are not met.

Studies on $L-L$ systems with low dispersed phase fraction, ϕ_d , are extensive and the majority have primarily been used to understand the physics behind droplet formation. This has led to the development of empirical correlations for droplet size estimation (Hiraoka *et al.*, 1990; Gnanasundaram, 1979; Brooks, 1979). Whilst these correlations are suitable for approximating droplet size in such model systems, extrapolation to scaled-up systems where process variability exists from both mechanical and chemical aspects presents significant risk.

In the design of a mixer, the disadvantage of using correlations could be the overestimation or underestimation of the interfacial area for a given extraction efficiency, which subsequently could lead to inadequate mixer sizing. Obtaining an understanding of how the interfacial area of $L-L$ systems changes with respect to the hydrodynamics in a mixer is usually achieved by conducting a study on the effects of operating conditions such as the power input, P/V (where P

and V are the power and volume respectively), continuous to dispersed phase flow ratio, ϕ_c/ϕ_d , (where ϕ_c is the continuous phase fraction), impeller type and impeller diameter, D , to vessel diameter, T , ratio.

In this Chapter, the effects of changing these operating conditions on the droplet size distribution of $L-L$ systems for Platinum Group Metal (PGM) extraction in a box mixer equipped with a single 6 bladed Rushton disc turbine (RDT) was investigated. Three different $RDTs$ were used with different D/T ratios (categorised as small, mid-range and large) to agitate a previously equilibrated aqueous in organic LIX84-A system at three different ϕ_c/ϕ_d and P/V . Two of the P/V used were above and below the ideal P/V that can maintain a stable dispersion, dispersed phase holdup (ϕ_d) and deter emulsification. The ϕ_c/ϕ_d was varied to consider possible changes to ϕ_c/ϕ_d that could be required during plant operation due to the degradation of the extractant.

The aqueous phase contained Copper (Cu) rather than PGM salts to prevent skin sensitisation. Theoretical relationships such as the relationship between droplet size and Weber number (We) and droplet size and specific power input ($\bar{\varepsilon}_T$) were used to analyse the effects of P/V on droplet size, whilst the relationship between droplet size and impeller tip speed (U_{tip}), droplet size and pumping capacity (Q) and droplet size and ϕ_d , were analysed on the basis of fundamental engineering principles.

The Chapter begins with a literature review on droplet studies. The droplet breakup process in turbulent systems is given to provide a phenomenological understanding of the breakup process.

Then droplet coalescence and the factors that promote it are discussed. This is followed by a review of the general impeller flow patterns in agitated systems and the techniques that are used to measure droplet size distributions. Then materials and methods used are described and then the results of the study are presented and discussed.

2.2. Literature review

2.2.1. Droplet breakup in turbulent L-L systems

When *L-L* systems are agitated, one of the phases is dispersed into the other, forming a dispersion. During the mixing process, equilibrium between droplet breakup and droplet coalescence is established.

The droplet size distribution that emerges in the process will depend on the specific turbulent energy dissipation per unit mass of fluid (ε_T), which is a measure of the turbulence intensity, viscosity of the fluid (μ) and the ϕ_c/ϕ_d .

Richardson's (1926) work inspired studies on how turbulence alters system properties. Turbulence was considered as being composed of a series of whorls or 'eddies'. Eddies are individual events, which can be categorised in terms of characteristic lengths, or frequencies.

He introduced the concept of an energy cascade wherein large eddies breakup to form smaller eddies, transferring most of their kinetic energy in the process and dissipating very little in the form of heat. The smaller eddies generate yet even smaller eddies until most of the turbulent energy is dissipated by viscous forces.

Following Richardson's (1926) work, Kolmogoroff (1941) showed that eddy dissipation follows a transitional process. It was reasoned that the size of the smallest fluctuations in the turbulent field are independent of the size of the initial large eddies and only a function of the fluid properties and energy input to the system. The initial large eddy is an eddy that has a length scale based on the problem domain geometry.

The next scale is called an integral scale, which provides a measure of the extent of the problem domain and finally the Kolmogoroff scale which is the smallest of the turbulence scales. Eddies smaller than the Kolmogoroff scales are dissipated as heat.

Using dimensionless analysis, the Kolmogoroff length scale (λ_K) and velocity scale (u_K) are related to the ε_T and the kinematic viscosity (ν) by the relationships:

$$\lambda_K = \left(\frac{\nu^3}{\varepsilon_T} \right)^{1/4}, \quad (2.1)$$

$$u_K = (\varepsilon_T \nu)^{1/4}. \quad (2.2)$$

The Reynolds number, (Re) is a dimensionless number that is used to quantify the balance of viscous and inertial forces acting on fluids. It is estimated using the general equation given below:

$$Re = \frac{ul\rho}{\mu}, \quad (2.3)$$

where u denotes the fluid velocity, l is a characteristic length scale and ρ is the fluid density. In agitated vessels the length and velocity are based on the D and $U_{tip} \propto ND$ respectively, giving the equation below:

$$Re_{imp} = \frac{ND^2\rho}{\mu}, \quad (2.4)$$

where N is the rotational speed. For vessels with a turbine impeller having a D which is equal to 0.5 or 0.33 T of a baffled vessel, the flow will be turbulent if the Re exceeds 10000. The flow will be transitional when Re rests between 10 and 10000, whilst laminar flow will be observed at the $Re \approx 10$ (Perry *et al.*, 1984).

Kolmogoroff (1941) suggested that at high Re , turbulence within a small domain may be considered as being isotropic. The assumption was based on the consideration that anisotropy within the bulk flow would be considerably larger than anisotropy in a small domain.

Turbulent flow was considered as being isotropic when the distribution of magnitude and frequency of the velocity fluctuations are equal in all directions. However, anisotropy will always exist regardless of domain size.

Batchelor (1952) applied Kolmogoroff's (1941) theory to L - L systems. A model that can be used to estimate the maximum attainable droplet size (d_{max}) in turbulent flow was developed. It was based on the assumption that if a droplet is larger than λ_K , then it will fall within a turbulent-inertial regime, where inertial forces will dominate droplet breakup. However, if the droplet is smaller than λ_K , then it will fall within a turbulent-viscous regime where viscous forces will dominate droplet breakup.

When inertial forces dominate droplet breakup, the mean fluctuating part of the turbulent decomposition velocity (u') over the droplet surface will be responsible. This property is made up of ε_T and the eddy length scale, d , as shown by the relationship below:

$$u'^2 = c_1 \varepsilon_T^{2/3} d^{2/3}. \quad (2.5)$$

Batchelor (1952) found c_1 to be equal to 2. In conditions where viscous forces dominate, the relationship can be explained by the correlation below:

$$\bar{U}^2 = c_2 \frac{\varepsilon_T d^2}{\nu}, \quad (2.6)$$

where c_2 is a constant and \bar{U} is the mean velocity of the turbulent decomposition fluctuation. By combining u' and \bar{U} the Reynolds turbulent decomposition velocity (u) shown below is obtained:

$$u = \bar{U} + u'. \quad (2.7)$$

The balance between the Laplace pressure, which opposes deformation of the droplet and the u' , which deforms the droplet results in the Weber number (We). We is a dimensionless group, which is the ratio of inertial to Laplace forces. It is expressed as:

$$We = \frac{du'^2 \rho_c}{\sigma}, \quad (2.8)$$

where σ is the surface tension and ρ_c is the density of the continuous phase. In impeller agitated systems, when inertial forces dominate break-up, it is usual to use an impeller Weber number (We_{imp}), which is expressed as:

$$We_{imp} = \frac{N^2 D^3 \rho_c}{\sigma}. \quad (2.9)$$

In agitated systems, a distribution of droplet sizes is normally produced in which a d_{max} exists. In such a case, a critical We can be calculated. d_{max} in the inertial regime can be determined by assuming that We is equal to 1 and substituting for u^2 in Equation 2.8. This leads to the expression below:

$$d_{max} = \left(\frac{\sigma}{c_1 \rho_c \varepsilon_T^{2/3}} \right)^{3/5}. \quad (2.10)$$

For a fully baffled vessel, $\varepsilon_T = KN^3 D^2$, where K is a constant. For energy dissipated at the impeller tip, by substituting for ε_T in Equation 2.10, the expression below is obtained for d_{max} :

$$d_{max} = Kc_1 \sigma^{3/5} \rho_c^{-3/5} N^{-6/5} D^{-4/5}. \quad (2.11)$$

It is very important to understand that this approach is only valid for non-coalescing systems (Hinze, 1955). Brown and Pitt (1972) showed that the Sauter mean diameter (d_{32}) can be directly correlated to the d_{max} of a given droplet size distribution. d_{32} is the ratio of the droplet's cumulative volume and its overall surface area as denoted below:

$$d_{32} = \frac{\sum (n_i d_i)^3}{\sum (n_i d_i)^2}, \quad (2.12)$$

where n_i is the number of droplets with diameter, d_i .

d_{32} is important because it can be used to estimate the interfacial area of contact between the phases per unit volume (a) of a dispersed system. ' a ' can be obtained from the expression:

$$a = \frac{6\phi_d}{d_{32}}, \quad (2.13)$$

where ϕ_d is the dispersed phase volume fraction. Chen and Middleman (1967), Brown and Pitt (1972), Sprow (1967) and many others have shown that d_{max} is linearly related to d_{32} by the relationship:

$$d_{32} = K_2 d_{max}, \quad (2.14)$$

where the constant K_2 varies from 0.38 to 0.7. Calabrese *et al.* (1986b) used a value of 0.6 for *RDT*, whilst Pacek *et al.* (1998) assessed the advantage of K_2 from the droplet size distributions of several dispersions.

For dilute and low μ systems, the equation below has been obtained for *RDT*.

$$\frac{d_{32}}{D} = K_3 We_{imp}^{-0.6}. \quad (2.15)$$

This correlation was found suitable for predicting d_{32} in turbulent systems at high *Re* where the assumption of local isotropy is permitted.

2.2.2. Droplet size in turbine agitated vessels

A large amount of studies on droplet breakup have been carried out in turbine agitated vessels. Most authors have worked with organic dispersed *L-L* systems and their results have been reported in terms of d_{32} .

The first set of expressions developed for the estimation of droplet sizes was developed by Chen and Middleman (1967) and Sprow (1967). The systems they used contained very dilute

dispersions, where the role of coalescence was considered as negligible and the expression was therefore assumed to agree with Kolmogorov-Hinze's theory (Hinze, 1955).

Vermeulen *et al.* (1955) indirectly measured the interfacial area of $L-L$ dispersions with ϕ_d within the range of 10 to 40 % by means of a light transmittance technique in a baffled cylindrical vessel. A wide range of interfacial tensions was studied and led to the development of a We correlation that was based on the density of the dispersion as denoted below:

$$\frac{d_{32}}{D} = K_4(1 + B\phi_d)We^{-0.6}, \quad (2.16)$$

where the ϕ_d in the expression took into account the effects of coalescence. Their data deviated by $\sim \pm 60\%$.

Shinnar and Church (1960) also developed a correlation that incorporated the effects of coalescence. This is given below:

$$\frac{d_{32}}{D} = K_5We^{-0.375} \left(\frac{A(h)}{\sigma D} \right)^{0.375}, \quad (2.17)$$

where $A(h)$ is the adhesion force which is equal to the energy of adhesion between two droplets separated by a distance h .

Kafarov and Babanov (1959) measured the average droplet size generated in geometrically similar vessels with ϕ_d within the range of 5 to 35 %. By using dimensional analysis Equation 2.18 was developed:

$$\frac{d_{32}}{D} = K_6 We^{-0.5} Re^{-0.1} \varphi^{0.16}, \quad (2.18)$$

where K_6 varies with impeller type. All authors agreed that beyond a critical ϕ_d of $\sim 15\%$ coalescence should be taken into account.

2.2.3. Droplet coalescence in L-L systems

The droplets that are produced during agitation depend on the dynamic balance between droplet break-up and droplet coalescence. At equilibrium, droplet break up will depend on the balance between the interfacial forces that hold the droplets together and the disruptive forces that pull them apart. This will lead to a constant droplet size distribution.

Droplet coalescence takes place in three steps. The first is droplet-droplet interaction, then the thin film drainage between the colliding droplets before the rupturing and exchange of their contents to form a single droplet.

The first two steps control the rate of coalescence independently, whilst the latter is faster and may not occur in all droplet encounters. Shinnar and Church (1960) suggested that there is a minimum stable droplet size (d_{min}) wherein separation after collision can happen and where also for droplets with diameters larger than d_{min} coalescence will be impossible. d_{min} is also the size of the smallest droplets for which coalescence will be slowed by turbulence.

Using $A(h)$ and the kinetic energy droplet-droplet collision the expression denoted below for the minimum droplet volume as a function of droplet diameter was obtained.

$$d_{\min} = c_3 N^{-3/4} D^{-1/2} \rho_c^{-3/8} A(h_o)^{3/8} . \quad (2.19)$$

The expression was confirmed experimentally in a coalescing system. For a system where viscous effects dominate, the equation below was also developed:

$$d_{\min} = c_4 F^{-3/4} V_c^{1/4} \mu_c^{-1/2} N^{-3/4} D^{-1/2} , \quad (2.20)$$

where c_3 and c_4 are factors that depend on the critical rupture thickness whilst F is a force parameter.

2.2.4. Droplet size distribution

Droplets are usually assumed to be spherical in shape. If droplets in a dispersion are of identical size, they are said to be monodisperse. However, in practice dispersions are made up of a distribution of droplet sizes, thus they are polydisperse.

Droplet size distributions can be characterised by their cumulative distribution or density distribution functions. The cumulative distribution is defined as:

$$\frac{\textit{The amount of droplets} \leq \textit{droplet size}}{\textit{Total amount of droplets}} , \quad (2.21)$$

where $0 \leq \text{cumulative distribution} \leq 1$.

The normal distribution function, which is widely used in the study of the random occurrence on which it is based, is represented by the expression below:

$$f_n(d) = \frac{1}{s\sqrt{2\pi}} \exp \frac{-(d - d_{10})^2}{2s^2} , \quad (2.22)$$

where d_{10} is the arithmetic mean, which is arithmetic mean value of the total number of droplets in a sample, π is a mathematical constant, which is approximately equal to 3.14159, $f_n(d)$ is the probability density, whilst s and s^2 are the standard deviation and variance respectively. d_{10} and s are important parameters that determine the shape of the function.

The log normal distribution produces a normal distribution about the geometric mean (d_{50}). d_{50} is a mean which indicates the central tendency or typical value of a set of numbers. A straight line is obtained when the natural log is plotted against the cumulative percentage frequency. The log normal distribution is expressed as:

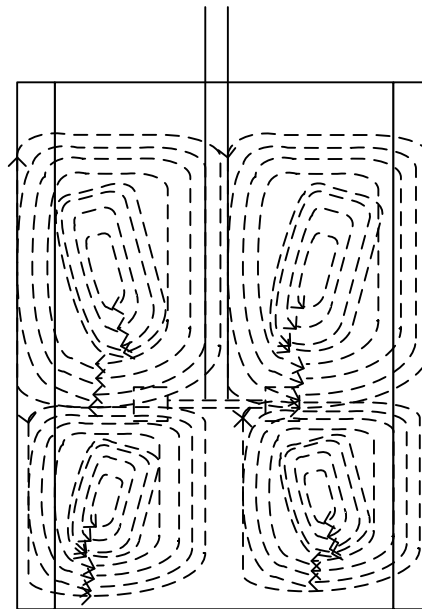
$$f'(d) = \frac{1}{s \sqrt{2\pi}} \exp \frac{-(\ln d - \ln d_{v0.5})^2}{2s^2}, \quad (2.23)$$

where $d_{v0.5}$ is the droplet size measured in volume corresponding to 50 % of the cumulative droplet population. Generally, the droplet size distribution is preferred to the d_{32} when estimating the mass transfer in $L-L$ systems. This is because the droplet size distribution takes into account the polydisperse nature of dispersions to produce a more accurate measure of 'a'. d_{32} however is a single representative value.

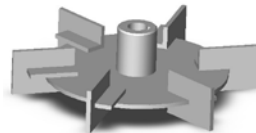
Sprow (1967), Brown and Pitt (1972), Coualoglou and Tavlarides (1976), Brooks (1979) and Narasimhan *et al.* (1980) all studied the droplet size distributions of systems absent of mass transfer. Using a photography technique, Brown and Pitt (1972) found a normal distribution by measuring the volume of droplets normalised by d_{32} . They derived an expression for estimating the droplet size distribution based on the droplet volume.

2.2.5. Turbines and flow patterns

Turbines used to agitate $L-L$ systems can be categorised as turbines that produce radial or axial flow patterns, or a mixed flow which is a combination of the two. Turbines such as RDT produce radial flow, whilst pitched blade turbines (PBT) produce axial flow, tending towards mixed flow as D/T is increased (Young *et al.*, 2003). Radial flow exists when fluid is ejected from a turbine perpendicular to its axis of rotation whilst axial flow exists when the discharge is parallel to the axis of rotation. These flow patterns are illustrated below.



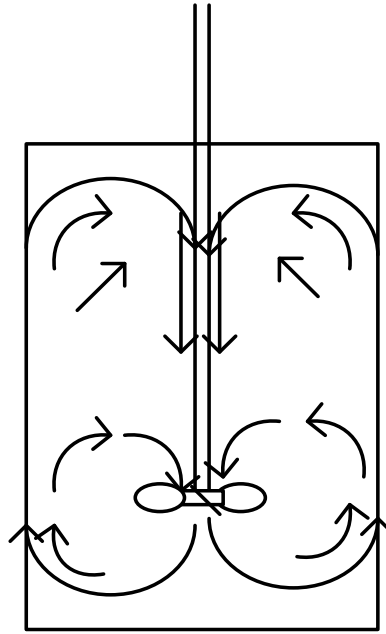
(a)



(b)

Figure 2.1. (a) Radial flow pattern of a fully baffled vessel (b) Rushton disc turbine (RDT)

(Taken from <http://www.postmixing.com/mixing%20forum/impellers/rt.htm>)



(a)



(b)

Figure 2.2. (a) Axial flow pattern of (b) Pitched blade turbine (PBT)

(Taken from <http://www.postmixing.com/mixing%20forum/impellers/rt.htm>)

The flow pattern of viscous fluids was investigated by Metzner and Taylor (1960). They compared Newtonian and non-Newtonian fluids, by varying agitation intensities and Re . They found out that the flow pattern in non-Newtonian fluids was centered around the impeller periphery whilst the flow pattern in Newtonian fluids spread into the bulk fluid.

In unbaffled vessels, agitation by impellers produces tangential flow which causes bulk fluid rotation as a solid body. This leads to poor mixing efficiency due to the creation of a vortex. To

prevent this, the addition of baffles is necessary; however the consequence is higher power demand.

During the discharge from the impeller tip, the horizontal velocity of the fluid decreases towards the vessel wall due to the decrease in momentum. The stream splits at the wall leading to tangential fields towards the bottom and top of the vessel and then circulation loops develop. The circulation loop is comprised of four zones. These are the horizontal discharge jet, which commences from the impeller tip to the vessel wall, the vertical flow parallel to the wall, the horizontal flow parallel to the impeller, and finally a downward vertical flow to the impeller.

The discharge and subsequent spreading of the jet towards the vessel wall leads to an initial rapid decrease of the fluid velocity from the impeller, whilst in other zones of the vessel the velocity gradients are smaller in magnitude. The mean velocity of the circulation loop during agitation was determined by Holmes *et al.* (1963) and estimated to be equal to the velocity at the end of the discharge jet.

Droplets will travel at a velocity relative to the carrier fluid known as the slip velocity. This velocity is needed for hydrodynamic and mass transfer calculations. It cannot be estimated in agitated dispersions due to the complication of the superimposition of other components of motion such as the turbulent fluctuations of the droplets in complex regions of turbulence. The slip velocity is a function of droplet size and will vary from point to point, making a representative mean value difficult to estimate. In practice, the slip velocity is crudely estimated from the terminal settling velocity of droplets.

2.2.6. Power requirements for low viscosity fluids

In dissimilar sized vessels, typical geometric, kinematic and dynamic properties are required if similar flow patterns and power consumption are desired upon scale-up. Geometric similarity can be achieved when the ratio of the dimensions of two or more systems are similar. Kinematic similarity is achieved when the ratio of velocity vectors at typical points in the system are similar. Dynamic similarity occurs when both geometric and kinematic similarities are achieved.

White and Brenner (1934) suggested a correlation by dimensional analysis to determine the power consumed in single phase systems by geometrically similar vessels, which is denoted below:

$$P_o = C(Re)^m (Fr)^n , \quad (2.24)$$

where Fr is the Froude number, which is ratio of inertial to gravity forces expressed as:

$$Fr = \frac{u}{(g l)^{1/2}} , \quad (2.25)$$

where g is the gravitational force and P_o is the power number, expressed as:

$$P_o = \frac{P}{\rho_m N^3 D^5} , \quad (2.26)$$

Where P represents the power whilst C , m and n are constants that vary with impeller type. In fully baffled vessels, where gravitational forces are considered negligible due to the absence of vorticing, viscous forces will dominate the flow pattern reducing Equation 2.24 to the form:

$$P_o = K_7 (Re)^m . \quad (2.27)$$

Therefore, for baffled vessels, dynamic similarity can be obtained in geometrically similar vessels operated under the same Re . For $Re \leq 10$, m is -1 therefore the equation becomes:

$$P = K_7 \mu N^2 D^3. \quad (2.28)$$

K_7 varies with impeller type, D/T and vessel configuration. For higher values of Re , Fr will affect the pumping number (N_q), which is defined later below.

2.2.7. Pumping capacity and circulation flowrates

The pumping capacity, Q , of an impeller is the volumetric flowrate that leaves the impeller blades. It is the product of the fluid velocity leaving the impeller blades by the area described by the blade tip. Q can be estimated from the impeller swept volume, as shown by the relationship below:

$$Q = \int_{w/z^-}^{w/z^+} \pi D (v_r)_{r^+} dz + \int_0^{r^+} 2\pi r (v_z)_{z^+} dr + \int_0^{r^+} 2\pi r (v_z)_{z^-} dr, \quad (2.29)$$

where z^+ and z^- are the axial boundaries of the swept volume, whilst r^+ is the radial boundary.

The expression accounts for the radial and axial flowrates from impellers.

For axial impellers the radial components of the equation are zero, whilst the axial components are zero for radial impeller. The Q can be normalised to N_q by the expression:

$$N_q = \frac{Q}{ND^3}. \quad (2.30)$$

The circulation flow rate (Q_{cf}) in the vessel is the total volumetric turnover rate that occurs in the vessel (Aubin *et al.*, 2001). It is obtained by combining the discharged fluid flow and the flow entrained by the impeller (Tatterson, 1991).

When axial symmetry is assumed, the absolute maximum values of the axial flow rate (Q_z) will be equal to the total Q_{cf} as shown below:

$$Q_z = Q_{cf} = \int_r^R 2\pi r (v_z)_{z^*} dr . \quad (2.31)$$

The total Q_{cf} can be evaluated by calculating the flowrate through a plane that passes through the centre of the circulation loop having radial and axial coordinates (r^* , z^*).

For two circulation loops, the axial Q_{cf} is given by the sum of the flow entrained by the lower loop and the flow entrained by the upper loop i.e.

$$Q_{cf} = Q_{cf1} + Q_{cf2} , \quad (2.32)$$

where

$$Q_{cf1} = \int_r^R 2\pi r (v_z)_{z^{*1}} dr \quad (2.33)$$

and

$$Q_{cf2} = \int_r^R 2\pi r (v_z)_{z^{*2}} dr . \quad (2.34)$$

By normalising the Q_{cf} by ND^3 a dimensionless circulation flowrate (N_c) is obtained:

$$N_c = \frac{Q_c}{ND^3} . \quad (2.35)$$

To quantify the effectiveness of an agitator, the N_q , N_c and P_o can be used to develop two indices. These are the pumping effectiveness (η_E) and the circulation efficiency number (E_c). E_c is used to calculate the impeller's capacity to circulate the liquid with respect to its power

consumption. η_E is used to obtain the pumping rate of the impeller per unit power consumption and can be calculated from the expression:

$$\eta_E = \frac{N_q}{P_o}. \quad (2.36)$$

Jaworski *et al.* (1991) developed relationships that can enable the comparison of different types of impellers and sizes in the turbulent flow regime independent of N . It is denoted below:

$$E_c = \frac{N_c}{P_o} \left(\frac{D}{T} \right)^4. \quad (2.37)$$

2.2.8. Circulation capacity and circulation time

The vessel geometry and Q of a given impeller determines the circulation capacity. The circulation capacity is equal to the contents of the vessel over circulation time (t_c) in the absence of stagnation. The circulation capacity governs the mixing time (θ_t) of a system and is of greater importance than Q . t_c is $\sim 1/5$ of θ_t .

A decolourisation technique was used by Brennan and Lehrer (1976) to study impeller mixing in vessels. They used methyl red indicator with neutralisation of sodium hydroxide ($NaOH$) by hydrochloric acid (HCl). The θ_t commenced when HCl was added into the methyl red - $NaOH$ solution and it ended when the colour changed. They found that for $10^4 \leq Re \leq 3 \times 10^5$.

$$N\theta_t \propto Fr^{0.063}. \quad (2.38)$$

Sano and Usui (1985) used a different technique to determine the θ_t in stirred vessels. By using a conductivity probe they followed the change in the mixing conditions by monitoring the electrical disturbance in the system. Ruszkowski (1994) and Sano and Usui (1985) showed that θ_t could be expressed by the correlations given below for a paddle and *RDT* respectively:

$$N\theta_t = 2.1(D/T)^{-1.67} (W_b/T)^{-0.74} n_b^{-0.47}, \quad (2.39)$$

$$N\theta_t = 3.8(D/T)^{-1.8} (W_b/T)^{-0.51} n_b^{-0.47}, \quad (2.40)$$

where n_b represents the number of blades and W_b is the blade width.

2.2.9. Droplet measurement techniques

A number of measurement techniques can be used to characterise droplets and they can be categorised as direct or indirect methods. Direct methods are photographic techniques such as vessel wall photography, photographic probe and microscopic photography. Indirect methods are sound and laser measurement techniques such as light scattering, Coulter counter and acoustic wave techniques.

2.2.9.1. Direct methods

These techniques are considered as accurate methods of obtaining droplet shape, droplet size and droplet size distributions. In these techniques still images are taken for analysis and the continuous phase interface has to be distinguishable from the droplets for image clarity and analysis.

Photography through vessel walls

Using a single-lens reflex (*SLR*) magnification camera with a high speed flash unit affixed, Calabrese *et al.* (1986a) observed droplets breaking up above an impeller from the wall of a vessel. Optical distortion was reduced by using a water-filled Plexiglass box that surrounded the vessel wall. A low ϕ_d of 0.0015 was investigated.

The droplet sizes obtained from the experiments were estimated from photographs taken. An issue highlighted with this technique was that the photographs of droplets could overlap leading to unrepresentative droplet sizes. Godfrey and Slater (1994) also stated that the droplet hydrodynamics at the wall may be such as to give non-representative droplet size distributions.

Photography with probes

Pacek and Nienow (1995) used a high quality image camera to obtain droplet size from high ϕ_d systems through a stereo microscope from the outer and inner part of their vessel through a light tube. The light source was synchronised with the camera and the pictures obtained were scanned for overlapping droplets by a recognition software.

With this technique droplet size of $\geq 25 \mu m$ were obtained. The technique is fast and benefits from data acquisition and probe manoeuvrability. However the technique is intrusive since light scattering has to be achieved behind the focal plane by a strobe light. Nevertheless intrusion can be considered negligible where the probe to vessel size ratio is very small.

Sample withdrawal and photography

This technique is the simplest way of measuring droplet size distributions. Samples are simply withdrawn from dispersions and placed on a microscope for photographing before image analysis. Lagisetty *et al.* (1986) used the sample withdrawal and microscopic photography technique to study droplet breakup in agitated dispersions. By using low ϕ_d they avoided the issue of coalescence and developed a correlation that was suitable for estimating d_{32} and d_{max} .

Collias and Prud'homme (1992) looked at the effect of shear and elongation on droplet production via the same technique to obtain d_{max} expressions for *RDT*. Nishikawa *et al.* (1987) used the technique to investigate droplet breakup within coalescence and breakup regions of a stirred vessel. Yang *et al.* (2000b) withdrew dispersions unto petri dishes for photography with a microscope. Due to the tendency for the droplets to coalesce Polyvinyl Acetate (*PVA*) was added to stabilise the droplets

2.2.9.2. Indirect methods

Sound measurement techniques

This technique can be divided into acoustic and electroacoustic spectroscopy. Acoustic spectroscopy measures the attenuation and sound speed of ultrasound pulses over a wide range of frequencies as they pass through dispersions. Smith *et al.* (1974) developed the technique for the simultaneous determination of ϕ_d and droplet size by analysing the difference in transmission of sound waves in dispersions.

The most significant advantage of the technique is its ability to process information received without time delay, however it is limited on the ϕ_d and droplet size that can be detected. The upper limit of the ϕ_d that has been investigated by acoustic spectroscopy is 0.05 (Cents *et al.*, 2004). Electroacoustic spectroscopy on the other hand takes measurements of the interaction between the electric and acoustic fields for zeta potential measurements. It is a relatively new technique and an extensive review is given by Dukhin and Goetz (2002).

Laser techniques

These techniques are fast and provide qualitative information on dispersed systems which can be calibrated to obtain accurate mean droplet size. All measurements are obtained directly from the vessel without the need for sample withdrawal.

Rotating laser beam technique

In this technique, a beam from a laser diode is focused through a lens to produce a small focal point of high intensity. The lens is rotated at a known velocity to produce a circular scanning beam. When the beam meets a droplet, light is backscattered and recorded by a detector that is mounted behind the lens. Since the scanning velocity and time delay of backscatter is known, the characteristic diameter of the droplet can be obtained. The probability of the beam hitting any part of the projected droplet area is equal, thus a chord length is measured instead of a droplet diameter. The resulting cord length distribution can be transformed into a drop size distribution.

Phase-Doppler Anemometry (PDA)

PDA is used to measure droplet size and the velocity distribution of droplets. For droplet size measurements, laser beams from a transmitter cross a focal point in front of a lens. Receivers at a given angle are also focused at the same focal point. They collect the scattered light based on the refractive indexes of the continuous and dispersed phase intensity and the polarisation at their viewing angles. The droplet size is obtained based on the phase difference between the signals received by two detectors.

Zhou and Kresta (1998b) developed the technique for *L-L* systems. It was used to measure the droplet velocities by Crowe *et al.* (1997) and it was also used by Wille *et al.* (2001) to understand the effects of *D/T* on droplet size. The limitations associated with the technique include its application to only low ϕ_d and the requirement of highly dissimilar diffractive indices.

Laser Diffraction

This is a laser based technique that follows the Fraunhofer diffraction theory, which states that for particles larger than the wavelength of an incident light, the majority of the light is diffracted in the forward direction. To obtain droplet size measurements, collimated and vertically polarised laser beams are directed into droplets, which diffract the rays with a primary undiffracted ray located central to the diffracted rays. A concentric light sensitive detector measures the diffraction intensity which is then transformed by Fourier optics into a spatial intensity distribution that is proportional to the droplet sizes.

Kissa (1999) stated that the technique is advantageous because droplet size measurements can be obtained regardless of droplet movement because the diffraction pattern remains stationary making the technique suitable for in-line analysis. The diffraction patterns can be affected by droplet shape because of the assumption of droplet sphericity used to develop the technique. Another issue is the appearance of so-called “ghost” droplets in the distribution due to droplet transparency.

Coulter Counter

The Coulter counter method is an electrically applied technique which is based on measurements of electrical disturbance brought about by droplets suspended in ionic solutions. Key to this technique is the stabilisation of droplets to avoid coalescence.

Stabilised droplets are passed through an orifice with electrodes that permit electrical flow. Droplets that pass through the orifice displace a family of electrolytes which are proportional to the volume of the droplet altering the electrical potential between the electrodes. This creates an electrical pulse with an amplitude proportional to the droplet volume.

Droplets within the range of 0.4 to 400 μm have been measured by this method (Kissa 1999). As highlighted initially, a key requirement when using this technique is droplet stabilisation which is an issue in practice because contaminants are not welcome. Thus optionally samples could be withdrawn and stabilised. Distorted pulse shapes are technical issues that can arise in this technique if two or more droplets pass through the orifice, thus the dilution of concentrated dispersions is necessary.

2.3. Conclusion from literature review

The literature review has shown that the physics, including the part played by inertial and the interfacial forces on droplet breakup in *L-L* agitated systems is well documented. The techniques that can be used to measure droplet size distributions are abundant and correlations that can be used to estimate droplet sizes are also well established.

However, a major theme from the review was that the correlations and understanding of droplet behaviour in *L-L* systems were primarily obtained from low ϕ_d experimental systems. Most solvent extraction mixers are operated at high ϕ_d , which will increase the tendency for error if predictions were employed.

Likewise, most studies were carried out with organic dispersed system, which further complicates the case for using correlations since in practice different phase continuities are used. In this study, an aqueous dispersed system is investigated at high ϕ_d .

2.4. Materials and methods

2.4.1. The phases

The effects of mass transfer on droplet size was not investigated, therefore pre-equilibrated organic and aqueous phases were used. A mimic system in which *Cu* was substituted for the *PGM* species due to cost and sensitisation issues. The organic was comprised of 12 mL of LIX 84-A (Cognis) for every 100 mL of organic (i.e. 12 % *v/v*), 87.8 % *v/v* of Solvesso 150 (Exxon Mobil) and 0.15 % *v/v* of Primene™ JM-T (DOW group). The aqueous phase was made up of 33 g of *Cu* for every litre of the aqueous phase solution (g L⁻¹). The aqueous phase was comprised

of *Cu* as copper sulphate solution ($CuSO_4$) in 0.7 Molar (*M*) *HCl*. Three ϕ_c/ϕ_d were used i.e. 1:1, 3.5:2 and 3.5:1. For all ϕ_c/ϕ_d , the total flowrate of the organic and aqueous phase, $Q_t = 2.96 \text{ L hr}^{-1}$. They corresponded to ϕ_d of 0.5, 0.36 and 0.22 respectively.

Table 2.1. Flowrates

ϕ_c/ϕ_d	Flowrate (L hr ⁻¹)	
	Organic	Aqueous
1:1	1.48	1.48
3.5:2	1.89	1.07
3.5:1	2.30	0.66

2.4.2. Mixer-settler design considerations

An integrated box mixer-settler unit was used. A computer aided design (*CAD*) is given in Figure 2.3 and a flow diagram is shown in Figure 2.4. Polymethyl methacrylate (Perspex) was used as the material of construction. It was not chemically inert to the organic and did unavoidably deteriorate gradually with usage. However, to avoid cross contamination in subsequent runs, the walls of the vessel were washed thoroughly after each run with propanol and distilled water to remove degraded Perspex.

2.4.3. The Mixer

The mixer was fully baffled with a square cross section. It had a $T = 0.13 \text{ m}$ and height, $H = 0.77T$. The baffles had a thickness of 0.005 m. Three six-bladed *RDT* with D/T of 4/13, 5/13 and 6/13 were used. They were located at a clearance, C , to height ratio, $C/H = 3/10$. The drawings with dimensions are given in Figure 2.5, Figure 2.6 and Figure 2.7.

A variable speed motor (Eurostar power control-visc, IKA, Germany) was found suitable to supply the N for the experiment. The phases were delivered with peristaltic pumps (Watson Marlow, type 505S with pump head type 501 RL, USA) and transfer lines connected by a two-way push fit connection. The flowrates of the organic and aqueous phases were set on the pump's dials, whilst the feed port into the mixer was located below the vessel with a bore diameter of 0.0065 m (~ 1/4 inches).

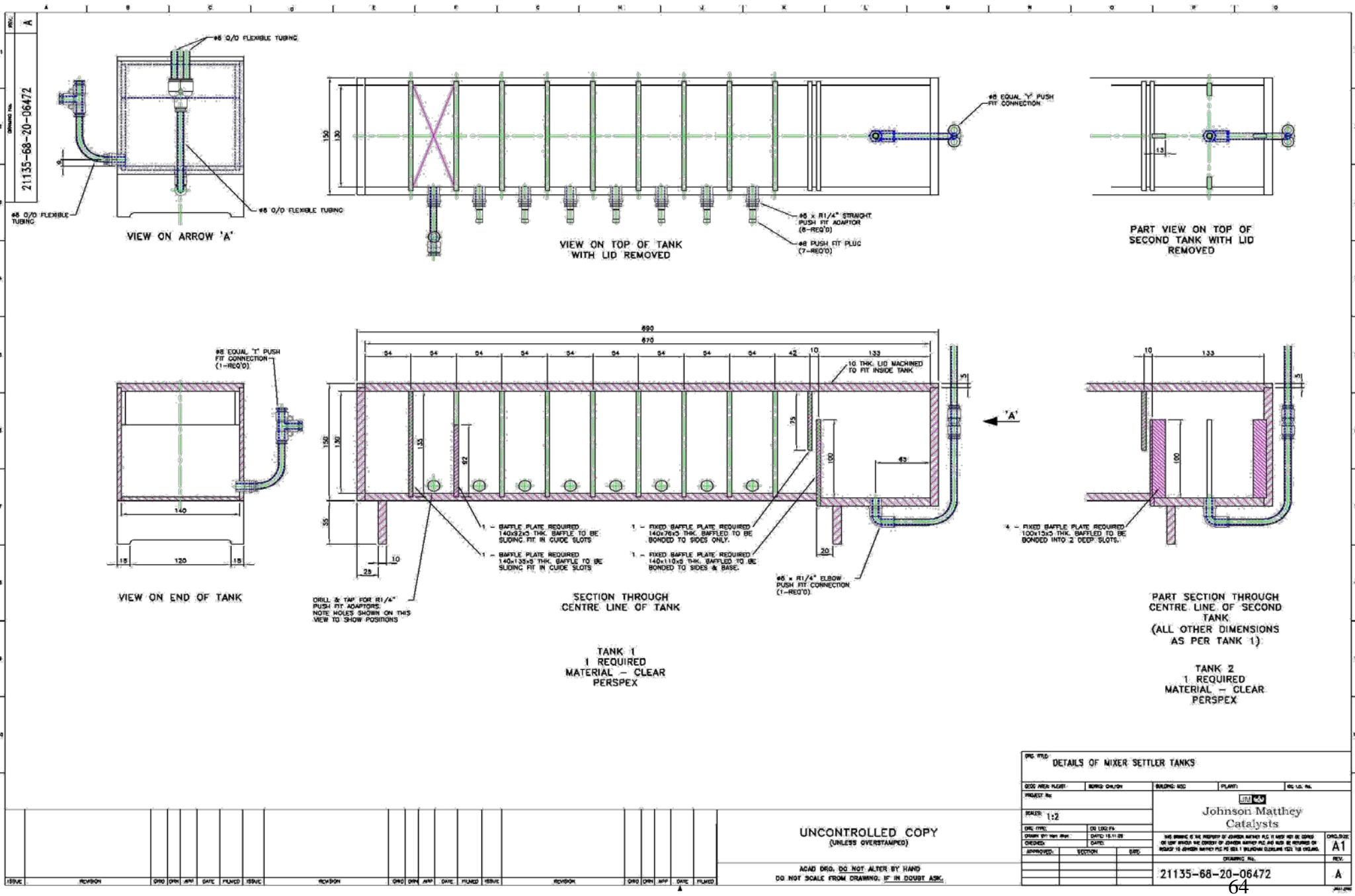


Figure 2.3. CAD drawing of mixer settler

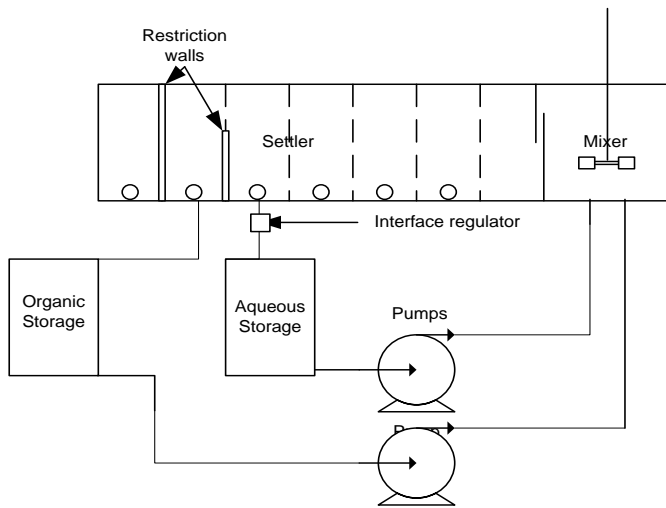


Figure 2.4. Mixer settler flow diagram

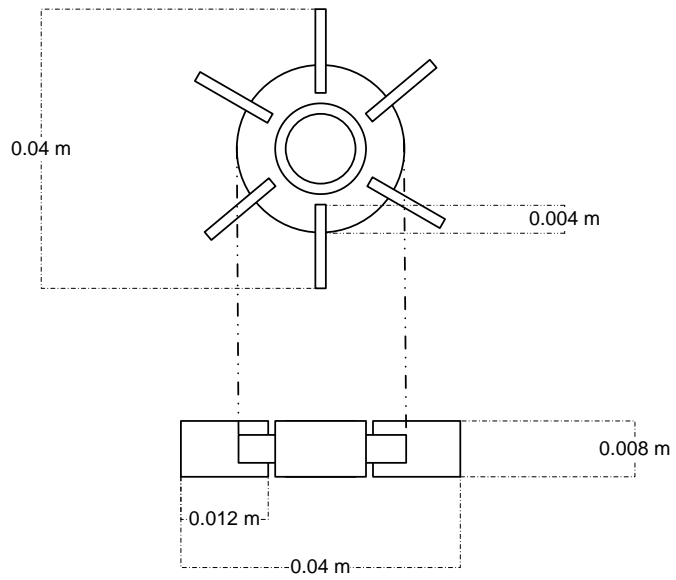


Figure 2.5. *RDT* of $D/T = 4/13$

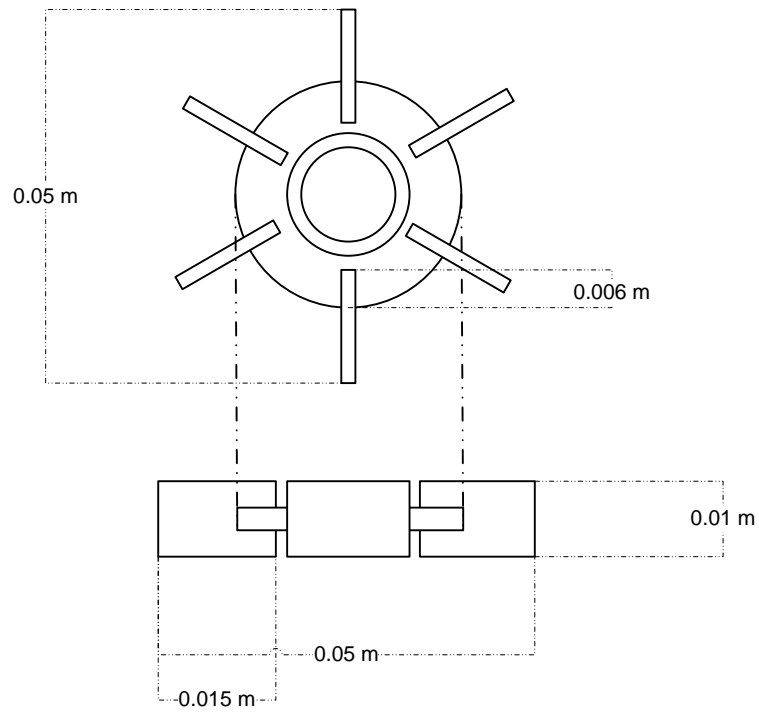


Figure 2.6. *RDT* of $D/T = 5/13$

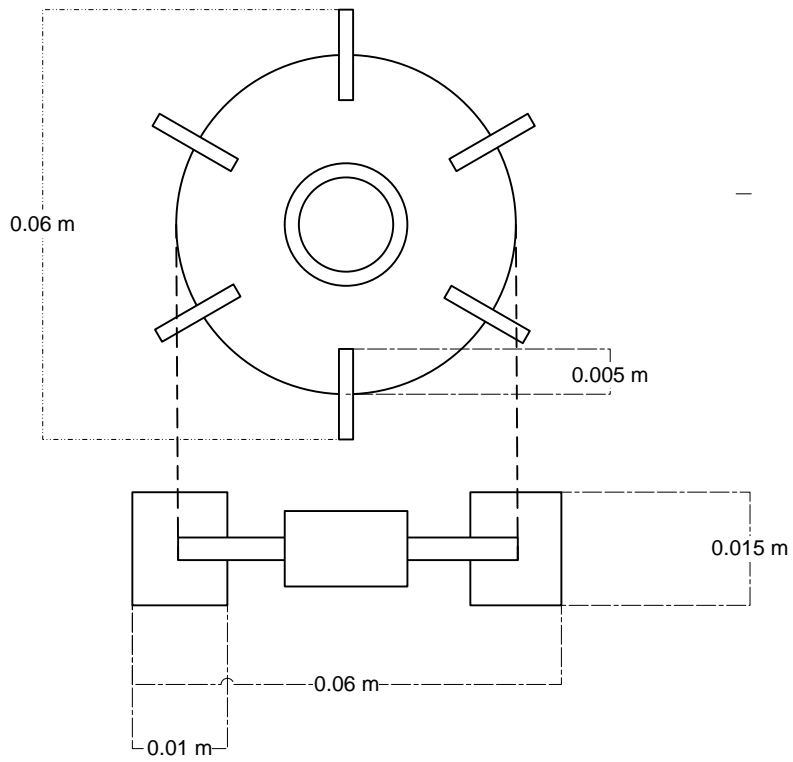


Figure 2.7. *RDT* of $D/T = 6/13$

2.4.4. Impeller operating conditions

Table 2.2 lists the operating conditions used for the ϕ_c/ϕ_d of 1:1, 3.5:2 and 3.5:1; with the N in revolutions per second (s^{-1}), P_o and U_{tip} .

Three P/V were used: 0.3, 0.9 and 2.7 kW m^{-3} , the extremes provided poor and excessive agitation conditions, with the mid-value providing an ideal mixing condition.

The ideal P/V of 0.9 kW m^{-3} was obtained from the correlation by Skelland and Ramsey (1987) (Equation 2.41) for the optimum impeller speed required to maintain a stable dispersion (N_{sd}).

$$(Fr_m)_{\min} = 1.03 \left(\frac{T}{D} \right)^{2.76} (\phi_d)^{0.106} (Ga Bo)^{-0.084}, \quad (2.41)$$

where the Galileo number (Ga) is expressed as:

$$Ga = \frac{D^3 \rho_m g \Delta \rho}{\mu_m^2},$$

and the Bodenstein number (Bo) is expressed as:

$$Bo = \frac{D^2 g \Delta \rho}{\sigma}.$$

The chosen poor and extreme P/V were obtained by scaling down and up the ideal P/V by a factor of 1/3 and 3 respectively.

The Re of the lowest and ideal P/V resided within low and high ends of the transitional regime of turbulence, whilst the extreme P/V resided within the turbulent regime. The plot of P_o versus Re is given in Appendix A.

To obtain power measurements a torque sensor (with a range of 0 to 30 N-m and a sensitivity of 66.66 mV N-m⁻¹) was used to measure the instantaneous torque values. The torque sensor was Whetstone Bridge with four strain gauges attached to a steel metal rod. The strain gauges are excited by a constant voltage of 12 V supplied through a slip ring. The sensor measures the instantaneous strain developed in the shaft which is transmitted to a data acquisition system as a voltage signal via a telemetry system through the slip ring. A pressure transducer with a range of 34.46 kPa, a resolution of 0.000482 kPa, and a sensitivity of 72.54 mV k⁻¹ Pa⁻¹ was used (PCB Piezoelectronics Inc., U.S.A., Model 106B50) to measure pressure fluctuations. The transducer was powered by an ICP battery unit (PCB Piezoelectronics Inc., U.S.A., Model 480E06), which acted as an amplifier.

Table 2.2. Impeller operating conditions for ϕ_c / ϕ_d of 1:1

Impeller diameter (D/T)	Impeller Speed (rps)	P/V (kW m^{-3})	U_{tip} (m s^{-1})	Weber Number (We)	Power Number (P_o)	Reynolds Number (Re)
4/13	5.1	0.3	1.0	370	5	2366
5/13	4.8	0.3	0.9	334	5.8	3514
6/13	4.6	0.3	0.9	300	6.8	4797
4/13	7.3	0.9	1.4	769	5	3413
5/13	6.6	0.9	1.2	625	6.8	4808
6/13	6.5	0.9	1.2	612	7	6853
4/13	10.5	2.7	2.0	1598	5	4920
5/13	9.4	2.7	1.8	1272	7	6858
6/13	9.3	2.7	1.8	1263	7	9840

ϕ_c/ϕ_d of 3.5:2

Impeller diameter (D/T)	Impeller Speed (rps)	P/V (kW m ⁻³)	U_{tip} (m s ⁻¹)	Weber Number (We)	Power Number (P _o)	Reynolds Number (Re)
4/13	5.1	0.3	1.0	375	5	3084
5/13	4.8	0.3	0.9	339	5.8	4582
6/13	4.6	0.3	0.9	309	6.8	6303
4/13	7.4	0.9	1.4	783	5	4460
5/13	6.6	0.9	1.3	638	6.8	6289
6/13	6.6	0.9	1.2	625	7	8965
4/13	10.6	2.7	2.0	1629	5	6432
5/13	9.5	2.7	1.8	1299	7	8975
6/13	9.5	2.7	1.8	1299	7	12924

ϕ_c/ϕ_d of 3.5:1

Impeller diameter (D/T)	Impeller Speed (rps)	P/V (kW m ⁻³)	U_{tip} (m s ⁻¹)	Weber Number (We)	Power Number (P _o)	Reynolds Number (Re)
4/13	5.1	0.3	1.0	375	5	4221
5/13	4.8	0.3	0.9	339	5.8	6271
6/13	4.6	0.3	0.9	309	6.8	8625
4/13	7.4	0.9	1.4	783	5	6103
5/13	6.6	0.9	1.3	638	6.8	8606
6/13	6.6	0.9	1.2	625	7	12268
4/13	10.6	2.7	2.0	1634	5	8788
5/13	9.5	2.7	1.8	1304	7	12303
6/13	9.5	2.7	1.8	1304	7	17717

2.4.5. Achieving the desired dispersion and avoiding phase inversion

An aqueous in organic dispersion desired for the study was obtained by initially filling up the mixer with the amount of organic (continuous phase) required, then starting the impeller before feeding the aqueous phase at the desired flowrate. When the motor was stopped, the direction of movement of

the dispersion band was used to establish the type of dispersion that was generated. In all cases the non-coalescing interface of the dispersion was in the organic and it moved downwards which is always the case for aqueous dispersed systems (Reeve and Godfrey, 2002).

2.4.6. Droplet sizing technique

A sample withdrawal and photography technique was used to determine the droplet size distribution in the mixer. The technique required the use of an optical trinocular microscope (Nikon Eclipse ME600, Nikon Co, Japan) with a camera mounted onto an ocular piece, two zoom lenses (5 x, 10 x zoom), an integrated light source, a 1 mm graticule for droplet size measurements and a dip tube, which was 5 mm in diameter. 40 g of Polyglycerol polyricinoleate for every 100 g of stabilising solution was used to stabilise the aqueous phase. A clear pre-equilibrated organic phase made up the rest of the solution.

To obtain the droplet sizes, some of the stabilising solution was placed on a microscopic slide and then the sample was picked from the mixer and transferred into the slide. The transfer process took place under one second.

After transferring the sample into the slide, the droplets were initially observed under the microscope to ensure that coalescence did not take place before images were taken. An example of an image taken is given in Figure 2.8.

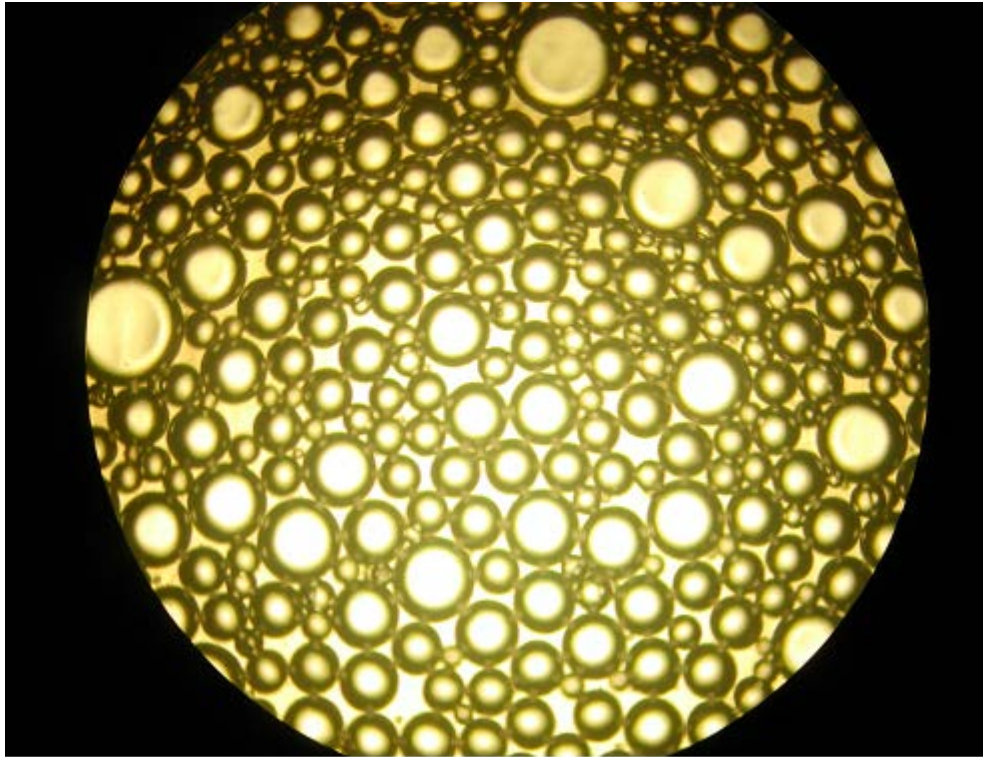


Figure 2.8. An image of droplets stabilised by Polyglycerol polyricinoleate solution and captured.

The images were analysed using Bubble pro software (School of Chemical Engineering, University of Birmingham). A Photron Fastcam SA-5 (Engineering and Physical Sciences Research Council, EPSRC, UK) high speed camera was also used to capture images of droplets from the vessel wall to estimate and validate the d_{10} obtained by the sample withdrawal and photography technique.

An image taken is shown in Figure 2.9. An object of known diameter (500 μm) was placed in the field of focus before images were taken.

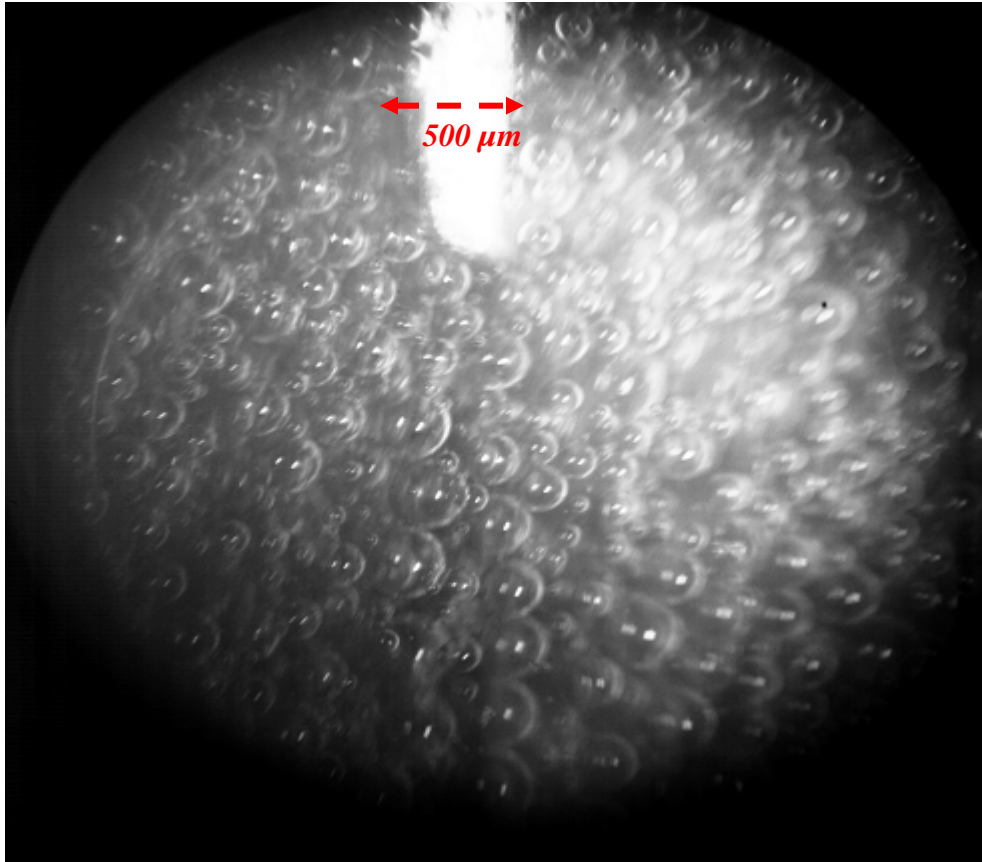


Figure 2.9. Image of droplets captured with the Photron Fastcam SA-5.

2.5. Results and discussion

2.5.1. The effect of P/V on dispersed phase holdup

At the $P/V = 0.3 \text{ kW m}^{-3}$, a dispersion was generated by all impellers and values of ϕ_c/ϕ_d . However, ϕ_d increased (Figure 2.11) and an organic supernatant layer accumulated on the surface of the mixture (Figure 2.10) as ϕ_c/ϕ_d and D/T decreased. For example, at the $\phi_c/\phi_d = 1:1$, the ϕ_d increased from $\sim 2\%$ to $\sim 10\%$ when the larger D/T was changed for the smaller D/T .

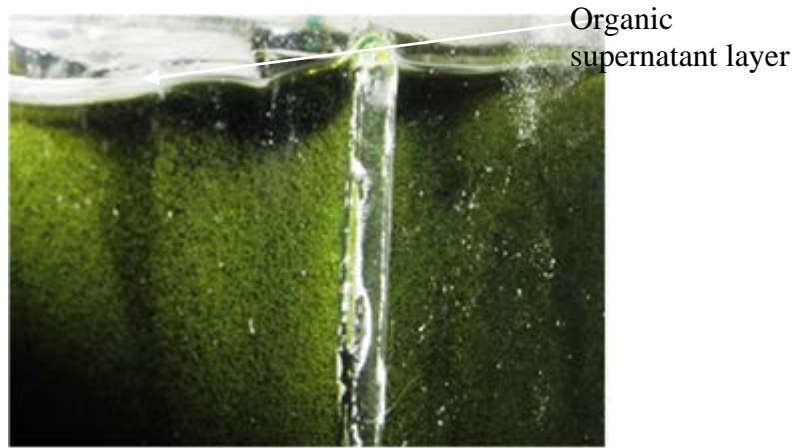


Figure 2.10. Organic supernatant layer at P/V of 0.3 kW m^{-3} and D/T of $4/13$

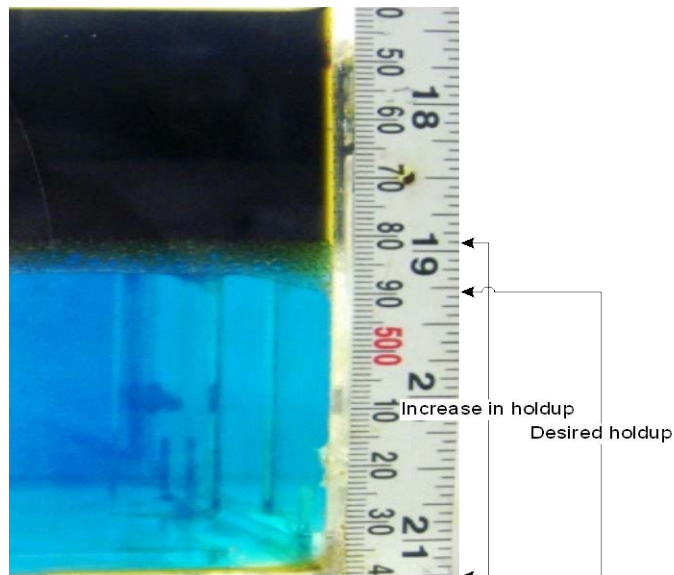


Figure 2.11. Change in ϕ_d at 0.3 kW m^{-3} and D/T of $4/13$

These observations showed that the dispersion generated was unstable at the $P/V = 0.3 \text{ kW m}^{-3}$. When the D/T is increased or decreased, Q changes in direct proportion, since $Q = N_q ND^3$, where N_q depends on Re . N_q is constant in the turbulent regime but will vary with D/T in the transitional or laminar regime.

At the given P/V , the value of Re resided at the lower end of the transitional regime and decreased with D/T (by definition) as shown in Table 2.2, where $Re = 2366, 3083$ and 4221 for $D/T = 4/13$ impeller at $\phi_c/\phi_d = 1:1, 3.5:2$ and $3.5:1$ respectively, whilst $Re = 6797, 6303$ and 8625 for the $D/T = 6/13$ impeller. This led to a decrease in N_q and Q , which are inversely proportional to t_c , leading to an increase in stagnation and subsequently φ_d . $\Delta\varphi_d$ was measured when agitation was ceased and the phases had completely disengaged.

2.5.2. The effects of D/T on droplet size and droplet size distribution

The d_{10} and d_{32} generated by all operating conditions are shown in Table 2.3, whilst selected droplet size distributions and the corresponding cumulative volume distributions (CVD) are shown in Figure 2.12. Generally, the results demonstrate that at a fixed ϕ_c/ϕ_d and P/V , increasing the D/T will lead to an increase d_{10} and d_{32} .

When the $D/T = 4/13$ impeller was changed to the $D/T = 5/13$ and $6/13$ impellers, droplet size increased by $\sim 15\%$ to 23% and 13 to 30% respectively at both the $P/V = 0.3 \text{ kW m}^{-3}$ and 0.9 kW m^{-3} . The droplet size distributions also broadened and the $d_{v0.5}$ in the CVD plot increased (Figure 2.12). Increasing the D/T at $P/V = 0.3 \text{ kW m}^{-3}$ and 0.9 kW m^{-3} also skewed the droplet size distributions towards larger droplet sizes and led to the emergence of a long tail of droplets with low count percentages on the left shoulder of the distribution.

At the $P/V = 2.7 \text{ kW m}^{-3}$, increasing the D/T at a fixed ϕ_c/ϕ_d led to an increase in droplet size, however the change in droplet size by $\sim 5\%$ with the $D/T = 5/13$ impeller was insignificant compared to the change of $\sim 20\%$ to 30% by the $D/T = 6/13$ impeller. At $P/V = 2.7 \text{ kW m}^{-3}$, the

droplet size distribution skewed towards large droplet sizes whilst the long tails and a low droplet count percentage emerged to the right of the distribution.

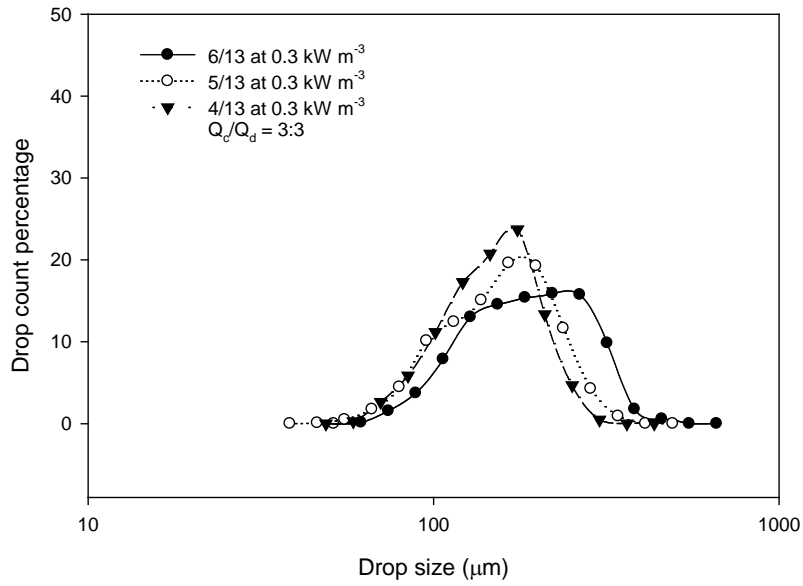
Air ingestion also took place at $P/V = 2.7 \text{ kW m}^{-3}$ which led to some inaccurate droplet size measurements as will be shown later below. The variance of the distributions was not calculated because the droplet size distributions obtained were not consistently similar, which is necessary for consistency in the comparisons.

Table 2.3. d_{10} and d_{32} for the various D/T , ϕ_c/ϕ_d and P/V .

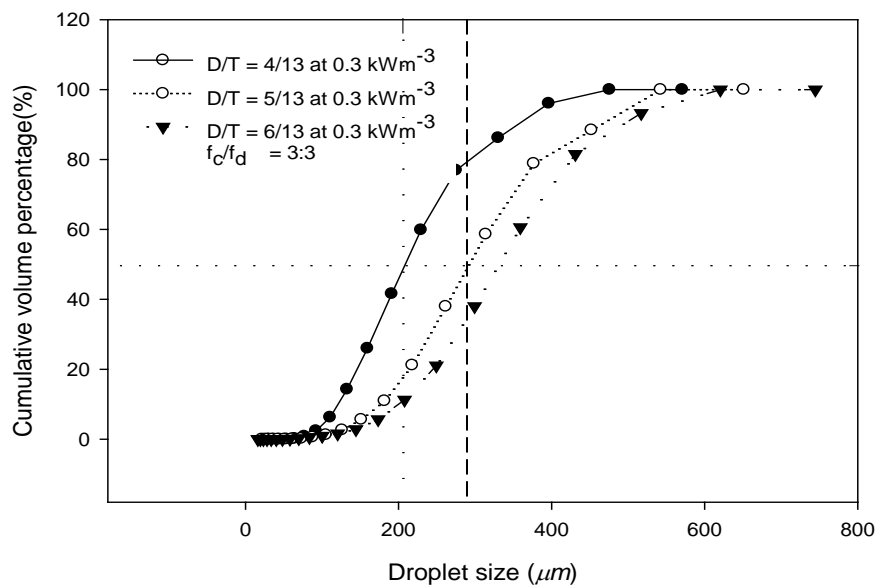
D/T	ϕ_c/ϕ_d	d_{10}	d_{32}	d_{10}	d_{32}	d_{10}	d_{32}
		0.3 kW m ⁻³		0.9 kW m ⁻³		2.7 kW m ⁻³	
4/13	1:1	163	228	91	116	59	71
5/13		193	288	111	150	60	73
6/13		186	322	120	162	68	97
4/13	3.5: 2	137	191	82	101	60	81
5/13		-	-	98	126	62	87
6/13		180	290	117	153	78	115
4/13	3.5: 1	149	181	62	88	53	66
5/13		141	182	81	103	56	88
6/13		148	194	107	141	80	108

As D/T was increased, a second peak emerged in the droplet size distributions. The intensity of the peak increased as the P/V and ϕ_c/ϕ_d increased. Gaussian distributions developed for all the D/T at $P/V = 0.3 \text{ kW m}^{-3}$ and $\phi_c/\phi_d = 1:1$ (Figure 2.12a) but as the D/T and ϕ_c/ϕ_d were both increased a second peak emerged to the left shoulder of the distribution. At the $\phi_c/\phi_d = 3.5:1$ and $P/V = 0.9 \text{ kW m}^{-3}$ the second peak was observed to the left shoulder of the distribution (Figure 2.12b) but changed

to Gaussian distributions as the D/T was increased and ϕ_c/ϕ_d decreased. At the $P/V = 2.7 \text{ kW m}^{-3}$ (Figure 2.12c) double peaks were consistently observed as the D/T was increased.

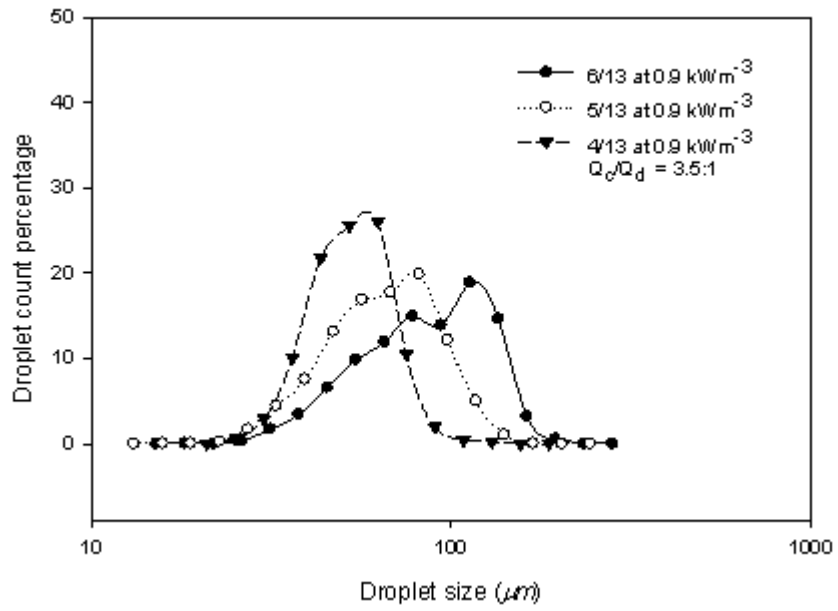


i

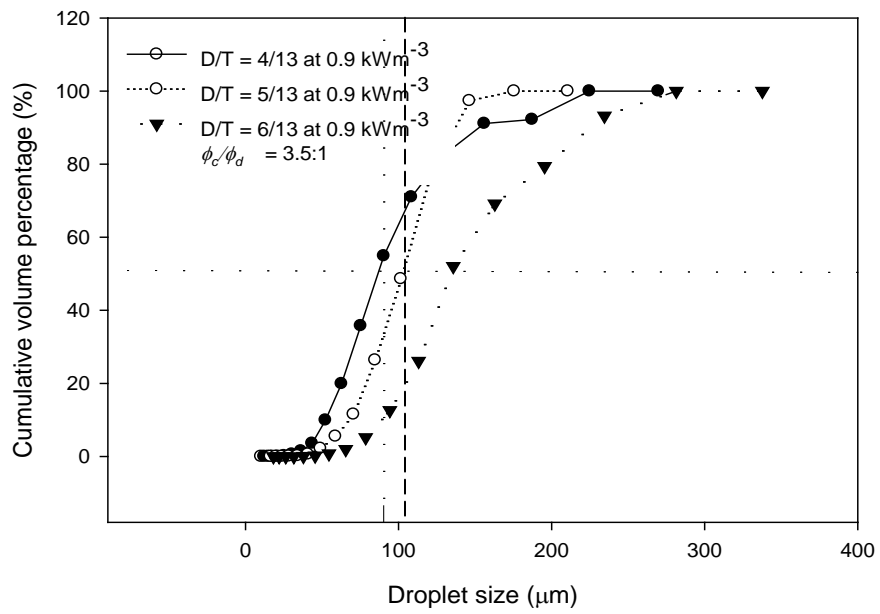


ii

(a)

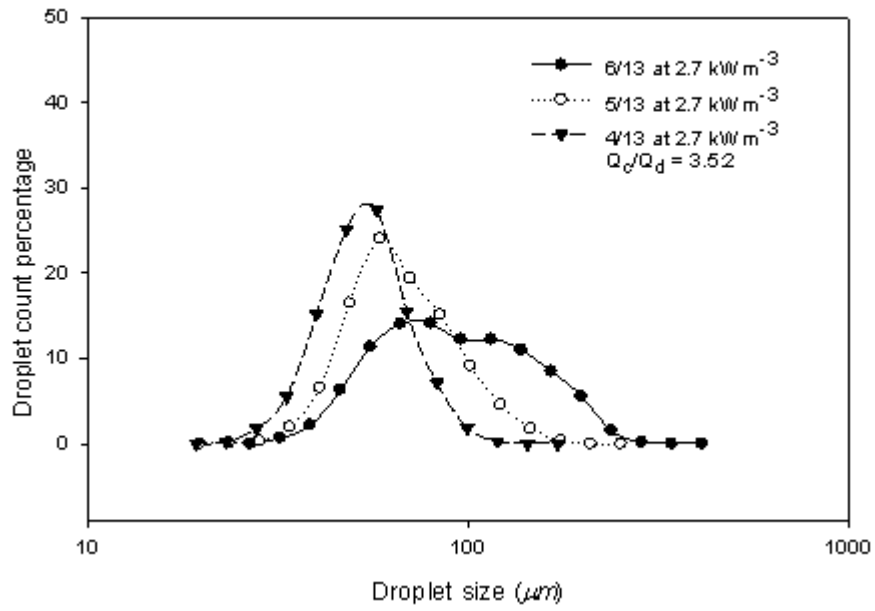


i

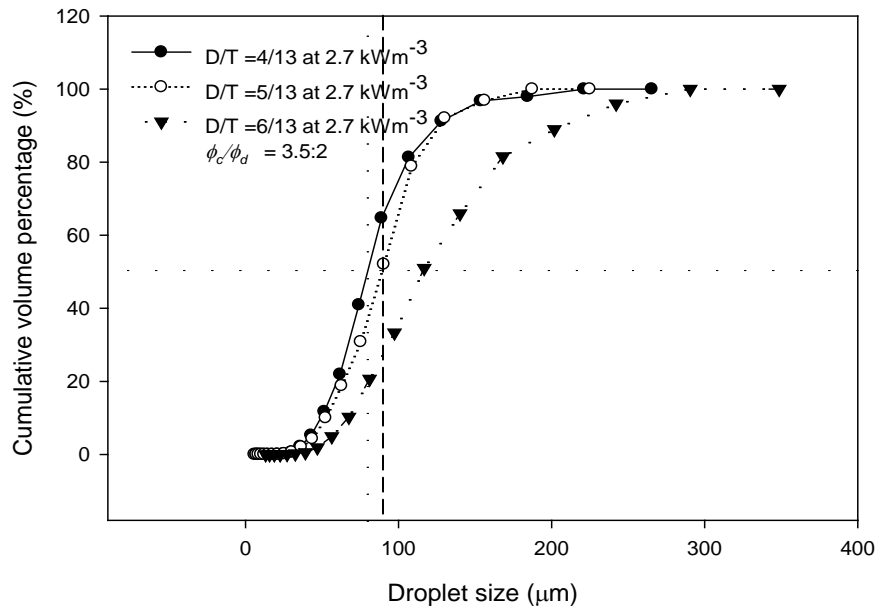


ii

(b)



i



ii

(c)

Figure 2.12. Droplet size distribution and cumulative volume percentage as a function of D/T at P/V of (a) 0.3 kW m^{-3} at $\phi_c/\phi_d=1:1$ (b) 0.9 kW m^{-3} at $\phi_c/\phi_d=3.5:1$ (c) 2.7 kW m^{-3} at $\phi_c/\phi_d=3.5:2$

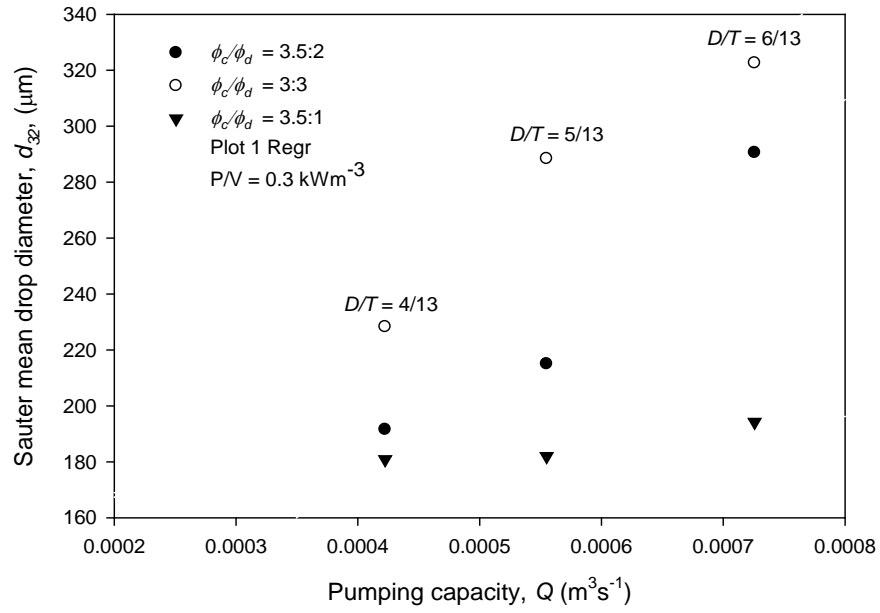
The droplet size increased as the D/T was increased, because the ratio of Q with U_{tip} increased. Q is essential for homogeneity because it is inversely proportional to t_c , where $t_c = \frac{V}{r_c Q}$ and r_c is the circulation ratio.

Assuming turbulent flow conditions i.e. $Re \geq 10^4$, N_q will be constant, making $Q \propto ND^3$. Equally, P_o will be constant making $P \propto N^3 D^5$. Thus as the D/T is increased, $Q \propto D^{4/3}$.

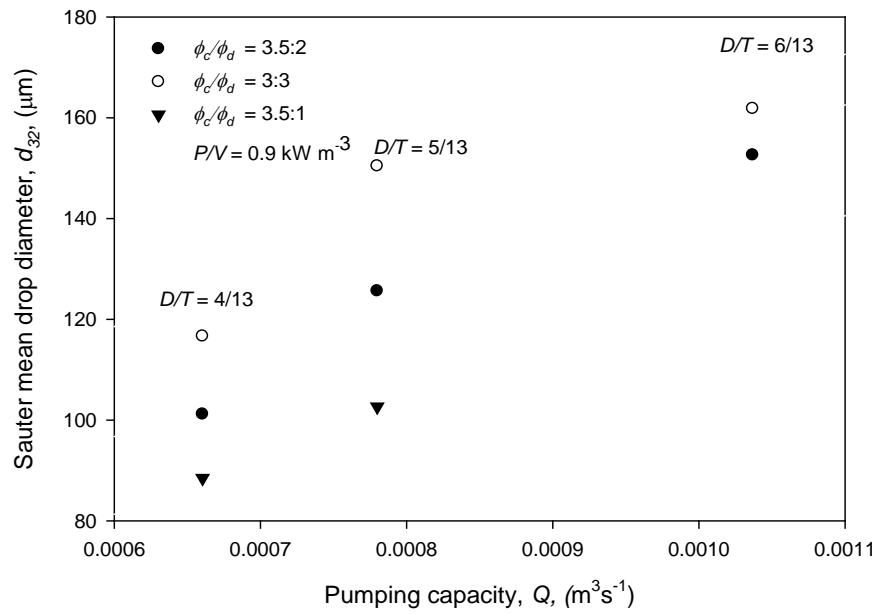
However, maximum shear rate ($\dot{\gamma}_m$) is proportional to $U_{tip} \propto ND$, making $U_{tip} \propto D^{-2/3}$ at constant P/V (or P). As a result, increasing the D/T , decreased the U_{tip} , and $\dot{\gamma}_m$ accordingly, but Q increased, leading to the increase in droplet size.

Therefore, a larger D/T should be used at the expense of smaller droplet sizes if t_c demonstrates a larger limiting effect to the extraction rate. Stagnation and excessive short circuiting will also be averted with this D/T .

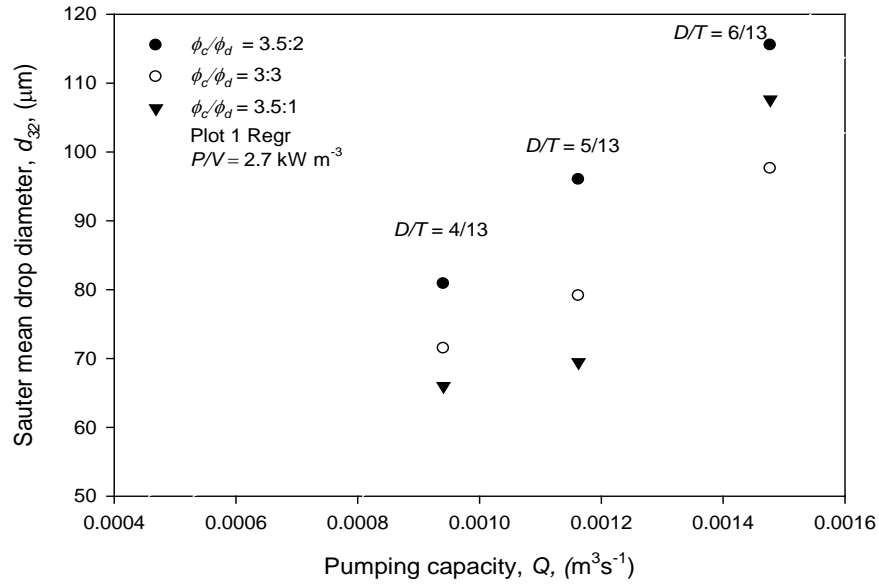
Figure 2.13 (a) to (c) show plots of Q as a function of d_{32} at a fixed N_q of 0.72 (Rushton *et al.*, 1950). The plots show how d_{32} changes with Q . Q increased by $\sim 40\%$ when the smallest D/T was changed for the largest D/T .



(a)



(b)



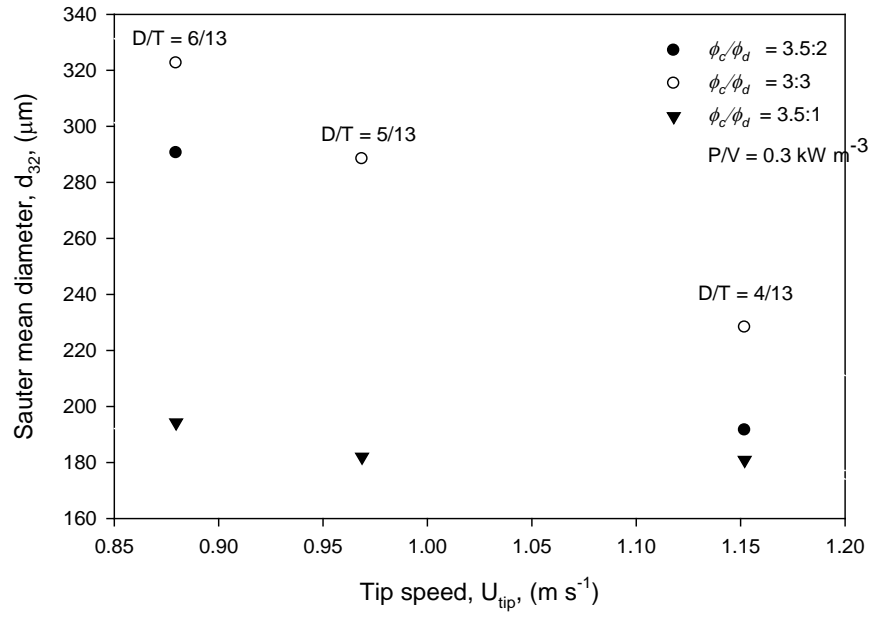
(c)

Figure 2.13. d_{32} as a function of Q for all operating conditions (a) 0.3 kW m^{-3} (b) 0.9 kW m^{-3}

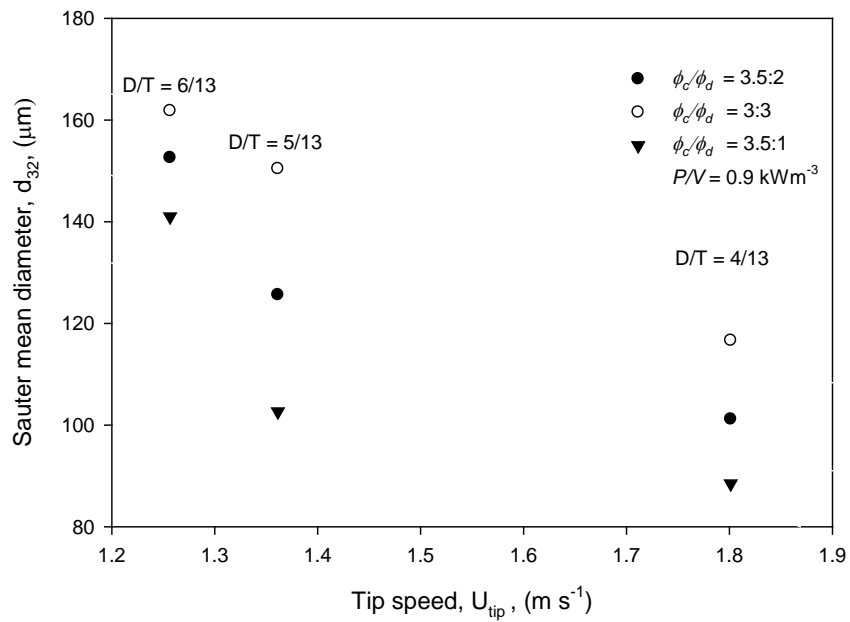
(c) 2.7 kW m^{-3}

Given that N decreased as the D/T increased at a constant P/V , Γ_m increased since $P = 2\pi N\Gamma_m =$ constant. Therefore, for a fixed P/V and ϕ_c/ϕ_d the smallest D/T should be used if droplet size and mass transfer are important limiting factors to the rate of extraction, since the ‘ a ’ and rate constant will increase with respect to the droplet size.

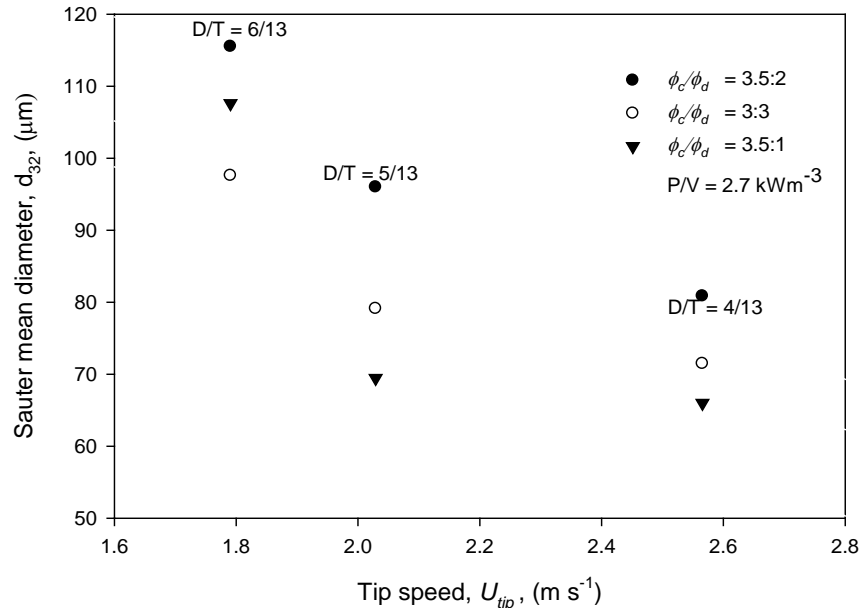
In Figure 2.14 (a) to (c) the relationship between U_{tip} and d_{32} is shown for all conditions. U_{tip} increased by $\sim 30\%$ when the largest D/T was changed to the smallest D/T .



(a)



(b)



(c)

Figure 2.14. d_{32} as a function of U_{tip} for all D/T and all ϕ_c/ϕ_d at (a) 0.3 kW m^{-3}

(b) 0.9 kW m^{-3} (c) 2.7 kW m^{-3}

The double peaks observed in the droplet size distributions occurred because bimodal distributions were emerging. As the ϕ_c/ϕ_d was increased, it is postulated that the mechanism of droplet rupture switches from a stretching to an erosive mechanism where small satellite droplets strip off their mother droplets creating a relatively vast amount of small droplets and the emergence of the second peak. As the D/T was increased this mode of droplet rupture is also favoured.

This pattern of droplet rupture was shown by Pacek *et al.* (1998). They demonstrated that double peaks depend on the state of the continuous phase. They also showed that double peaks developed in aqueous continuous systems at low N , but change to normal distributions as N increased. Similarly, Zhou and Kresta (1998a) showed that for a range of impeller types, the shape of the droplet size

distribution changed with N , from normal distributions at small droplet sizes to double peaks at intermediate and large droplet sizes. The peaks observed on the right shoulder at the $P/V = 2.7 \text{ kW m}^{-3}$, came about due to air entrainment. This will be explained with further reading in the section that follows.

2.5.3. The effects of ϕ_c/ϕ_d on droplet size

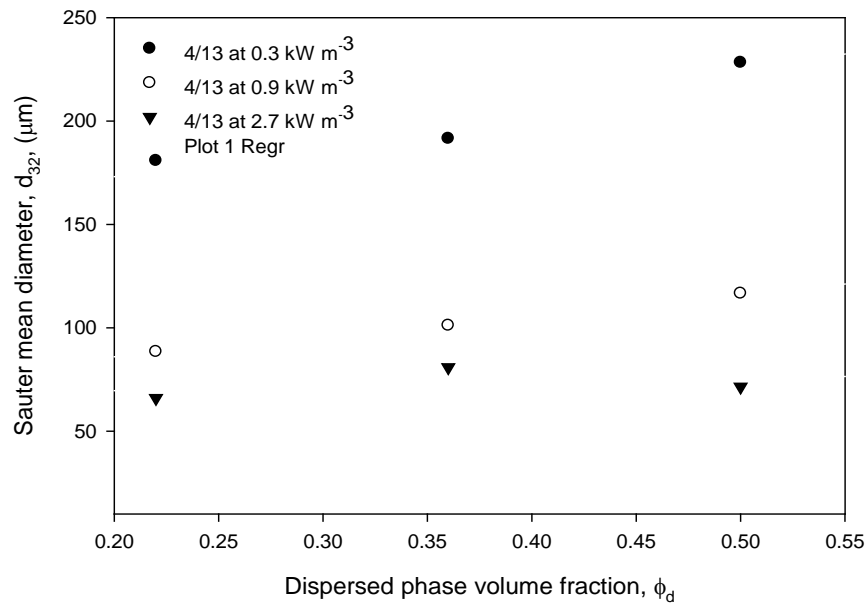
The plots of d_{32} as a function of ϕ_c/ϕ_d for all the operating conditions are shown in Figure 2.15 (a) to (c). It was generally observed that when the larger ϕ_c/ϕ_d was changed to the mid-range and smallest ϕ_c/ϕ_d at a fixed D/T and P/V , droplet size increased.

For the $D/T = 4/13$ impeller and $P/V = 0.3 \text{ kW m}^{-3}$, d_{32} increased by $\sim 10 \%$ and 20% as ϕ_c/ϕ_d was decreased from the 3.5:1 to 3.5:2 and 3.5:1 to 1:1, whilst at $P/V = 0.9 \text{ kW m}^{-3}$, d_{32} increased by 13% and 25% respectively.

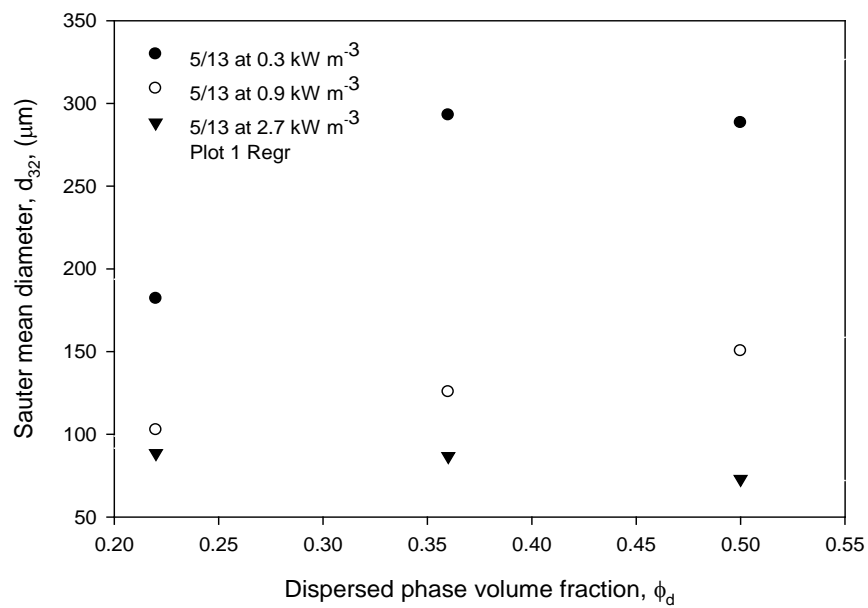
For the $D/T = 5/13$ and $6/13$ impellers at $P/V = 0.3 \text{ kW m}^{-3}$, d_{32} increased by $\sim 36 \%$ and 40% as ϕ_c/ϕ_d was decreased from 3.5:1 to 3.5:2 and 3.5:1 to 1:1, however at $P/V = 0.9 \text{ kW m}^{-3}$, the increase in d_{32} with the $D/T = 6/13$ impeller was $\sim 10 \%$ less than the change observed with the 5/13, wherein d_{32} increased by $\sim 20 \%$ and 30% respectively.

Figure 2.16 are plots of selected droplet size distributions. As ϕ_c/ϕ_d was varied, the droplet size distribution profiles looked similar but were spaced marginally with ϕ_c/ϕ_d . The images of droplets

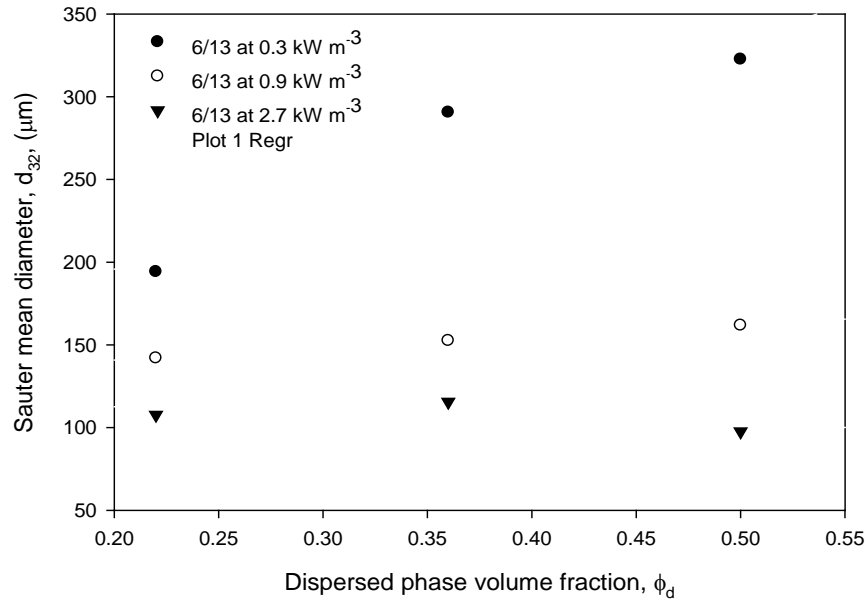
produced by the $D/T = 4/13$ impeller at 0.9 kW m^{-3} and $\phi_c/\phi_d = 3.5:1$ and $1:1$ are shown in Figure 2.17 (a) and (b).



(a)

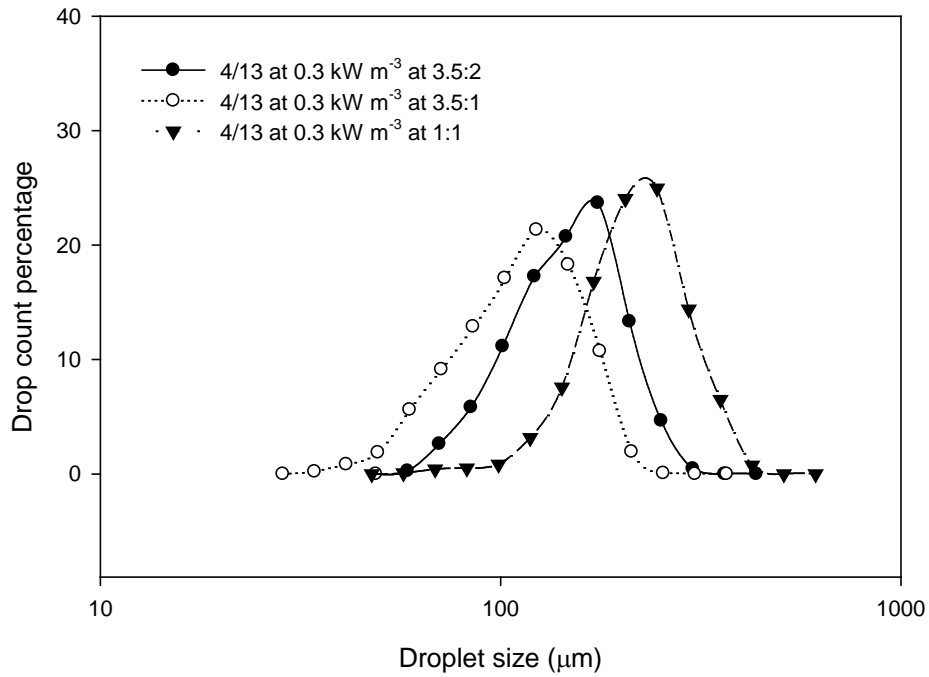


(b)

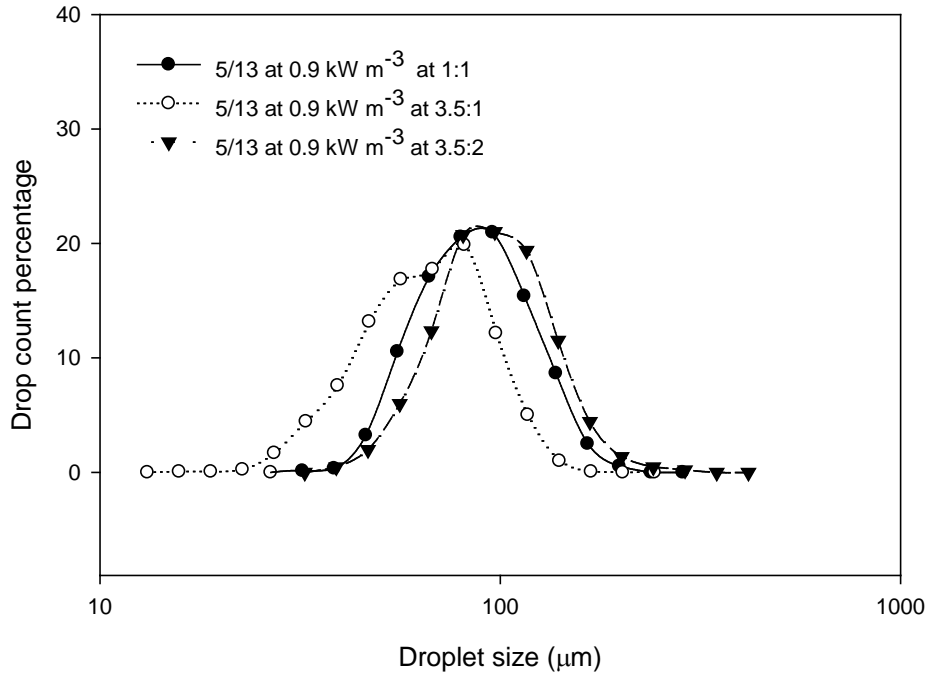


(c)

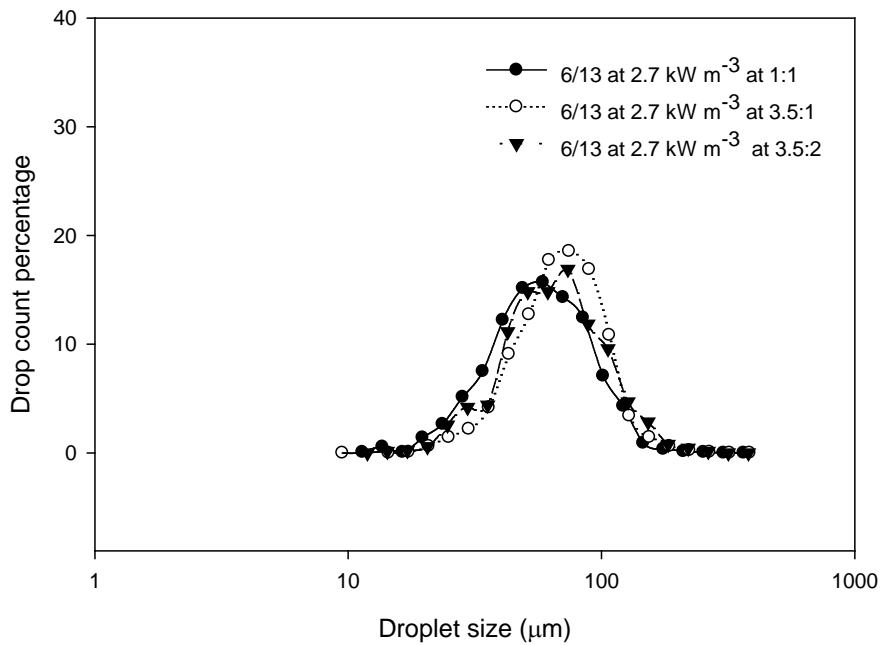
Figure 2.15. d_{32} as a function of ϕ_d for (a) $D/T = 4/13$ (b) $D/T = 5/13$ (c) $D/T = 6/13$



(a)

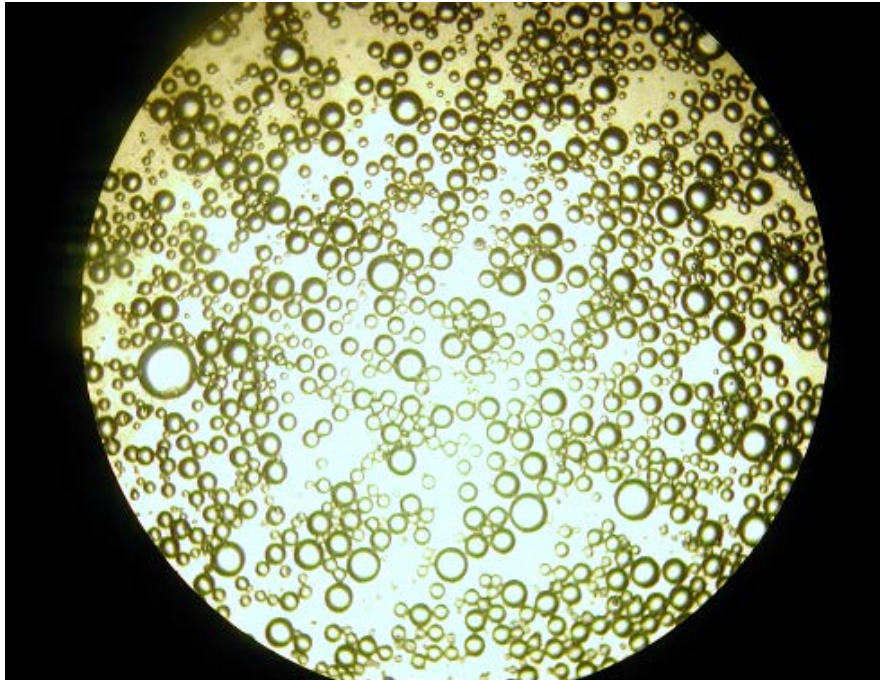


(b)

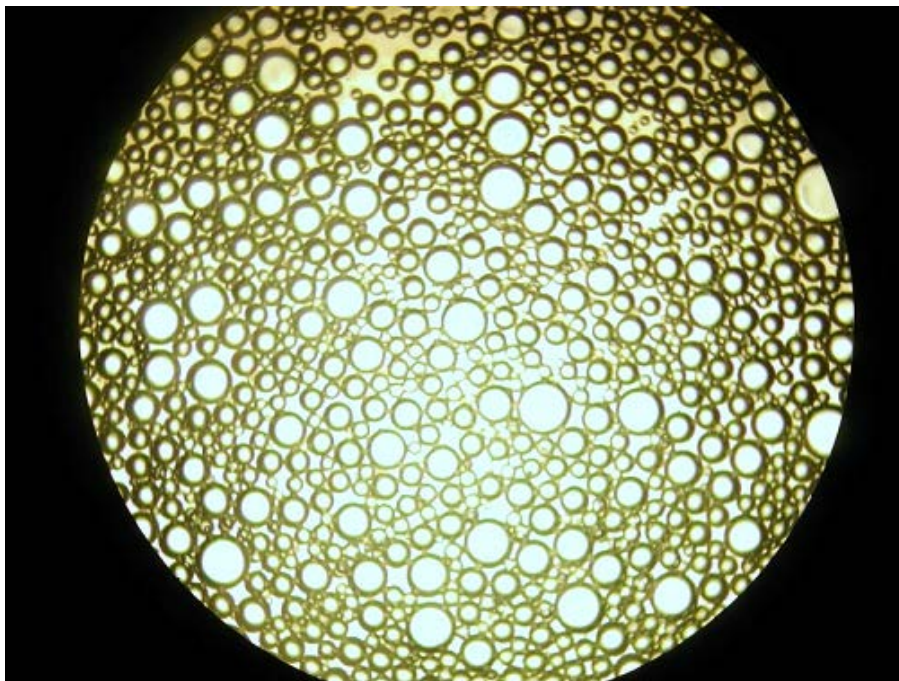


(c)

Figure 2.16. Variation in droplet size distribution with ϕ_c/ϕ_d for (a) 4/13 at 0.3 kW m^{-3} (b) 5/13 at 0.9 kW m^{-3} (c) 6/13 at 2.7 kW m^{-3}



(a)



(b)

Figure 2.17. Droplet size images for ϕ_c/ϕ_d of (a) 3.5:1 with $d_{32} = 88 \mu\text{m}$ (b) 1:1 with $d_{32} = 116 \mu\text{m}$; for $D/T = 4/13$ and $P/V = 0.9 \text{ kW m}^{-3}$ at similar magnifications.

Agitation at the $P/V = 2.7 \text{ kW m}^{-3}$ led to air ingress, which was exacerbated as the $\phi_c/\phi_d \sim 5\%$ to 15% when the $D/T = 5/13$ impeller was changed for the $D/T = 6/13$ impeller, whilst increasing ϕ_c/ϕ_d from 1:1 to 3.5:1 increased air holdup from $\sim 15\%$ to 25% .

The presence of air led to an expected increase in droplet size. The evidence of an air entrained system and a system previously occupied by air are shown in Figure 2.18 and Figure 2.19.

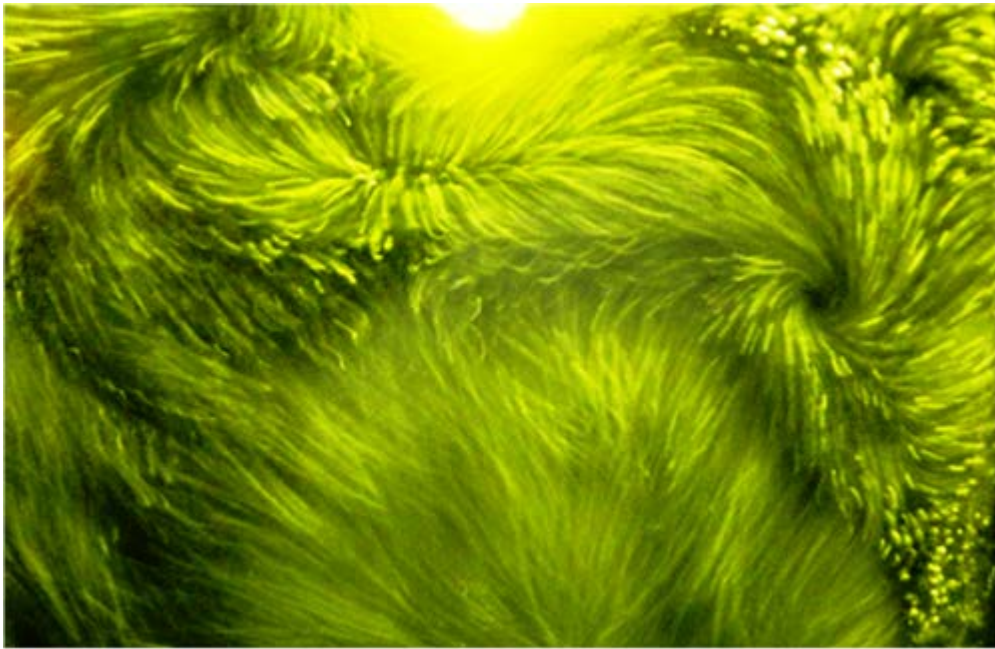


Figure 2.18. Evidence of air entrained at ϕ_c/ϕ_d of 3.5:1 for D/T of 6/13

The expression by Calderbank (1958) i.e. $d_{32} = \left(\frac{\sigma^{0.6}}{(P/V)^{0.4} \rho_c^{0.2}} \right) \phi_d^{0.5} \left(\frac{\mu_d}{\mu_c} \right)^{0.25}$; can be used to explain

why droplet size varied with ϕ_c/ϕ_d . When the viscous and interfacial properties of the fluids i.e. ρ_c ,

σ , μ_d and μ_c ; and P/V are fixed, $d_{32} \propto \phi_d^{0.5}$.

Therefore as ϕ_d was decreased, d_{32} decreased. Turbulent dampening and the viscous resistance to $\dot{\gamma}_m$ decreased with ϕ_d leading to small droplet sizes, since the average $\rho \propto \phi_c/\phi_d$.

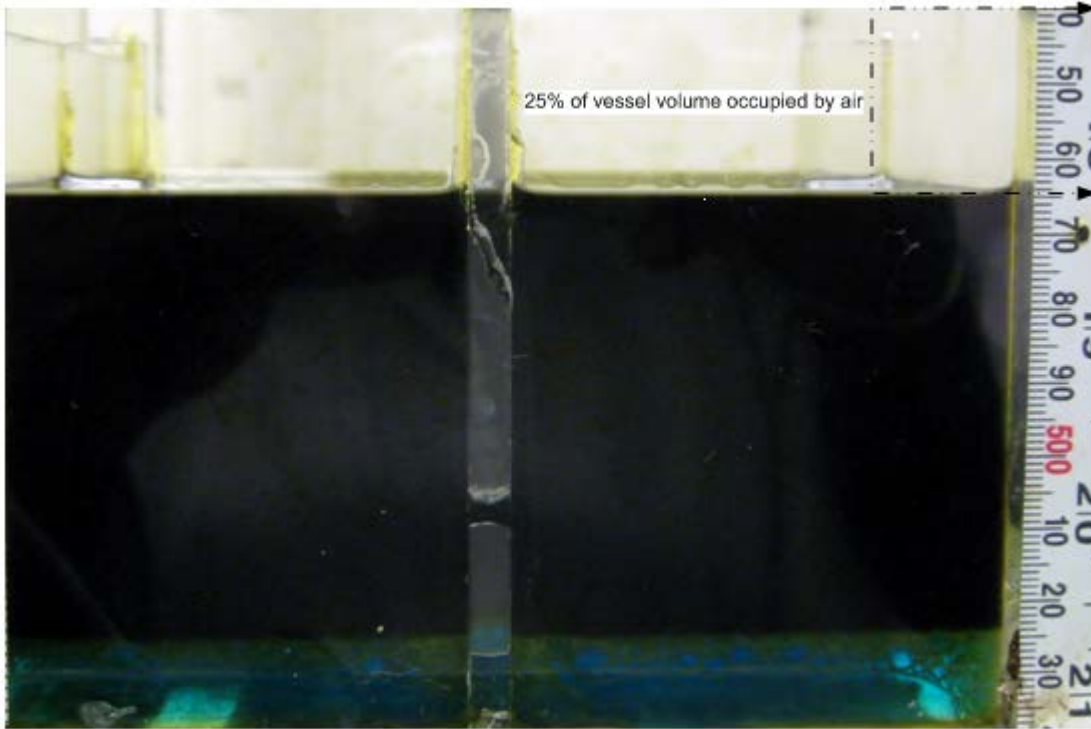


Figure 2.19. Loss in volume of organic and aqueous phase due to air

The decrease in ϕ_c/ϕ_d increased the concentration of droplets in the mixer and their likelihood of collision to larger droplet sizes. Air holdup also increased as the ϕ_d decreased since the viscous resistance to dispersion circulation decreased. The presence of air, reduced droplet shear which subsequently led to the increase in droplet size.

2.5.4. The effects of P/V on droplet size

Functional relationships between d_{32} and We as well as d_{32} versus $\bar{\varepsilon}_T$ can be used in place of P/V to analyse the effects of inertial forces on droplet size because P/V does not sufficiently describe the breakup features across impellers. Both relationships have been shown theoretically to be governed by power law relationships with specific power law constants.

By satisfying these constants the results obtained will agree with Kolmogorov-Hinze's theory (Hinze, 1955) and scale-up of mixers can be achieved fairly accurately. In the relationship between d_{32} versus We , a theoretical constant of -0.6 has been identified for agitated $L-L$ systems, whilst a constant within the range of -0.4 to -0.47 has been suggested for d_{32} as a function of $\bar{\varepsilon}_T$.

2.5.5. We and $\bar{\varepsilon}_T$ as functions of d_{32}

The plots of the dimensionless d_{32} (i.e. d_{32}/D) as a function of We for all operating conditions studied are shown in Figure 2.20 (a) to (c). Generally, the relative droplet size error at $P/V = 2.7 \text{ kW m}^{-3}$ increased from $\sim 2 \%$ to 7% as D/T was increased whilst at $P/V = 0.9 \text{ kW m}^{-3}$ and 0.3 kW m^{-3} it increased from 2.8% to 12% and 6.5% to 16% respectively. The comprehensive list of errors is given in Appendix A (ii).

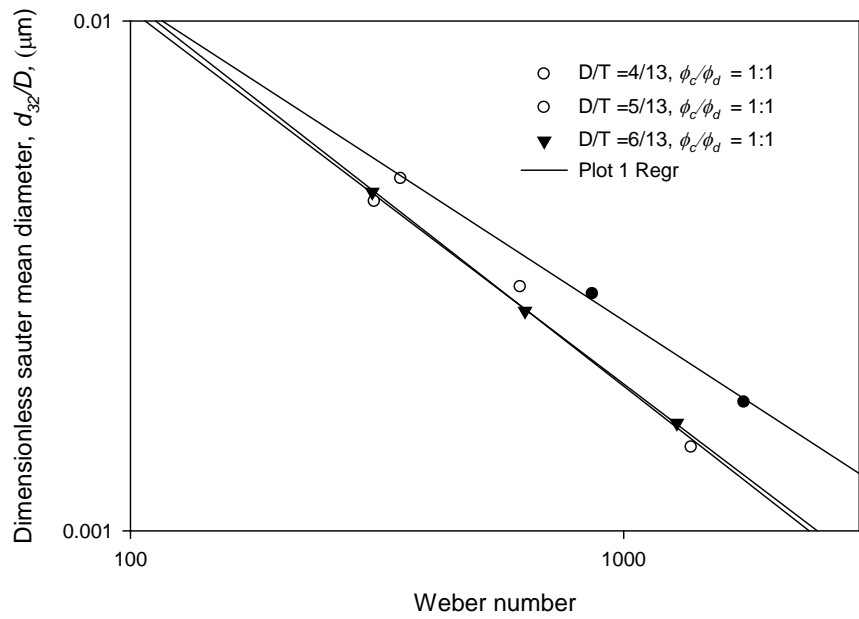
It was also generally observed that as the We increased, d_{32} decreased. As anticipated the smallest D/T impeller produced the much smaller droplet size. A similar trend for RDT agitated systems has been shown by Brown and Pitt (1972). An increase in d_{32} by $\sim 70 \%$ was estimated between the lowest and largest We for all operating conditions.

This increase is proportional to the percentage increase in ‘a’. The equations that governed the distributions are shown in Table 2.4. Careful consideration should be placed on the predicted distributions and the given exponents because only three data points were used in the regression analysis. The statistical tests are shown in Appendix A(iii).

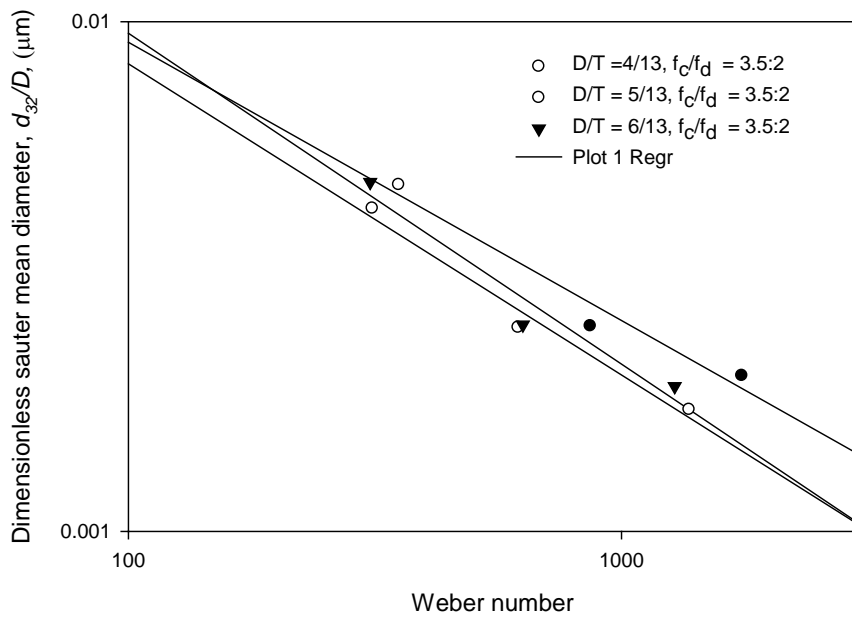
Table 2.4. *We* power law exponents for all *P/V*, *D/T* and ϕ_c/ϕ_d

ϕ_c/ϕ_d	<i>D/T</i>		
	4/13	5/13	6/13
	<i>We</i> power law exponents		
1:1	-0.63	-0.75	-0.73
3.5:2	-0.55	-0.61	-0.65
3.5:1	-0.64	-0.47	-0.42

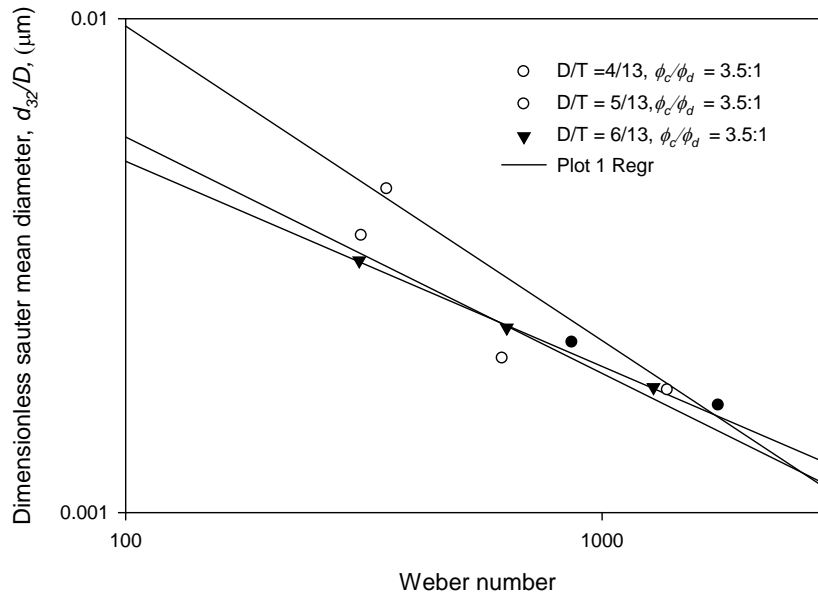
In the *We* relationship it was observed that the constants obtained with the *D/T* = 4/13 impeller for all the ϕ_c/ϕ_d were very close to the theoretical value of -0.6. The exponents obtained with the *D/T* = 5/13 and 6/13 impeller, were lower at the $\phi_c/\phi_d = 1:1$ (-0.75 and 0.75) and higher at the $\phi_c/\phi_d = 3.5:1$ (-0.47 and 0.41). However at the $\phi_c/\phi_d = 3.5:2$ all the *D/T* produced exponents that were close to the theoretical value.



(a)



(b)



(c)

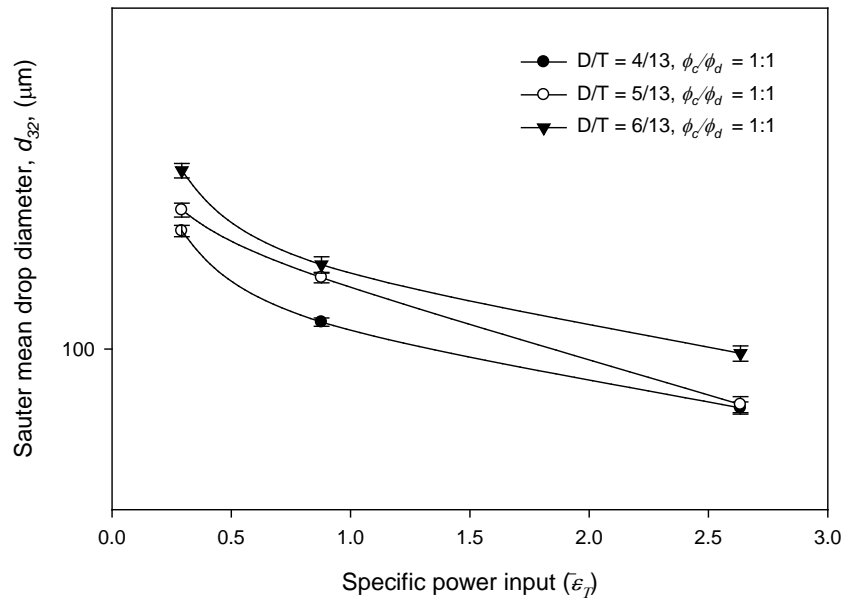
Figure 2.20. Dimensionless d_{32} as a function of We for all ϕ_c/ϕ_d (a) 1:1 (b) 3.5:2

(c) 3.5:1 at varying D/T

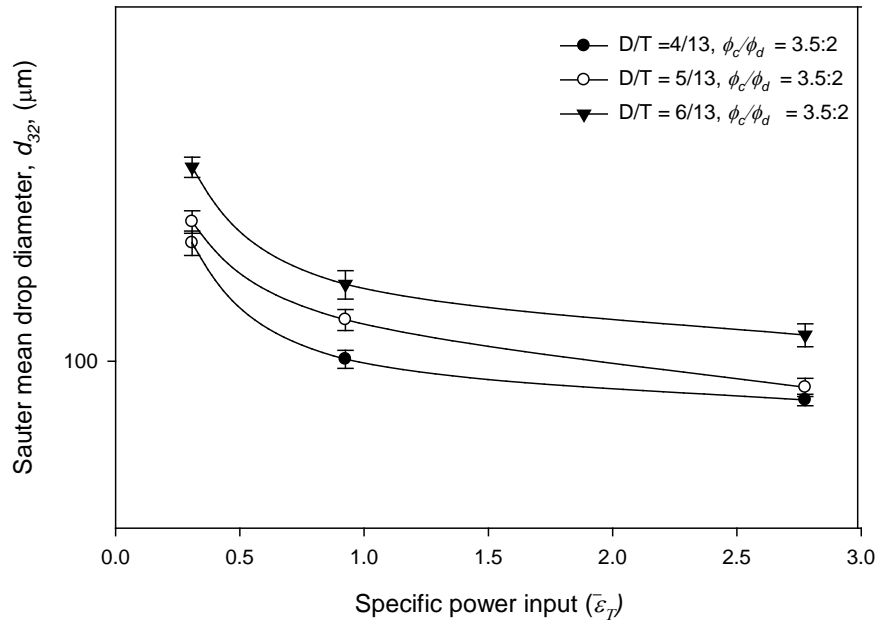
The plots of the d_{32} as a function of $\bar{\varepsilon}_T$ for all operating conditions are also shown in Figure 2.21 (a) to (c). In a similar manner to the We relationship all operating conditions showed that as the $\bar{\varepsilon}_T$ was increased, d_{32} decreased. At the lowest $\bar{\varepsilon}_T$, the d_{32} initially decreased abruptly until a point was reached when it decreased gradually. It was also observed that at the $\phi_c/\phi_d = 3.5:2$ all the D/T satisfied the exponential range of -0.4 to -0.47 ; however discrepancies were observed with the $D/T = 5/13$ impeller and $\phi_c/\phi_d = 1:1$ and $3.5:1$ as well as $D/T = 4/13$ impeller at $\phi_c/\phi_d = 3.5:1$. The list of power law exponents is given in Table 2.5.

Table 2.5. $\bar{\varepsilon}_T$ Power law exponents for all P/V , D/T and ϕ_c/ϕ_d

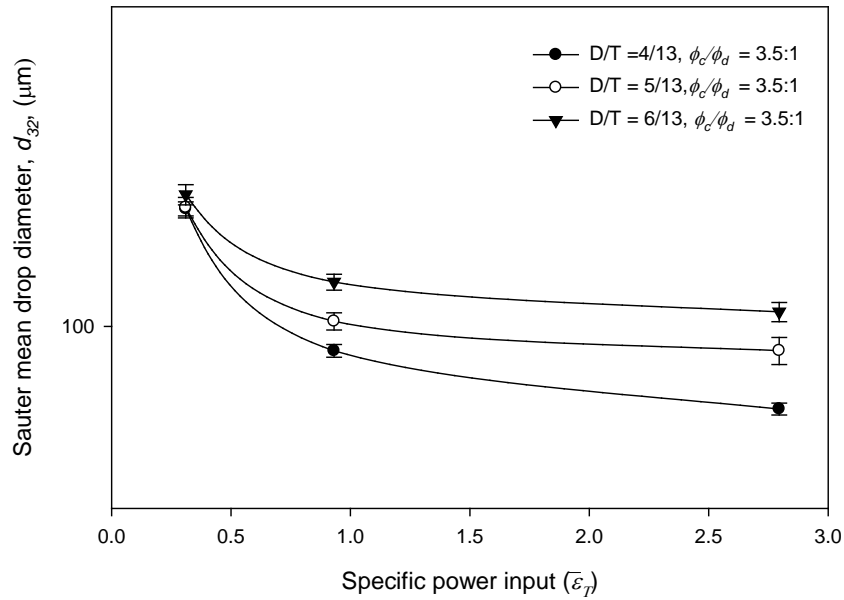
ϕ_c/ϕ_d	D/T		
	4/13	5/13	6/13
	$\bar{\varepsilon}_T$ power law exponents		
1:1	-0.47	-0.5	-0.46
3.5:2	-0.42	-0.41	-0.4
3.5:1	-0.27	-0.33	-0.46



(a)



(b)



(c)

Figure 2.21. The effects of $\bar{\varepsilon}_T$ on d_{32} for all D/T and ϕ_c/ϕ_d (a) 1:1 (b) 3.5:2 (c) 3.5:1

There are two possible reasons for the discrepant constants observed in the $\overline{\varepsilon_T}$ and We relationships. This first reason is attributed to the departure of the systems studied from the homogenous isotropic turbulence structure assumed by the Kolmogoroff-Hinze theory. The constants in the isotropic turbulence model were obtained from studies with high ϕ_c/ϕ_d ($\phi_d = 0.05$ to 0.5 %) compared to the low ϕ_c/ϕ_d used in this work ($\phi_d = 22$ to 50 %). As ϕ_c/ϕ_d decreases, coalescence increases especially in the regions of high macro instabilities which exist away from the impeller shear zone.

These will lead to an increase in droplet size from the predicted droplet size by the model (Pacek *et al.*, 1999; Godfrey *et al.*, 1989; Davies, 1992). The second and most significant reason is attributed to the interaction of the droplets with air bubbles which were shown previously at the $P/V = 2.7$ kW m^{-3} with the $D/T = 5/13$ and $6/13$ impeller. The presence of air decreased the available u' required for droplet breakup thus increasing the droplet size significantly from the theoretical droplet size.

The distributions that did satisfy the exponents showed that the governing equations scaled - but not exclusively - according to the isotropic turbulence structure as assumed by Kolmogoroff-Hinze's theory. They showed that flow within the vessels should be sufficiently turbulent beyond $Re \geq \sim 5 \times 10^3$ and that $\overline{\varepsilon_T}$ should be fixed upon scale up at the given D/T and ϕ_c/ϕ_d for similar droplet sizes to be obtained. This should guarantee the same micro and meso-mixing scales and distributions at the large scale.

The Re turbulent decomposition velocity is comprised of u' and \overline{U} . Since the requirements of $\overline{\varepsilon_T}$ is to maintain the specific ϕ_d of the system and achieve droplet breakup, it could be assumed that as

Re increased for the set of operating conditions that satisfied the Kolmogorov-Hinze's theory, a reduction in the amplitude of u' to lengths comparable to the droplet size and the increased frequency of its contact with droplets led to an increase in the oscillatory effects on the droplet's surface, which promoted droplet breakup. The corresponding increase in \bar{U} increased the mass flowrate of the dispersion, which maintained ϕ_d .

2.6. Conclusion

The effects of varying the P/V , ϕ_c/ϕ_d and D/T of a RDT , on droplet size in an agitated aqueous-organic LIX84-A system in a mixer have been investigated. These studies were carried out to obtain design requirements to scale up a mixer. Within the range of operating conditions studied, the change in P/V at fixed ϕ_c/ϕ_d and D/T demonstrated the greatest effect on droplet size. By changing the smallest D/T for the midrange and largest D/T d_{10} and d_{32} increased because the droplet size distribution broadened and skewed towards large droplet sizes. This was expected and occurred because of the consequent increase in the ratio of Q with U_{tip} .

At fixed ϕ_c/ϕ_d and D/T , the largest D/T had a larger Q and it promoted system homogeneity whilst the smallest D/T had the larger U_{tip} which produces smaller droplets and benefits mass transfer. By changing the largest ϕ_c/ϕ_d for the midrange and smallest ϕ_c/ϕ_d at fixed P/V and D/T , the droplet size increased because turbulent dampening increased as the ρ and the viscous resistance of the dispersion increased. Air ingression and holdup increased as ϕ_c/ϕ_d increased and when the midrange and larger D/T were used at $P/V = 2.7 \text{ kW m}^{-3}$. This led to the reduction in droplet shear and the increase in droplet size.

Values of We and $\overline{\varepsilon_T}$ were used to analyse the effects of P/V on droplet size since P/V cannot suitably describe turbulent features in agitated systems. The relationships between both functions and droplet size have been theoretically shown to satisfy specific power law constants according to the Kolmogoroff-Hinze's theory. A theoretical constant of -0.6 exists for We versus d_{32} relationship, whilst a constant within the range of -0.41 to -0.47 exists for $\overline{\varepsilon_T}$ and d_{32} . From the study, a selection of distributions did satisfy these constants with error margins given, whilst air ingress led to poor agreements with the remainder. Only three data points were used per plot and these were obtained from a line of best fit from statistical tests; warranting care during data interpretation.

The accurate set of results demonstrated that $\overline{\varepsilon_T}$ should be fixed upon scale up at the given D/T and ϕ_c / ϕ_d for similar droplet sizes to be obtained because the inertial forces and u' in turbulent decomposition function scaled in a manner analogous to the Kolmogorov-Hinze's theory. They also showed that flow will be sufficiently turbulent beyond the lowest Re .

Chapter 3: The study of a settler for the separation of Copper/HCl dispersion in organic LIX 84-A

3.1. Introduction

Following the mixer section discussed in Chapter 2, where the organic is loaded with the solute, the dispersion is transferred into the settler to separate under gravity and coalesce. The settler constitutes ~ 90 % of the total mixer-settler size and it is traditionally designed to handle high total dispersed and continuous phase flowrates, Q_t , and traces of suspended solids.

Within industry, there is motivation to reduce the settler size required for phase separation because large settlers denote high capital cost, large equipment footprint and high organic and solute inventory. However, design procedures have proven unreliable because they rely on large safety factors.

Modifications to settlers such as the introduction of flow distributors, baffles and picket fences have also been used in some designs to enhance phase separation. The temperature of dispersions, density ($\Delta\rho$) and viscosity difference ($\Delta\mu$), and droplet size, are some other factors that can also be altered. When temperature, ρ and μ are fixed, droplet size becomes the limiting factor.

Droplet size distributions depend on the phase continuity, power input, P/V (where P is the power and V is the volume of the fluid), the continuous phase to dispersed phase flow ratio, Q_c/Q_d (where Q_d and Q_c are the dispersed and continuous phase flowrates), the impeller diameter, D , to vessel diameter, T , ratio, (D/T) and Q_t . Chemical composition can also influence settler performance where dissimilar systems may behave differently. Thus to have a confident design procedure to

conservatively design a settler without the need for safety factors, the effects of these parameters should be understood.

Relationships that incorporate P/V , dispersed phase throughput, Q_d/A , (where A is the horizontal area), and dispersed phase fraction (ϕ_d) have been devised and shown to apply to most liquid-liquid ($L-L$) systems, despite the differences in operating conditions and phase properties (Barnea and Mizrahi, 1975a). However the authors of these correlations have always stressed the necessity of practical investigations if a reduction in unit cost is required, since the reduction in practical errors at the onset of settler design is important to avoid overestimating or underestimating large-scale units. Correlations cannot fully guarantee this. Thus reliable data is desired from laboratory and/or pilot-scale runs.

This Chapter carries on from Chapter 2, where the effects of P/V , Q_c/Q_d and D/T of a 6 bladed Rushton Disc Turbine (RDT) on the droplet size were investigated in a box mixer. The consequent effects of these factors on phase separation in the settler are presented. At the onset, the dense packed region of the dispersion band is analysed and the contribution of each factor to the region is quantified with Minitab[®].

The sedimentation of droplets and transition to the dense packed region of the dispersion band are analysed to estimate the critical droplet sizes that are most and least susceptible to hindered settling in the sedimenting region. The effects of each factor on dispersed phase concentration, C_a , in the vertical plane of the dispersion band is also investigated before proceeding to formulate relationships between the Q_d/A and C_a for settler design purposes.

However, before proceeding to the results section, a literature review on the $L-L$ separation is given, focussing initially on the different modes of settler operation and factors that affect droplet coalescence. A generic sedimentation profile that emerges during sedimentation and coalescence in $L-L$ systems is then discussed before reviewing correlations that can and have been used for settler design.

3.2. Literature review

3.2.1. Settlers

Dispersions have an intermediate density to the organic and aqueous phase. When transferred into a horizontal settler, wedge shaped or deep layer dispersion bands can develop. These are shown schematically in Figure 3.1 and Figure 3.2. Jeelani and Hartland (1985) showed that two distinct regions also exist in dispersion bands.

The first is an apparent region called the dense packed region. It is made up of droplets with relatively high terminal settling velocities (V_t). The other region is called the sedimenting region. It is a less apparent region comprised of hindered droplets with low V_t . These droplets remain in this region after droplets with much higher V_t have sedimented to the dense packed region.

The type of dispersion band that develops depends on P/V and Q_d/A when all other properties are fixed. By increasing P/V or Q_d/A the dispersion band will change from wedge shaped to deep layer dispersion bands until the thickness of the deep layer dispersion band reaches the overflow and discharge ports of the continuous and dispersed phase within the settler. This condition is called flooding.

Wedge shaped dispersion bands emerge because the rate of sedimentation and coalescence (ψ) of droplets in the vertical plane of the dispersion band is greater than their rate of spreading in the horizontal plane. Deep layer dispersion bands develop when sedimentation and ψ of droplets in the vertical plane is less than their rate of spreading in the horizontal plane (Barnea and Mizrahi, 1975a).

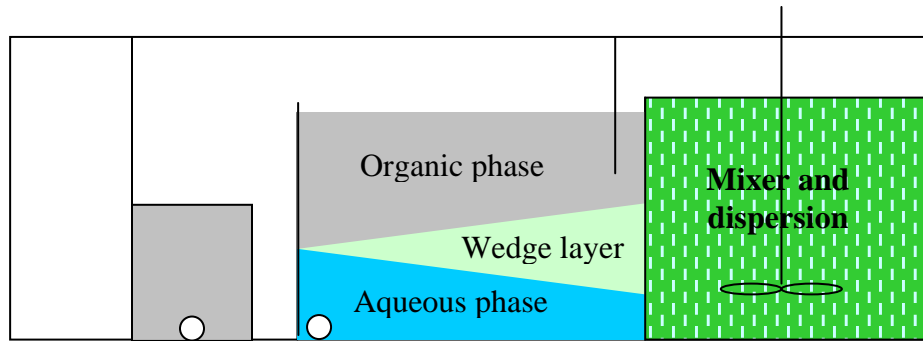


Figure 3.1. Schematic of a wedge shaped dispersion band

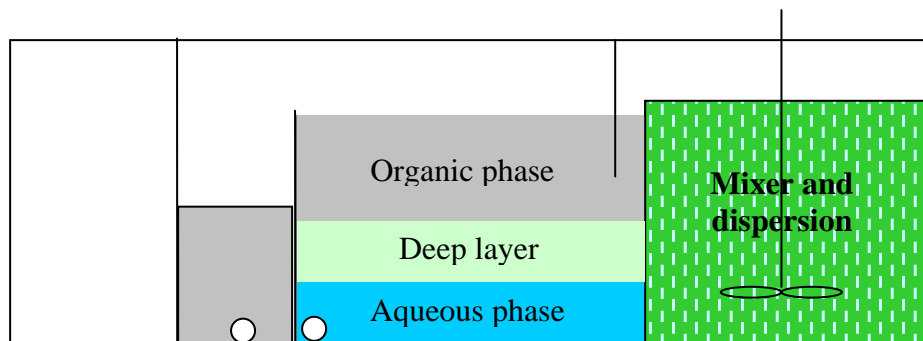


Figure 3.2. Schematic of a deep layer dispersion band

Two boundary layers also exist in both dispersion bands. The first boundary layer is called the coalescing interface and it is located between the dispersion band and the separated dispersed phase. The other boundary layer is called the non-coalescing interface and it is located between the dispersion band and the continuous phase.

3.2.2. Droplet coalescence

Phase separation is a complicated process because of constantly changing force distributions in the dispersion band. Within the dispersion band, chaotic settling of droplets at all scales occurs because of short-range forces, long-range forces and hindered settling. Hindered settling takes place when the velocity gradients of droplets are hindered by the presence of other droplets (McCabe, 2001).

The drag force (F_d) on hindered droplets is greater than F_d of free settling droplets. Short-range forces are short periodic molecular interactions, which are independent of hydrodynamic forces, whilst long-range forces are long periodic interactions that depend on the hydrodynamic forces. They affect the mobility of droplets and the drainage of continuous phase films that exist between coalescing droplets.

Droplet coalescence commences by droplet-droplet collision. This is followed by the drainage of thin films between the droplets before they rupture and merge their contents. Hydrodynamic, hydrostatic and physicochemical forces can promote film drainage. The magnitude of the force that brings the droplets together will determine the film drainage time. During drainage a critical film thickness has to be reached before coalescence can take place.

To reach this thickness the driving force has to be large enough to cause the droplet's surface to deform and create a dimple. The driving force should also be large enough to oppose repulsive forces between the droplets and it should cause the dimple to transit to a plane parallel film with a radius equivalent to the repulsive force.

The parallel film fluctuates due to thermal disturbances before shrinking again. At this point a critical film develops before the droplets exchange their contents (Ivanov and Dimitrov, 1988). The stability of the critical film will increase as the droplet size increases and sometimes the critical film will rupture before drainage is complete.

3.2.3. Coalescence rate

Three main factors affect the coalescence rate, ψ , of droplets. These are droplet size, external forces and physical properties of the organic and aqueous phases. Amongst these, droplet size is the most important factor.

Droplet size

Increased droplet breakup is necessary for enhanced mass transfer in the mixer; however this comes at the expense of speedy droplet separation. Since both stages are important in the extraction process, this poses a difficulty in the settler design. Sareen *et al.* (1966) and Magiera and Blass (1997) suggested that ideal dispersions are dispersions in which the droplet diameters are $\geq 100 \mu\text{m}$.

For such dispersions, droplets readily sediment by gravity and collect at the dense packed layer where ψ is relatively rapid. In the dense packed layer, droplet stability increases as droplet size increases since larger droplets deform easily and film drainage takes place quickly. The contact time and frequency of droplet collision will also increase with droplet size.

Liu and Li (1999) showed that a droplet size range exists wherein droplets smaller than a minimum droplet size (d_{min}) will coalesce, whilst droplets larger than a maximum droplet size (d_{max}) will break up. Sareen *et al.* (1966) also showed that secondary dispersions exist, which are made up of

droplets that do not readily sediment or coalesce. To simplify separation, the droplet size distribution should be controlled to minimise the formation of secondary dispersions.

External forces

Externally applied forces such as vibration, electrical charges and pH modification can enhance ψ by decreasing the film drainage rate and increasing the film area caused by droplet deformation.

Jeelani and Hartland (1991) showed that vibrations intensify the force transmitted to coalescing droplets by increasing the resistance to repulsive forces between droplets and the thin films. Lang and Wilke (1971a) showed that vibrations reduce ψ , which may have a significant effect, depending on whether the determining step is thin film drainage or droplet rupture (Lang and Wilke, 1971b).

Direct current (*DC*) fields can also improve coalescence of aqueous droplets (Allan and Mason, 1961; Bailes and Larkhi, 1981). *DC* fields flatten droplets, which promotes film drainage by accelerating the rate of film thinning. Leng and Calabrese (2004) showed that by applying electric fields, electrostatic forces alter the surface charges on droplets to encourage droplet coalescence; however they could also encourage repulsive forces which promote repulsion.

As $\Delta\rho$ of the continuous and dispersed phase increases, droplets flatten and film draining increases, while the hydrostatic forces causing the drainage do not increase proportionally so that the coalescence time increases (Jeffreys and Davies, 1971). In settlers the ψ of droplets at the dispersion entry point is high because the largest hydrodynamic disturbance can be found there and the largest percentage of droplets sizes $\geq d_{min}$ are also found there.

Physical properties

The higher the interfacial tension (ζ) the greater the droplet resistance to deformation, which decreases the film drainage area and subsequently increases ψ (Hartland and Jeelani, 1994). However, increasing ζ will impede flow in the film which increases rest times.

By increasing continuous phase viscosity (μ_c), film drainage and ψ will decrease. Dreher *et al.* (1999) showed that the increase in elasticity of the continuous phase was responsible for this. The effect of elasticity was also shown to increase as droplet size decreased. ψ is independent of the dispersed phase viscosity (μ_d) if film thinning is the ψ determining step, but it increases with μ_d if the rupture process is the ψ determining step (Lang and Wilke, 1971b).

Changes in surface tension (σ) can also complicate ψ by developing Marangoni stresses wherein the phase with high σ pulls away strongly from the low σ creating a gradient in σ .

Finally, Leng and Calabrese (2004), Lawson (1967) and Jeffreys and Hawksley (1965a) showed that as the temperature increases ψ will increase because μ_c and the temperature gradients weaken the thin films.

Sedimentation profiles

Dispersions transferred into settlers accumulate in the interfacial boundary until they reach a steady state dispersion height. At this steady state dispersion height, the rate of sedimentation and ψ of droplets will be constant. The steady state dispersion height will only change with A , since the

continuous phase throughput (Q_c/A), Q_d/A and the dispersion's confinement in the settler alter the dispersion residence time.

At steady state, droplets spread in both vertical and the horizontal planes of the settler creating a disengagement profile described by the dispersion flow pattern, ψ and sedimentation rates (Figure 3.3). Jeelani and Hartland (1985) developed a theory to explain this disengagement profile from batch $L-L$ separation tests called the dispersion layer theory, where they examined the sedimentation and coalescence process.

The theory was based on the assumptions that:

- The dispersion volume in the settler is proportional to the dispersed phase flow.
- Droplet exchange commences from the continuous phase, through the sedimenting region and then the dense packed region in a stack-wise manner before coalescing into the homophase.
- Droplets settling through the continuous phase are hindered, where the hindered settling velocity can be estimated by the expression given below:

$$v = \frac{\Delta\rho g d^2}{18\mu} \frac{(1 - \phi_d)^2}{1 + 4.56\phi_d}, \quad (3.1)$$

where g is the gravitational constant, ϕ_d is the dispersed phase fraction and d is the droplet size.

- The ψ of a given droplet size in the dispersion band can be correlated from experiments or calculated by theory (Artzen, 2001).

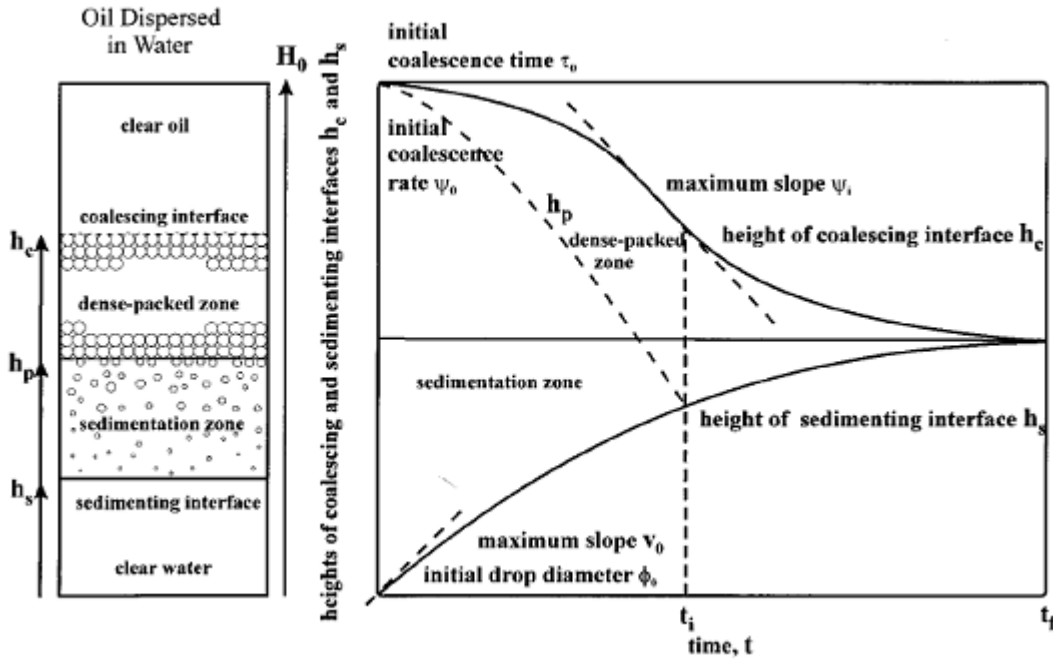


Figure 3.3. Batch dispersion decay (Jeelani and Hartland, 1985)

They suggested that a time (t_i) called the inflection point (see Figure 3.3) is when the last droplet will settle on the dispersion band. At this point a mass balance can be carried out to describe the height of the boundary of the dispersion band in both horizontal and vertical planes. The ψ until the inflection point was described by Equation 3.2 for a given characteristic droplet size (d_o) and interfacial coalescence time (t_o^c):

$$\psi_{*i} = \frac{2\phi_* d_o}{3t_o^c} \left(\frac{y_{*i}}{d_o} \right)^p, \quad (3.2)$$

where ψ_{*i} is the coalescence rate at the inflection point, ϕ_* is the dispersed phase holdup and y_{*i} is a unit length in the vertical plane.

To apply their theory to continuous settlers, modifications and assumptions were considered necessary. First of all sedimentation was considered a steady state and gravity driven process

because the continuous phase momentum will be low compared to the size of the settler. Then the ψ across the dispersion band was required to correspond to the incoming dispersed phase (Artzen, 2001).

3.2.4. Settler scale-up correlations

In a comprehensive study of settlers, Barnea (1980b) concluded that deep layer dispersion bands should be operated rather than a wedge shape dispersion band if capital costs and equipment footprint are obstacles to settler design. This was because a lot of emphasis has been placed on the role of the horizontal plane over the vertical plane especially for industries such as the copper industry where settler space is a compromise. Thus wedge shaped dispersion bands overcompensate for A but deep layer dispersion bands account for both planes. Even more significantly, the thick dense packed region can be used as a filter to coalesce small droplets.

If a settler is large enough to reduce wall effects and the dispersed phase can ensure a band of nearly even thickness at a fixed A , Mizrahi and Barnea (1975a) and Ryon *et al.* (1959) showed that by altering A , Q_d will change in direct proportion. Eckert (1989), Mizrahi and Barnea (1975a) and Ryon *et al.* (1959) used dispersion band thickness, H_d , as the dependent variable to relate the change in C_a to A . The general relationship obtained is shown below.

$$H_d = K(Q_d/A)^y, \quad (3.3)$$

where K and y are experimentally determined.

Barnea (1980b) stated that y can rest within the range of 2 to 7, whilst Ryon *et al.* (1959) showed that the correlation is applicable to scale up ratios as high as 1000:1. Mizrahi and Barnea (1975a) and Gondo and Kusunoki (1969) called to question the validity of Equation 3.3 for all operating

conditions because of its simplicity and the omission of factors such as the Q_c/Q_d and P/V . Gondo and Kusonoki (1969) showed that by accounting for Q_c/Q_d and P/V , ΔH_d can be expressed by Equation (3.4):

$$H_d = \phi_a^{4.9} N^{2.8} (Q_d/A)^{3.1}, \quad (3.4)$$

where N is the impeller speed.

Previously Treybal (1963) suggested that a vessel length to diameter ratio of 4 should be used for horizontal settler sizing (Equation 3.5). His correlation was based on a Q_t/A of $12.6 \text{ m}^3 \text{ m}^{-2} \text{ hr}^{-1}$.

$$D_s = 8.4(Q_c + Q_d)^{0.5}, \quad (3.5)$$

where D_s is the settler diameter. Equation (3.5) and the total dispersed and continuous throughput (Q_t/A) of $12.6 \text{ m}^3 \text{ m}^{-2} \text{ hr}^{-1}$ were considered as rules of thumb for scale up and they were intended for estimation purposes only when operating data were not available.

Another rule of thumb that was used for settler design in copper extraction was a Q_t/A of $2.5 \text{ m}^3 \text{ m}^{-2} \text{ hr}^{-1}$ (Eckert, 1989). This value was based on a large A and shallow base for separation in the copper industry compared to the greater settler depth in Treybal's (1963) estimation (Eckert, 1989).

3.2.5. Coalescence enhancement

The thickness of deep layer dispersion bands can also be used to assess the point of flooding in settlers, which is an incipient point used by designers to evaluate where coalescence enhancers are introduced. Coalescence enhancers are retrofits found in settlers, which speed up coalescence and deal with entrainment or secondary dispersions. The most common coalescence enhancer used in settlers is the picket fence.

The picket fence generally serves to evenly distribute flow and dampen the dispersion from the mixer. However it has found use in the retention of the deep layer dispersion bands along the settler, acting like a filtration unit by collecting small droplets and inducing coalescence to bigger droplets by droplet-droplet coalescence (Miller, 2001).

Multiple picket fences can be ordered within settlers wherein the first picket fence, which is directed towards the mixer's overflow, decreases the initial deep layer dispersion band thickness which is subsequently reduced by the following picket fences until the band is non-existent (Kankaanpaa, 2005).

Other coalescence enhancers that have been used to encourage phase separation are packed media and electrocoalescence. Electrocoalescence is used in petroleum industries where water droplets are separated from crude oil by high voltage alternating current (AC) (Cottrell and Speed, 1911) and, to a lesser extent, direct current (DC), Bailes and Larkai (1981).

After separation in the settler, the continuous phase will typically carry entrainment of the dispersed phase and the separated homophase will show low levels of entrainment of the continuous phase. Packed beds are thus primarily installed in settlers to reduce entrainment. They are efficient but require provision to be made in settlers for periodic removal because they can be blinded and cause channel flow around edges of the packed bed or through non-blinded sections of the coalescer (Madia *et al.*, 1976).

3.3. Conclusions from literature review

Phase separation in settlers and settler scale-up considerations have been reviewed, wherein the two types of dispersion bands that can develop and their structures were examined. The factors that favour one dispersion band over the other and changes that can be made to promote droplet coalescence were discussed, and the theories that define the general phase separation profile were examined. Finally, the well-known correlations for phase separation and their limitations were presented.

The main disadvantage of all these correlations was their need for practical studies to obtain parameters for the models, such as those by Ryon *et al.* (1959) and Gondo and Kusonoki (1969). In this study, settler design is investigated via the phase separation of an agitated $L-L$ system in a pilot-scale settler for the design of a settler. The effects of given operating conditions on the dispersion band, phase separation and entrainment will be examined.

3.4. Materials and methods

3.4.1. Settler

The details of the phases used were previously given in §2.4.1 of Chapter 2 and the dimensions of the settler were shown in Figure 2.3. The dispersion generated in the mixer was transferred into the settler via a full width overflow weir. The settler had a total length (L_s) and width (W_s) of 0.5 m and 0.13 m respectively. It also had two weirs at the settler end; one which directed the organic to storage and the other which directed the aqueous phase to storage.

An interface regulator was attached to the aqueous phase piping and used to control the location of the coalescing interface. A baffle minimised turbulence associated with the inlet flow from the mixer. Measurements of C_a in the dispersion band were carried out in the vertical plane after the baffle and the horizontal plane along the organic surface from the baffle to the organic weir. The settler was compartmented and each compartment had slots with outlets to the organic or aqueous phase storage. The slots enabled the weirs to be moved along the settler to decrease or increase A .

Each Q_c/Q_d split into a Q_c/A and Q_d/A at a fixed A . For example, at the Q_c/Q_d of 1:1, 3.5:2 and 3.5:1 and fixed A of 0.0195 m^2 , Q_d/A was $0.076 \text{ m}^3 \text{ m}^{-2} \cdot \text{hr}^{-1}$, $0.055 \text{ m}^3 \text{ m}^{-2} \cdot \text{hr}^{-1}$ and $0.033 \text{ m}^3 \text{ m}^{-2} \cdot \text{hr}^{-1}$ respectively, whilst the Q_c/A was $0.076 \text{ m}^3 \text{ m}^{-2} \cdot \text{hr}^{-1}$, $0.099 \text{ m}^3 \text{ m}^{-2} \cdot \text{hr}^{-1}$ and $0.121 \text{ m}^3 \text{ m}^{-2} \cdot \text{hr}^{-1}$ respectively. The operating conditions, D/T and P/V used were also previously given in §2.4.4 and Table 2.2 whilst the flow diagram from the mixer into the settler was given in Figure 2.4.

3.4.2. Dispersion measurement technique

The sampling technique is illustrated by the red arrows in Figure 3.4. The C_a in the dispersion band was measured at equally spaced points in the vertical plane of the settler (behind the baffles) at right angles to the vertical plane and in the horizontal plane on the surface of the settler at right angles to the horizontal plane of flow using an off line turbidity meter (Palintest Micro 950, Palintest, USA), standard containers, an eppendorf adjustable volume pipette and 5 mL pipette tips. This was carried out to avoid local measurements which would have given unrepresentative sample readings.

The number of points sampled in the horizontal plane varied with L_s . For example at a L_s of 0.15 m four equally spaced points were sampled. Prior to any measurement, the device was calibrated with

calibration standards that came with the device. For a completely clear organic, turbidity readings were zero nephelometric turbidity units (*NTU*), which is equal to 0 ml of aqueous phase for every 100 mL of the dispersion.

The actual C_a of the aqueous phase in the organic were determined by relating the values in *NTU* to previously determined volumes of the aqueous phase in a completely de-entrained organic. The calibrations are given in Appendix B.

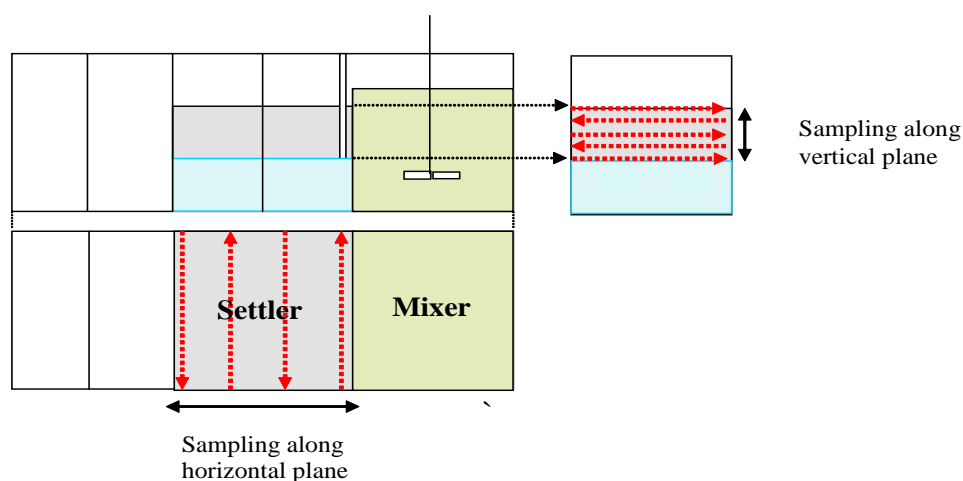


Figure 3.4. Description of sampling process

3.4.3. Properties of the aqueous and organic phases

The σ and ζ of both phases were obtained at room temperature using a torsion balance (White Electrical Instrument Company, UK) with a platinum Du Nouy ring. A 40 mL beaker containing ~ 10 mL of the organic and 10 mL of the aqueous phase was used to measure the ζ of both phases, whilst a watch glass was used to measure their individual σ . Multiple measurements were taken to obtain an average value. The average densities of the dispersions were calculated using the expressions by Godfrey and Slater (1994) and actual measurements. The physical properties of the phases and their mixtures are given in Table 3.1.

$$\rho_m = \phi_d \rho_d + (1 - \phi_d) \rho_c, \quad (3.6)$$

$$\mu_m = \frac{\mu_c}{1 - \phi_c} \left(1 + \frac{1.5\mu_d\phi_d}{\mu_c + \mu_d} \right). \quad (3.7)$$

Table 3.1. Physical properties of the phases

Flow Ratio (-)	Density of dispersion (kg m ⁻³)	Density of solvent mixture LIX 84-A and Solvesso 150 (kg m ⁻³)	Interfacial Tension (N m ⁻¹)	Surface tension (N m ⁻¹)		Average viscosity of organic and aqueous (kg m ⁻¹ s ⁻¹)
1:1	1025	920	0.0235	0.014 (org)	0.07 (aq)	0.0035
3.5:2	986					0.0026
3.5:1	966					0.00193

3.5. Results and discussion

3.5.1. Dense packed region analysis

The dense packed regions of the dispersion bands were analysed at a fixed dispersion band depth of 0.05 m away from the settler bottom and a fixed A of 0.0195 m².

Generally, wedge shaped and deep dense packed regions developed across the range of operating conditions studied. Initial examinations suggested that the dense packed region changed from the wedge to a deep region as P/V was increased.

However the effects of Q_c/Q_d and D/T could not be accurately ascertained. Minitab[®] was thus used to quantify their contributions. A 2³ factorial approach was used to analyse each factor, their levels and variables as given in Table 3.2.

Table 3.2. Factors, levels and variables for the dense packed region.

Factor	Levels	Variables	
P/V	2	0.9	2.7
Q_c/Q_d	2	3.5:2	1:1
D/T	2	4/13	5/13

The samples analysed were obtained behind the baffle and within the transition to the dense region. Since the system was at steady state it was assumed that the ratio of samples obtained at the given point would be similar to the ratio of samples that would have been obtained elsewhere along the transition.

Minitab[®] analysed the samples to a confidence level (p-value) of 0.05. The results obtained are shown in Table 3.3 and in the normal plot in Figure 3.5. P/V was the most significant factor with a p-value of ~ 0 , then D/T with ~ 0.024 and finally Q_c/Q_d with ~ 0.045 . P/V resided at the opposite end of the confidence line to D/T and Q_c/Q_d , because C_a increased with P/V , whilst decreasing Q_c/Q_d and increasing D/T decreased C_a .

Table 3.3. Estimated effects and coefficients table

Factor	Effect	Coefficient	Standard error	T-ratio	P-value
Constant		3.4525	0.1008	34.25	0.000
D/T	-0.7150	-0.3575	0.1008	-3.55	0.024
Q_c/Q_d	-0.5800	-0.2900	0.1008	-2.88	0.045
P/V	5.6900	2.8450	0.1008	28.23	0.000

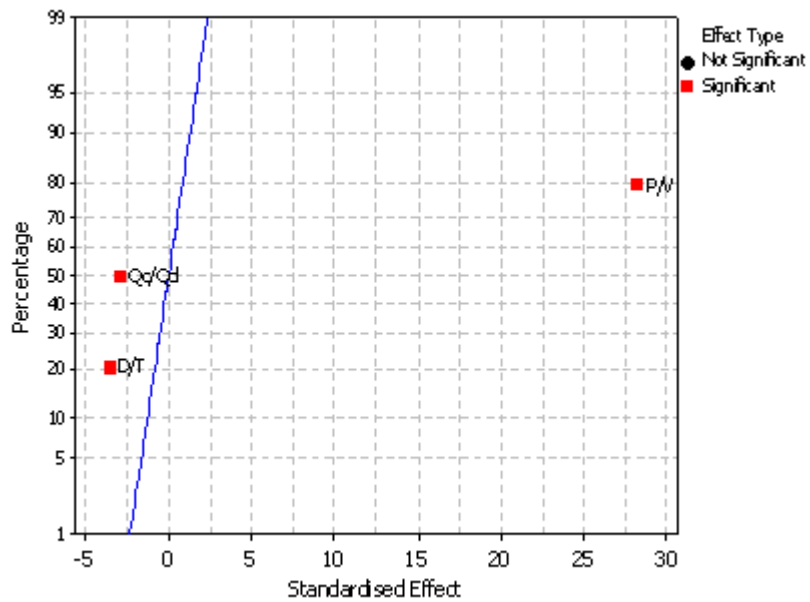


Figure 3.5. Normal plot of the effects of the P/V , Q_c/Q_d and D/T on the dense packed region.

In the Pareto plot (Figure 3.6) the main effects are distributed according to their significance. P/V contributed $\sim 84\%$ to the dense packed region, then D/T by $\sim 9\%$ and finally Q_c/Q_d by $\sim 7\%$.

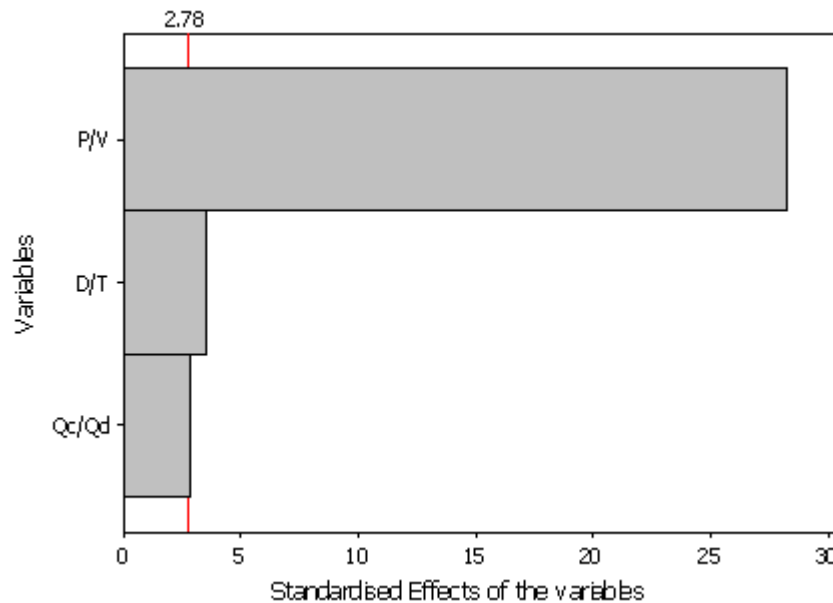


Figure 3.6. Pareto plot of the standardised effect of each factor on the dense packed region

Thus, it can be summarised that at $P/V = 0.3 \text{ kW m}^{-3}$, the wedge regions shown in Figure 3.7 were unambiguous. At $P/V = 0.9 \text{ kW m}^{-3}$ (Figure 3.8) they were still evident but partially emulsified. Both types of wedges tapered from a thickness of $\sim 0.01 \text{ m}$ at the settler entry and were exacerbated as D/T and Q_c/Q_d decreased.

Wedge regions also emerged with $D/T = 6/13$ impeller and $P/V = 2.7 \text{ kW m}^{-3}$ for all Q_c/Q_d as well as $D/T = 5/13$ impeller and the $Q_c/Q_d = 3.5:2$ and $1:1$. However, due to air entrainment by these impellers (the reader is referred to §2.5.3) it was uncertain if they would have resulted.

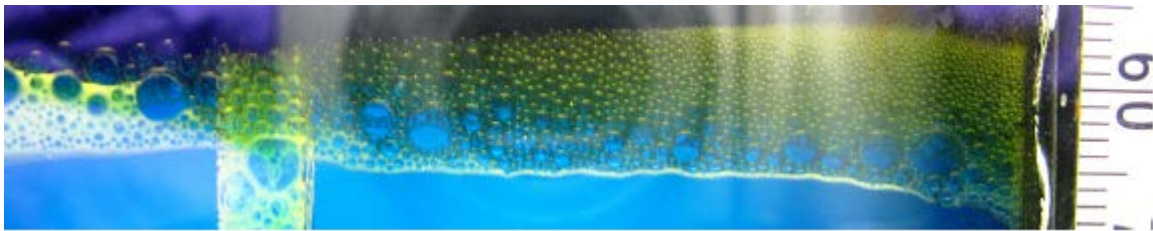


Figure 3.7. Clear wedge shaped region at the $P/V = 0.3 \text{ kW m}^{-3}$

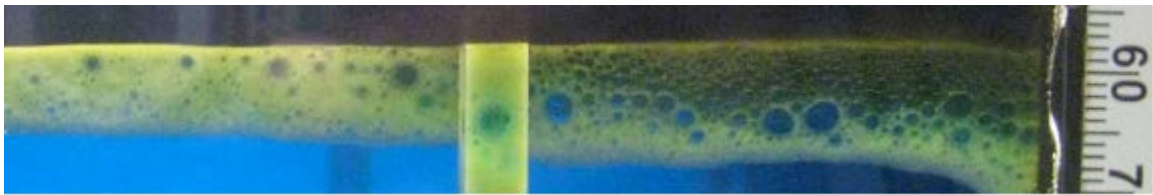


Figure 3.8. Emulsified wedge shaped region observed at the $P/V = 0.9 \text{ kW m}^{-3}$

Deep regions were observed with the $D/T = 4/13$ impeller and $P/V = 2.7 \text{ kW m}^{-3}$ for all Q_c/Q_d (Figure 3.9). They were completely emulsified and varied in thickness with Q_c/Q_d . At the $Q_c/Q_d = 1:1$, the layer was $\sim 0.001 \text{ m}$ thick but increased to $\sim 0.015 \text{ m}$ at the $Q_c/Q_d = 3.5:1$.

At these thicknesses, they accounted for ~ 1 % to 10 % of the total settler volume. Finally, the coalescing interface was unambiguous for the clear wedge but partly and totally obscured for emulsified wedge and deep dense packed regions respectively. The evenness of the non-coalescing interface also faded as Q_c/Q_d increased.

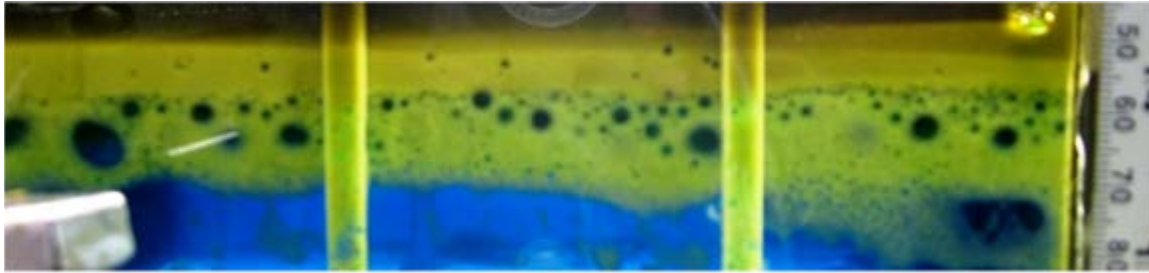


Figure 3.9. A typical deep layer dispersion band at the $P/V = 2.7 \text{ kW m}^{-3}$

As P/V was increased at a fixed Q_c/Q_d and D/T , the wedge changed to a deep dense packed region, because the average shear rate ($\dot{\gamma}_a$) of the dispersion increased, since $\dot{\gamma}_a \approx N^{1.5}$. This decreased droplet size and consequently the V_t of droplets, because $V_t \propto d^2$.

This is illustrated by the cumulative volume distribution (CVD) in Figure 3.10, where droplet sizes that make up 10 % of the total volume of droplets ($d_{v,0.1}$) increased as P/V decreased in the mixer.

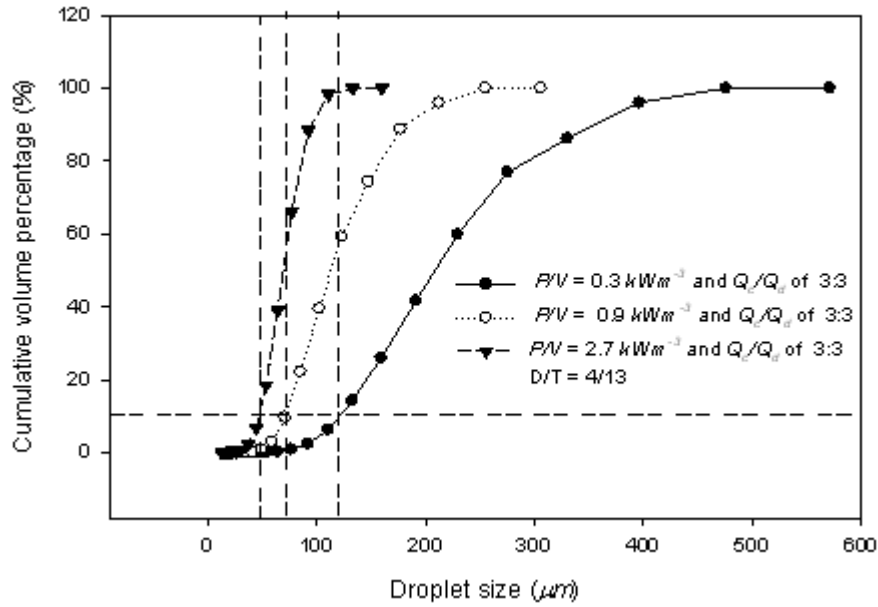


Figure 3.10. CVD illustrating the change in the uniformity of droplet size distribution as P/V was increased.

The relative span factor (RSP) of the CVD also decreased from ~ 1.14 to 0.66 as a more uniform

droplet size distribution emerged, where also $RSP = \frac{(d_{v0.9} - d_{v0.1})}{d_{v0.5}}$.

Assuming steady state conditions and Stokes' law i.e. $Re \leq 0.2$, $F_d \propto V_t^2$, thus the rate of droplet sedimentation decreased compared to the rate of droplet spreading across the settler.

ψ also decreased, since $\psi \approx \frac{d_o}{t_o}$ (Jeelani and Hartland, 1985) at a fixed ϕ_* and y_{*i} , which increased

hindered settling and decreased phase disengagement. At a fixed P/V and Q_c/Q_d , decreasing the D/T

increased the maximum shear rate ($\dot{\gamma}_m$) at the impeller jet boundary, since tip speed, $U_{tip} \propto D^{-2/3}$,

thus droplet size decreased and contributed to hindered settling. Similarly, at fixed P/V and D/T , increasing Q_c/Q_d decreased droplet size, because $d \approx \phi_d^{0.5}$ (Calderbank *et al.*, 1958).

The droplet size distribution in the sedimenting region and transition to dense region was analysed in the following section to estimate the droplet size responsible for C_a in the sedimenting region and critical droplet size least hindered in the sedimenting region. The analysis was carried out at a fixed dispersion band depth of 0.05 m away from the settler bottom and A of 0.0195 m².

3.5.2. Droplet size within the sedimenting and transition to the dense packed region in the turbulent mixing regime

The droplet size distributions in the sedimenting region of the dispersion band for $D/T = 4/13$ impeller, $P/V = 2.7 \text{ kW m}^{-3}$ and $Q_c/Q_d = 1:1$ and 3.5:2 are shown in Figure 3.11. Samples were obtained behind the baffle, ~ 0.03 m away from the coalescing interface.

Small droplets with a narrow droplet size distribution, spanning ~ 6 to 40 μm and 6 to 100 μm for $Q_c/Q_d = 1:1$ and 3.5:2 respectively and with a similar geometric mean droplet size (d_{50}) of $\sim 16 \mu\text{m}$ were observed in the sedimenting region. The percentage d_{50} decreased as Q_c/Q_d increased and a tail emerged towards larger droplet sizes.

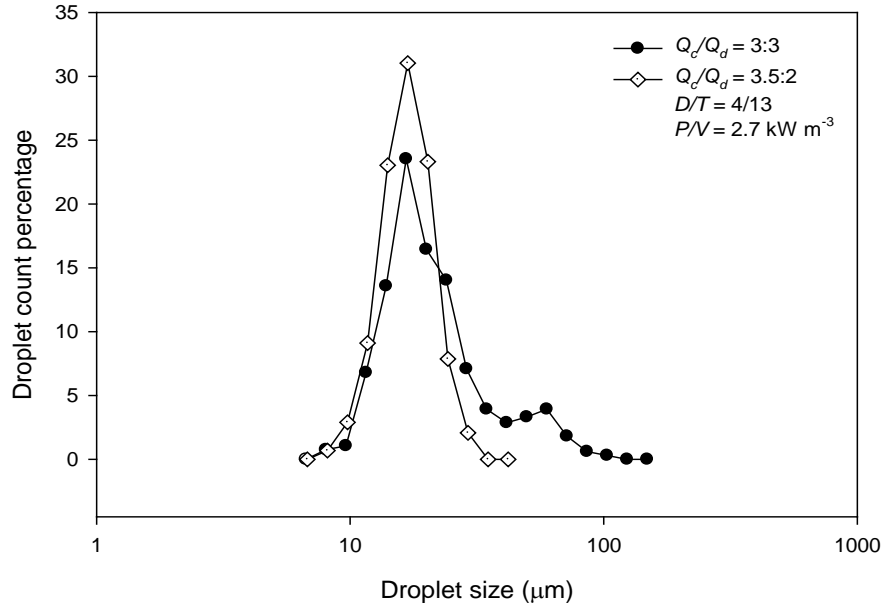


Figure 3.11. Droplet size distributions of samples withdrawn from the sedimenting region for $D/T = 4/13$, $P/V = 2.7 \text{ kW m}^{-3}$ and $Q_c/Q_d = 1:1$ and $3.5:2$.

The droplet size distribution and *CVD* of droplets in the transition and sedimenting region for the $D/T = 4/13$ impeller, $P/V = 2.7 \text{ kW m}^{-3}$ and $Q_c/Q_d = 3.5:2$ are also shown in Figure 3.12. The C_a in both locations was $\sim 4.5 \text{ \% v/v}$ and 3.38 \% v/v respectively.

In the transition, as expected larger droplets with a broad droplet size distribution ($RSP \approx 1.05$) were observed against the small droplets with narrow droplet size distributions ($RSP \approx 0.45$) previously shown in the sedimenting region.

The d_{50} in the transition was $\sim 30 \text{ }\mu\text{m}$, which is $\sim 50 \text{ \%}$ more than the d_{50} in the sedimenting layer. 60 \% of the droplets in the transition were within $\pm 33 \text{ \%}$ of a $d_{v,0.5}$ of $\sim 60 \text{ }\mu\text{m}$, compared to $\sim 75 \text{ \%}$ of the droplet size within $\pm 67 \text{ \%}$ of a $d_{v,0.5}$ of $\sim 20 \text{ }\mu\text{m}$ in the sedimenting region. The V_t of the d_{50} in the transition was ~ 4 times more than the V_t of the d_{50} in the sedimenting region (at $\sim 2.6 \times 10^{-5} \text{ m}$

s^{-1}) and 4 times more than Q_c/A . Its settling velocity was estimated to have reduced by $\sim 25\%$ due to hindered settling.

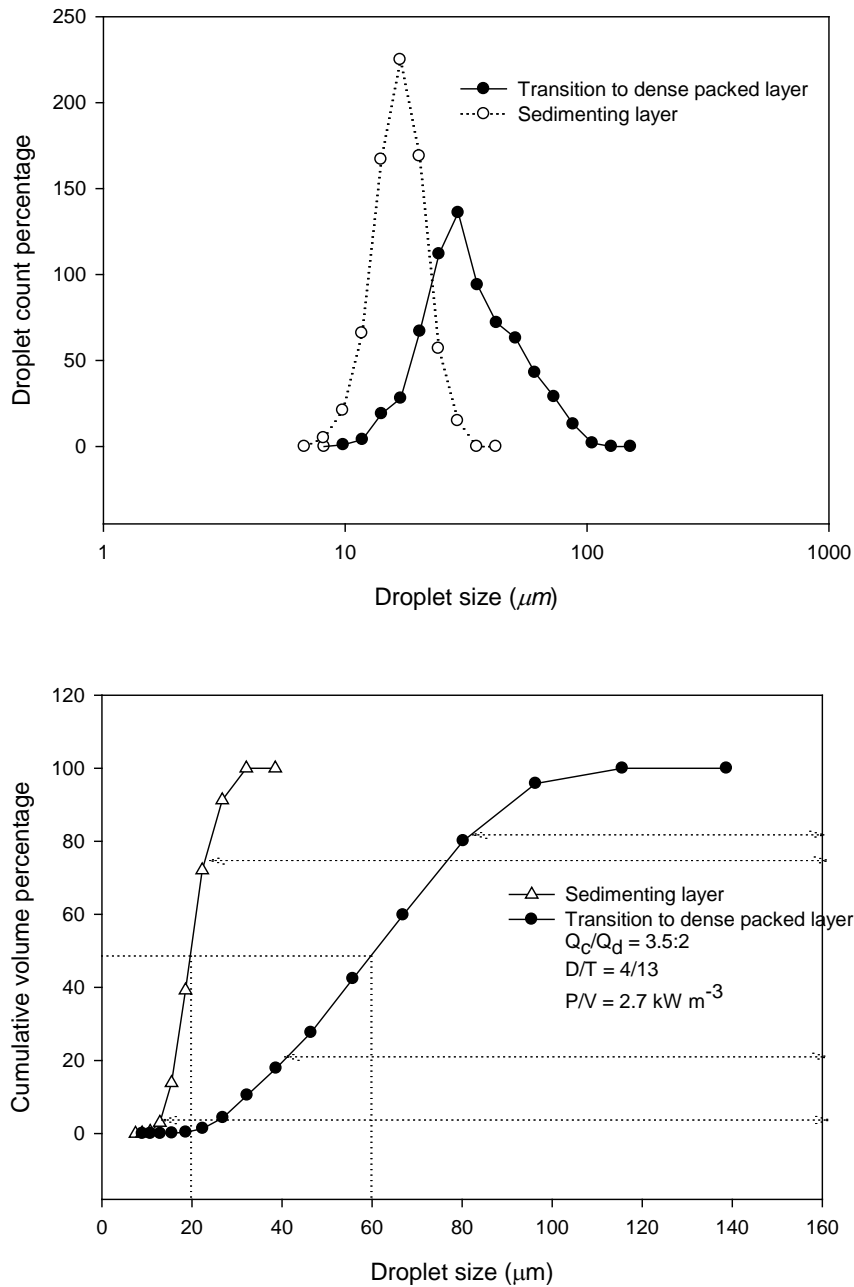


Figure 3.12. Droplet size distribution and CVD of samples taken from the sedimenting region and transition to the dense packed region for $D/T = 4/13$, $P/V = 2.7 \text{ kW m}^{-3}$ and $Q_c/Q_d = 3.5:2$.

Similar d_{50} were observed in sedimenting regions at both Q_c/Q_d because viscous resistance due to $\Delta\rho$ of $\sim 4\%$ was insufficient to dampen the turbulent fluctuations at $P/V = 2.7 \text{ kW m}^{-3}$ responsible for the droplet size, since $Re > 10^4$.

Also, the difference in counter flow due to the change in Q_c was insufficient at the given A to change the d_{50} . However, the decrease in counter flow increased the residence time which was sufficient and responsible for the slight decrease in the percentage d_{50} observed, because drag and hindered settling decreased and sedimentation was encouraged.

In the mixer, droplet-droplet coalescence due to the decrease in Q_c/Q_d would have also led to the decrease in the given d_{50} . The droplet size least susceptible to hindered settling in the sedimenting region was $\sim 30 \text{ }\mu\text{m}$; however as Q_c/A increases, this droplet size should increase in direct proportion. The settling velocity of the d_{50} in the sedimenting region was less than Q_c/A , thus droplets less than or equal to this d_{50} will be pending sedimentation or entrained.

The effects of D/T , Q_c/Q_d and P/V on C_a in the vertical plane of the settler is analysed in the subsequent sections. Similarly, A was fixed at 0.0195 m^2 and samples were obtained behind the baffle at a dispersion band depth of 0.05 m away from the settler bottom. For the analysis, C_a along the vertical plane was averaged.

3.5.3. The effects of D/T on C_a in the vertical plane

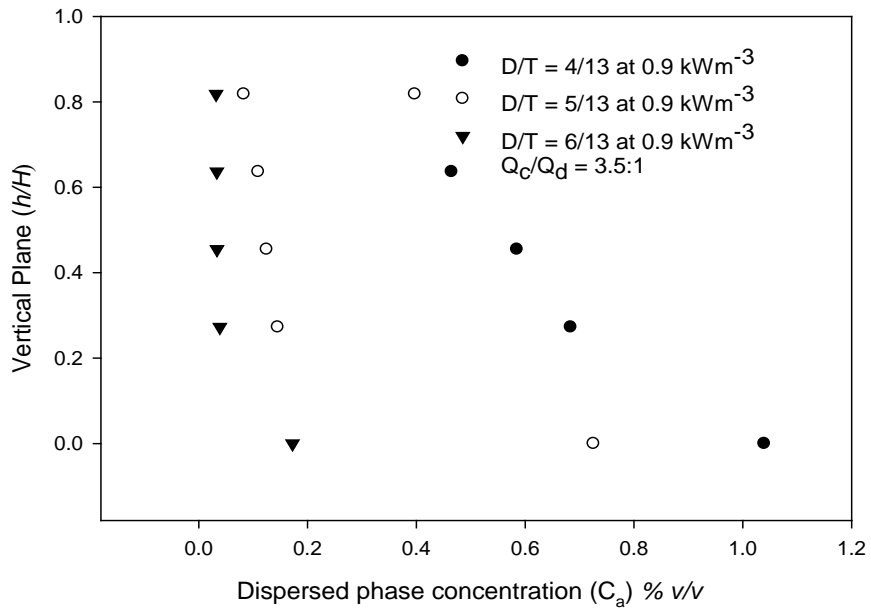
The effects of D/T on the values of C_a in the vertical plane of the settler are shown in Figure 3.13 and Figure 3.14 for all Q_c/Q_d , $P/V = 0.9 \text{ kW m}^{-3}$ and 2.7 kW m^{-3} . At $P/V = 0.3 \text{ kW m}^{-3}$, C_a was very low and considered insignificant to this analysis.

The steepest part of the distribution is the sedimenting region, whilst the gentle slope is the transition to the dense region.

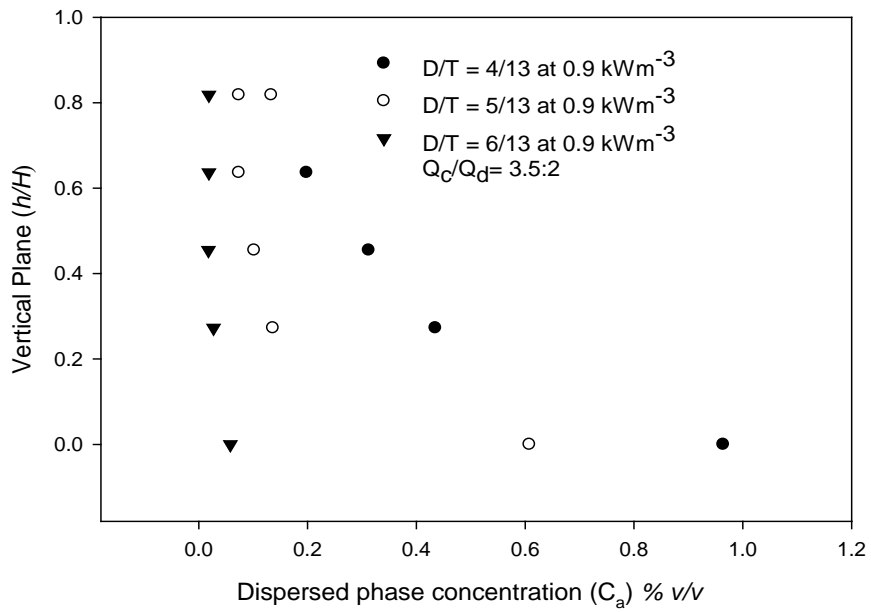
At $P/V = 0.9 \text{ kW m}^{-3}$, changing the largest and midrange D/T for the smallest D/T , decreased C_a by $\sim 60\%$ to 70% and 80% to 90% respectively, whilst at $P/V = 2.7 \text{ kW m}^{-3}$, C_a measurements were inconsistent because air ingress took place with the $D/T = 5/13$ and $6/13$ impellers.

With the $D/T = 5/13$ impeller, C_a was estimated to have reduced by $\sim 17\%$ to 25% . As the D/T was increased from the $4/13$ to $6/13$ impeller, the gradient of the sedimenting region increased and the transition point became less apparent.

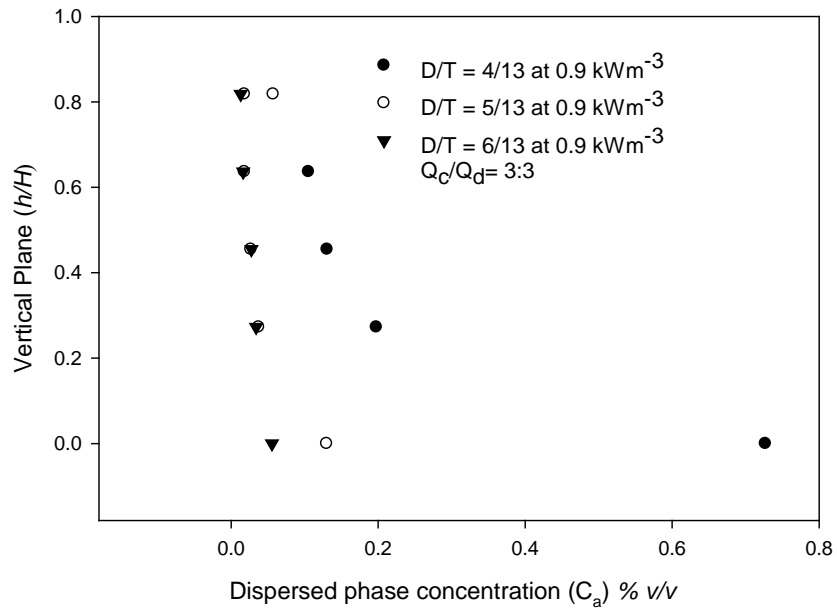
However, transition regions were present as demonstrated previously by Barnea and Mizrahi (1975a), Nadiv *et al.* (1995), Jeelani *et al.* (1985) and Eckert (1989) who have also shown similar behaviour.



(a)

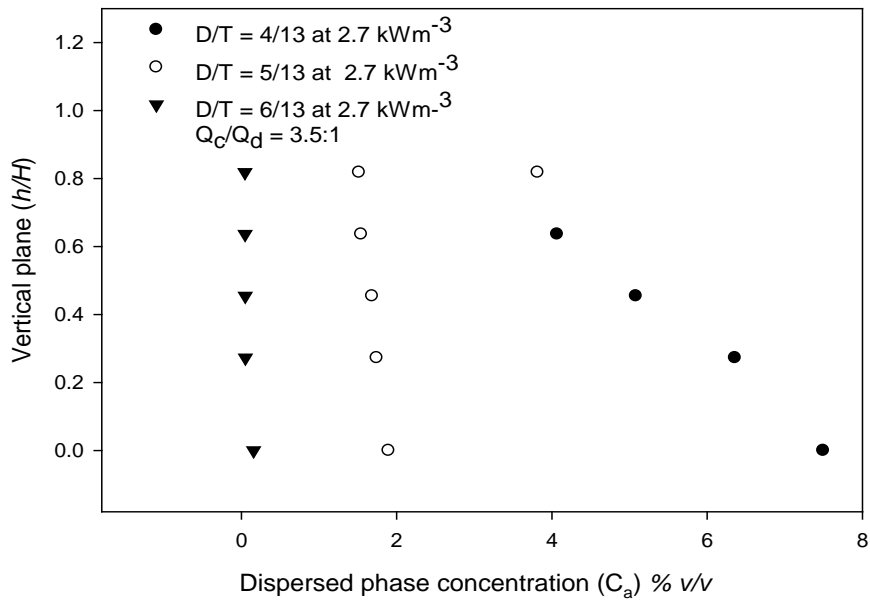


(b)



(c)

Figure 3.13. C_a as D/T changes for $P/V = 0.9 \text{ kW m}^{-3}$ and Q_c/Q_d of (a) 3.5:1 (b) 3.5:2 (c) 1:1



(a)

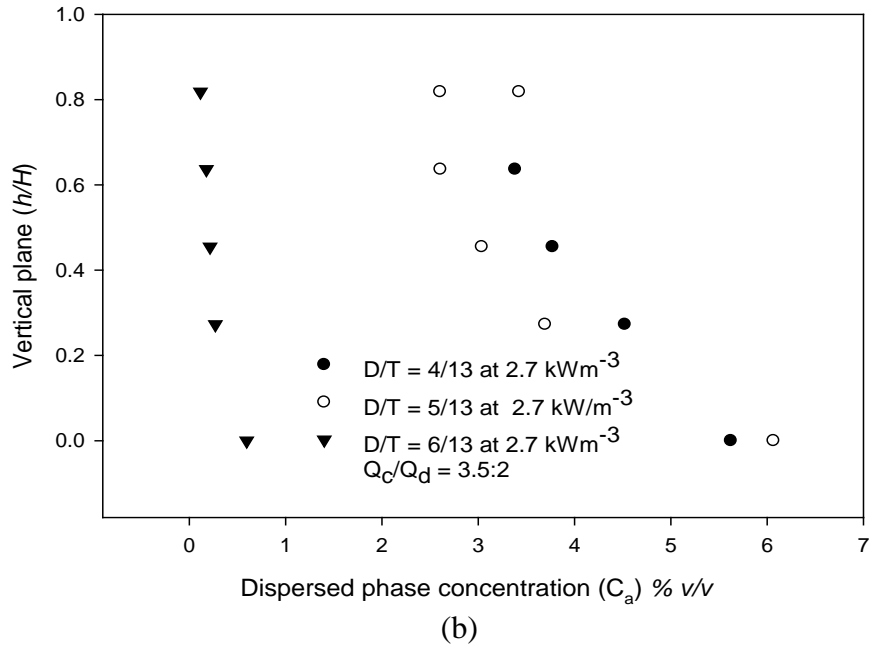
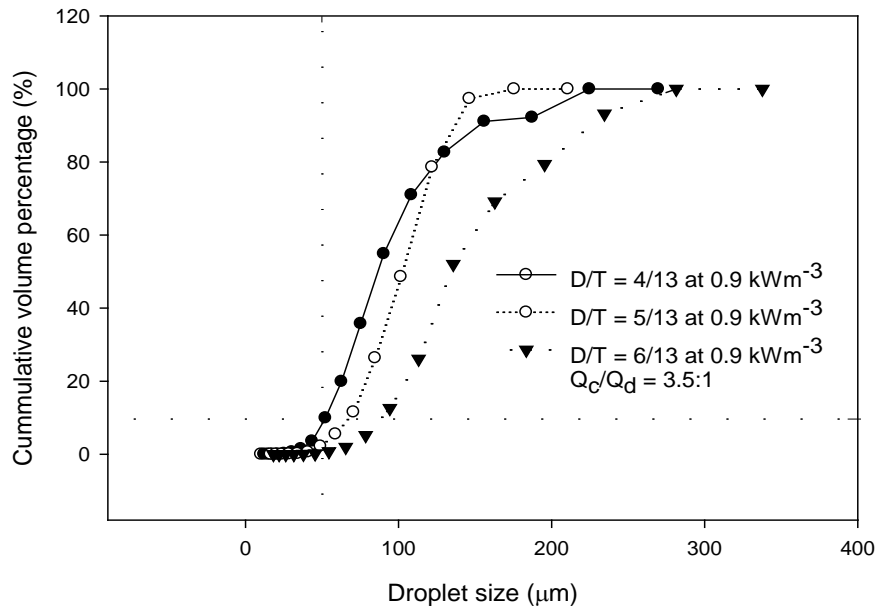


Figure 3.14. C_a as D/T changes for $P/V = 2.7 \text{ kW m}^{-3}$ and $Q_c/Q_d =$ (a) 3.5:1 (b) 3.5:2

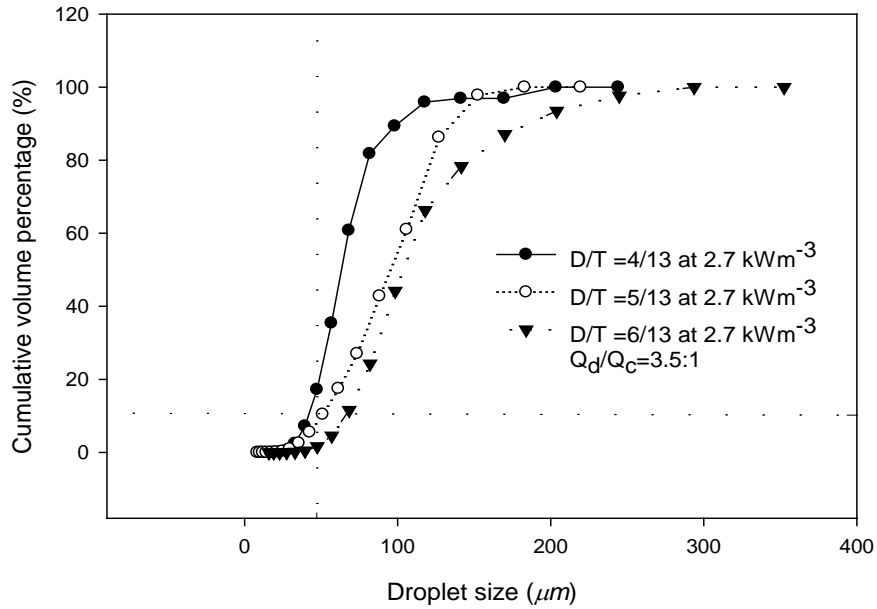
Since $\dot{\gamma}_m$ increases as D/T decreases at a fixed Q_c/Q_d and P/V , droplet size decreases and the fraction of small droplets sizes increases, as illustrated by the increase in $d_{v,0.1}$ for selected operating conditions in Figure 3.15. Given that $F_d \propto V_t^2$, where $V_t \propto d^2$, the rate of sedimentation of these small droplets decreased.

Since ψ also decreased, hydrostatic pressure gradients (due to the increase in C_a) increased the rate of permeation of thin organic films found between packed and coalescing droplets, hence increasing hindered settling.

The emergence of broader droplet size distributions was responsible for the decrease in the gradients (Nadiv *et al.*, 1995) of both the sedimenting and transition regions. Thus the separation time with the $D/T = 4/13$ impeller will be more than for $D/T = 5/13$ or $6/13$ impellers.



(a)



(b)

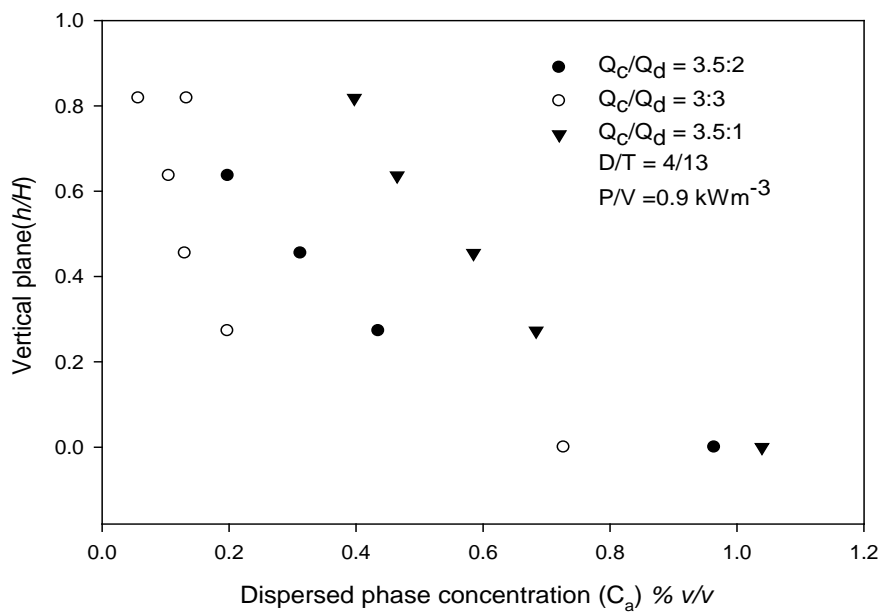
Figure 3.15. The effects of D/T on the CVD of droplets in the mixer at the

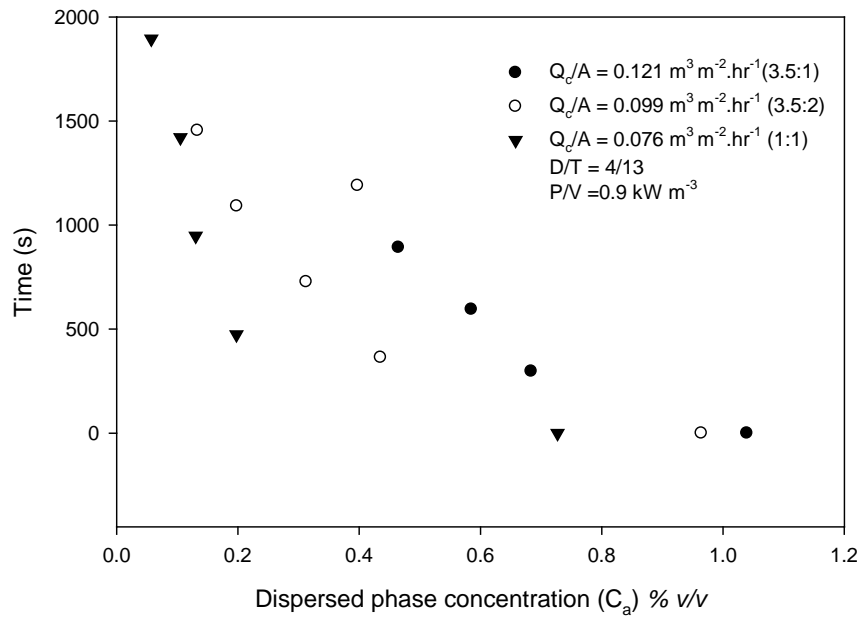
$$Q_c/Q_d = 3.5:1 \text{ and } P/V = \text{(a) } 0.9 \text{ kW m}^{-3} \text{ (b) } 2.7 \text{ kW m}^{-3}$$

3.5.4. The effects of Q_c/Q_d on C_a in the vertical plane

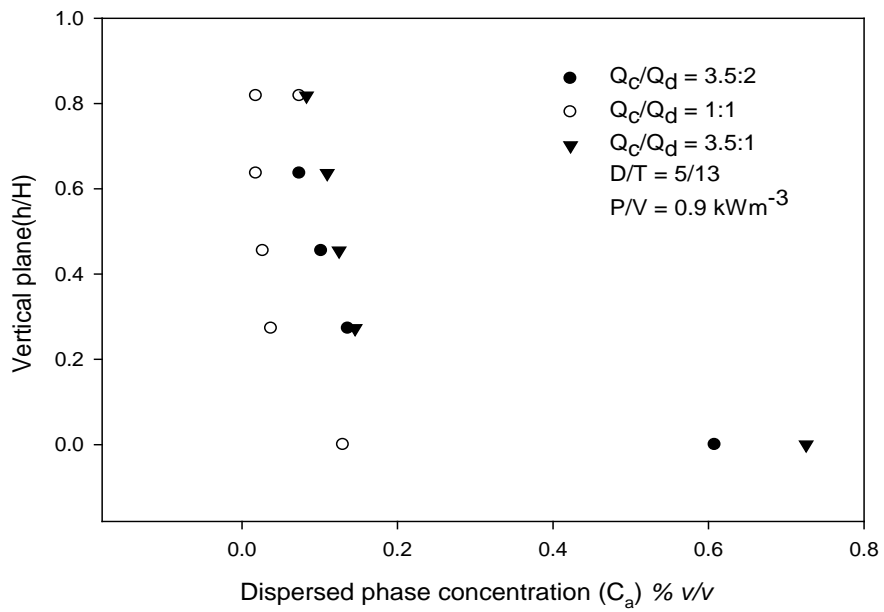
Since the Q_t is constant (i.e. $Q_c + Q_d$), a constant total residence time was observed in the mixer. However within the settler, the residence time of Q_c and Q_d varied. Thus the effects of Q_c/Q_d is also given as residence time as a function of C_a in the vertical plane of the settler in Figure 3.16 and Figure 3.17 for $P/V = 0.9 \text{ kW m}^{-3}$ and 2.7 kW m^{-3} . Wherein, as Q_c increased the residence time increased and vice versa. With the $D/T = 6/13$ impeller and $P/V = 0.9 \text{ kW m}^{-3}$, by changing $Q_c/Q_d = 3.5:1$ to $3.5:2$ and $1:1$, C_a decreased by $\sim 43 \%$ and 56% respectively, whilst with the $D/T = 5/13$ impeller, C_a decreased by $\sim 22 \%$ and 80% .

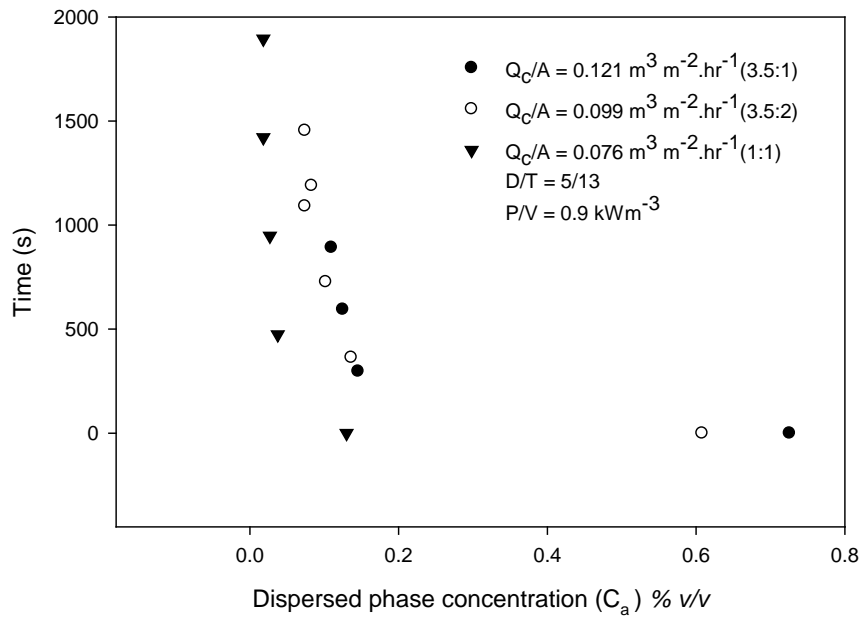
With the $D/T = 4/13$ impeller, C_a decreased by $\sim 52\%$ and 78% respectively. As Q_c/Q_d was varied, somewhat parallel distribution profiles were observed, which suggested that unique functions described the change in C_a . Barnea and Mizrahi (1975a) and Nadiv *et al.* (1995) have also shown similar behaviours. The less apparent transition regions previously noted as D/T was increased are also clearly observed. With the $D/T = 5/13$ and $6/13$ impellers, and $P/V = 2.7 \text{ kW m}^{-3}$, air ingression led to inaccurate trends, however similar distribution profiles would have been expected.



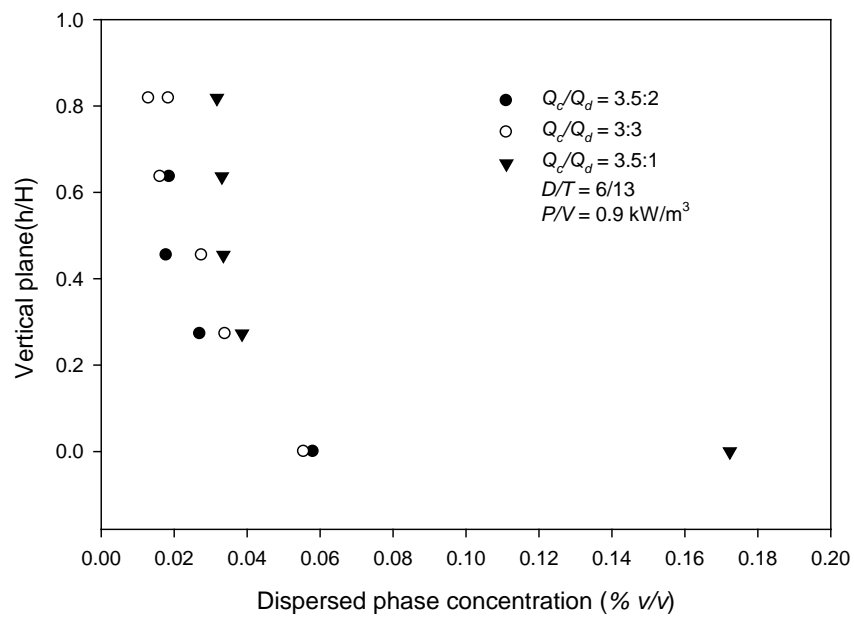


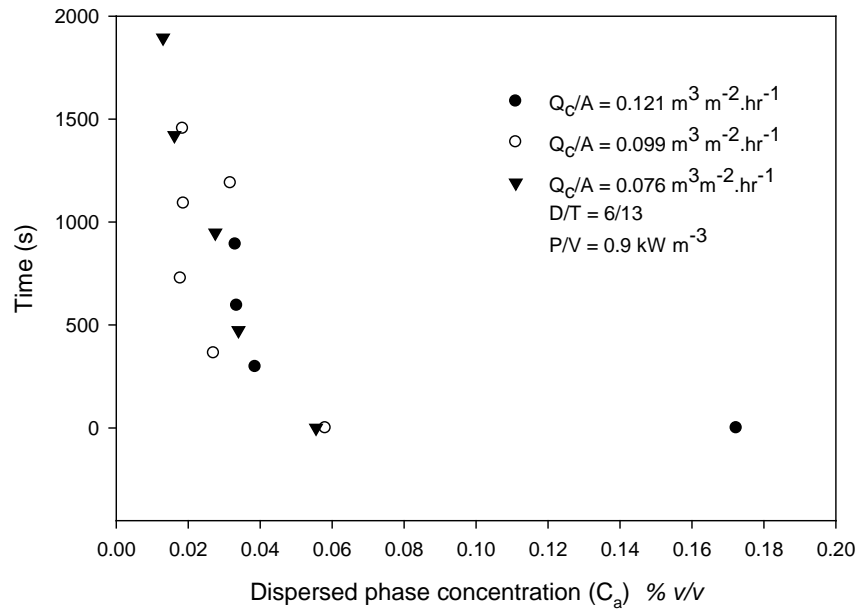
(a)





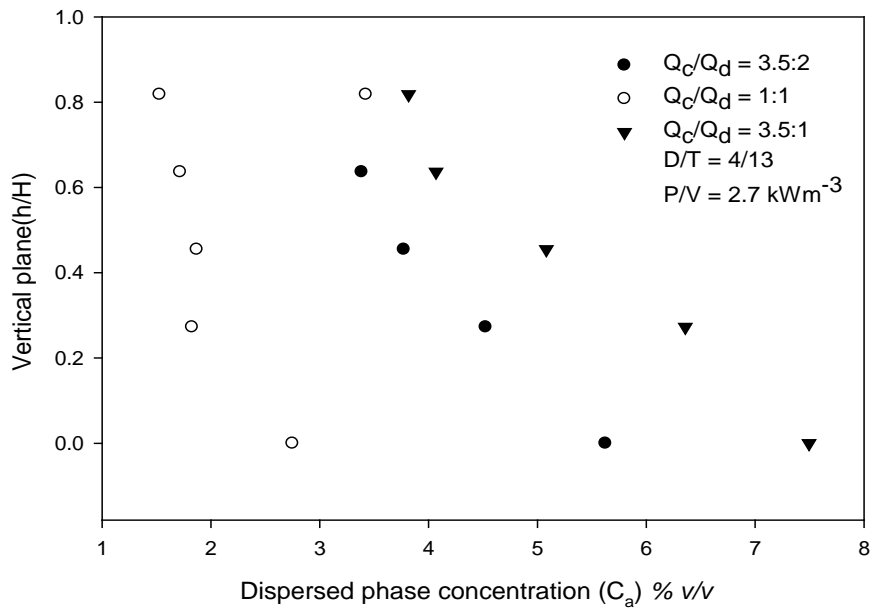
(b)

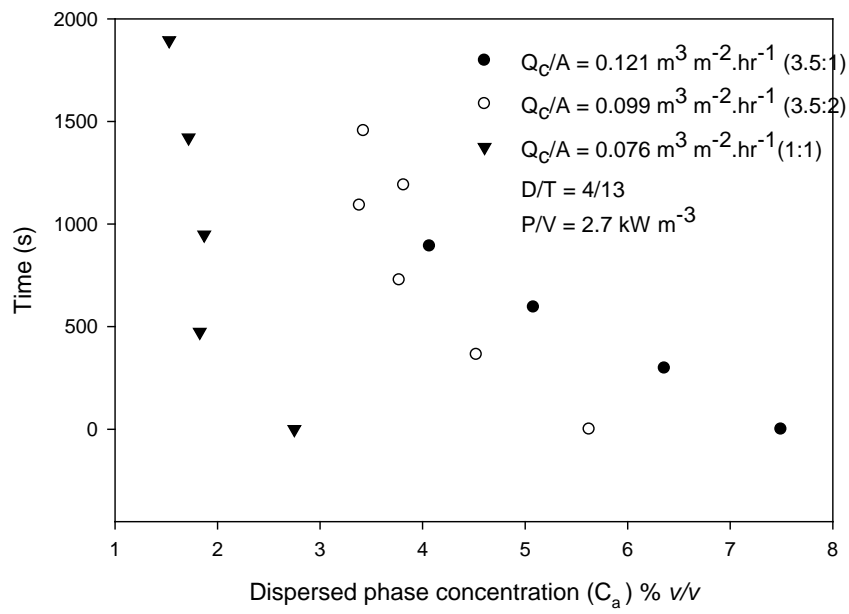




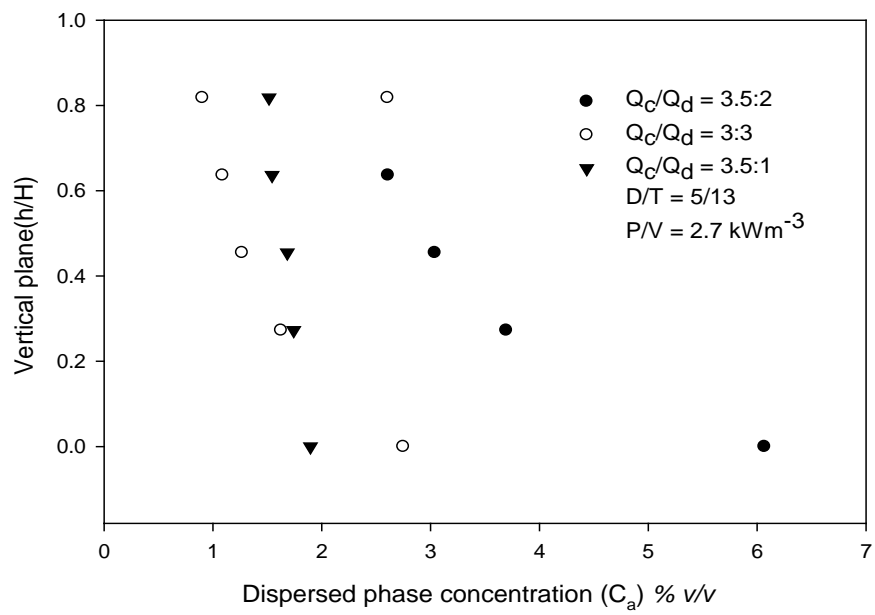
(c)

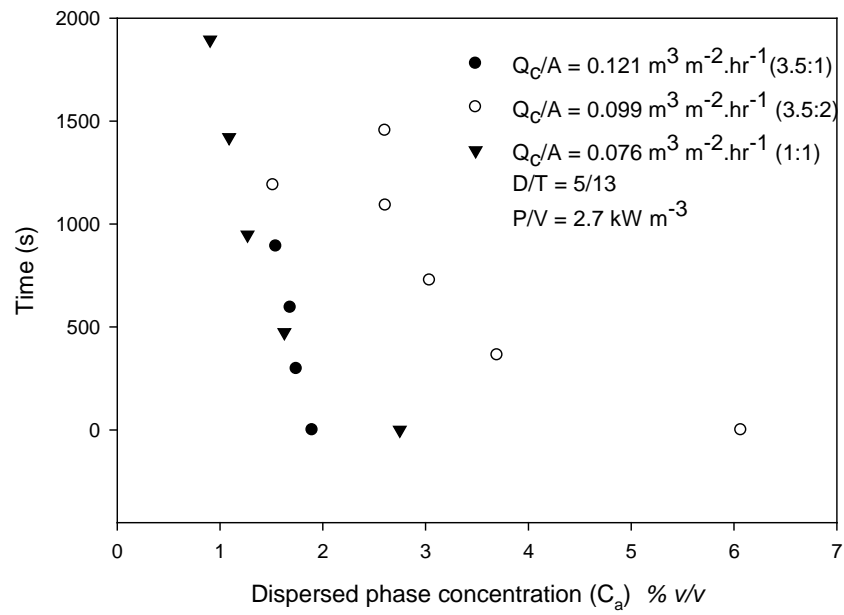
Figure 3.16. C_a as Q_c/Q_d changes for $P/V = 0.9 \text{ kW m}^{-3}$ and $D/T =$ (a) 4/13 (b) 5/13 (c) 6/13



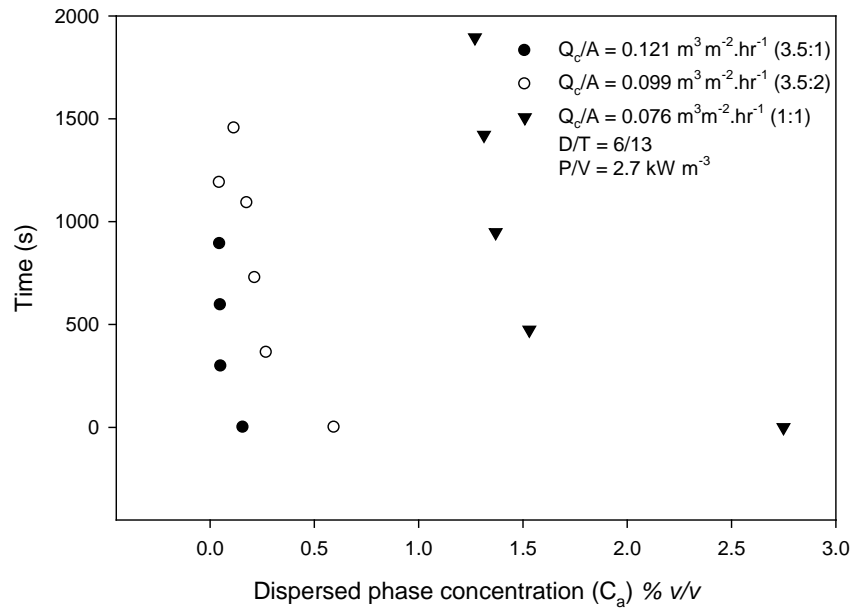
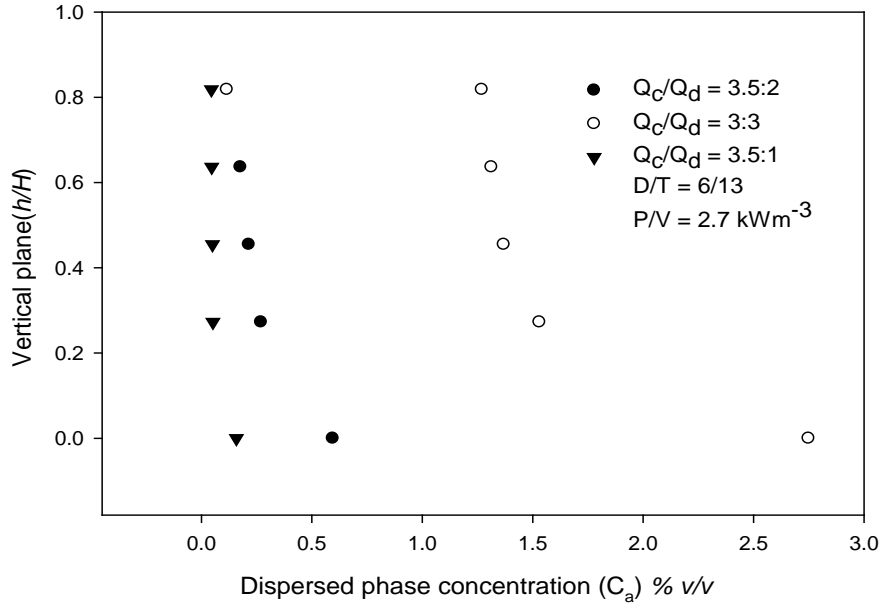


(a)





(b)

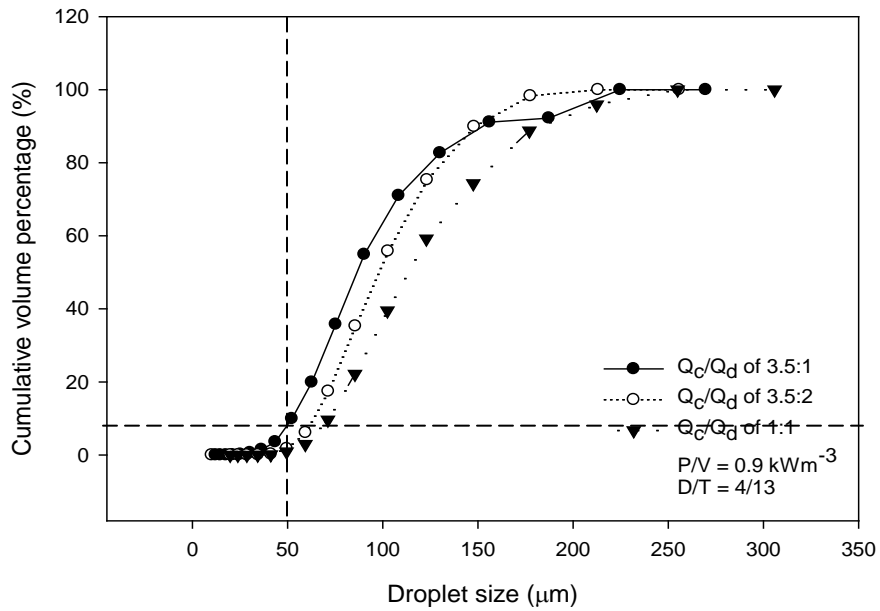


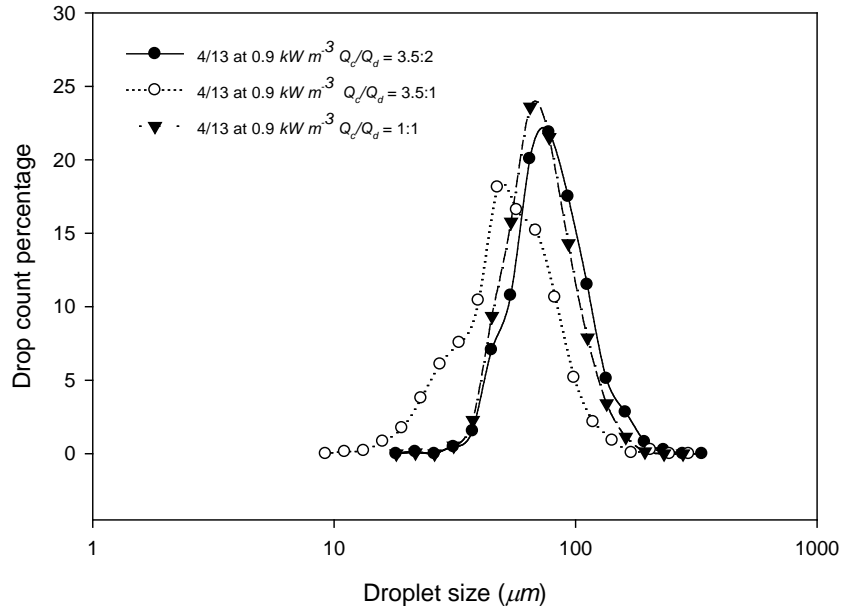
(c)

Figure 3.17. C_a as Q_c/Q_d changes for $P/V = 2.7 \text{ kW m}^{-3}$ and $D/T =$ (a) 4/13 (b) 5/13 (c) 6/13.

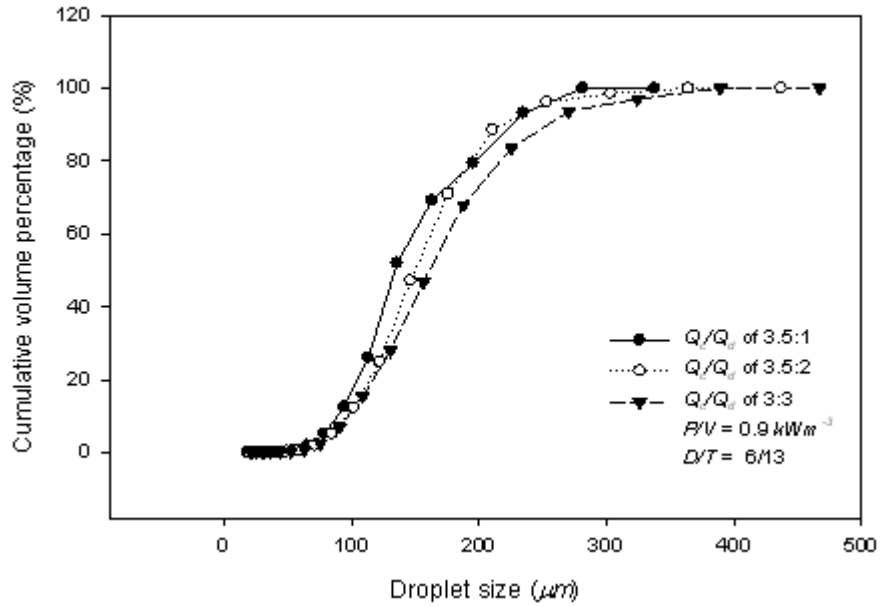
At a fixed D/T and P/V , turbulent dampening decreased as Q_c/Q_d increased, because viscous resistance decreased, encouraging droplet breakup. Thus the fraction of small droplet sizes increased as illustrated by the change in $d_{v,0.1}$ for selected operating conditions in Figure 3.18 a(i)

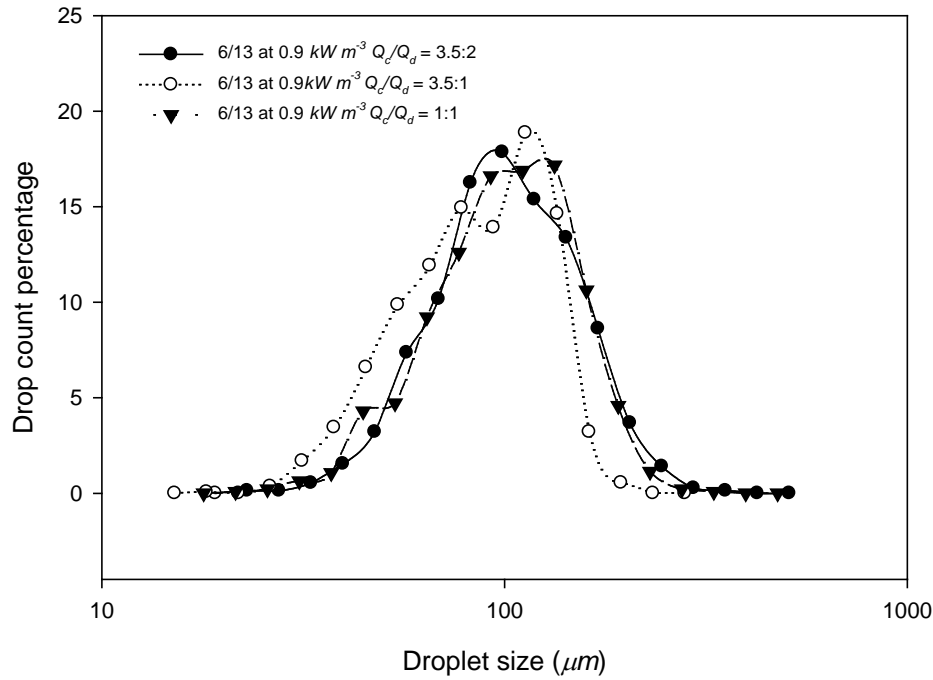
and b(i), whilst C_a and hindered settling increased, as explained previously. As Q_c increased, counter current flow increased, reducing the absolute V_t of the droplets in the interface which decreased their residence time. The parallel distribution profiles showed that similar separation mechanics governed phase disengagement (Nadiv *et al.*, 1995) which can be attributed to the similarities in droplet size distributions profiles from the mixer (Figure 3.18a and b). Barnea and Mizrahi (1975d) also attributed parallel distributions to creeping flow conditions. Thus at fixed D/T and P/V , the required A will decrease as Q_c/Q_d decreases.





(a)





(b)

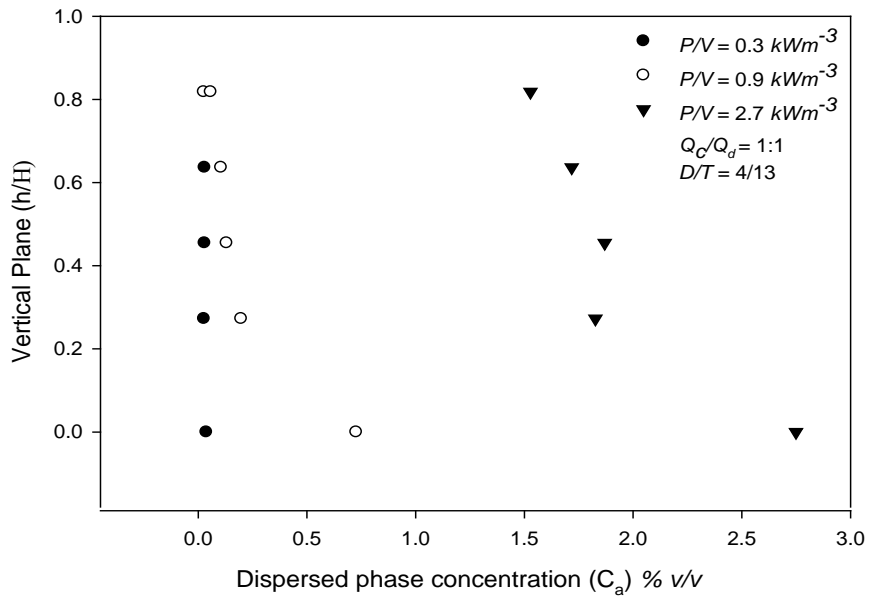
Figure 3.18. The effects of Q_c/Q_d on the cumulative volume distribution of droplets and droplet size distribution in the mixer for the $P/V = 0.9 \text{ kW m}^{-3}$ and $D/T =$ (a) 4/13 (b) 6/13

3.5.5. The effects of P/V on the C_a in the vertical plane.

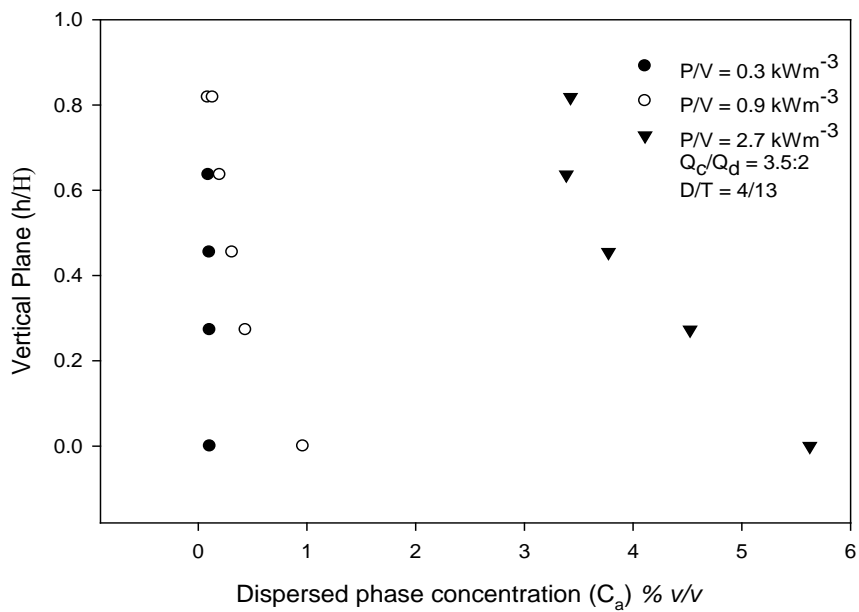
The effects of P/V on the C_a in the vertical plane is shown in Figure 3.19 (a) to (c) for all Q_c/Q_d and the $D/T = 4/13$ impeller. As P/V was increased from 0.3 to 0.9 kW m^{-3} and 2.7 kW m^{-3} , C_a increased by $\sim 94\%$ to 100% , 64% to 98% and 78% to 98% for decreasing Q_c/Q_d . Similar percentage changes were also observed with the $D/T = 5/13$ impeller, but actually the specific C_a was more with the $D/T = 4/13$.

With the $D/T = 6/13$ impeller, air ingestion in the mixer occurred at the $P/V = 2.7 \text{ kW m}^{-3}$ leading to inconsistent trends, however at $P/V = 0.9 \text{ kW m}^{-3}$, C_a increased by $\approx 50\%$ for all Q_c/Q_d . At the

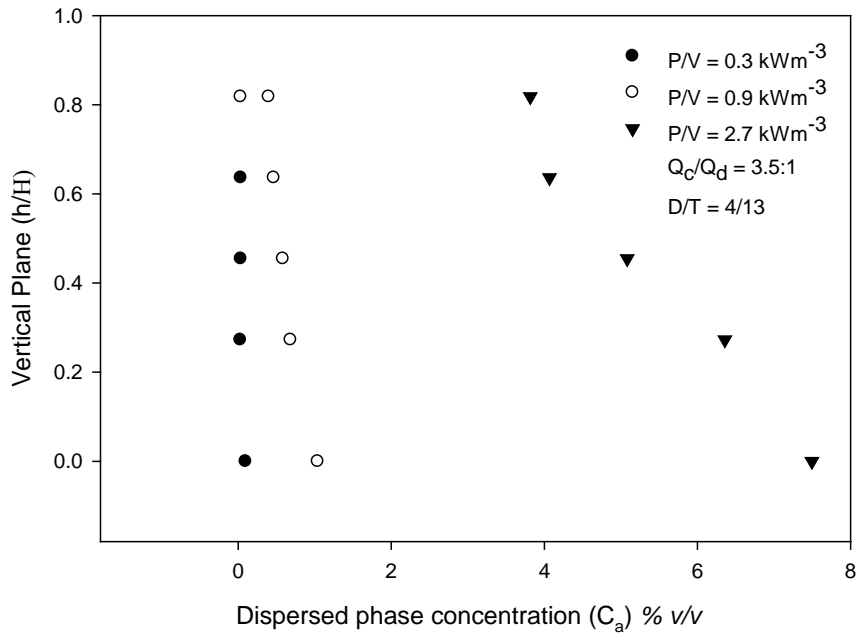
$P/V = 0.3 \text{ kW m}^{-3}$, the sedimenting region steepened and the transition to the dense region was not apparent, however when P/V increased from 0.9 kW m^{-3} to 2.7 kW m^{-3} , the transition region emerged and increased from $\sim 25 \%$ of the dispersion band to $\sim 80 \%$.



(a)



(b)



(c)

Figure 3.19. C_a as P/V changes using $D/T = 4/13$ and $Q_c/Q_d =$ (a) 1:1 (b) 3.5:2 (c) 3.5:1

Since at a fixed Q_c/Q_d and D/T , increasing P/V increases the average shear rate, $\dot{\gamma}_a$, of droplets in the mixer, where $\dot{\gamma}_a \approx N^{1.5}$, droplet size will decrease and the fraction of small droplets with low V_t and ψ will increase.

They will subsequently increase C_a in the sedimenting and dense regions, as demonstrated by the decreasing concentration gradients of both regions and as previously explained. Large droplets at the $P/V = 0.3 \text{ kW m}^{-3}$ sedimented and coalesced quickly leading to the emergence of the wedge shown previously in Figure 3.7.

At the $P/V = 0.9 \text{ kW m}^{-3}$ and 2.7 kW m^{-3} , the transition to the dense packed region emerged and increased, since ψ became the limiting factor to phase separation leading to the partly emulsified wedge and deep dense packed regions previously shown in Figure 3.8 and Figure 3.9. The contributions by D/T , Q_d , P/V and the fixed dispersion band depth of 0.05 m away from the settler bottom at a fixed A of 0.0195 m^2 were quantified with Minitab[®] in the subsequent section.

3.5.6. Factor analysis of the effects of D/T , Q_d , P/V and fixed dispersion band depth on C_a

The factors and 2 levels of each of the variables studied are given in Table 3.4. Minitab[®] was used to analyse the samples by a 2^4 factorial approach.

Table 3.4. Factors, levels and variables along the vertical plane

Factor	Levels	Variables	
D/T	2	4/13	5/13
P/V	2	0.9	2.7
Q_d	2	3.5 : 2	1 : 1
Dispersion band depth (m)	2	0	0.05

Samples were obtained at extreme ends of the dispersion band and analysed to a confidence level of 0.05. Interactions with confidence levels above 0.05 were omitted because they played no significant part to the change in C_a . The final results are given in Table 3.5.

Table 3.5. Estimated effects and coefficients for the C_a in the vertical plane

Factor	Effect	Coefficient	Standard error	T-ratio	P-value
Constant		2.271	0.08698	26.11	0.000
D/T	-0.549	-0.274	0.08698	-3.15	0.012
P/V	3.863	1.931	0.08698	22.21	0.000
Dispersion band depth	-2.358	-1.179	0.08698	-13.55	0.000
Q_d	-0.757	-0.379	0.08698	-4.35	0.002
P/V * Dispersion band depth	-1.822	-0.911	0.08698	-10.47	0.000
P/V * Q_d	-0.548	0.274	0.08698	-3.15	0.012

The results were presented as main effects plots (Figure 3.20) and interaction plots (Figure 3.21). In the former case, as expected P/V and dispersion band depth caused the largest but opposite changes to C_a i.e. increasing P/V increased C_a , whilst increasing dispersion band depth decreased C_a .

The effect of P/V was greater as depicted by its steeper gradient. Q_c/Q_d and D/T caused the least but similar changes to C_a as depicted by their gradients.

In the interaction plot shown in Figure 3.21, the interaction between P/V and dispersion band depth had the largest effect on C_a since their distributions showed the largest deviation from parallelism amongst all other interactions, followed by P/V and Q_c/Q_d .

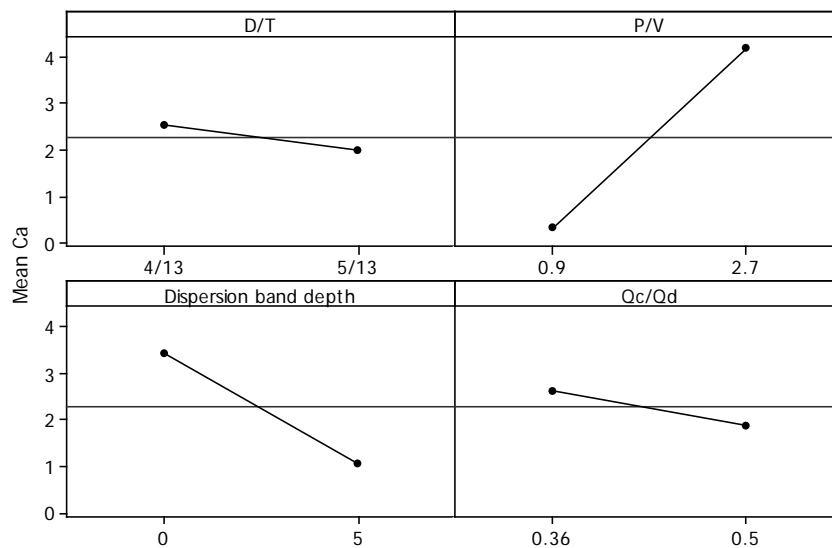


Figure 3.20. Main effects to the C_a in the vertical plane

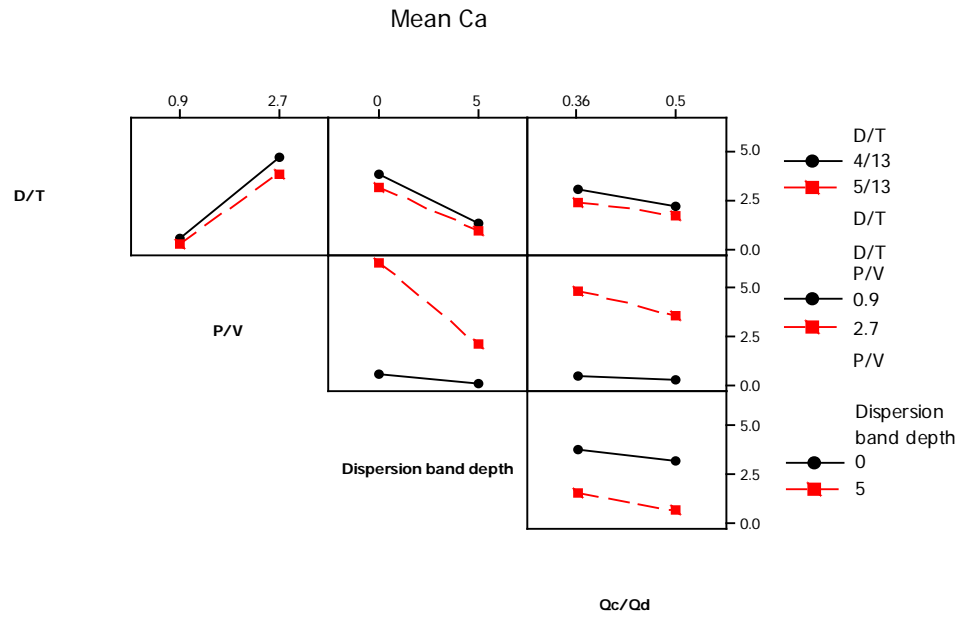


Figure 3.21. Interaction of the variables.

In the Pareto plot shown in Figure 3.22, the main effects and interactions are distributed according to their significance to C_a .

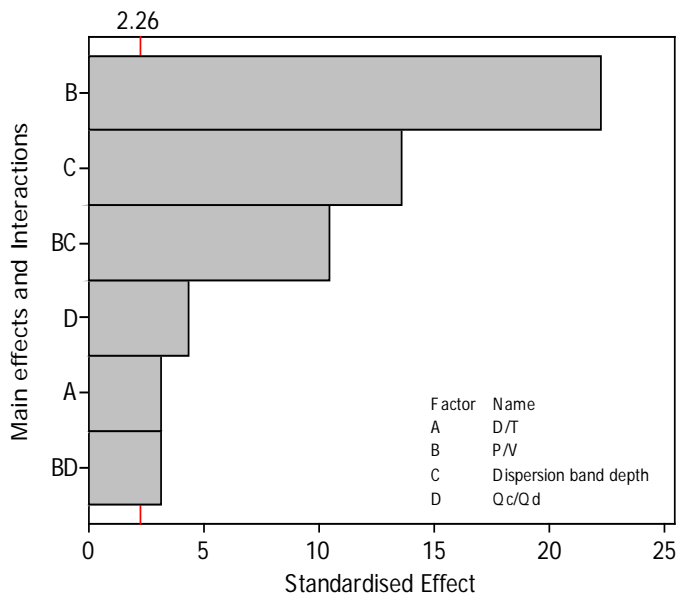


Figure 3.22. Pareto plot of the Factors and interactions.

P/V contributed $\sim 38\%$ to C_a , followed by dispersion band depth by $\sim 23\%$, then the interaction between P/V and dispersion band depth by $\sim 19\%$, finally Q_c/Q_d , D/T , and the interaction between P/V and Q_c/Q_d contributed $\sim 9\%$, 6% and 6% respectively.

Since increasing P/V will increase $\dot{\gamma}_a$, droplet size will decrease and the C_a in the vertical plane will increase, since $V_t \propto d^2$, where $F_d \propto V_t^2$. Thus to compensate for the increase in C_a , the depth of the settler should be increased to boost retention time. By decreasing Q_c/Q_d or increasing D/T , residence time and droplet size will increase, as well as their rate of sedimentation and ψ . This will decrease C_a and the required settler depth.

However, taking this measure could be at the expense of extraction efficiency in the mixer if the extraction rate is mass transfer limited. Minitab[®] generated the model in Equation (3.8) which includes the factors and interactions, to estimate C_a along the vertical plane. H_d is the settler depth.

$$\Delta C_a = 2.27 - 0.27(D/T) + 1.93(P/V) - 1.18(H_d) - 0.38(Q_d) - 1.82(P/V \times H_d) - 0.55(P/V \times Q_d) \quad (3.8)$$

The effects of Q_d/A on C_a is discussed in the next section.

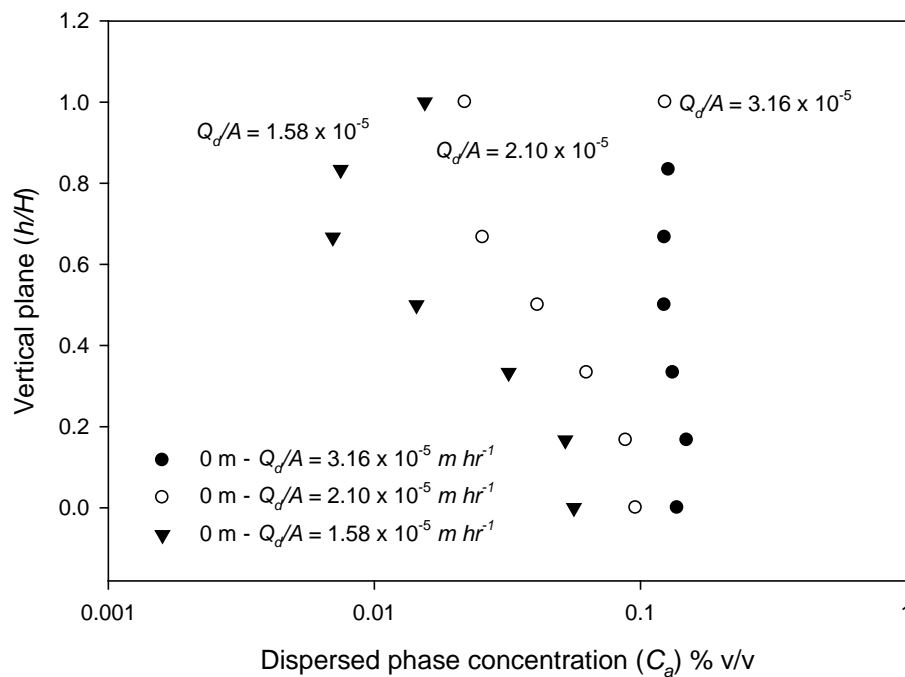
3.5.7. The effects of Q_d/A on C_a .

Ryon *et al.* (1959) and Barnea and Mizrahi (1975d) showed that a power law relationship between H_d and Q_d/A (Equation 3.3) should be used as the criteria for settler scale-up. In this study, it was difficult to determine H_d because the organic was opaque. Thus the change in C_a with Q_d/A at a dispersion band depth of 0.06 m away from the vessel bottom was investigated. A was varied from

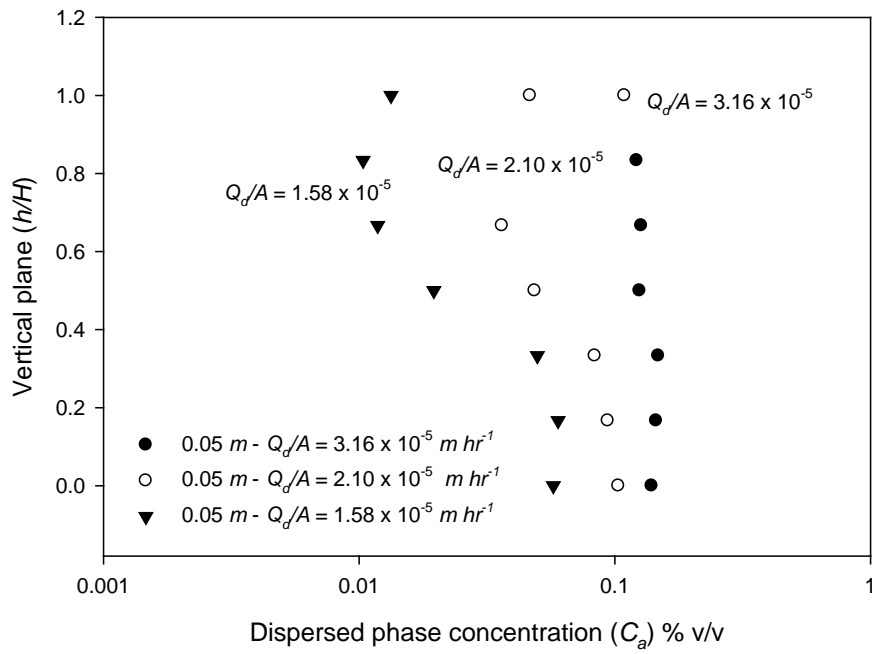
0.026 m², 0.0195 m² and 0.013 m², which equates to evenly spaced L_s of 0.2 m, 0.15 m and 0.1 m and $Q_d/A = 1.58 \times 10^{-5} \text{ m hr}^{-1}$, $2.1 \times 10^{-5} \text{ m hr}^{-1}$ and $3.16 \times 10^{-5} \text{ m hr}^{-1}$ respectively for $Q_c/Q_d=1:1$.

In Figure 3.23, the effects of Q_d/A on C_a in the vertical plane of the settler for $D/T = 4/13$, $P/V = 0.9 \text{ kW m}^{-3}$ and $Q_c/Q_d=1:1$ at $L_s = 0 \text{ m}$, 0.05 m and 0.1 m are shown. L_s was varied because insignificant changes to C_a at a fixed A were observed since the d_{50} of droplets towards the dense packed layer were considerably small and pending sedimentation (the reader is referred to §3.5.2).

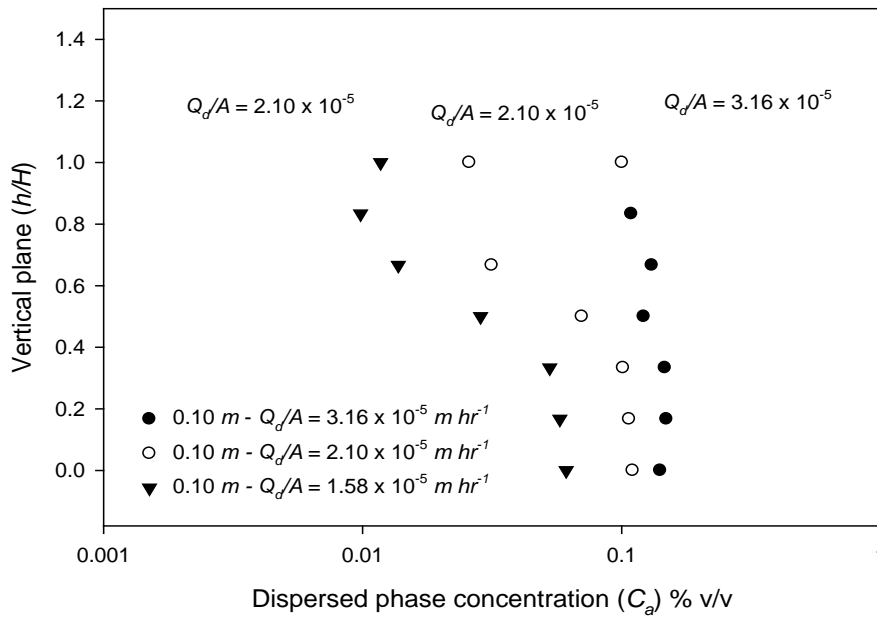
As Q_d/A was increased from $1.58 \times 10^{-5} \text{ m hr}^{-1}$ to $2.1 \times 10^{-5} \text{ m hr}^{-1}$ and $3.16 \times 10^{-5} \text{ m hr}^{-1}$, C_a increased by ~ 42 % and 72 % respectively. The concentration profiles deviated from a non-linear to linear distribution, wherein the transition to the dense packed region became less apparent as expected.



(a)



(b)



(c)

Figure 3.23. The effects of Q_d/A on the C_a along the horizontal plane at $L_s =$ (a) 0 m (b) 0.05 m (c)

0.1 m, for $P/V = 0.9 \text{ kW m}^{-3}$ and $Q_d/Q_d = 1:1$

Power law relationships were obtained by plotting the values of C_a at the Q_c overflow as a function of Q_d/A (Figure 3.24) in a manner analogous to power law relationships previously reported by Ryon *et al.* (1959) and Barnea and Mizrahi (1975d).

As also expected, at the fixed D/T and P/V , as Q_c/Q_d was decreased, C_a decreased and the individual power law exponents increased from 2.5 to 3.3.

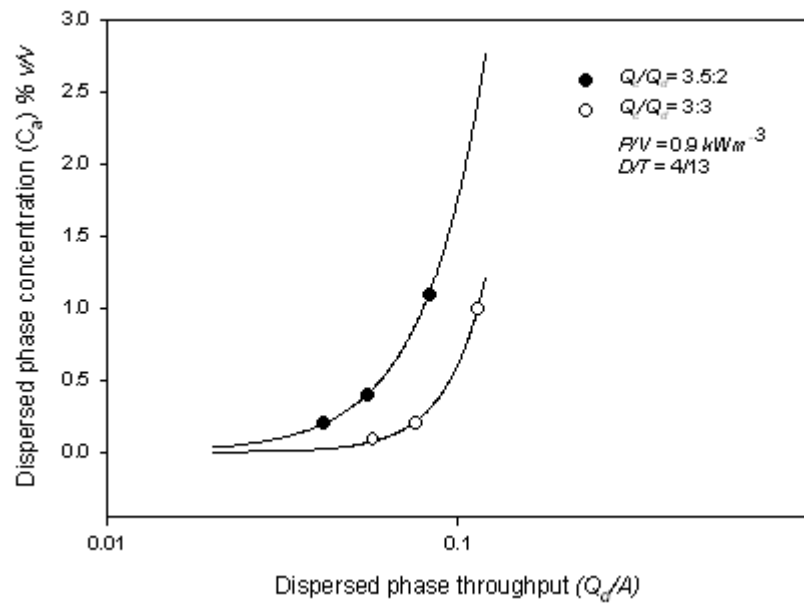
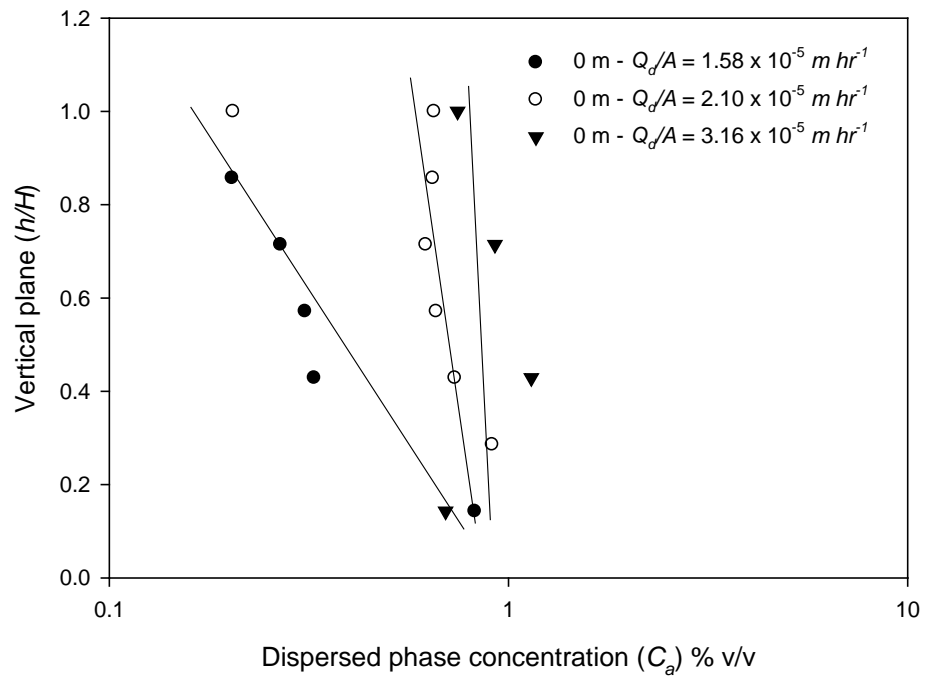


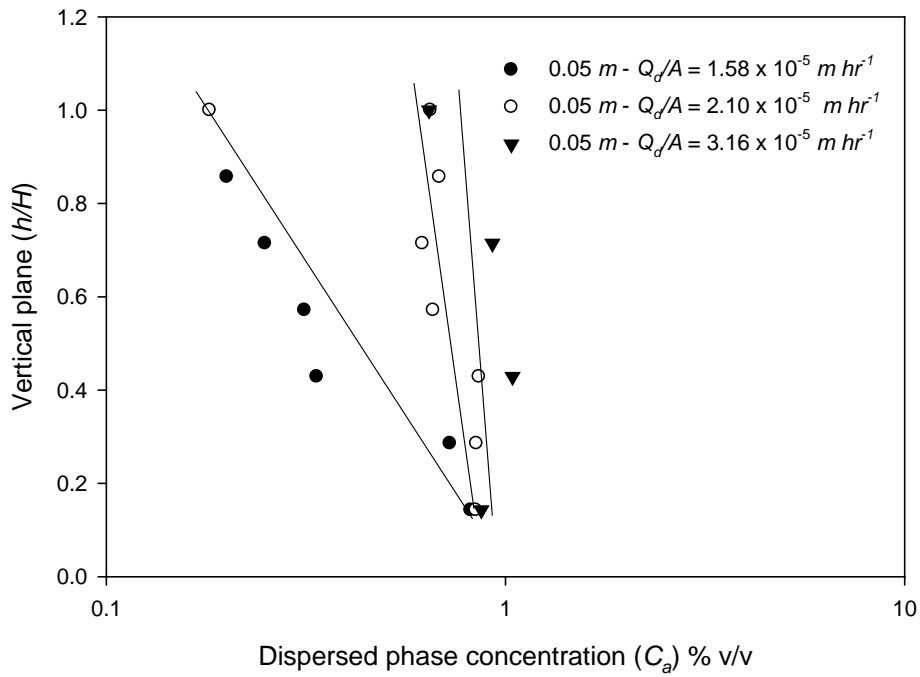
Figure 3.24. C_a as a function of Q_d/A for the $D/T = 4/13$ and $Q_c/Q_d = 3.5:2$ and $1:1$ agitated with a $P/V = 0.9 \text{ k W m}^{-3}$

At $P/V = 2.7 \text{ kW m}^{-3}$ (Figure 3.25) and similar Q_c/Q_d and L_s , increasing Q_d/A from $1.58 \times 10^{-5} \text{ m hr}^{-1}$ to $2.1 \times 10^{-5} \text{ m hr}^{-1}$ and $3.16 \times 10^{-5} \text{ m hr}^{-1}$, increased C_a by $\sim 47 \%$ and 56% respectively. All the

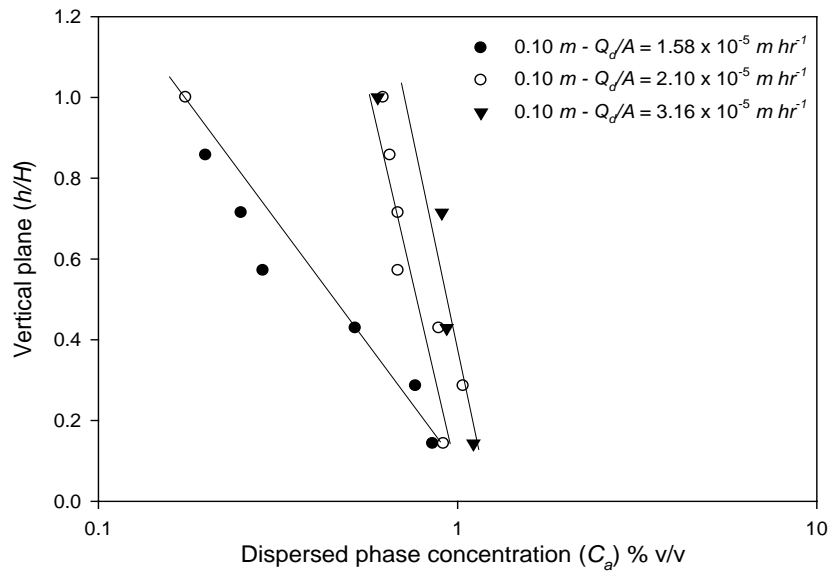
concentration profiles were described by linear functions which increased in gradient with Q_d/A . The transition was also not evident, although a case could be argued for $1.58 \times 10^{-5} \text{ m hr}^{-1}$.



(a)



(b)



(c)

Figure 3.25. The effects of Q_d/A on the dispersed phase C_a along the horizontal plane at (a) 0 m (b)

0.05 m (c) 0.1 m, for $P/V = 2.7 \text{ kW m}^{-3}$ and $Q_c/Q_d = 1:1$

A linear function was also expected by plotting C_a at the Q_c overflow as a function of Q_d/A .

A line of best fit is given in Figure 3.26

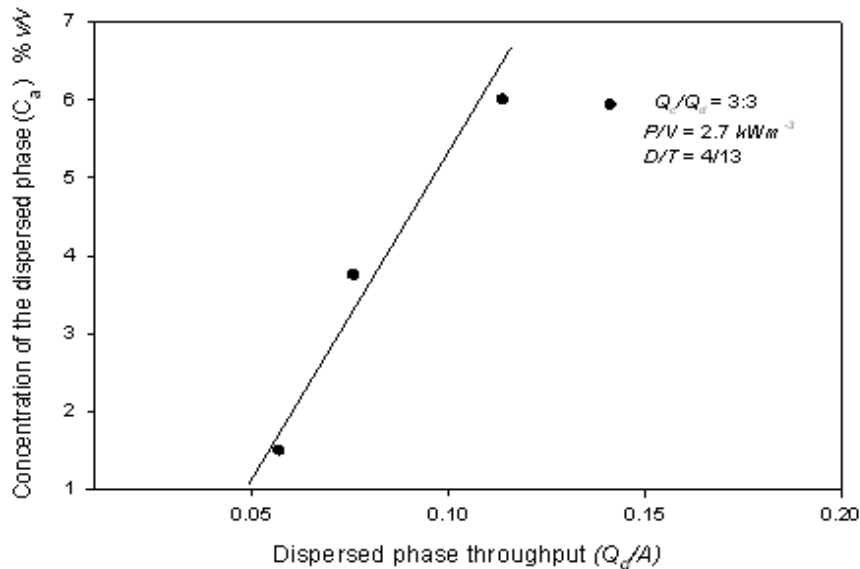


Figure 3.26. C_a as a function of Q_d/A for the $D/T = 4/13$ and Q_c/Q_d and 1:1

C_a increased with Q_d/A because by decreasing A , the dispersed phase confinement increased and counter flow by Q_c/A increased F_d on the droplet's surface. They both increased the permeation of the continuous phase through the droplet swarm, which decreased the absolute V_t of the droplets and increased hindered settling.

The power law relationship observed between C_a and Q_d/A at the $P/V = 0.9 \text{ kW m}^{-3}$ demonstrated that the settler will be unflooded at the given operating conditions, although any further decrease in A will increase the tendency for flooding. By decreasing A , Q_d/A increased in direct linear proportion and C_a contributed 0.4 and 0.3 powers.

Thus the contribution by C_a will be less than the contribution by either Q_d or A . For each Q_c/Q_d , the functional relationship obtained indicates that settler capacity is a not function of the mean residence

time. The change in constants obtained can be attributed to changes in C_a due to the effects of viscous resistance to droplet shear in the mixer as Q_c/Q_d decreased.

The linear relationship between C_a and Q_d/A at the $P/V = 2.7 \text{ kW m}^{-3}$ showed that the settler will be flooded due to dispersion carryover. $Q_d \propto A$ whilst C_a played no significant part. Thus the flooding point essential for the introduction of coalescence enhancers such as picket fences is reached at a much larger A at the $P/V = 2.7 \text{ kW m}^{-3}$ compared to $P/V = 0.9 \text{ kW m}^{-3}$.

3.6. Conclusions

The effects of P/V , Q_c/Q_d , D/T , dispersion band depth and Q_d/A on the separation of a Copper/HCl solution from organic-LIX84-A have been investigated in a settler. It was observed that the effects of $P/V > D/T > Q_c/Q_d$ during the evolution of a deep dense packed dispersion band from a wedge dispersion band.

Within the set of operating conditions studied, P/V demonstrated a much larger contribution to the C_a than the dispersion band depth which was $> D/T > Q_c/Q_d$ along the vertical plane of the dispersion band. A critical droplet size which had least susceptibility to hindered settling in the sedimenting region was twice the diameter of a primary droplet size that was considerably susceptible to hindered settling at the same location.

The relationship between Q_d/A and C_a was shown to depend on P/V , wherein power law relationships described the function at $P/V = 0.9 \text{ kW m}^{-3}$ whilst linear relationships described the function at $P/V = 2.7 \text{ kW m}^{-3}$. At $P/V = 0.9 \text{ kW m}^{-3}$ the settler's capacity was dominated by the

effects of Q_d/A and C_a over residence time whilst at $P/V = 2.7 \text{ kW m}^{-3}$ the settler was flooded due of dispersion carryover and $Q_d \propto A$.

Chapter 4. Hydrodynamics of gas evolving solid – liquid reactions

4.1. Introduction

During the leach process, base metal-platinum group metal alloys (*BM-PGM*) are contacted with lixivants which remove the *BM* and leave behind a *PGM* sponge. During this reaction, the system transitions from a solid-liquid (*S-L*) system to a three phase gas-liquid-solid system (*GLS*) because gas is generated as an unwanted by-product. The gas can hinder solids suspension and the diffusion of the lixiviant, thus reducing leach efficiency.

In the design of reactors for such systems, model gas-sparged *GLS* systems will either complicate or simplify the hydrodynamic phenomena observed, since the solids that have been used to obtain scale-up models have usually been smooth and spherical objects, whereas in actual fact the solids can be spongy and can collect gas bubbles in their pores when a reaction takes place with the liquid phase, making the particles buoyant due to the gas entrapment. There is also no literature that explains solids behaviour in gas evolving *S-L* systems.

The work presented in this Chapter is aimed at improving fundamental understanding of gas-evolving *S-L* systems by studying the hydrodynamics of a mimic system comprised of sponge nickel[®] (*Ni*) and sodium hypochlorite. A *BM-PGM* and lixiviant system was not studied due to the prohibitive cost of the *BM-PGM* alloys.

This Chapter contains a literature review on the chemical reaction between *Ni* and sodium hypochlorite, to understand the simplicity of the chemistry and the reason why such a system was

selected as a suitable mimic. Then a literature review on *S-L*, Gas-liquid (*G-L*), and *GLS* agitation is presented to understand the problems encountered during the mixing of such systems as well as the engineering fundamentals behind such systems.

Following the literature reviews, the results are presented. In this section, the effects of varying *Ni* and sodium hypochlorite concentrations on gas evolution rate are studied to demonstrate the relationship between *Ni* and sodium hypochlorite reaction. Then gas holdup (ϕ_g) and disengagement in gas evolving reactions are both investigated to understand particle behaviour during gas emitting reactions.

4.2. Literature Review

4.2.1. Nickel-Hypochlorite chemical reaction

Ni is a catalyst that decomposes hypochlorite ions on its surface, liberating oxygen in the process.

According to Hancock *et al.* (1996), the governing reactions are denoted below:

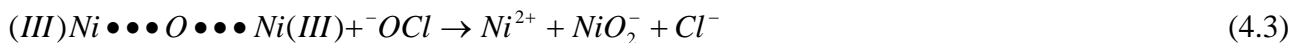
Activation (1):



Ni (III) dimer formation (2):



Peroxy formation (3):



The kinetics of the catalytic decomposition of hypochlorite ions by *Ni* was previously studied by Lister *et al.* (1956). Their work focused on the effective abatement and destruction of effluents containing sodium hypochlorite within the chlorine and other related industries. Hancock *et al.* (1996) showed that the governing mechanism was a complex reaction process involving high oxidation states of *Ni* (Equation 4.1 to 4.3).

Lister *et al.* (1956) showed that during the reaction process, higher metal oxides are generated which lose oxygen (Equation 4.4) before being re-oxidised. They both showed that the rate of reaction was first order with little dependence on the hypochlorite concentration. It was alleged that since the rate was slightly dependent on hypochlorite, Equation 4.4 must be the slow reaction step and the rate-determining step, requiring much the same amount of hypochlorite ion ($^{\ominus}OCl$) adsorbed on the catalyst surface over a range of concentrations.

If the catalyst surface is not completely covered, it is impossible to predict what the reaction kinetics would be. Lister *et al.* (1956) showed that *Ni* behaved as though the catalyst was essentially covered with adsorbed ions.

4.2.2. Gas-Liquid-Solid (GLS) systems

To understand the complications encountered in *GLS* systems, it is best to review the principles behind *S-L* and *G-L* mixing since they are the backbone to understanding *GLS* mixing.

Solid-Liquid (S-L) systems

In *S-L* processes, the solids have to be homogeneously dispersed to optimise *S-L* reactions. To obtain a well distributed system, the mechanical energy from the stirrers is converted to kinetic energy in the liquid to the particles. Generally, factors that influence solid dispersion are the impeller type,

impeller diameter, D , to tank diameter, T , ratio, (D/T) , impeller clearance, C , to T ratio (C/T) , and the physical properties of the system, such as the density (ρ) and viscosity (μ) and the solids concentration. By increasing the impeller speed, N , particles are lifted from the vessel bottom and suspended in the liquid. Zwietering (1958) defined a condition where no particle spends less than one second on the vessel bottom. It is called the just suspended speed; N_{js} . N_{js} can be estimated from the Zwietering correlation denoted as:

$$N_{js} = \frac{S\mu^{0.1}(g_r \Delta\rho/\rho_L)^{0.45} d_p^{0.2} X_N^{0.33}}{D^{0.85}}, \quad (4.5)$$

where S depends on D/T and impeller type, d_p is the particle diameter, g is the gravitational constant and X_N is the solids to liquids mass percentage.

At N_{js} , axial and radial concentration gradients are still observed, thus an ideal operating speed, N , which is 10 % above N_{js} will improve homogeneity. Nienow (1975) proposed that S can be estimated for disc turbines using:

$$S = 2\left(\frac{T}{D}\right)^{1.33}, \quad (4.6)$$

whilst Dutta and Pangarkar (1995) revised the correlation by Zwietering (1958) for multiple turbine systems:

$$N_{js} = \frac{3.5\mu^{0.1}(g \Delta\rho/\rho_L)^{0.42} d_p^{0.18} X^{0.15} T^{0.58}}{D^{1.5}} \quad (4.7)$$

Gas-liquid (G-L) systems

$G-L$ systems and reactions are usually encountered in exothermic heterogeneous systems with multiple series and parallel reaction pathways with selectivity issues. The standard impeller geometry for agitated $G-L$ systems is given as a C/T and D/T of 1/2 to 1/4. During agitation, the

impellers break up the gas into small bubbles, increasing the interfacial area, whilst at the same time dispersing the gas bubbles throughout the liquid and increasing φ_g .

Gas holdup and flow Patterns

Gas holdup, φ_g , is the fraction of gas retained in a $G-L$ system. The range of φ_g encountered in the industry is usually between 10% to 20% and 50% in extreme situations. There are several ways of measuring φ_g . The change in height of a $G-L$ mixture upon gas injection is one technique.

This method lacks accuracy for very low values of φ_g and when waves and foams form on the surface of the blend. An alternative to the technique is the manometric or dynamic disengagement method. By using differential pressure cells, the pressure difference between two points in a reactor is measured. Chapman *et al.* (1983) proposed the equation below to estimate φ_g by this method:

$$\varphi_g = \left(\frac{H^g - H}{H^g} \right) = 1.97(\bar{\varepsilon}_T)^{0.31} U_g^{0.67}, \quad (4.8)$$

where H^g and H are the height of the mixture after and before gas introduction, $\bar{\varepsilon}_T$ is the specific power input and U_g is the superficial rise velocity.

Figueiredo and Calderbank (1979) also proposed the equation given below:

$$\varphi_g = 0.34 \left(\frac{P_g}{V} \right)^{0.25} U_g^{0.75}, \quad (4.9)$$

where P_g is the gassed power and V is the volume of the liquid. Other techniques are the electrical resistivity probe technique and X-ray tomography. However their use has been limited.

A range of flow patterns develop as N increases at constant U_g , or as U_g decreases at constant N . These are shown in Figure 4.1. The first point is called the flooding point, where the gas passes through the impeller and the liquid flows over the outer blades of the impeller. As N increases, the loading point (N_F) is reached. On this occasion the gas is captured by the impeller blades. A further increase in N leads to the completely dispersed point (N_{CD}), where gas is dispersed throughout the liquid. Finally the completely recirculated state is reached (N_R).

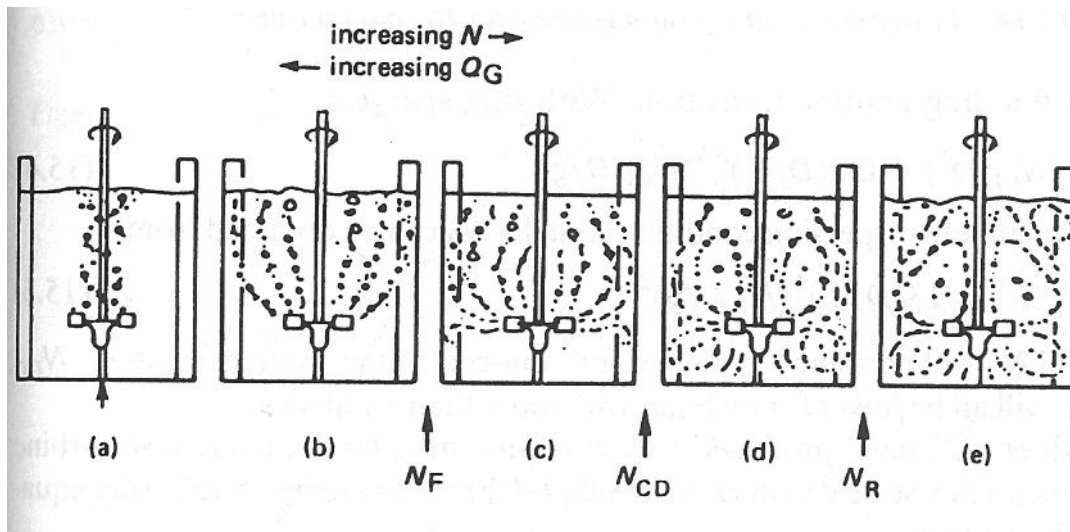


Figure 4.1. $G-L$ flow patterns. (Harnby *et al.*, 1992)

N_{CD} is expressed in terms of the aeration number (Fl_g), which is the ratio of the aeration rate (Q_g) to the impeller tip speed (U_{tip}), expressed as:

$$Fl_g = \frac{Q_g}{ND^3} \quad (4.10)$$

and Froude number (Fr), which is the ratio of inertial to gravitational forces, expressed as:

$$(4.11) \quad Fr = N^2 D / g,$$

where g is the gravitational constant.

During agitation, different types of cavities develop behind the impeller blades. These cavities depend on the impeller type, Q_g and N . For a Rushton disc turbine (*RDT*) the most common cavities are vortex, clinging, large and ragged cavities. Some of these are shown in Figure 4.2.

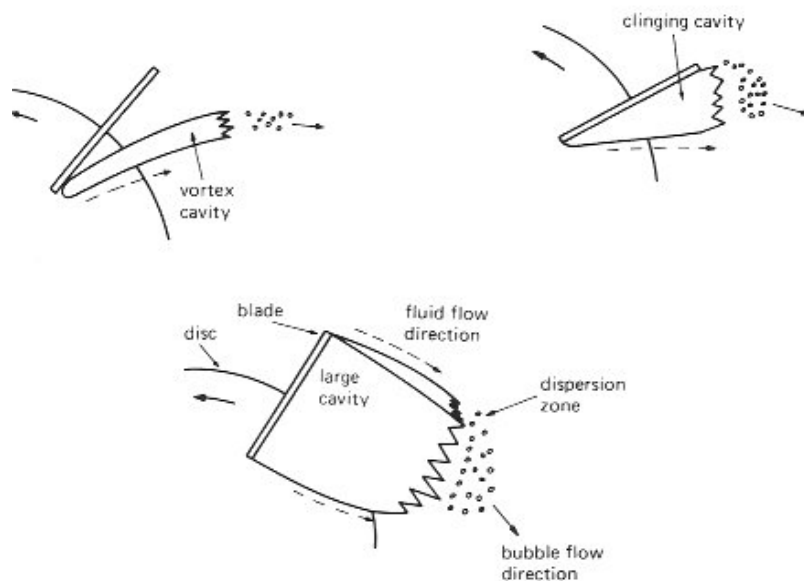


Figure 4.2. Cavity structures observed behind *RDT* blades. (Harnby *et al.*, 1992)

Warmoeskerken and Smith (1985) and Nienow *et al.* (1985) reported that vortex cavities are formed at low Q_g . By increasing Q_g , they evolve to clinging cavities. Three large and clinging cavities are then formed. At still higher Q_g , bridging cavities may be formed and ultimately ragged cavities are formed wherein the impeller is said to be flooded. Radial and axial impellers such as concave blades (Scaba *SRGT*) and up-pumping pitched blade turbines (*UPBT*) are stable blade designs that have been used to avert the formation of gas cavities behind impeller blades. A dimensionless P_g versus Fl_g plot can be used to estimate the effects of cavity types on power draw (Figure 4.3).

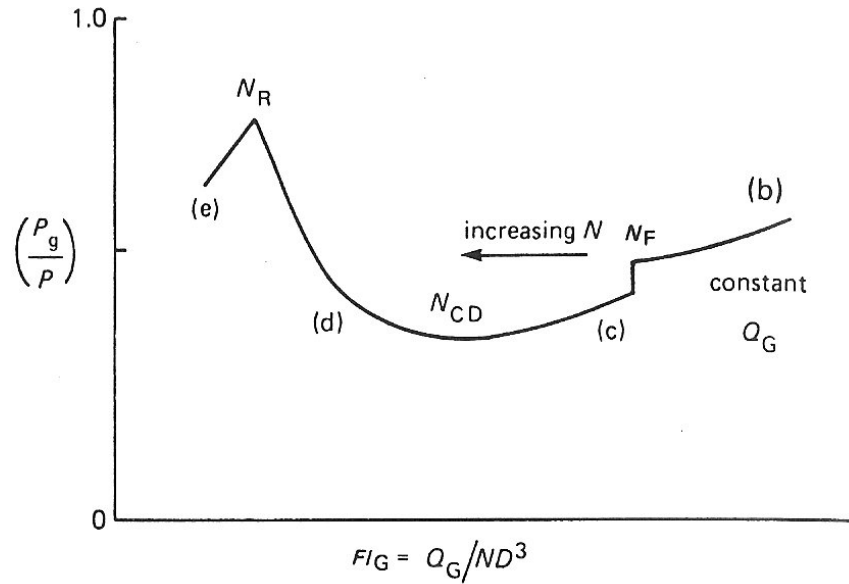


Figure 4.3. Relationship between P_g/P and Fl_g . (Harnby *et al.*, 1992)

Initially, the dimensionless gassed power (P_g/P) drops from ~ 0.8 at N_R to ~ 0.3 at N_{CD} before rising to 0.6 at N_F . Oyama and Endoh (1955), Bruijn *et al.* (1974), Treybal and Barnett (1982), Greaves and Barigou (1988) and Smith and Katsanevakis (1993) were some of the first authors to quantify P_g .

Greaves and Barigou (1988) investigated P_g of disk turbines in ionic and non-ionic solutions in a 1m vessel. They developed correlations to estimate P_g at the various dispersed states in $G-L$ agitated systems for Q_g from $1.6 \times 10^{-3} \text{ m}^3 \text{ s}^{-1}$ to $8.3 \times 10^{-3} \text{ m}^3 \text{ s}^{-1}$. The overall equation took the form:

$$P_g = 706.3N^{3.01}Q_g^{-0.45}\left(\frac{D}{T}\right)^{5.38}, \quad (4.12)$$

for clinging and vortex cavities, the equation took the form:

$$P_g = 441.4N^{3.13}Q_g^{-0.45}\left(\frac{D}{T}\right)^{5.82}, \quad (4.13)$$

whilst for large cavities the equation was expressed as:

$$P_g = 1737.1N^{2.99}Q_g^{-0.31}\left(\frac{D}{T}\right)^{5.98} \quad (4.14)$$

These correlations were expressed in terms of directly measurable parameters making them practicable.

GLS systems

The agitation of *GLS* systems encompasses the complications encountered in *S-L* and *G-L* systems i.e. the simultaneous impacts of *S-L* and *G-L* on the hydrodynamics have to be considered. By adding solids to a *G-L* system, new parameters that characterise particle deposition on the bottom have to be considered. Agitation also has to ensure that the solids and the gas are homogenised. When the effects of the solids on the hydrodynamics of the impeller are negligible, *G-L* characterisation can be a good starting point for *GLS* examination.

The solids affect the performance of the impellers because the viscosity, density and the vortices behind the impeller blades are altered. In concentrated suspensions, there is considerable change in the circulation around the impeller blades. Besides this, unsuspended solids create a false bottom, which reduces clearance (*C*), thus affecting power consumption. Warmoeskerken *et al.* (1984) studied a *GLS* system with disc turbines, and sand as the solid phase. It was shown that the transition from clinging to three large and three clinging cavities occurred at $Fl = 0.03$ for solids concentrations of 25 % (*w/v*).

The same cavities were observed in a *G-L* system under the same operating conditions, suggesting that *G-L* hydrodynamics is not significantly altered upon solids introduction. Using a similar turbine

with ballotini balls as the solids phase, Wiedmann *et al.* (1982) also showed that *G-L* hydrodynamics is not significantly affected by solids concentrations within the range of 2 to 30 % (*w/v*). Previously, Wiedmann *et al.* (1980) had shown that at low Q_g and solid concentrations, gas bubbles and solids will be circulated by impellers without significantly disrupting flow pattern.

Frijlink (1987) compared how effective disc and open turbines were at homogenising solids and gases at similar *GLS* configurations. Sand was used at a concentration of 25 % (*w/v*). It was concluded that $C = 0.25T$ was a good compromise for impellers and vessels. It was also shown that radial pumping impellers performed best at low Q_g . Radial pumping impellers show weak increases in the required speed and power for complete suspension, whilst curved blade impellers are advantageous in *GLS* systems. The up-pumping configuration was indicated as requiring high power inputs than radial impellers. A 60°- 6 blade type turbine can be used at high Fl_g .

It was also shown that for most open turbines, a maximum Fl_g is reached when the relative increase of N for complete suspension becomes larger than Q_g . Frijlink (1987) stated that the down-pumping turbine is energy efficient at small Q_g , however it has large variations in the power number (Po), just suspended gassed speed, N_{jsg} and power input, P/V , (where P represents power and V represents volume), which leads to the conclusion that radial impellers are preferred. Frijlink (1987) concluded that in most industrial applications the range of small Q_g is not very important and variations of Q_g during a process are quite usual. These may cause unstable performance in the downwards mode.

Chapman *et al.* (1983) showed that:

$$\Delta N_{js} = N_{jsg} - N_{js} = 0.94Q_g \quad (4.15)$$

4.3. Conclusions from literature review

Adequate studies have been carried out towards the understanding of particle and gas behaviour in *GLS* systems, unfortunately studies have usually utilised materials (such as ballotini balls and sand) that are unrepresentative of gas evolving *S-L* systems and would be deemed as not ideal in the evaluation of particle dynamics in gas evolving processes. Thus, this study will address solid and gas behaviour in gas evolving *S-L* systems. Sponge Nickel[®], *Ni* is an alloy of nickel and aluminum that is activated when aluminium is treated with sodium hydroxide to leave behind a porous structure that has a large surface area, which gives high catalytic activity.

4.4. Materials and Methods

Sponge Nickel[®], *Ni*, (Alfa Aesar, UK) particles with a geometric mean particle size (d_{50}) of 29 μm was characterised for pore volume, 0.99 ml g^{-1} , by a nitrogen sorption technique (Micromeritics 2020 physisorption analysis, USA) and had a surface area, 55.3 $\text{m}^2 \text{g}^{-1}$ (Micromeritics ASAP2010, USA).

14 g of sodium hypochlorite for every 100 ml of water, 14% (w/v), (Alfa Aesar, UK) was titrated with potassium iodide and acetic acid with a Metrohm 857 titrando, USA; equipped with a platinum titrode, beaker and stirrer to confirm the amount of sodium hypochlorite. Titration confirmed 13.7 % (w/v) sodium hypochlorite. The solutions used in this study were diluted to a range of 8 % (w/v) to 2 % (w/v) for safety reasons.

4.4.1. Gas evolution rate

Gas evolution rate due to the decomposition of the sodium hypochlorite by *Ni* was initially investigated in an apparatus consisting of a three neck beaker, fitted valves, a magnetic stirrer, a bubble column, stopper, delivery tube, retort stand, thermocouple. The range of concentrations of sodium hypochlorite and *Ni* is given in Table 4.1.

Table 4.1. Concentrations of *Ni* and sodium hypochlorite investigated.

<i>Ni</i> %(w/v)	Sodium hypochlorite (g ml ⁻¹)
4.76	0.07
5.66	0.13
6.54	0.2
7.4	0.23
8.25	0.26

A stop clock was used to monitor the time it took for the meniscus in the bubble column to rise to the top of the column (Figure 4.4).

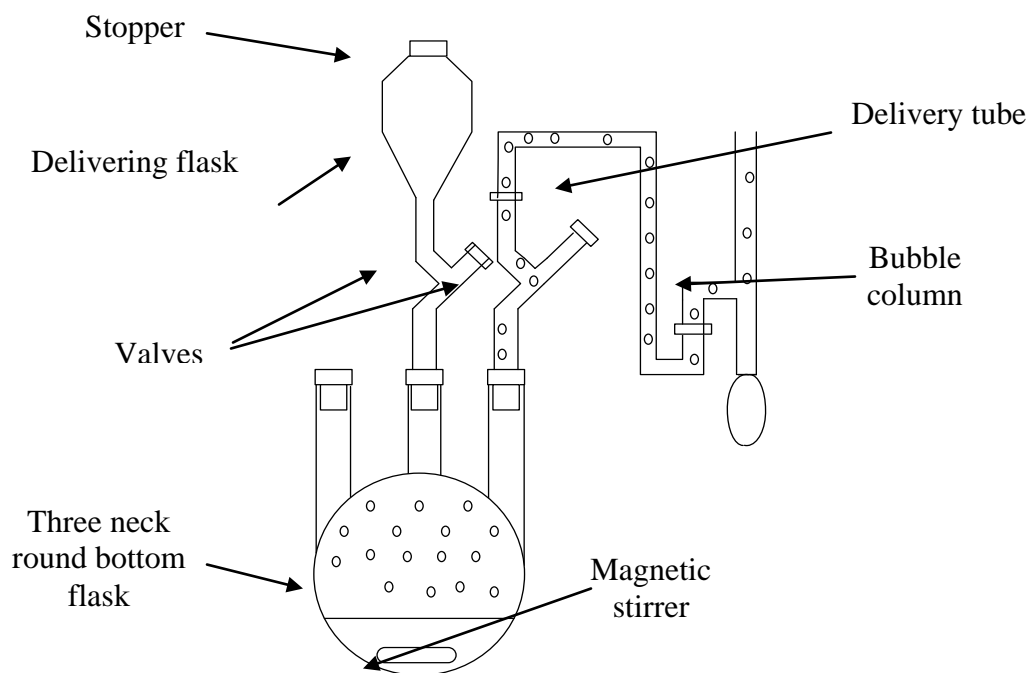


Figure 4.4. Gas evolution rate measuring apparatus

Each Ni quantity was initially weighed and transferred into the three-necked flask. Then 100 ml of the sodium hypochlorite solution, previously held in the delivery flask, was dropped into the three-necked flask with all valves and stoppers shut. As the gas was generated, the bubble column, which had soap solution, was constricted, generating a bubble, which rose up the column due to pressure build up by the gas generated. The time of rise between two points on the column was noted. During agitation, N_{js} was judged by visual observation. The gas evolution rate was determined and plotted against Ni and sodium hypochlorite concentrations.

4.4.2. Terminal settling velocity

The terminal settling velocity (V_t) of Ni in sodium hypochlorite was also determined by measuring the free fall velocity of particles in a measuring cylinder containing sodium hypochlorite. Multiple measurements were carried out to obtain an average.

4.4.3. Vessel design, configuration and impeller type

A Perspex vessel with $T = 0.145$ m equipped with 4 equally spaced baffles with widths, $W = 0.1T$ and thickness of $0.01T$ was used to carry out the studies. A 6 blade RDT with $D/T = 3/7$ and $C/T = 1/4$ was used to agitate the slurry. Rotational motion was supplied to the impeller using an overhead motor (Eurostar Power control-visc, IKA, Germany). To obtain power measurements a torque sensor (with a range of 0 to 30 N-m and a sensitivity of $66.66 \text{ mV N-m}^{-1}$) was used to measure the instantaneous torque values. The torque sensor was Whetstone Bridge with four strain gauges attached to a steel metal rod. The strain gauges are excited by a constant voltage of 12 V supplied through a slip ring. The sensor measures the instantaneous strain developed in the shaft which is transmitted to a data acquisition system as a voltage signal via a telemetry system through the slip ring. A pressure transducer with a range of 34.46 kPa, a resolution of 0.000482 kPa, and a

sensitivity of $72.54 \text{ mV k}^{-1} \text{ Pa}^{-1}$ was used (PCB Piezoelectronics Inc., U.S.A., Model 106B50) to measure pressure fluctuations. The transducer was powered by an ICP battery unit (PCB Piezoelectronics Inc., U.S.A., Model 480E06), which acted as an amplifier.

4.4.4. Just suspended speed, N_{js} , of gassing and ungassed systems

The N_{js} of gas evolving Ni and sodium hypochlorite systems and Ni in brine solution was investigated and compared. Five combinations were investigated as shown in Table 4.2. N_{js} was judged by the visual observation of the vessel bottom according to Zwietering (1958).

Table 4.2. Ni and sodium hypochlorite concentrations investigated

Ni Concentration % (w/v)	Sodium hypochlorite (g mL ⁻¹)
9	8
9	4
7	6
5	8
5	4

4.5. Results and discussion

4.5.1. The effects of Sponge Nickel[®] and Sodium hypochlorite concentration on gas evolution rate

The effects of Ni loading and sodium hypochlorite concentration on the gas evolution rate are shown in Figure 4.5 and Figure 4.6.

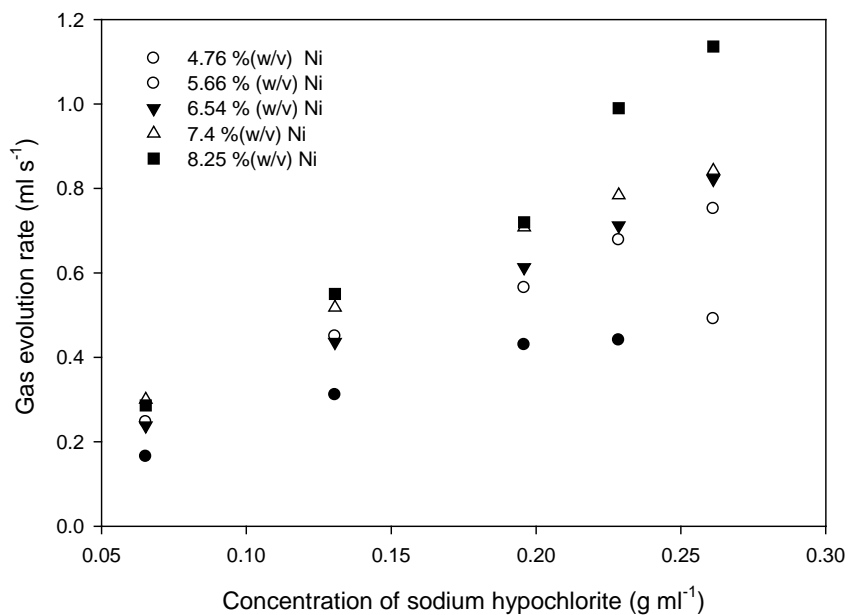


Figure 4.5. The effects of sodium hypochlorite concentration on gas evolution rate

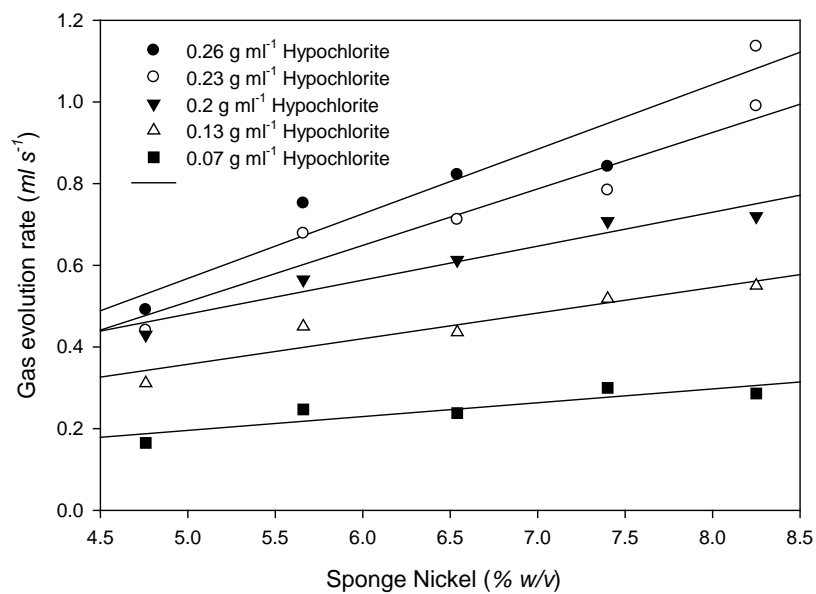


Figure 4.6. The effects of *Ni* concentration on gas evolution rate

As expected, a direct linear relationship between *Ni*, sodium hypochlorite concentration and gas evolution rate is observed, because the rate of reaction is proportional to the amount *Ni* available

and hypochlorite ion adsorbed on the catalyst surface over the range of concentrations (Lister *et al.*,1956 and Hancock *et al.*,1996).

There are noteworthy dissimilarities between *PGM* leaching and sodium hypochlorite decomposition by *Ni*. Both reactions differ in reaction mechanism, activation energy, gas evolution pattern and entrapment. *Ni* is also spongy, whilst a sponge evolves during the leach.

These intricacies thus make the selection of a sodium hypochlorite and *Ni* system that corroborates with the leach system quite difficult. As a result, the experiments are limited to ascertaining particle behaviour regardless of kinetics.

4.5.2. Particle and gas hold-up in gas evolving reactions

4.74 % (w/v) of *Ni* was reacted with 2.5 L of the sodium hypochlorite concentrations given in Table 4.1 and φ_g was measured by the dynamic disengagement method.

When agitation was ceased, a fluctuation of the φ_g was observed and the explanation behind the fluctuations is given in Figure 4.7 and Figure 4.8 with reference to annotations.

Level A: When the impeller was stopped, as expected, the gas disengaged and most of the particles sedimented to the vessel bottom.

The liquid depth thus fell to a height that was equal to the initial liquid height, when solids were added, no significant reaction took place and no agitation took place.

This is given as Level A in Figure 4.7. From henceforth, the sedimented particle bed is postulated to be comprised of three layers, namely an upper (U), middle (M) and lower (L) particle bed.

Level C: Adsorbed ^-OCl ions remained on the surface of the sedimented particles post-Level A. Since gas evolution rate is proportional to the amount of ^-OCl adsorbed on the particle surface; the ions within regions M & L, decomposed at similar rates until little or zero ions were left.

During decomposition, the liquid level increased to level C due to gas expansion. This level was called a primary φ_g level.

Level D: After a given period, little or zero adsorbed ^-OCl remained on the particles found in M & L. Thus the effects of gas expansion subsided causing the liquid level to drop again to Level D. This level was called the secondary φ_g level. Gas generation took place in bed U by particles in imminent contact with ^-OCl within the bulk liquid.

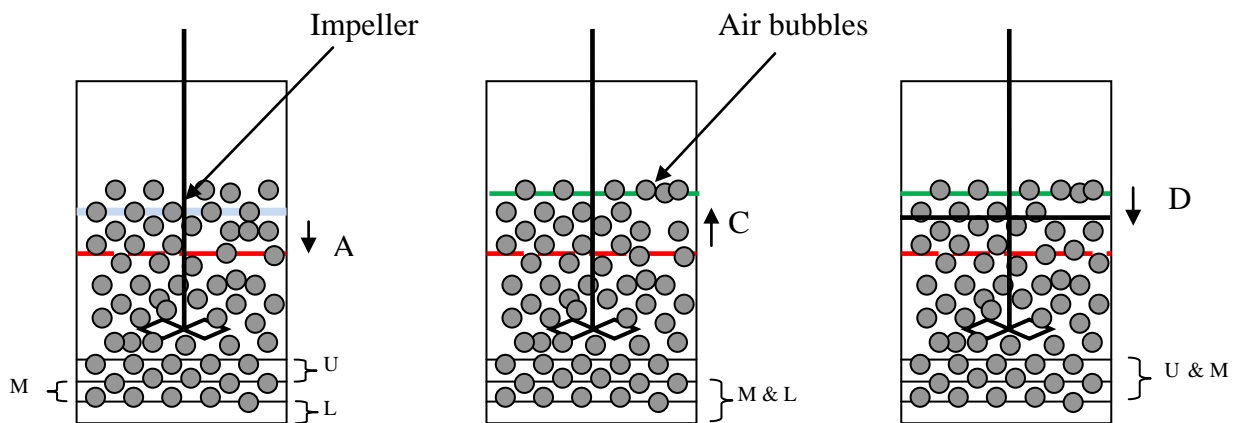


Figure 4.7. φ_g and liquid levels associated with particle settling, gas expansion and contraction.

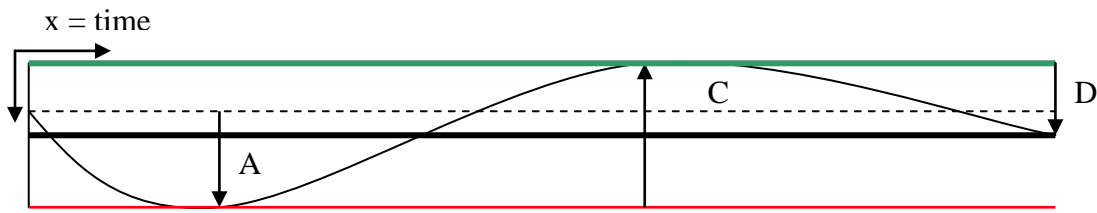


Figure 4.8. Telemetry of ϕ_g and liquid levels associated with particle settling, gas expansion and contraction.

The change in ϕ_g expressed in vessel volumes per volume minute (vvm) with respect to gas evolution rate in the vessel is shown in Figure 4.9. ϕ_g can be observed to increase with gas evolution rate. For the range of sodium hypochlorite concentrations investigated, Fl_g , took values in the range $1.13 - 2.6 \times 10^{-4}$.

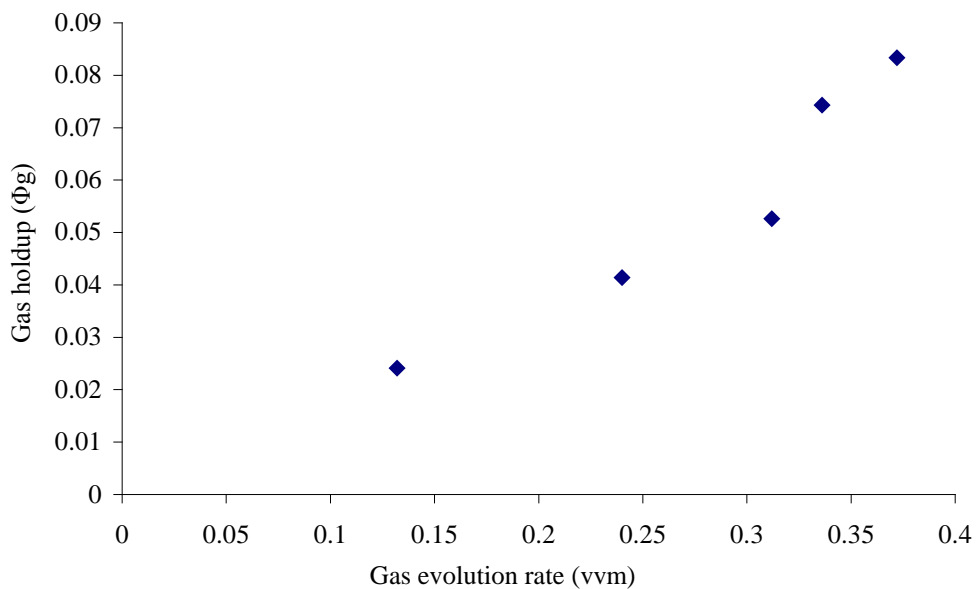


Figure 4.9. ϕ_g before ceasing agitation and Level A and as a function of gas evolution rate for 4.74 % (w/v) Ni in 8, 7, 6, 4 and 2 % sodium hypochlorite solutions.

At these values, the bubble flow regime in a sparged, stirred tank would generally lie within the fully dispersed regime.

Whilst there are undoubtedly differences in the bubble flow behaviour between sparged and gas-evolving *S-L* systems, it is proposed that these differences are minimised towards the fully dispersed (low gas flow - high impeller speed) end of the regime spectrum.

Conversely, the differences are maximised at the high gas flow – low impeller speed end of the regime, as it is unlikely that impeller flooding or large trailing cavity formation could occur in a gas-evolving system since the formation of gas occurs off the bulk of the particles' surface and is not isolated in one region (e.g. due to a sparger). Over the full range of operating conditions studied, the bubble flow regime is classified as fully dispersed.

The impeller-driven flow is therefore dominant over the natural bubble convection behaviour, and φ_g is therefore a function of gas evolution rate alone.

4.5.3. Solid phase suspension and settling behaviour in gas evolving reactions

Five *Ni* and sodium hypochlorite combinations were investigated as shown in Table 4.2.

Measured values of N_{js} and power draw at N_{js} (P_{js}) for the ungasged and gasged systems are shown as functions of *Ni* and sodium hydrochlorite concentrations in Table 4.3.

Plots of the data are given in Figure 4.10 and Figure 4.11. The results clearly show that gas evolution reduces the ease of suspension of the *Ni* particles.

Table 4.3. Summary of just suspended speed for gassed and ungassed systems.

N_i Concentration % (w/v)	Sodium hypochlorite (g ml ⁻¹)	Gas evolution rate (vvm)	N_{js} (Ungassed system) rpm	N_{js} (gassed system) rpm	P_g/P_u (Ratio of gassed to ungassed power draw)	Gas hold-up ϕ_g (%)
9	8	0.70	430	670	2.34	7.36
9	4	0.36	430	550	2.98	3.21
7	6	0.378	410	604	4.05	3.82
5	8	0.372	400	665	4.24	9.04
5	4	0.24	380	570	4.55	3.21

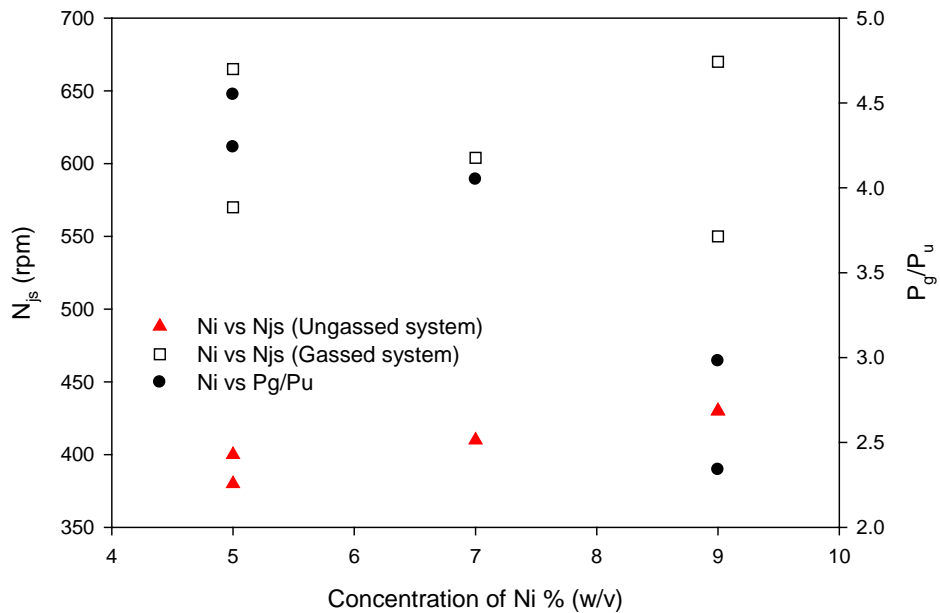


Figure 4.10. N_{js} and P_g/P_u as functions of N_i and sodium hypochlorite concentrations (see Table 4.3)

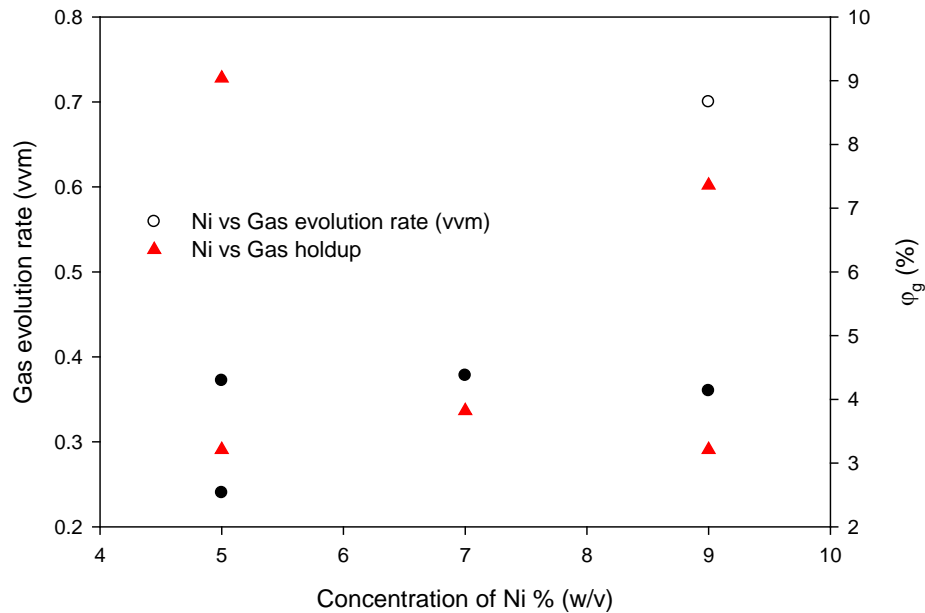


Figure 4.11. Gas evolution rate and gas holdup as functions of *Ni* and sodium hypochlorite concentrations (see Table 4.3)

N_{js} was greater for the gas evolving S-L system than for the two-phase system. This is indicative of the high gas phase concentrations surrounding the particles, which act as energy sinks via the action of compression and expansion in a fluctuating pressure field. The absorbance of energy by the bubbles reduces the available energy in the fluid to lift the particles from the vessel base and only high energy turbulent eddies have sufficient capability to do so.

This effect is offset by the reduced effective density of the particles once their pores are filled with gas. The terminal settling velocity of a 75 μm diameter particle prior to pore filling (immediately upon addition to the hypochlorite solution and before full adsorption of hypochlorite ions to the nickel surface) was found to be 0.58 cm s^{-1} . Once gas generation commenced, the terminal falling

velocity of the same particle was found to reduce to 0.40 cm s^{-1} . This equates to a reduction in fall velocity by 31 % and a pore volume gas filling of 38 %.

4.6. Conclusions

Gas evolution rate was characterised for a model nickel-sodium hypochlorite system over a range of operating conditions. Gas evolution rate was found to exhibit dependence on both parameters.

φ_g was found to lie in the range 3 – 7 %, and was not dependent upon agitation speed over the range of operating conditions studied here, as the gas evolution rate was low enough to let impeller flow dominate the bubble flow regime.

The solids suspension performances for 2-phase *S-L* and 3-phase *GLS* systems were quantified using Zwietering's just-suspended impeller speed condition. Although the presence of gas was found to markedly increase the impeller speed required to fulfill this criterion, a coherent pattern to the relationship between N_{js} (ungassed) and N_{js} (gassed) could not be readily ascertained with respect to the concentrations of *Ni* and sodium hypochlorite.

Positron Emission Particle Tracking (*PEPT*) was trialled to evaluate the significance of each variable and to provide insight into which parameter controlled solids suspension in gas-evolving *S-L* systems, however the particles were too small to be labeled in order to obtain meaningful data.

Chapter 5. The use of Electrical Resistance Spectro- Tomography for Phase Discrimination in Gas-Liquid-Solid (GLS) mixing.

5.1. Introduction

During the hydrometallurgical leach process, base metals (*BM*) are leached off platinum group metal (*PGM*) alloys in an agitated vessel, leaving behind a solid comprised of *PGM* and some unleached *BM*. During the reaction process, the solid-liquid (*S-L*) system evolves to a *GLS* system as gas is evolved.

The gas is an unwanted by-product and its presence can cause particle deposition by acting as an energy sink and reducing the inertial forces required for solids suspension and dispersion. If this takes place the leach efficiency will decrease since it depends on the ability to disperse solids and distribute gas bubbles simultaneously and efficiently. Their distribution should be assessed by observing phase distribution data.

Such information is important from a practical and academic viewpoint as well as for mathematical models and simulations, for example in establishing closure definitions in Computational Fluid Dynamics (*CFD*). It is also critical for optimal sizing of reactors. However, obtaining this information is not easy since phase interference and opacity complicates data capture, especially in systems operated at high gas and/or solid fractions.

These issues limit the use of optical non-intrusive characterisation techniques such as Laser-Doppler Velocimetry (*LDV*) and digital Particle Image Velocimetry (*PIV*) which are the benchmark methods

for obtaining high resolution hydrodynamic data. Only a few studies exist which used these techniques for very low dispersed phase fractions in gas-liquid (*G-L*) (Montante *et al.* 2008) and *S-L* systems (Unadkat *et al.* 2009; Gabriele *et al.* 2011). There is therefore a paucity of qualitative data in the literature on the characterisation of *GLS* systems in terms of industrially relevant solid or gas hold-ups (ϕ_g) because the interrogation of these systems requires highly sophisticated techniques which can cope with both opacity and complex system dynamics.

Phase discrimination in *GLS* systems can be attempted by use of multiple measurement techniques simultaneously or in sequence on the same system, or more conveniently by a single technique. Nahvi *et al.* (2008a) described a spectro-tomography approach with Electrical Impedance Tomography (*EIT*) to isolate materials with dissimilar dielectric permittivities in a system. They showed that by varying the frequency of an alternating current (*AC*), the permittivity of the materials could be manipulated to a point where they are either eliminated or isolated in a multicomponent system, allowing for the measurements of the individual dielectric permittivities to be carried out. Dielectrics are electrical insulators that can be polarised by an applied electric field.

In this Chapter, a technique is proposed for *GLS* characterisation analogous to Nahvi's (2008) concept, wherein Electrical Resistance Tomography (*ERT*) is used to manipulate the effective resistance of a conducting solid allowing for measurements of ϕ_g to be carried out without significant interference by the solid and vice versa.

A literature review of the characterisation techniques that have been used for phase discrimination is initially given followed by an overview and fundamentals of the characterisation technique proposed and the phenomena behind the characterisation technique. Following these reviews, an agitated

GLS system; comprised of air, nickel nitrate solution and stainless steel particles using the modified *ERT* approach is characterised. By varying the frequency of a given *AC*, the gas phase is isolated from a conducting solid phase in an ionic solution allowing for gas distribution measurements to be obtained without significant interference by the solid.

Verification experiments were initially carried out with a static phantom of the solid phase (i.e. a stainless steel rod) and plumes of air in a circular array *ERT* vessel to demonstrate and verify the concept. A related study was then carried out with agitated stainless steel particles and air in individual *S-L* and *G-L* studies with a linear *ERT* probe to show that the findings in the static systems would correlate with those obtained for the agitated systems. Finally, the frequencies obtained were applied to an agitated *GLS* system.

5.2. Literature Review

Various diagnostic techniques have been used to obtain phase distribution information in complex and multiphase systems. Techniques for phase discrimination are generally types of tomography, which refers to imaging by sections or sectioning. For the purpose of this review, the tomographic methods discussed are categorised into electrical, ionising and non-ionising radiation based techniques.

Electrical based techniques are referred to as soft-field measurement techniques because the field distribution depends on the material distribution in the imaging domain, whilst radiation based techniques are hard-field methods since the direction of energy propagation or the field of the sensor is not influenced by the material distribution in the imaging domain.

Ionising and non-ionising radiation based tomography techniques are hard-field techniques. Their distinction is one of associated energy. In the ionising technique, the incident energy upon a material is large enough to remove an electron from an atom orbit to produce ionisation. In the latter, rather than producing electrons, the electromagnetic radiation has sufficient energy only for excitation and movement of the electron to a higher energy state. They are not affected by what is outside their measurement volume if precise collimation is applied compared to soft-field methods.

To obtain measurements from a two phase system such as *G-L* or *S-L* system, it is essential that the technique being considered is sensitive to the physical property of one component in the system such as electrical permittivity or density. However, to study three phase systems the physical properties of two components in a continuum needs to ensure that they can be individually identified without interference. Dual source energy or multi-modal techniques are used to achieve this. In dual energy source characterisation, dissimilar energy sources are used to isolate and obtain measurements of the individual components in the system, whilst multi-modal techniques involve the use of two or more diagnostic techniques to obtain measurements in a system via their independent measurement principles.

5.2.1. Electrical based tomography techniques

The electrical based tomography techniques are relatively low cost and real-time imaging and data acquisition techniques that have the added benefit of being non-intrusive, posing little or no safety risk and being robust to harsh processing conditions. However they have low spatial resolution, which lies within the range of ~ 10 to 15% of the lengthscale of the interrogated region (Tapp *et al.* 1999) and require a screen (Faraday cage).

EIT encompasses *ERT* and *ECT*, wherein specific electric properties of materials in a system are sensed by each technique. *ERT* is a specific case of *EIT* where the real component of impedance is sensed and reconstructed as Tomograms. However, *ECT* measures dielectric permittivity of materials within a non-conductive continuous phase. *EIT* is applied to processes that have a conductive continuous phase.

ERT and EIT

Generally, all electrical based tomography techniques are composed of three parts, namely the electrodes, data acquisition system (*DAS*) and image reconstruction system. The electrodes in *EIT* and *ERT* systems tend to be in contact with electrolytes inside process vessels and they are more conductive than the electrolyte to obtain reliable measurements. The electrodes are also located equidistantly around the process vessel to map resistivity changes across the planes of interest. During operation, electrical current (*I*) is induced between a pair of neighbouring electrodes, whilst the voltage distribution (*V*) is measured between the remaining set of neighbouring electrodes (Figure 5.1).

This process is repeated by all neighbouring pairs of electrodes until a full rotation and scan of the system is obtained, thus $16 \times 16 = 256$ voltage measurements make up a full scan. The data is processed in the *DAS*, which communicates with a host computer to transfer logged data for subsequent image reconstruction. This process of data acquisition is called the adjacent electrode pair strategy and its shortcoming is that it has a non-uniform current distribution, since most of the current travels near the peripheral electrodes. Thus the current density at the centre of the system is relatively low which makes the strategy very sensitive to measurement error and noise.

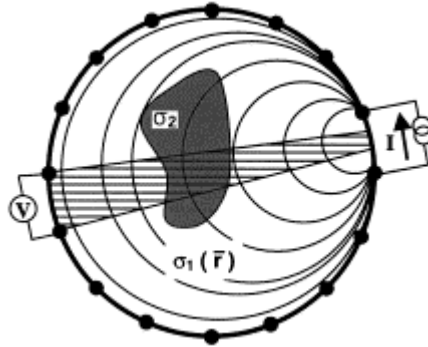


Figure 5.1. Adjacent electrode pair strategy for 16 electrodes sensor (Dyakowski *et al.*, 2000)

Historically, *EIT* and *ERT* have been used to interrogate phase distribution with circular array electrode sensors in stirred vessels. Each electrode plane produces cross-sectional maps of electrical and phase conductivity distribution (Bolton *et al.*, 2002). The results are then displayed as 3D reconstructed interpolations of the planes as demonstrated by Holden *et al.* (1998) and Mann *et al.* (1997).

Recently, Kourunen *et al.* (2008) used a circular array *EIT* to observe the mixing of a liquid-liquid (*L-L*) system in turbulent flow to determine the efficiency of a new ‘Trumpjet’ mixing system (Wetend Technologies Ltd, Finland) against a conventional injection system. Stephenson *et al.* (2009) also used circular array *EIT* to observe miscible liquids in a semi-tech scale stirred tank to demonstrate the performance of three-dimensional reconstruction algorithms in monitoring the mixing of a pulsed high conductivity tracer. They showed that *EIT* performed well for surface feeds and mixing times compared well to literature correlations. Accurate flow visualisation *EIT* images were obtained by using a regularisation parameter of 1×10^{-4} .

Circular array *ERT* however has been widely used as a visualisation tool for two-phase systems such as *G-L* (Wang *et al.*, 2000) and *S-L* distribution (Ricard *et al.*, 2005, Stanley *et al.*, 2002). Stanley *et*

al. (2002) monitored the concentration distribution of a single feed semi-batch *S-L* system and highlighted concentration fields in the system by monitoring conductivity plumes of the solids in the liquid.

Circular array *ERT* was recently used in a multi-modal manner with a fibre optic probe to interrogate *GLS* systems (Razzak *et al.*, 2009). Local conductivity measurements of the φ_g and non-conducting solid phase holdup were obtained. The average solids phase holdup was quantified using pressure gradient measurements in a riser whilst the fibre optic probe measured φ_g independently. By combining these results, φ_g and solid holdups were differentiated. Liter *et al.* (2002) used Gamma Densitometry Tomography (*GDT*) and circular array *ERT* to characterise a pilot-scale slurry bubble-column. *ERT* distinguished the conducting liquid phase from the gas and the solid phase, whilst *GDT* discriminated the non-attenuating gas phase from the liquid and the solid phases.

Bolton *et al.* (2002) stated that circular array *ERT* setups are valuable and attractive to industry, however the radial information obtained and their reconstructions were unlikely to be absolutely necessary in processing environments. Similarly, the practicability of fitting 128 electrodes on an industrial reactor was likely to preclude circular array *ERT* as an option.

Thus Bolton *et al.* (2002) introduced and recommended a linear *ERT* probe that also operates under the same adjacent measurement strategy as the circular array *ERT* but rather provides axial distribution information. Such information is the vital information sought from tomographic measurements in industry since inadequate axial mixing is a cause of many industrial mixing

problems. The sensor is intrusive but suitable for installation in industrial systems. The effects of intrusion are overcome by deploying the probe beside baffles.

Bolton *et al.* (2002) interrogated laboratory and pilot-scale stirred vessels and demonstrated measurements of solids concentrations and distributions. Ricard *et al.* (2005) also deployed the linear *ERT* probe into stirred tanks and compared on-line monitoring information and *CFD* modeling results of *L-L* dispersion and solids suspension in stirred tanks to the axial distribution information obtained with the probe. Since the measurement techniques are electrical it also presents the usual benefits and drawbacks previously given.

ECT

ECT reconstructs dielectric properties of materials from capacitance measurements obtained between all possible pairs of electrodes. Unlike *EIT* or *ERT*, during interrogation of a system the electrodes are individually fired and the capacitance values between the excited electrode and the remaining ones are measured. The measurement protocol is a rotation (Figure 5.2) of the electrical field around a cross-section in discrete steps, analogous to the source detector movement in computerised tomography (*CT*) which is used in medical imaging (Dyakowski *et al.*, 2000).

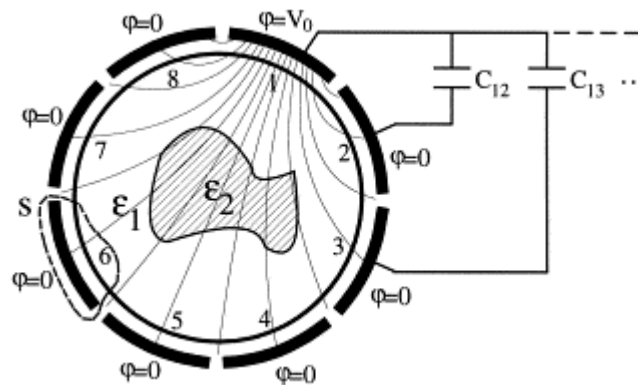


Figure 5.2. Rotating electrical field measurement strategy with *ECT* (Dyakowski *et al.*, 2000)

Previously, Warsito *et al.* (2001) used a mono-modal tomography approach to characterise *GLS* systems. *ECT* was applied to a bubble column where air was used as the gas phase, Norpar 15 (a kerosene) and Paratherm (a heat transfer liquid) as the liquid phase and polystyrene beads whose permittivity were similar to Paratherm were used as the solid phase. In both cases visualisation of one of the dispersed phases was made possible by ascribing electrical properties to the continuous liquid phase, making it electrically invisible. *ECT* has also been used in a multi-modal manner with *ERT* to study oil-water-gas distribution in pipelines (Li and Yang, 2009). The *ECT* mode was used to measure an oil-continuous whilst the *ERT* mode was used to measure water-continuous flows.

5.2.2. Radiation based tomography techniques

Gamma (γ) rays and X-rays are non-intrusive ionising tomography techniques that have been used to obtain phase distribution information in multiphase systems. They are relatively time consuming compared to the electrical techniques because data acquisition and processing times are lengthy, since the counting times required for useful statistics are extended. In these techniques, the loss in intensity of radiation sources due to flow is low, which enables information on phase distribution to be accurately obtained. Information from these techniques can be obtained by measuring the change in flux of the radiation.

X-ray CT

X-ray computed tomography (*CT*) has been widely used in the process industry to study multiphase flow in static systems because of its high spatial resolution. It is made-up of three components, namely an X-ray source, a detector and a rotor, which alternates the X-ray source and detector around the system being examined.

During the scanning process, X-rays are transmitted through the system to the detectors. After a scan, the source and detectors rotate at preset angles until a 360° rotation has been achieved. All the diagnosed frames obtained are collated and converted to digital images called projections. These images are maps of the relative linear attenuation value of objects in the system. A *CT* reconstruction algorithm produces the projections, which reveals the internal structure of the process. The projections are a sequence of 2D slice images that are based on the X-ray absorption of objects in the system. These *CT* slices serve as input datasets for 3D visualisation softwares.

Single energy X-ray CT

The conventional X-ray *CT* diagnosing technique described above is called a single energy measurement strategy. This is because a specific X-ray energy is used to obtain the density distribution of materials in the system. It has generally been used to study two phase flows in packed and trickle beds, owing to complex flow patterns observed in them. Recently, Caulkin *et al.* (2009) validated packed bed simulations obtained from DigiPac® with X-ray *CT* scans in terms of bulk density, local packing density profiles, and pellet orientation distributions. DigiPac simulates object movements in a random, collision-guided or discrete elemental method. Marchot *et al.* (2001) investigated the sources and the nature of small-scale liquid and gas maldistributions in packed beds with an irrigated packing structure. Toyé *et al.* (1998) investigated void fractions and liquid holdup in packed columns. Holdup measurements for fluidised and trickle beds were also investigated by Kantzas *et al.* (1994) with a modified medical X-ray *CT* scanner. A plot of average φ_g against bed height suggested that a relatively constant φ_g existed throughout the column, whilst radial variation in φ_g were observed. Liquid distributions in trickle beds were initially investigated by Lutran *et al.* (1991). As the liquid flowrate through the trickle bed was increased, the liquid structure was shown

to transit from tortuous filaments down the column, through to branching filaments, until the column became flooded.

Ford *et al.* (2008) used X-ray *CT* to explore differences in gas dispersion regimes in stirred vessels. At the completely dispersed condition, a relatively uniform holdup profile was shown; whilst at flooded conditions a high φ_g near the impeller shaft was observed. The high resolution of X-ray *CT* allowed for accurate reconstructions of the recirculation regions behind the baffles to be visualised. Recently, an ultrafast 3D X-ray *CT* method based on electron beam scanning was introduced by Bieberle *et al.* (2010) and shown to be able to recover the structure of the phase boundaries found in Gas-Solid (*G-S*) and *G-L* flows which undergo 3D structural changes.

Dual energy X-ray CT

For multicomponent systems, the use of single energy strategies is difficult because it is hard to distinguish the attenuation of the components in such systems. The use of dual X-ray *CT* has been suggested for the characterization of multicomponent systems. Coenen and Maas (1994) and Engler and Friedman (1990) showed that if the attenuation by gas is considered negligible and the attenuation properties of the two X-ray absorbing components are significantly different, then the two materials can be reconstructed and imaged separately.

Dual energy X-ray *CT* relies on Compton and Photoelectric absorption, where Compton scattering dominates the attenuation observed with high X-ray energy sources and the linear attenuation coefficients of the components are proportional to their densities. Attenuation with low energy sources is dominated by Photoelectric absorption, where the linear attenuation coefficients are strongly dependent on the effective atomic number or composition (Johansen, 2005). Compton

scattering is a process in which a photon transfers a portion of its energy to an orbital electron in matter and a lower energy photon is scattered at an angle to the original photon path.

Grassler *et al.* (1999) initially investigated the dual-energy X-ray *CT* with test objects made of thin latex films filled with aluminum silicate and water. They characterised both objects by single and dual-energy X-ray *CT*. The attenuation of the latex films around the objects were neglected in comparison to the solids and fluid. Due to the similar attenuation coefficients of both materials a single X-ray energy was shown to be incapable of distinguishing between aluminum silicate and water. By using dual-energy X-ray *CT* and calculating the integral solids and fluid concentrations by Beer's law (revised according to the energies used) the reconstruction process showed that both materials could be distinguished. Grassler *et al.* (2001) went on further to use dual-energy X-ray *CT* to determine solids, liquid and gas distributions in a three-phase bubble column. Granulated Polymethylmethacrylate (*PMMA*) with a diameter of about 3 mm and aluminium silicate particles with a diameter of about 0.1 mm were characterised in a repository. Gehrke and Wirth (2005) characterised a model fluid catalytic cracking reactor with air, water and glass beads as the process components.

Knowledge of hydrodynamics of such systems can help to improve their operation. The X-ray energy was switched between 80 keV and 140 keV after which the data acquisition for dual-energy tomography distributions of glass beads and water were calculated respectively. Low concentrations of the glass beads were observed in the center of the riser and an increase in concentration was observed towards the vessel wall. Above the injection zone, an increased glass bead and water concentration was observed. The downward-directed solid flux at the wall interacted with the injected water and accumulated above the nozzle. Behling and Mewes (2006) also distinguished 3

phases in a bubble column with dual-energy X-ray *CT*. Measurements were conducted with air as gas, water as liquid and *PVC* as solid phase.

Approximation errors (due to the large dynamic range of photoelectric coefficients), boundary constraints (due to noise, scatter, and other sources of errors), image artifacts and X-ray spectral drift with time are some of the limitations of dual energy techniques. Unlike γ -ray *CT* this approach has been limited in use within the chemical industry. The majority of its application can be found in rock characterisation for petrochemical industrial applications (Watson, 1989; Wellington and Vinegar, 1987), bone mineral density measurements (Dunscombe *et al.*, 1984) and radioactive waste drums (Robert-Coutant *et al.*, 1999).

γ -ray *CT*

γ -ray *CT* is the primary nucleonic technique that found application in the industry. It has a setup similar to X-ray *CT*, where a source emits radiation, which is detected by detectors before being reconstructed. γ -rays travel through the region of interest and are attenuated based on the density, composition of the system and the distance of travel. γ photon attenuation is based on Lambert-Beer's exponential attenuation law, denoted as:

$$I = I_o e^{-\mu x}, \quad (5.1)$$

where I_o is the initial intensity of the γ -rays beam, x is the region thickness having a characteristic linear attenuation coefficient, μ and I represents the remaining or un-attenuated beam intensity (Johansen, 2005). Thus, by selecting a γ -ray source with correct emission energy it is possible to discern the density of a region of interest and constant attenuation coefficient, or the attenuation coefficient of a region of a constant density. The spatial resolution of γ -ray *CT* depends on the

collimation of the detectors, the number of detectors per projection and the number of projections. Generally, as these increase the spatial resolution improves with spatial resolutions as low as 3 % being reported (Johansen, 2005).

Single energy γ -ray CT

The γ -ray sources that have been used are obtained from Caesium-137 (^{137}Cs) or Cobalt-60 (^{60}Co). Liu *et al.* (2011) measured the cross sectional φ_g distributions at 3/4 the dimensionless static liquid height in a *G-L* stirred tank. *CT* images and digital distribution curves of φ_g with a dimensionless radius based on the *CT* images explained the fluctuating changes of φ_g distribution. Kumar *et al.* (1995) used γ -ray *CT* to measure void fraction and distribution in two-phase flow systems, such as fluidised beds and bubble columns. The technique provided quantitative information that directly served flow modeling efforts, since it also produced time-averaged local void fraction data. Such measurements in two phase systems are obtained by uni-modal techniques, where a single γ source and strength is utilised.

Dual energy γ -ray CT

For multiphase systems, γ -ray *CT* has also been used in a dual energy approach, where energy sensitive detectors are used to measure transmission from high and low γ energy sources. The technique relies on the Compton and photoelectric absorption. LeVert (1973) was probably the first author to demonstrate the concept. His work showed that dual source γ energies can be used to measure void fractions in flowing media. The method was compared with the single source as a way of making measurements of dynamic fluid systems.

The dual source method was shown to be less severe when a static void assumption was initially made. It was also shown that the mean void fraction determined dual source γ energies was independent of the thickness of the flowing fluid. Both the single and the dual energy source methods were compared for an assumed case of Poisson-distributed voids passing the detector location. It was also emphasised that the dual source energy method does cause some additional difficulties in that one must be careful to correct errors caused by Compton-scattered high photons being counted as unscattered low energy photons.

Abouelwafa and Kendall (1980) applied the technique to an oil-air-water system. By studying a number of discrete γ energies, it was demonstrated that γ -ray *CT* could be extended in theory to cover many material types. Watt and Steffner (1985) used dual energy γ -ray to determine the concentration of lead in ores and concentrates on conveyors and the potential application to monitor the lead content of the tailings from heavy medium separation of high-and low-grade ore prior to the flotation process was discussed.

Johansen (2000) measured the gas volume fractions in oil-air-water pipe flows independent of the salinity of the water component. Temporal variations in the *G-L* distribution may disturb flow velocity measurements with this technique; with the major problem being the gas volume fraction.

Frøystein (2005) designed a fully automated dual energy γ -ray *CT* for use in a high pressure multiphase flow loop. The system facilitated the determination of phase distribution in multiphase systems. The system reconstructed the different fluid zones within a pipe cross section for different geometric configurations. It was shown that where different fluid mixtures having similar attenuation coefficient values were present, it was difficult to discern between the regions.

Varma (2006) carried out *GLS* studies and simulations with dual energy γ -ray *CT*. Algorithms for imaging *GLS* systems based on the Alternating Minimization technique by Benac and O'Sullivan (2002) were used. Tomograms were generated via computer programs for a theoretical *GLS* phantom. This data was processed via the algorithm developed for image-reconstruction. The reconstructed images described phase distribution of the three phases.

Varma (2007) further presented a novel dual source *CT* (*DSCT*) technique that used γ -ray photons from ^{137}Cs and ^{60}Co isotopes to measure phase holdup distribution in dynamic three phase systems. The algorithm developed for image reconstruction (Varma, 2006) provided accurate phase holdup distribution images and this technique was used to determine the phase holdup distribution in slurry bubble column (*SBC*) consisting of dynamic gas liquid and solid phases.

Yingxiang *et al.* (2007) also studied on oil-water-gas three phase flow measurement by a dual energy γ -ray *CT*. It was shown that as oil flow rate was increased, the total liquid flow rate increased, and gas volumetric fraction decreased. Dual energy γ -ray *CT* produced the appropriate response to changes in the process. Salgado (2009) used the principles of γ -ray absorption and scattering together with an appropriate geometry, comprised of three detectors and a dual-energy γ -ray source; to obtain data in annular, stratified and homogeneous oil–water–gas regimes, which could be adequately correlated to volume fractions of each phase by means of artificial neural networks.

Multi-modal γ -ray CT

γ -ray *CT* has also been used in a multimodal manner to diagnose multi-component systems. Duduković (2003) provides an overview of the studies that have utilised *CARPT* and γ -ray *CT* to

generate velocity and phase holdup profiles in *G-S*, *S-L*, slurry bubble columns and stirred tanks. *CARPT* monitors the motion of a single γ -ray emitting particle by an array of scintillation detectors located around the system being diagnosed.

Bjørn *et al.* (2005) conducted experiments with dual modality capacitance and dual energy γ -ray *CT* on three phase static phantoms, where oil, water and gas were simulated by polypropylene, ethanol and air, respectively. The experiments showed that three component imaging was possible on simple flow regimes, implementing a pixel-to-pixel mapping procedure of traditional hard-and soft-field sensor reconstruction algorithms. The two phase capacitance tomogram reconstructed using the Linear Back Projection (*LBP*) algorithm was very poor from a spatial point of view. By contrast the dual energy γ -ray tomography demonstrated good results with respect to image error rates both from a spatial and parameter point of view.

To monitor liquids motion neutrally buoyant particles are used, whilst for solids flow, a tracer of the same size and density of the solid in the system is used. Johansen *et al.* (1996) also combined *ECT* and γ -ray *CT* to enable oil-air-water flow regime in pipes to be identified. A comprehensive study by Boyer and Fanget (2002) quantified the error associated with γ -ray *CT* measurements. The authors were able to detect solids holdup within 3 % accuracy with a spatial resolution of ~ 2.5 mm.

Magnetic Resonance imaging (MRI)

MRI is a non-ionising tomography technique. In *MRI*, strong magnetic fields with known gradients are applied to a system. They cause the nuclei of matter within the system to emit radio signals by processing in phase with the field. Nuclei in different areas of the field orient to different frequencies enabling their positions to be determined. Commonly, the magnetic field is tuned to

cause resonance of hydrogen nuclei i.e. protons; in multiphase flows containing hydrocarbons or water.

MRI has found extensive use in the study of fluid dynamics in fixed and trickle bed reactors. Hanlon *et al.* (1998) measured the fluid velocities in a narrow-gap temperature-controlled Couette flow rheometer by using an alternative pulsed field based nuclear magnetic resonance strategy and a number of dimensional approaches. They showed that a two dimensional approach to obtaining measurements was accurate but time consuming whilst a one dimensional approach was less accurate but rapid.

Altobelli and Mondy (1998) measured the settling of glass micro-bubbles in flotation experiments by using the one dimensional approach. In a thoroughly mixed vertical cylinder comprised of glycerol and water, they showed that the glass micro-bubbles rose to the top of the suspension. *MRI* data was then taken continuously to measure the volume fraction axial distributions and phase velocities with time.

Mantle *et al.* (2003) provides a review of dynamic *MRI* techniques with emphasis placed on chemical engineering applications. In the application of *MRI* to fixed beds and trickle beds, Mantle *et al.* (2001) used a three dimensional *MRI* approach to characterise the structure of the interparticle pore space whilst *MRI* Velocimetry was used to determine the quantitative statistical information concerning single-phase flow field in a packed bed of catalyst.

Lim *et al.* (2004) used an ultrafast *MRI* to image liquid distributions in a *G-L* co-current downflow through a fixed bed of pellets. They reported images of local pulsing events within the bed occurring

during the trickle-to-pulse flow transition. The study by Gladden *et al.* (2007) looked at the characterisation of *GLS* reactions in a trickle bed.

5.2.3. Fundamentals of ERT Spectroscopy

Hoyle and Nahvi (2008) described a spectro-tomography method with *EIT* to characterise complex multi-component industrial processes. Spectro-tomography is a technique where a spectral range of excitation signals is used to isolate materials by the difference in their response and electrical potential at fixed currents.

A hypothetical case was shown in their work, where items, denoted as A, B and C (in Figure 5.3) with dissimilar physical properties peaked in conductivity intensity under dissimilar signals and troughed away from the signals.

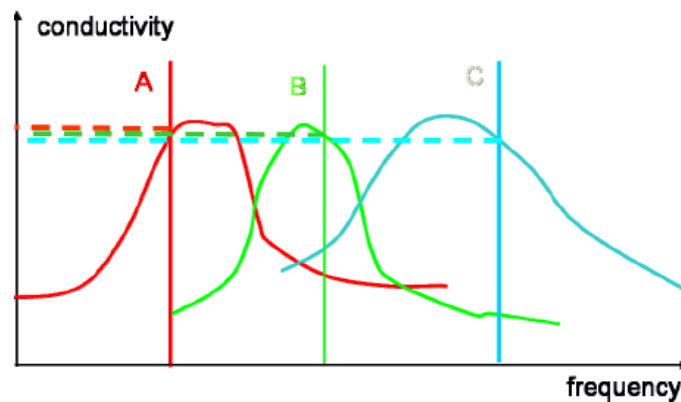


Figure 5.3. Multi-frequency excitation conductivity intersections (Hoyle and Nahvi, 2008)

Hoyle and Nahvi (2008a) further demonstrated the technique in a system composed of fruits (a banana and cucumber) in salt solution as shown in Figure 5.4. The colour scales to the right of the tomograms in Figure 5.4 are the relative intensities. By decreasing the frequency, they isolated cucumber from the banana.

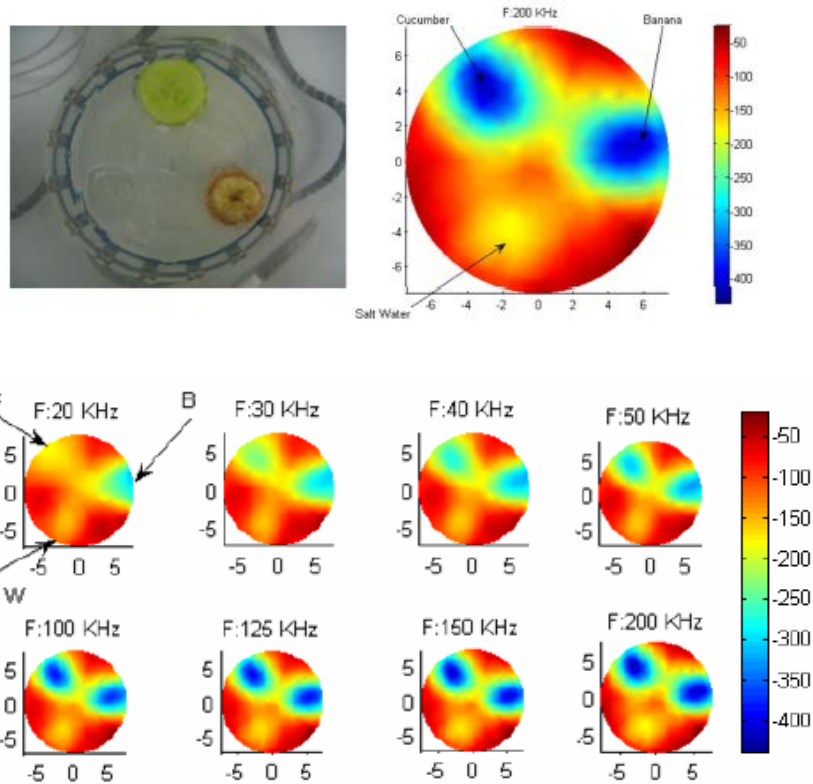


Figure 5.4. The effects of varying the frequency from 20 to 200 kHz on the isolation of banana from cucumber

Hoyle and Nahvi (2008b) investigated ways of meeting the process needs of the spectro-tomography technique, since the realisation of such a method in the industry requires a fast and efficient procedure of data capture. They proposed a novel chirp excitation spectro-tomography technique.

Chirp speeds up the scan process and allows for wideband frequency content for process measurements. Since the response contains the spectral information over the desired bandwidth, tomograms can be reconstructed for a given frequency and experimental data.

Generally, the fundamental concept that governs Hoyle and Nahvi's (2008a) technique is the dissimilar response in impedance with frequency of the materials in the multicomponent system. The span of each object's impedance should be wide enough for the technique to be successful.

Impedance is a measure of an object's response to a sinusoidal AC i.e. the change in amplitude and phase of an output signal relative to an initial input signal. It is comprised of dimensional vectorial functions denoted by the expression:

$$Z = R + jX, \quad (5.2)$$

where R is the static resistance and X is the reactance which varies with frequency, whilst the inclusion of the imaginary term, j , produces a composite impedance. For materials that exhibit dielectric properties, when $X < 0$, X becomes a capacitive reactance.

Generally, as the frequency of a sinusoidal AC through the dielectric is varied, the impedance to electrical charge comes about due to the alteration of molecular charges in the dielectric from their equilibrium positions by migration or orientation of permanent dipoles (Macdonald, 1991).

For conductors when $X > 0$, X becomes an inductive reactance and the impedance of the conductor becomes the sum of the static resistance and inductive reactance. The flow of an AC through a conductor is seldom uniform, due to skin and proximity effects. By increasing the frequency of the AC through the conductor, electrical charges saturate on its outer surface increasing the current per unit area and producing a measurable voltage on the conductor's surface as is illustrated in Figure 5.5 (a). This behaviour is known as skin effect (Gilberd, 1982).

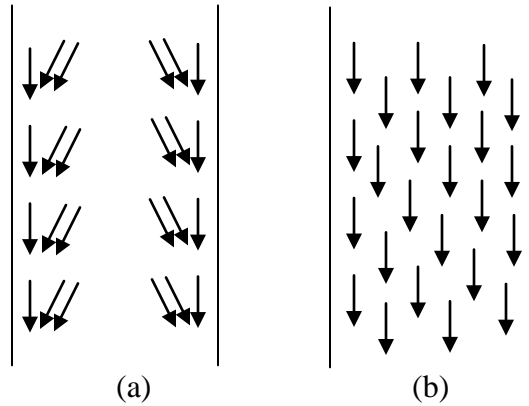


Figure 5.5. (a) Flow of charge on the surface of conductor due to self inductance

(b) Flow of charge across the entire cross section of a conductor

By decreasing the frequency of the *AC*, this behaviour relapses and the *AC* flows somewhat in a single direction across the cross-sectional area of the conductor (Figure 5.5b). The relationship between skin effect and frequency governs *ERT* spectroscopy in conductors. By placing a conductor into an ionic solution in *ERT* and varying the frequency at a fixed current, the impedance of the conductor changes and is represented as a change in conductivity. By phasing out the conductor, a third phase can be introduced and observed without significant interference by the conductor.

5.2.4. Conclusions from literature review

From the literature review, it is clear that there are techniques available for single and two phase characterisation; however multiphase characterisation requires either dual energy diagnosis of the region of interest by a single technique or by the coupling of independent techniques to observe individual phases. It has been shown that *GLS* characterisation has primarily been limited to bubble columns and trickle beds with little or no special emphasis placed on agitated systems.

ERT spectroscopy was applied to an agitated *GLS* system especially with conducting solids. This study extends the capability of *ERT* by manipulating the properties specific to *ERT* deployment in two phase systems and manoeuvring it to diagnosing three phase systems. The study also extends the list of possible techniques that can be used to characterise three phase systems.

5.3. Materials and methods

Two types of *ERT* sensors were used in this study. One was a linear *ERT* probe (Figure 5.6) whilst the other was a circular array *ERT* vessel (Figure 5.7). Both sensors were connected to p2000 Data Acquisition System (*DAS*) hardware (Industrial Tomography Systems, Manchester, UK).



Figure 5.6. Linear *ERT* probe with electrode arrangements



Figure 5.7. An overview of the external and internal electrode arrangements of the circular array *ERT* vessel

The circular array *ERT* vessel was used for studies involving vertical static phantoms and typically only one of the horizontal planes was used for demonstration and verification of the frequency

dependent effective resistance and the self-inducting capabilities of the material used. The schematic of the *ERT* setup is shown in Figure 5.8.

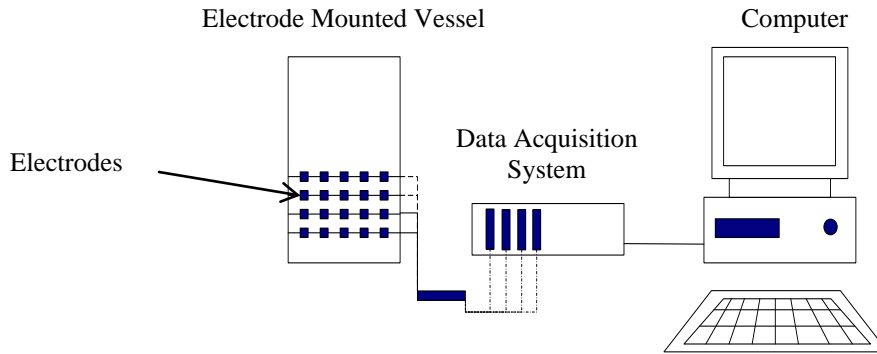


Figure 5.8. Schematic of *ERT* with the circular array *ERT* vessel

The conducting solution was nickel nitrate solution with a concentration of 27 g L^{-1} and conductivity of $\sim 1.07 \text{ mS cm}^{-1}$. The phantom was a hollow stainless steel rod of length 0.290 m with inner and outer diameters of 0.0250 m and 0.0350 m respectively. It was immersed central to the vessel in the conducting liquid phase as the heterogeneous conducting phase.

Plumes of air bubbles at an aeration rate (Q) of $0.83 \times 10^{-4} \text{ m}^3 \text{ s}^{-1}$ i.e. 2 volume per volume per minute (*vvm*). Air was delivered below the measurement plane by a rubber pipe located central to the vessel.

The circular array *ERT* vessel was unbaffled with a diameter (T) of 0.15 m. It incorporated 4 planes of 16 equally spaced electrodes on the vessel wall as shown in Figure 5.7 and is also described by Edwards *et al.* (2009). The sensors operate by injecting AC between sequential pairs of adjacent electrodes at a selected frequency.

After each injection, the voltage difference between adjacent pairs of non-injecting electrodes is obtained from the relative change in voltage across the vessel.

In this study a total of six frequencies were investigated: 9.6, 4.8, 2.4, 1.2, 0.6 and 0.3 kHz at a single injection current of 0.6 mA. Initial reference measurements of an undisturbed system are points of reference for comparison with a disturbed system.

The linear *ERT* probe had 16 equally spaced and vertically aligned electrodes, described previously by Bolton *et al.* (2002), Ricard *et al.* (2005) and Simmons *et al.* (2009). The probes provided axial tomogram images, axial conductivity measurements and mean axial relative conductivity measurements of the region of analysis, whilst the circular array *ERT* vessel provided radial or slice tomogram images, mean radial relative conductivity measurements and radial conductivity measurements of its region of analysis.

The linear probe was placed adjacent to the vessel wall, beside a baffle (in the direction of impeller rotation) and turned to face towards the impeller shaft in a separate Perspex vessel of $T = 0.14$ m. It was equipped with 4 equally spaced baffles of width, $B = T/10$, a ringed sparger of diameter 0.04 m with 0.5×10^{-3} m diameter orifices.

A Rushton disc turbine (*RDT*), as shown in Figure 5.9, with an impeller diameter to vessel diameter ratio (D/T) of $\sim 3/7$ was positioned at an impeller clearance to tank diameter ratio (C/T) of $\sim 4/14$ from the vessel base. The *RDT* was located below the last electrode plane close to the vessel bottom.

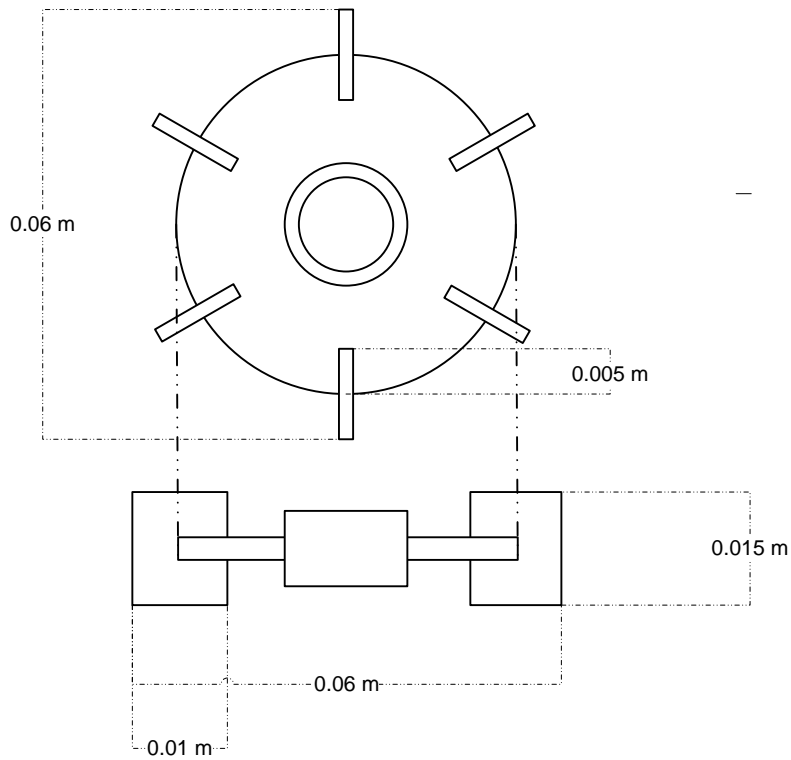


Figure 5.9. Rushton disc turbine (*RDT*)

Nickel nitrate solution of volume $2.6 \times 10^{-3} \text{ m}^3$, concentration of 27 g L^{-1} and conductivity of 1.07 mS cm^{-1} was also used as the conducting medium. The liquid height, $H = 0.17 \text{ m}$. The temperature of the solution was $\sim 25^\circ\text{C}$. Approximately 6 g of the stainless steel particles for every 100 g of the

slurry (6 % w/w) with a nominal size of 250 μm and density (ρ) of 7800 kg m^{-3} was agitated in the vessel with a variable speed motor (Eurostar power control-visc, IKA Germany).

Air was delivered at the same Q of $0.83 \times 10^{-4} \text{ m}^3 \text{ s}^{-1}$ (2 *vvm*). The just suspended impeller speed (N_{js}) that was found suitable to ensure that particles did not remain on the bottom of the vessel for more than one second to two seconds (Zwietering,1958) in the absence of the gas was $\sim 13.3 \text{ s}^{-1}$ which equates to an impeller Reynolds number of ~ 55280 . This was ascertained by observing the vessel bottom. The impeller speed (N) was also found suitable to disperse the gas beyond the incipient complete recirculation point. A schematic of the linear *ERT* probe's setup is shown in Figure 5.10.

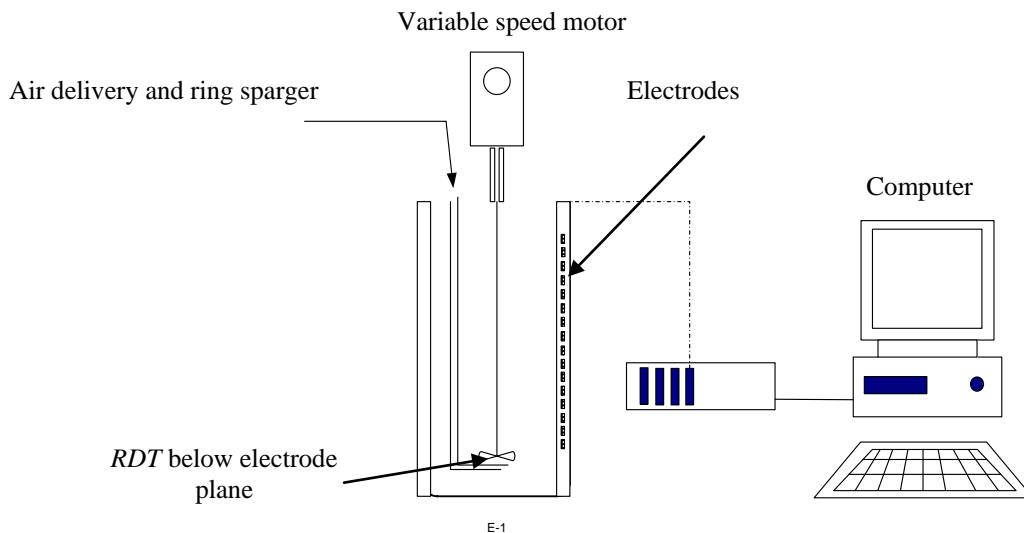


Figure 5.10. Schematic of the linear *ERT* probe arrangement

Three sets of studies were carried out with the linear *ERT* probe. Two of the studies were analogous to those carried out in the circular array *ERT* vessel with the stainless steel rod and gas plume i.e. individual *S-L* and *G-L* agitation experiments were investigated to verify the findings from the

experiments with the static phantom and plume of gas. Then a *GLS* study was carried out to apply the findings i.e. to isolate the gas phase from the solid allowing for measurements of the gas phase to be made without significant interference by the solid and vice versa. Three gas flow regimes were investigated. The operating conditions are shown in Table 5.1.

Table 5.1. *GLS* study operating conditions.

N (s^{-1})	Flg	Fr
13.3	0.029	1.08
10	0.0386	0.7
6.7	0.058	0.27

While the linear *ERT* probe is cited as providing a projected plane tomogram from the line of the probe (Bolton *et al.* 2002), the tomogram information was only used for qualitative analysis of the primary information obtained from the mean conductivity data. The mean conductivity inferred the vertical material distribution in the vessel; rather than the horizontal distribution as obtained with the circular array *ERT*. Conductivity readings were obtained by averaging the spatial conductivity of multiple tomograms. The reconstruction of these tomograms is based on the conventional LBP algorithm which has some uncertainties in regions further away from the probe. The range of frequencies and the injection current used with the linear *ERT* probe were the same to those used for the circular array *ERT* vessel.

5.3.1. Limitations of the technique

A few limitations to the technique were noted during development. At the outset, a limiting aqueous phase conductivity of 0.54 mS cm^{-1} was identified. Below this value, stainless steel was observed in the solution by all frequencies. Also, $\sim 6 \%$ w/w solids concentration was used at 0.3 kHz. Above

this concentration, the conductivity of the stainless steel particles increased and interfered with measurements. At the given operating configurations, as the period of operation increased, the temperature of the system increased due to turbulent energy dissipation as heat. This increased the conductivity readings.

In Figure 5.11 plots of increasing conductivity and temperature of the nickel nitrate solution due to agitation over a period of 30 minutes is shown. The conductivities were recorded against a baseline of 1 mS cm^{-1} on *ERT*. A $1 \text{ }^\circ\text{C}$ increase in temperature led to a $\sim 0.3 \text{ mS cm}^{-1}$ increase in conductivity, thus upon use the temperature should be measured and compensated in the conductivity readings.

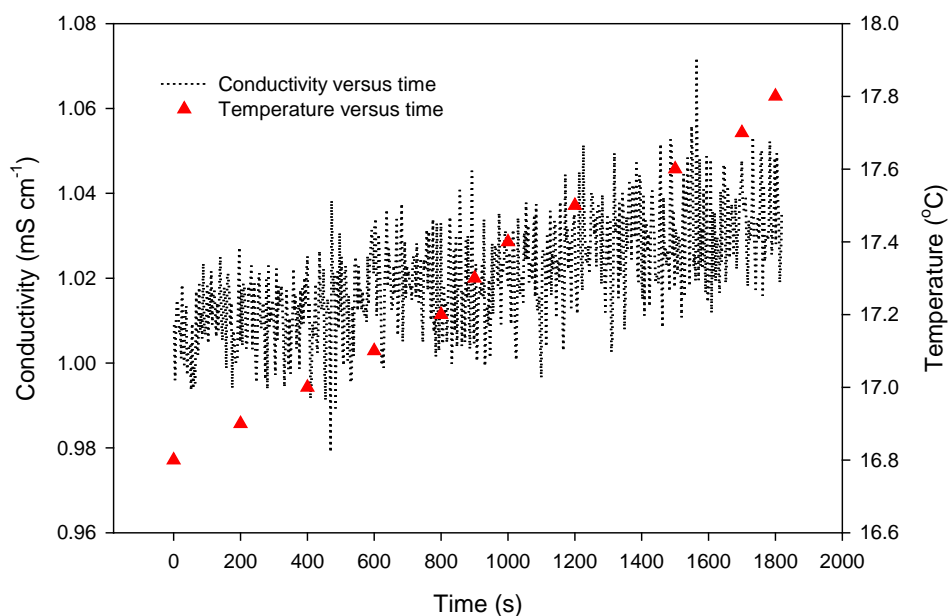


Figure 5.11. The effects of agitation on the conductivity and temperature of nickel nitrate solution

5.4. Results and discussion

5.4.1. The effects of frequency on the conductivity of the phantom and plume of air in nickel nitrate solution and the circular array ERT vessel.

In Figure 5.12, the effects of altering the frequency on the conductivity of the stainless steel phantom in the nickel nitrate solution and circular array *ERT* vessel are shown. The colour scale of blue–green–yellow–red in the tomogram allocates and expresses the conductivity intensity within the vessel. The red and yellow regions are the high conductivity regions whilst the green and blue are the low conductivity regions.

As the frequency was decreased from 9.6 kHz to 0.3 kHz, the colour of the phantom in the tomogram changed from red to green, which meant that the conductivity decreased. Between 9.6 kHz to 1.2 kHz a slight decrease in conductivity took place but was not clear from the tomograms.

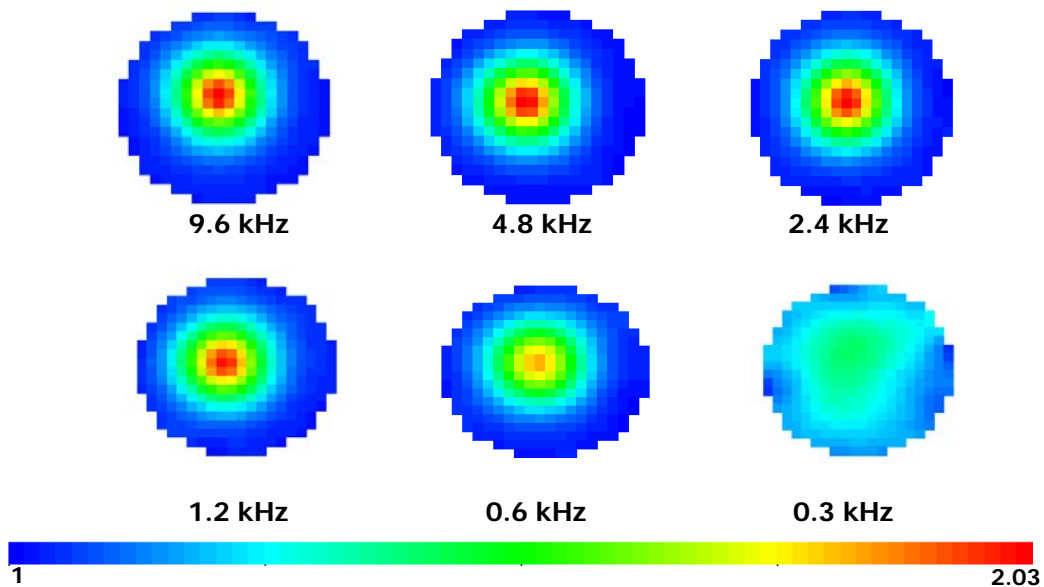


Figure 5.12. The effects of changing frequency on self inductance of the stainless steel phantom

In Figure 5.13, the planar conductivities of the tomograms are quantified and clearly show the dissimilarities between all frequencies. From the frequency of 0.6 kHz to 0.3 kHz the conductivity dropped considerably from a shade of yellow to green.

The blue regions are the reference conductivity of solution. This departure to green indicated that conductivity intensity reduced to values close to that of the liquid phase. From all the frequencies used, 0.3 kHz clearly produced the weakest image.

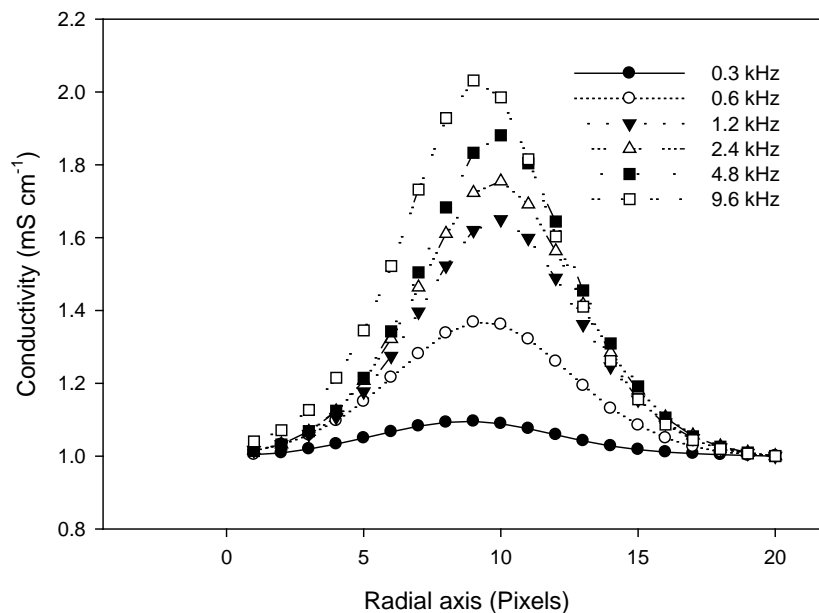


Figure 5.13. Relative change in conductivity across the plane of the tomogram

Figure 5.14 shows the change in mean axial conductivity of the stainless steel phantom and plumes of air with frequency. The faint distribution is the anticipated profile with frequency.

Each data point had an error of $\sim \pm 0.005\%$ which is very low since the system was practically undisturbed. As previously demonstrated, by decreasing the frequency, the mean conductivity of the

phantom decreased by ~ 90 %, however as anticipated there was no change in the conductivity of the plumes of air because air is a poor electrical conductor.

A gradual reduction in conductivity is further clearly observed between 9.6 kHz to 1.2 kHz before a sudden decrease from 0.6 kHz to 0.3 kHz, wherein the conductivity approached the reference conductivity. Frequencies below 0.3 kHz caused considerable noise which produced erroneous results. This took place because at low frequencies the noise spectral density increased since the power spectral density at low frequencies is inversely proportional to frequency. This makes the voltage noise spectral density inversely proportional to the square root of the frequency. The noise observed is referred to as 1/f noise (Walter, 2002).

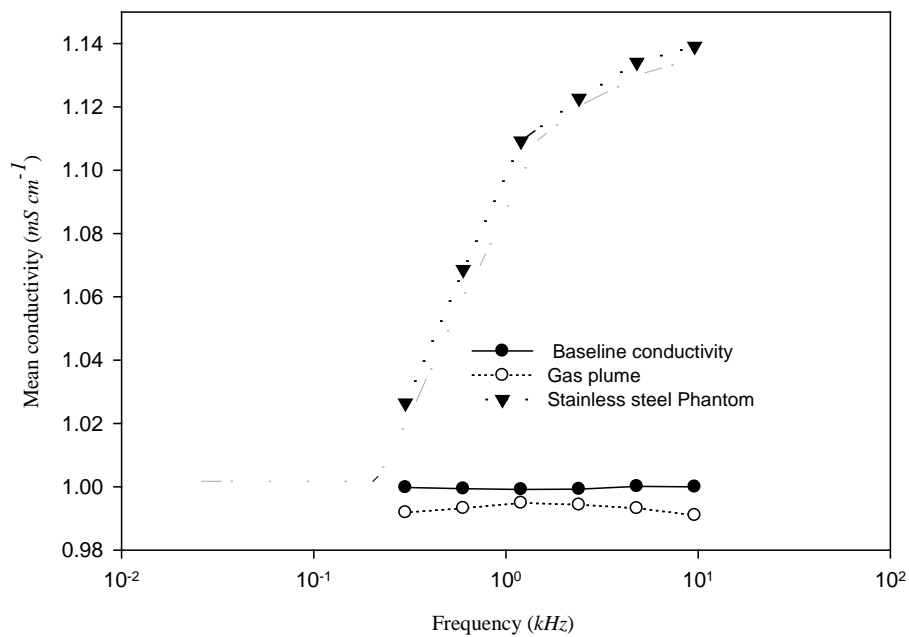


Figure 5.14. The effects of frequency on the mean conductivity of stainless steel phantom and air in nickel nitrate solution

When the frequency was increased, the conductivity of the phantom increased due to the skin effect phenomenon. As the frequency through a conductor increases, self-inductance takes place, causing an increase in the effective resistance on the conductor's surface. This increases the resistance to the flow of current and thus increases the current per unit area over the conductor's surface leading to the detection of a measurable voltage by *ERT*.

As the frequency was decreased, this phenomenon relapsed and the *AC* flowed in a manner analogous to a *DC*, thereby decreasing the current per unit area on the conductor's surface. The validation with the phantom and circular array *ERT* vessel set a platform for work to be carried out on agitated *S-L* and *G-L* systems in a stirred vessel equipped with a linear *ERT* probe.

5.4.2. Study of the effects of frequency on the conductivity of agitated S-L and G-L systems with a linear ERT probe

In Figure 5.15 the mean axial conductivity of agitated *S-L* (stainless steel in nickel nitrate solution) and *G-L* (air in nickel nitrate solution) systems are shown. Each data point had a maximum error of $\sim \pm 5\%$ due to noise during agitation.

As the frequency was decreased from 9.6 kHz to 0.3 kHz, the conductivity distributions for the agitated *S-L* and *G-L* systems were similar to the distributions observed in the phantom experiments.

In the *G-L* system, when the frequency was changed, the conductivity of air remained constant whilst in the *S-L* system, a gradual variation in conductivity was observed between 9.6 kHz and 1.2 kHz before the steep drop in conductivity between 0.6 kHz to 0.3 kHz.

These similarities demonstrated that the same electric principles in the circular array *ERT* vessel applied to the linear *ERT* probe and should apply to any other electrode arrangements. Below 0.3 kHz, considerable noise was observed due to the reasons that were previously given with the static phantoms.

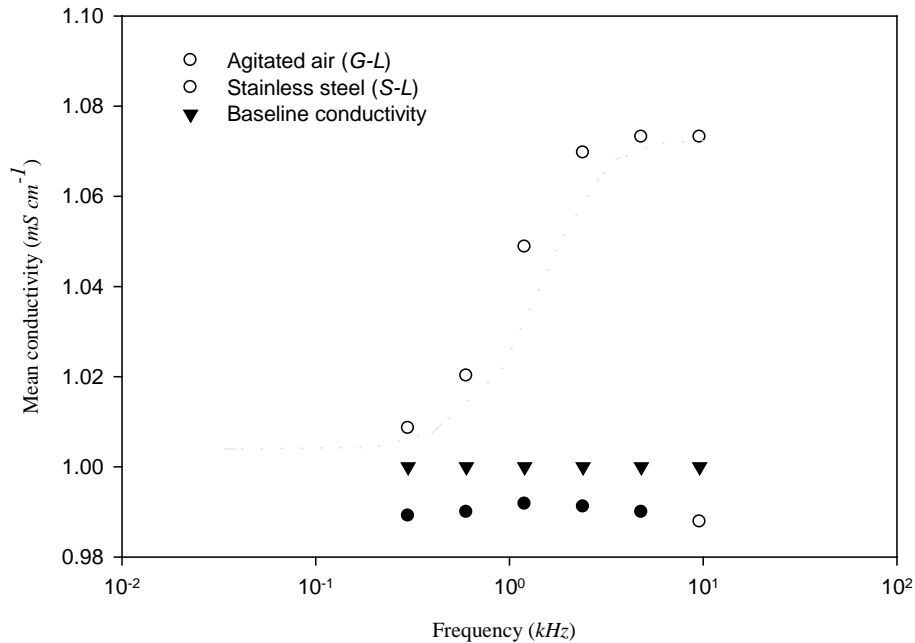


Figure 5.15. The effects of frequency on the mean conductivity of dispersed stainless steel particles (*S-L*) and air (*G-L*) system

Similar explanations to the phantom verification experiments thus apply to the agitated systems. As the frequency increased, the self-inductance on the surface of each individual particle in the slurry took place, leading to an increase in their effective resistance and current per unit area on each particle's surface.

Collectively the self-inducting particles produced a measurable voltage that could be detected by *ERT*. As the injection frequency was decreased the phenomenon reversed.

An important observation from the results is that self-inductance may be particle size independent but bulk measurements depend on the slurry concentration.

The study of an agitated *GLS* system that comprised of the stainless steel particles, air and the nickel nitrate solution was thus carried out with the frequency of 0.3 kHz; because it best isolated the gas phase from the *S-L* mixture and a frequency of 9.6 kHz because it produced the highest measurable voltage in the presence of solids. This was done to observe the response and demonstrate phase discrimination using *ERT* in the *GLS* system.

5.4.3. Agitated GLS system characterised at 9.6 kHz and 0.3 kHz with the linear ERT probe

Three gas flow regimes were specifically chosen for the study of solids and gas behaviour in the *GLS* system with the linear *ERT* probe. These flow regimes are shown in the gas flow regime map in Figure 5.16. The gas flow regimes resided within the completely recirculated regime, just above the complete and the limited recirculation boundary and within the limited recirculation region. At these regimes, the solids had been previously observed to be fully dispersed, poorly dispersed and sedimented respectively.

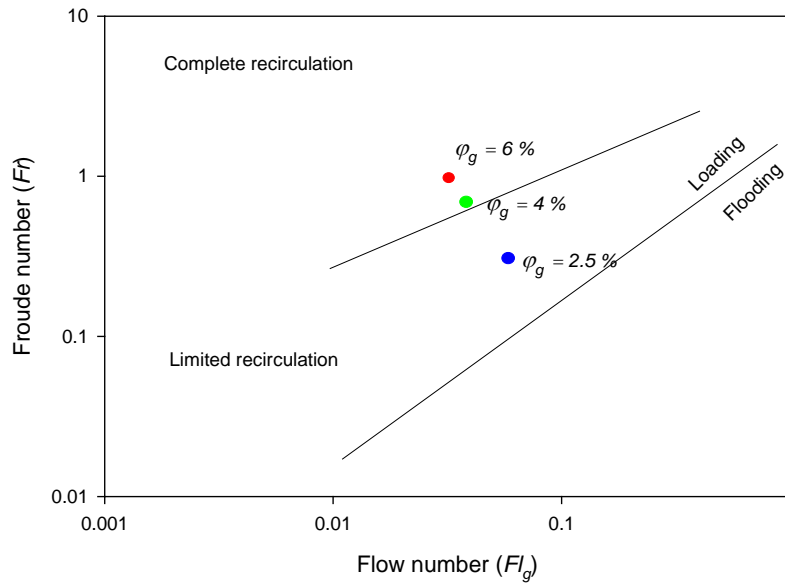


Figure 5.16. Gas flow regime map for the Rushton turbine (Harnby *et al.*, 1992)

In Figure 5.17 the change in mean axial conductivity of the agitated *GLS* system at the frequencies of 0.3 kHz and 9.6 kHz are shown. The linear *ERT* probe was used and each data point had a maximum error of $\sim \pm 5\%$. In region ‘a’ the solution alone was agitated, which led to the flat conductivity distribution observed at both frequencies.

Air ingress was also observed. In region ‘b’, the stainless steel particles were fed into the agitated solution and dispersed. At 9.6 kHz, the mean conductivity increased to $\sim 1.09 \text{ mS cm}^{-1}$, whilst a lower value of $\sim 1.01 \text{ mS cm}^{-1}$ was observed at 0.3 kHz.

As expected, the conductivity at 0.3 kHz was $\sim 10\%$ more than the baseline conductivity since the presence of the solids was still partially detectable at this frequency. This offset henceforth will be used as a point of reference for ease of analysis.

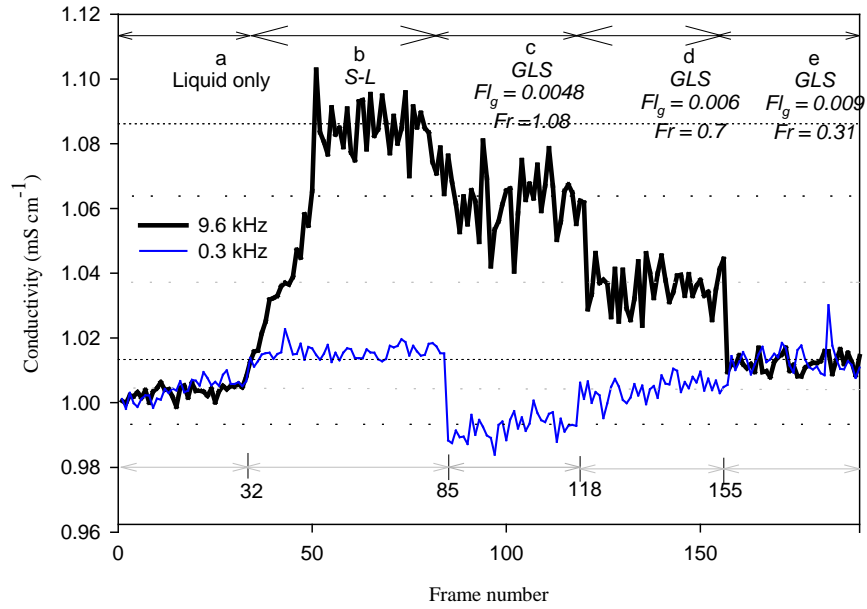


Figure 5.17. Mean conductivity plot of the *GLS* system characterised at 9.6 kHz and 0.3 kHz.

The image of the vessel and solids distribution is shown in Figure 5.18. Axial and radial concentration gradients of solids were observed, with the regions of highest solids holdup around the impeller periphery and the vessel bottom. This was expected, since operating at N_{js} does not guarantee a uniform concentration of solids throughout the vessel.

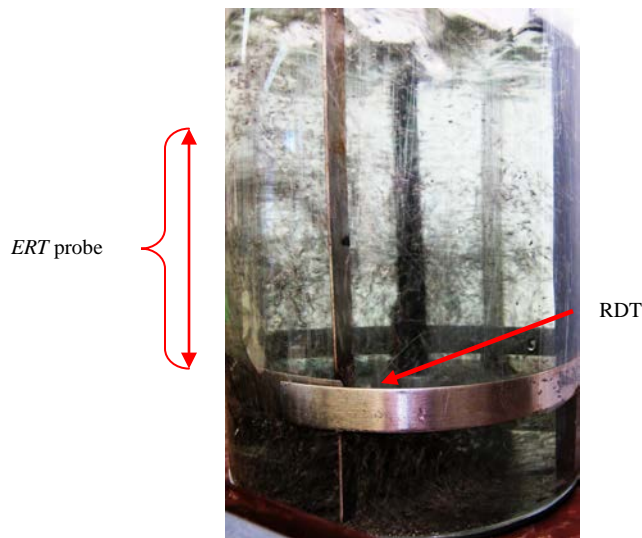


Figure 5.18. Image of *S-L* mixing

These visual results were also observable in axial conductivity profiles taken at 9.6 kHz and 0.3 kHz in Figure 5.19. In this graph and consequent axial conductivity graphs, the conductivity profile is represented as the mean conductivity plus or minus the maximum and minimum conductivity readings. The conductivity profile for liquid mixing alone (region a) at both frequencies is also given in Figure 5.19 for comparison. The conductivity oscillated between 1.01 mS cm^{-1} and 1.02 mS cm^{-1} at 0.3 kHz due to the offset previously explained; whilst at 9.6 kHz a higher conductivity range between 1.08 mS cm^{-1} and 1.09 mS cm^{-1} was observed.

The offset in the *S-L* distribution at 0.3 kHz was normalised by subtracting the value per plane from the liquid mixing distribution and then deducting the difference from similar planes in all gas flow regime readings at 0.3 kHz as is shown in Figure 5.20 (i) and latter readings. Figure 5.20 (ii) is a dimensionless distribution of the data. The dimensionless distribution was obtained by selecting the highest *S-L* conductivity, subtracting unity from the actual and maximum conductivity and then dividing both values.

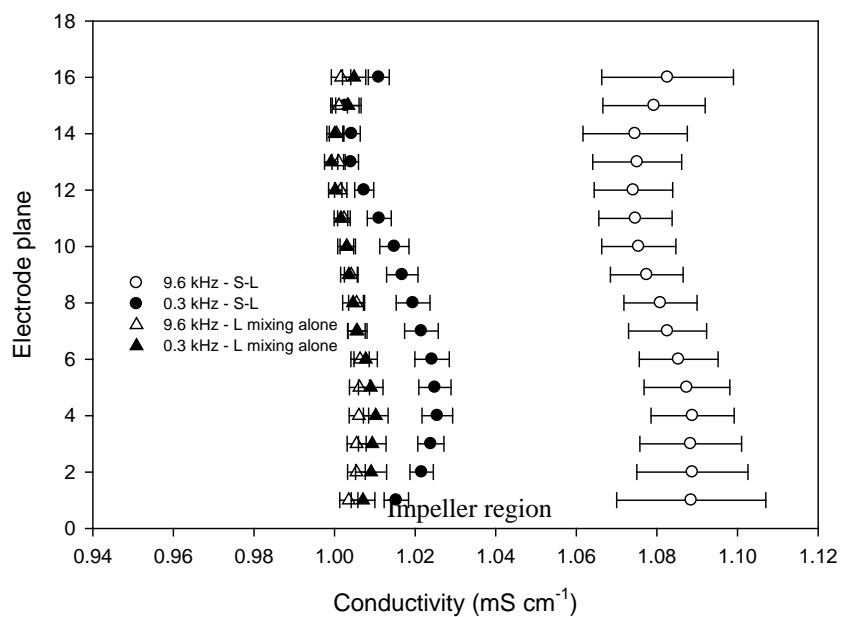
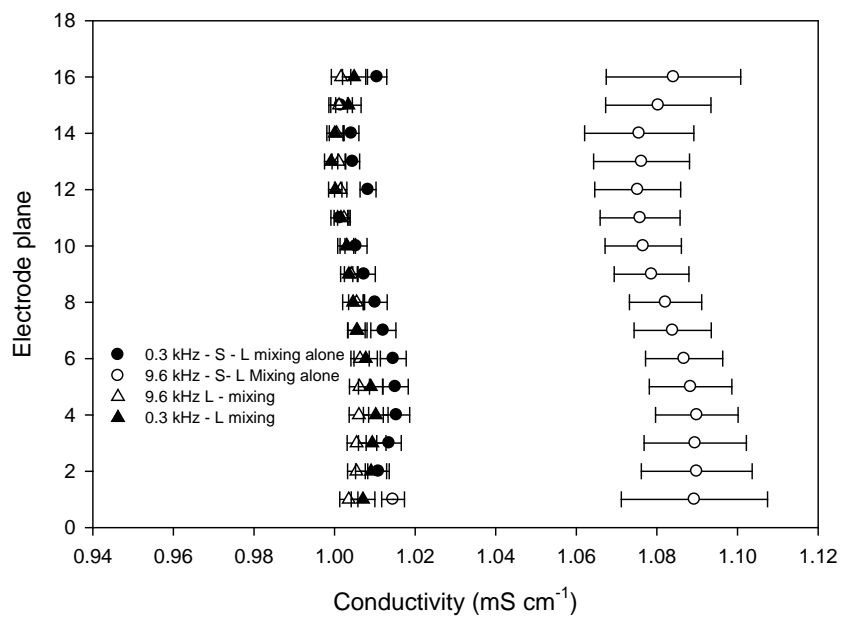
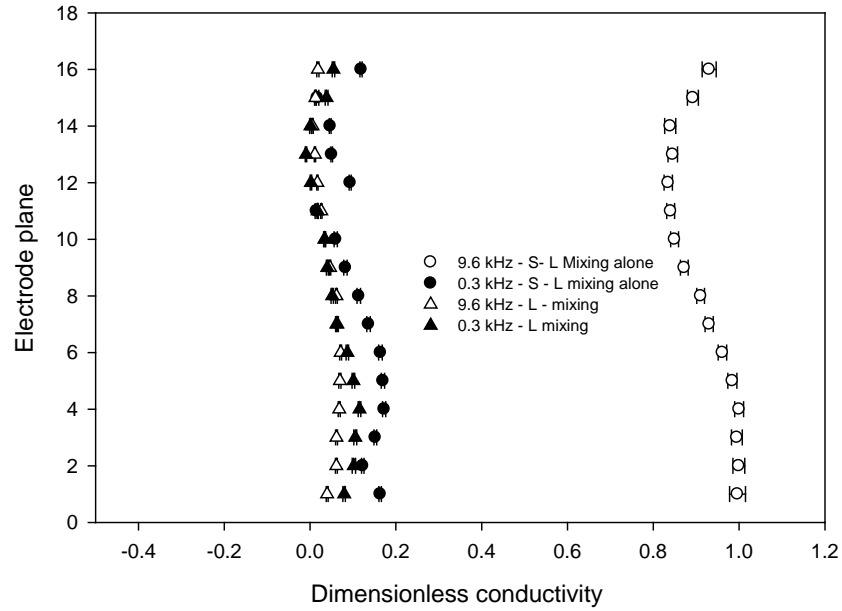


Figure 5.19. Conductivity profile for *S-L* mixing



(i)



(ii)

Figure 5.20. (i) Normalised conductivity and (ii) Dimensionless conductivity

for *S-L* mixing

Selected corresponding tomograms at 9.6 kHz and 0.3 kHz are shown in Figure 5.21 and Figure 5.22 respectively. These images are based on a conventional LBP algorithm which has some uncertainties in regions further away from the probe. In Figure 5.21 the red region is indicative of the maximum conductivity of $\sim 1.09 \text{ mS cm}^{-1}$ in the vessel bottom at 9.6 kHz, however at 0.3 kHz and the lower colour scales, such a value is not evident (Figure 5.22).

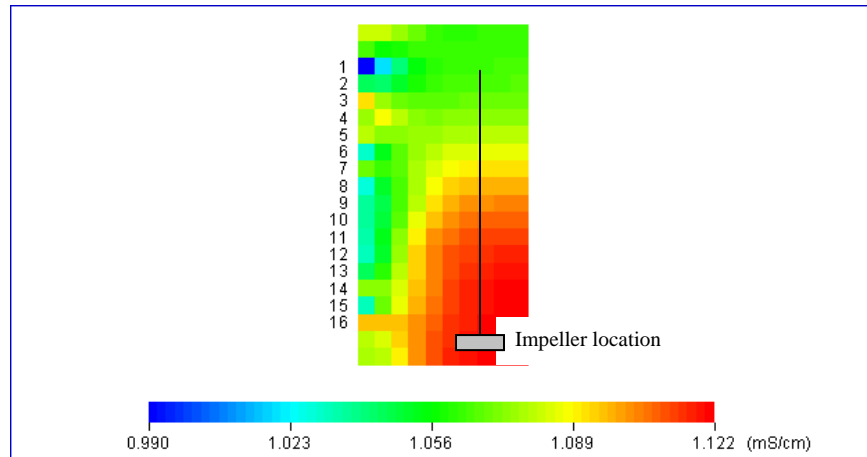


Figure 5.21. Tomogram of solids distribution in the vessel at 9.6 kHz

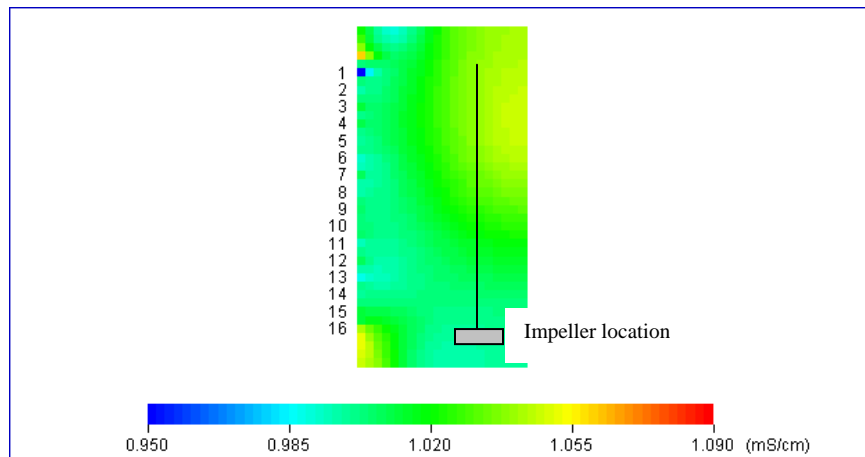


Figure 5.22. Tomogram of solids distribution in the vessel at 0.3 kHz

In region ‘c’ of the mean axial conductivity in Figure 5.17, air was introduced into the system. The aeration number (Fl_g), expressed as $\frac{Q}{ND^3}$, was ~ 0.029 , the Froude number (F_r), denoted as $\frac{N^2 D}{g_r}$, was 1.089 and φ_g was $\sim 6\%$ of the blend volume. Where N was 13.3 s^{-1} whilst Q was kept constant at $0.83 \times 10^{-4} \text{ m}^3 \text{ s}^{-1}$ (2 vvm). Fl_g versus F_r resided above the completely recirculated (N_R) boundary (Figure 5.16), which had previously been established by visual observation.

ϕ_g was estimated by the dynamic disengagement method (Chapman *et al.*,1983). Gas injection reduced the conductivity in region ‘c’ by $\sim 2.5\%$ at 9.6 kHz to $\sim 1.064\text{ mS cm}^{-1}$ and the conductivity at 0.3 kHz reduced by $\sim 4.3\%$ to 0.995 mS cm^{-1} . The image of the vessel is shown in Figure 5.23. Solids sedimented on the vessel bottom, since the gas acted like an inertial sink, reducing turbulent forces required for solids suspension. The highest region of ϕ_g was also observed around the impeller periphery.

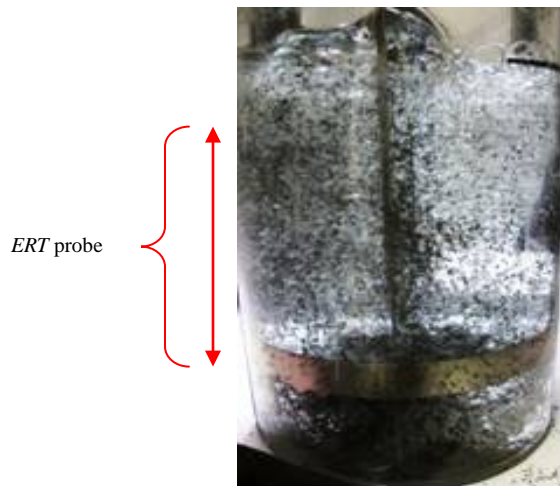


Figure 5.23. Image of GLS mixing in region ‘c’ for $Fl_g \approx 0.029$ and $Fr \approx 1.08$

The visual observations were reflected in axial conductivity distributions shown in Figure 5.24. The difference in conductivity between both frequencies is obvious and reduced by $\sim 2.1\%$ in region ‘c’ compared to ‘b’. This shows that the change in solids holdup is reflected by the electrical readings. The conductivity at the electrodes close to the impeller periphery and vessel bottom at both frequencies is much lower than the upper electrodes, postulating that ϕ_g was higher, as previously observed in the image.

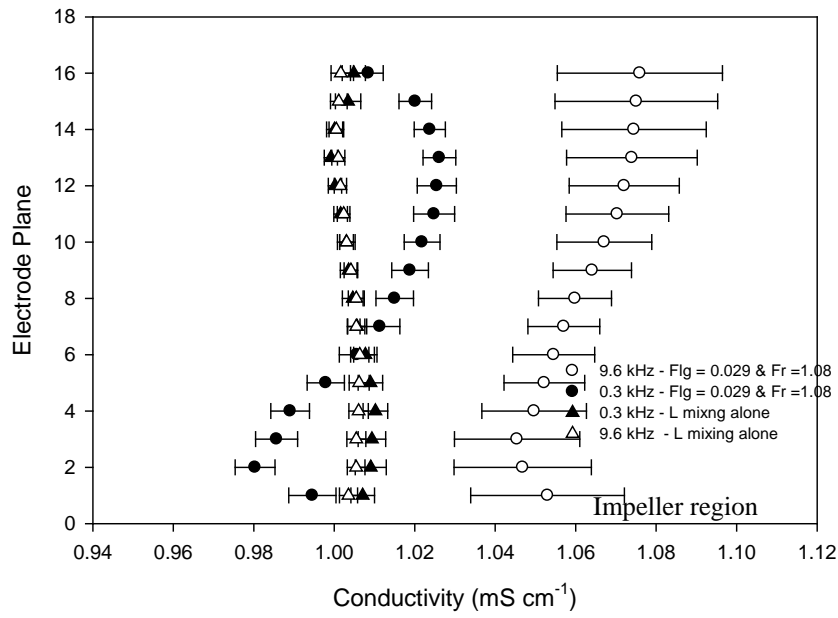
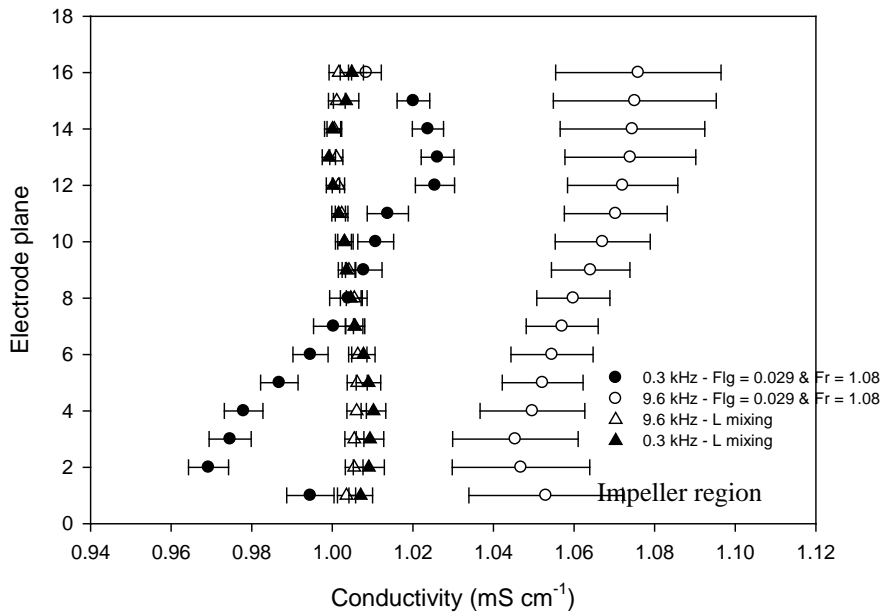


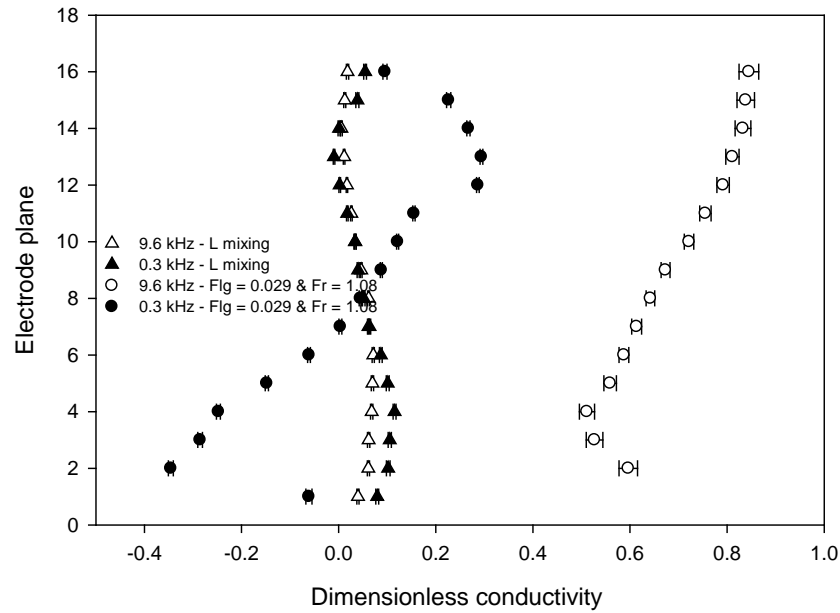
Figure 5.24. Conductivity profile for *GLS* mixing in region ‘c’ for

$$Fl_g \approx 0.029 \text{ and } Fr \approx 1.08$$

The normalised and dimensionless distribution for $Fl_g \approx 0.029$ and $Fr \approx 1.08$ at 9.6 kHz and 0.3 kHz are shown in Figure 5.25 (i) and (ii)



(i)



(ii)

Figure 5.25. (i) Normalised conductivity and (ii) Dimensionless conductivity

for $Fl_g \approx 0.029$ and $Fr \approx 1.08$

In the selected tomograms in Figure 5.26 and Figure 5.27, the region of high ϕ_g , depicted by the blue region, was observed at the lower electrodes. The gas stream splits at the vessel wall, creating tangential fields towards the vessel bottom and top, creating a circulation loop.

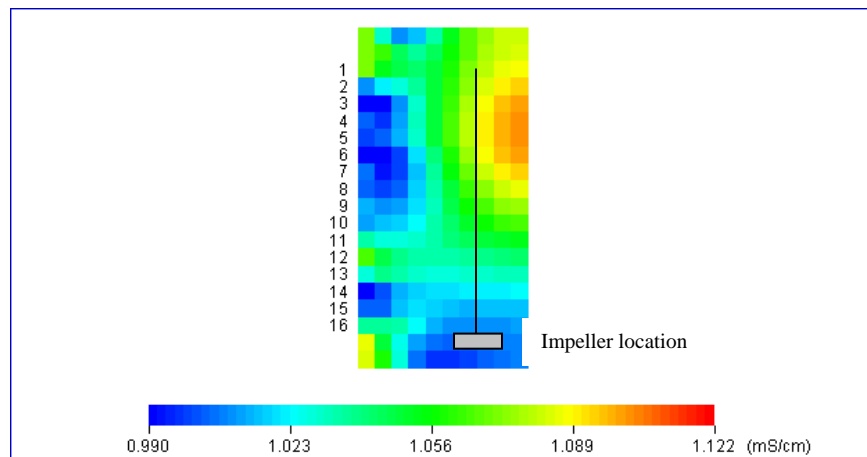


Figure 5.26. Tomograms of gas and solids distribution in region 'c' at $Fl_g \approx 0.029$

and $Fr \approx 1.08$ at 9.6 kHz

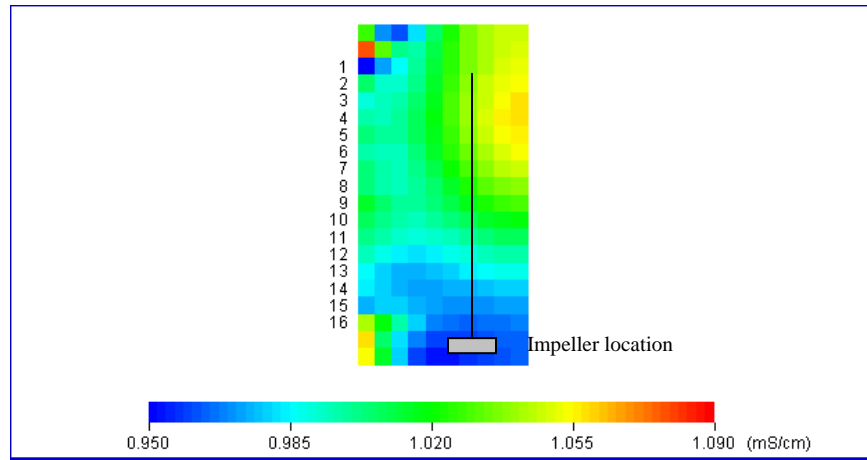


Figure 5.27. Tomograms of gas and solids distribution in region 'c' at $Fl_g \approx 0.029$

and $Fr \approx 1.08$ at 0.3 kHz

In region 'd', N was reduced by $\sim 25\%$ to 10 s^{-1} . Fl_g and Fr fell to ≈ 0.0386 and 0.7 respectively whilst N_R resided just above the complete and limited circulation boundary (Figure 5.16). φ_g decreased to $\sim 4\%$ of the blend volume, whilst the conductivity in region 'd' relative to region 'b' reduced by $\sim 6\%$ at 9.6 kHz to $\sim 1.038\text{ mS cm}^{-1}$ and the conductivity at 0.3 kHz increased by $\sim 2.3\%$ to 1.005 mS cm^{-1} . The image of the vessel is shown in Figure 5.28. Most of the solids were observed to have sedimented on the vessel bottom, whilst the gas discharge velocity from the impeller periphery decreased.

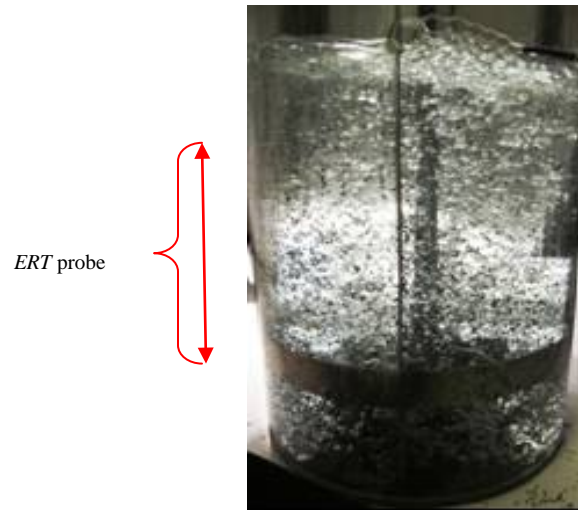


Figure 5.28. Image of *GLS* system in region 'd' at $Fl_g \approx 0.0386$ and $Fr \approx 0.7$

The visual observation is reproduced by axial conductivity distributions in Figure 5.29. The difference in conductivity between both frequencies is still obvious and reduced by $\sim 6.8\%$ in region 'd' compared to region 'b'.

This supports the observation of considerable solid sedimentation in Figure 5.28. The conductivity at the lower electrodes was still much lower than the upper region, postulating that φ_g was still higher around the impeller periphery.

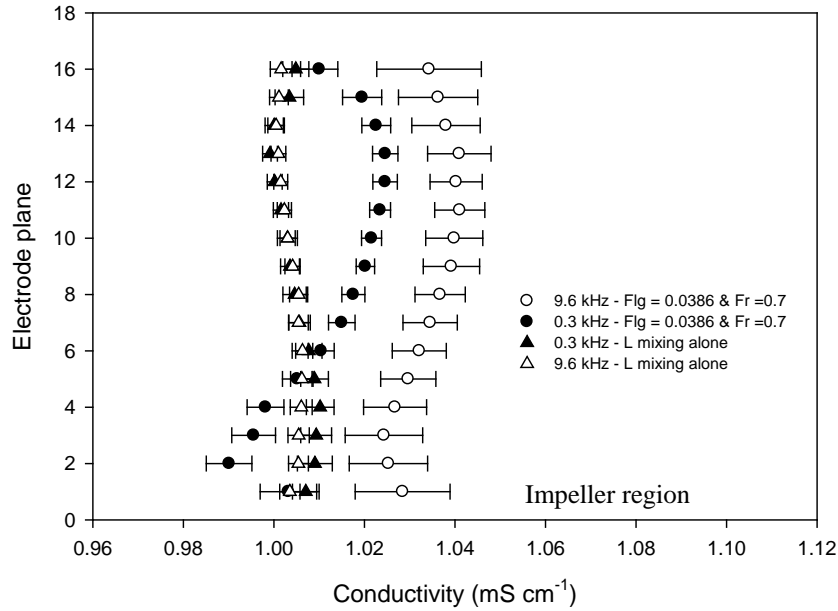
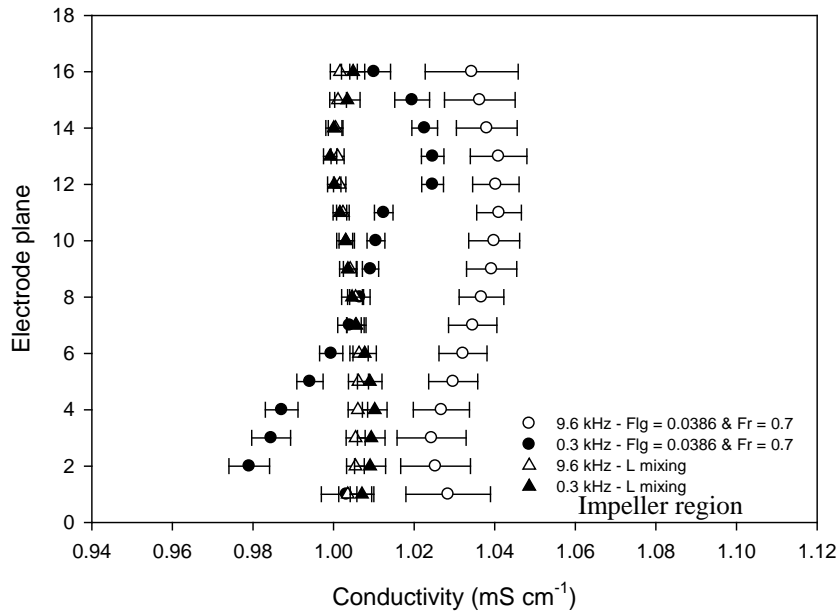


Figure 5.29. Conductivity profile for *GLS* mixing in region ‘d’ at $Fl_g \approx 0.0386$ and $Fr \approx 0.7$

At 0.3 kHz, the conductivity clearly increased from the minimum of 0.98 mS cm^{-1} in region ‘c’ to 0.99 mS cm^{-1} and decreased from 1.044 mS cm^{-1} to 1.02 mS cm^{-1} at 9.6 kHz. The normalised and dimensionless distribution for $Fl_g \approx 0.0386$ and $Fr \approx 0.7$ at 9.6 kHz and 0.3 kHz are given in Figure 5.30 (i) and (ii).



(i)

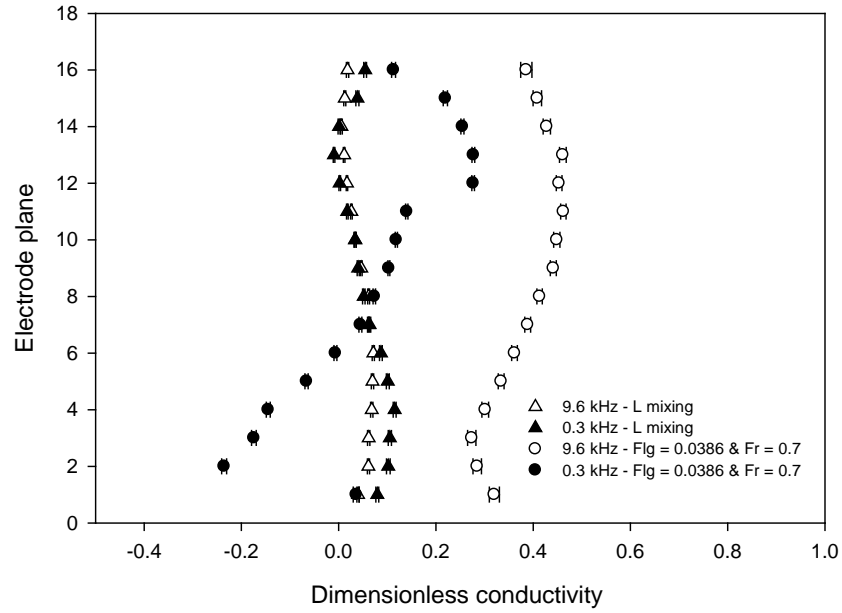


Figure 5.30. (i) Normalised conductivity and (ii) Dimensionless conductivity
for $Fl_g \approx 0.0386$ and $Fr \approx 0.7$

The selected tomograms in Figure 5.31 and Figure 5.32 show that the tangential gas streams towards the vessel wall were not as intense, as depicted by the fading blue region.

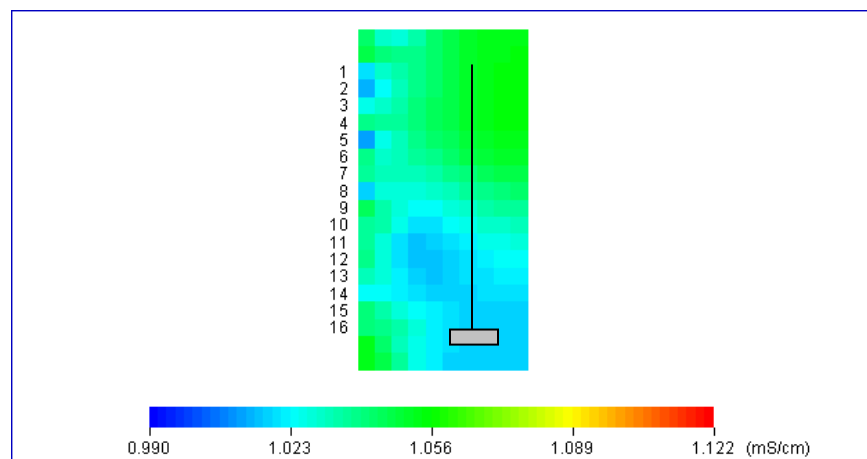


Figure 5.31. Tomograms of gas and solids distribution in region 'd' at $Fl_g \approx 0.0386$
and $Fr \approx 0.7$ at 9.6 kHz

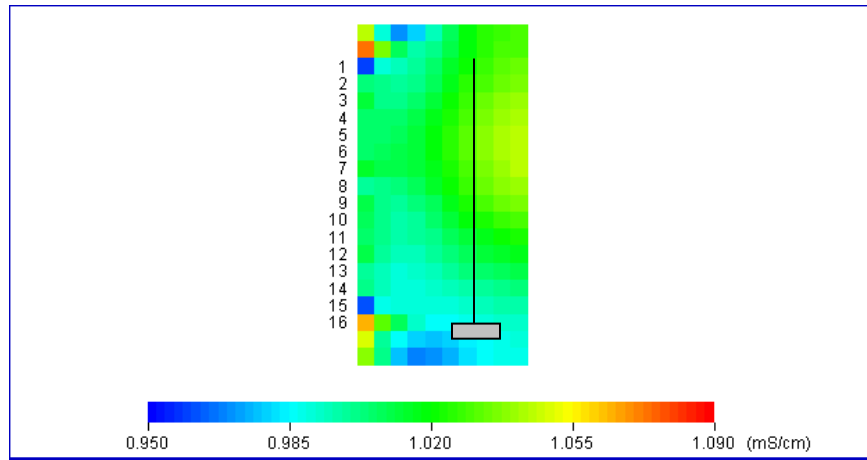


Figure 5.32. Tomograms of gas and solids distribution in region 'd' at $Fl_g \approx 0.0386$
and $Fr \approx 0.7$ at 0.3 kHz

Finally, in region 'e' of Figure 5.17, N was reduced by $\sim 50\%$ to 6.7 s^{-1} . Fr fell to ≈ 0.058 and 0.31 respectively and gas dispersion fell within the limited recirculation regime (N_{cd}), Figure 5.16. φ_g was $\sim 2.5\%$ of the blend volume. The conductivity at 9.6 kHz and 0.3 kHz reduced by 84% and 43% relative to region 'b' and intersected to the original value of 1.01 mS cm^{-1} . From the vessel image shown in Figure 5.33, all solids had completely sedimented as the gas discharge intensity from the impeller periphery decreased.

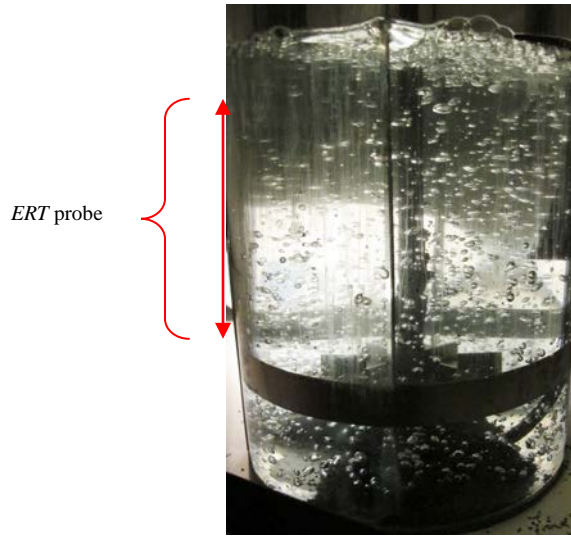


Figure 5.33. Image of *GLS* system in region ‘e’ at $Fl_g \approx 0.058$ and $Fr \approx 0.31$

The axial conductivity distributions are also shown in Figure 5.34. The conductivity distributions intersected. The conductivity at the lower electrodes was still lower than the upper electrodes, indicating high φ_g .

At 0.3 kHz, it increased from the minimum of 0.99 mS cm^{-1} in region ‘d’ to 1 mS cm^{-1} and decreased from 1.02 mS cm^{-1} to 1 mS cm^{-1} at 9.6 kHz.

The normalised and dimensionless distributions are given for $Fl_g \approx 0.058$ and $Fr \approx 0.31$ at 9.6 kHz and 0.3 kHz in Figure 5.35 (i) and (ii). The collimated axial conductivity distributions are shown in Figure 5.36 and Figure 5.37 without the error bars, demonstrating the evolution of each distribution at both frequencies as Fl_g was increased.

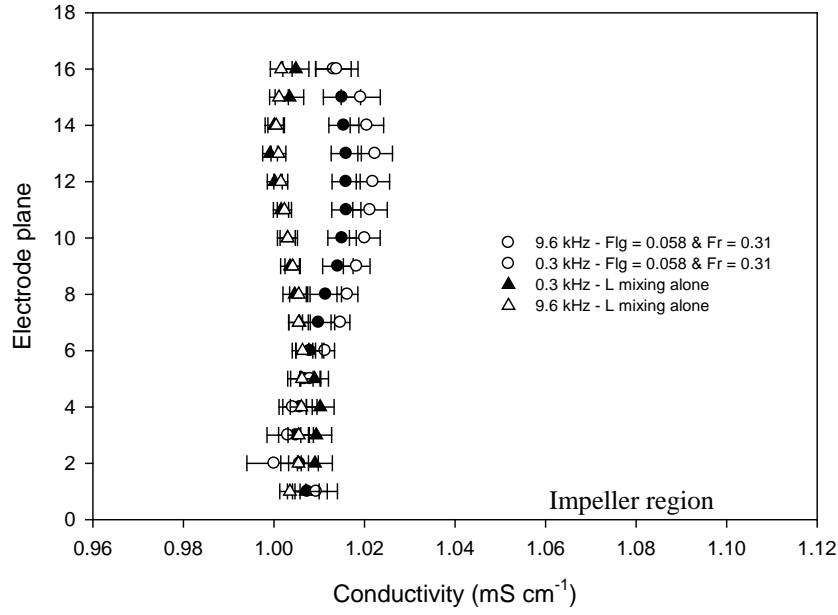
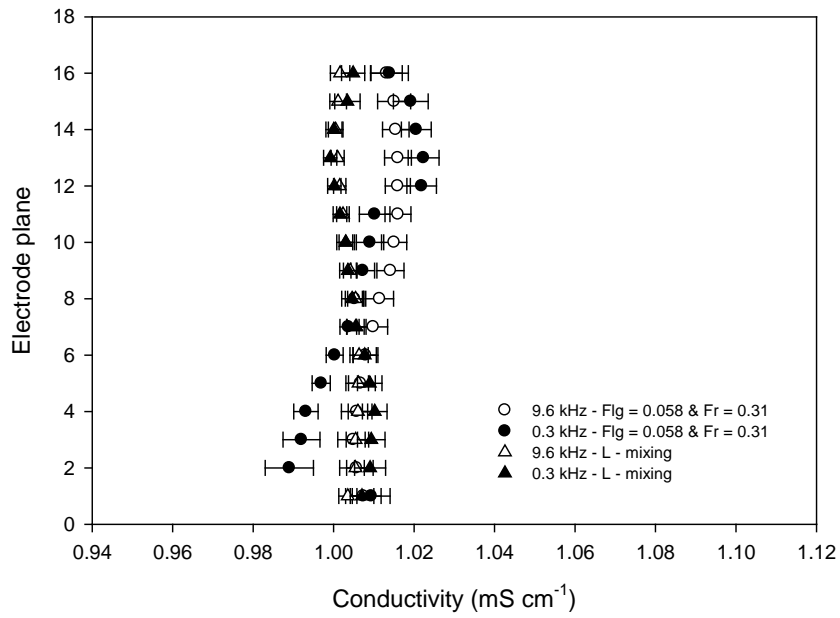


Figure 5.34. Conductivity profile for *GLS* mixing in region ‘e’
at $Fl_g \approx 0.058$ and $Fr \approx 0.31$



(i)

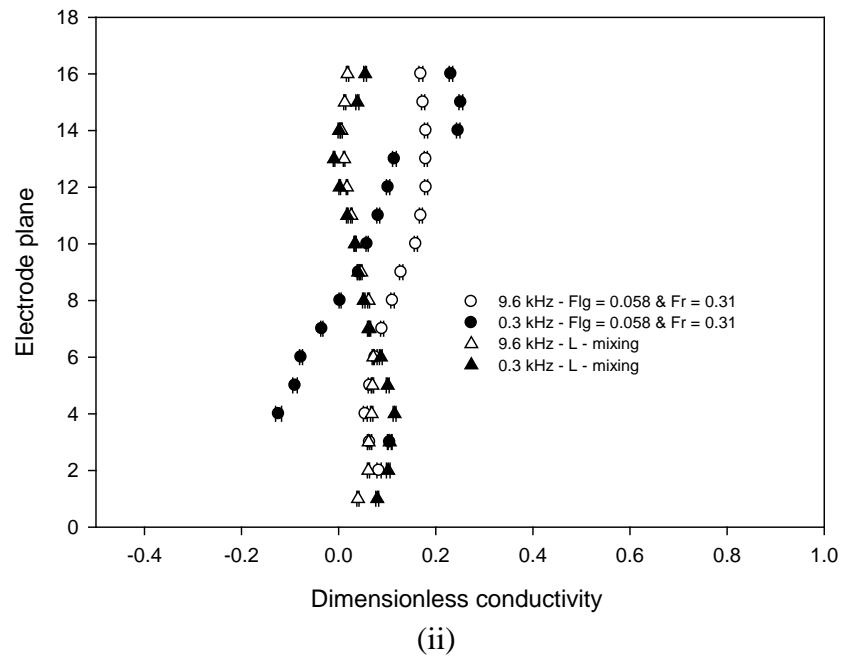


Figure 5.35. Normalised conductivity and (ii) Dimensionless conductivity
for $Fl_g \approx 0.058$ and $Fr \approx 0.31$

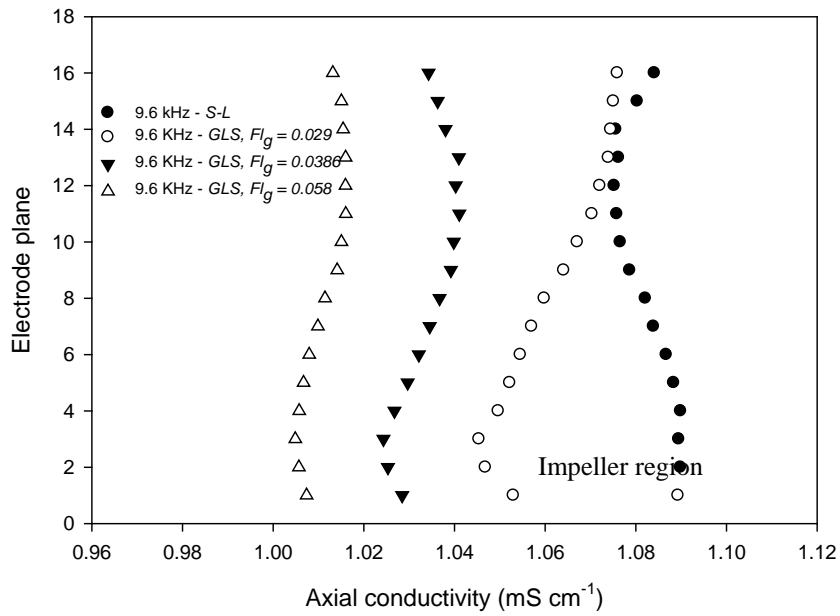


Figure 5.36. Collimated conductivity distributions at 9.6 kHz

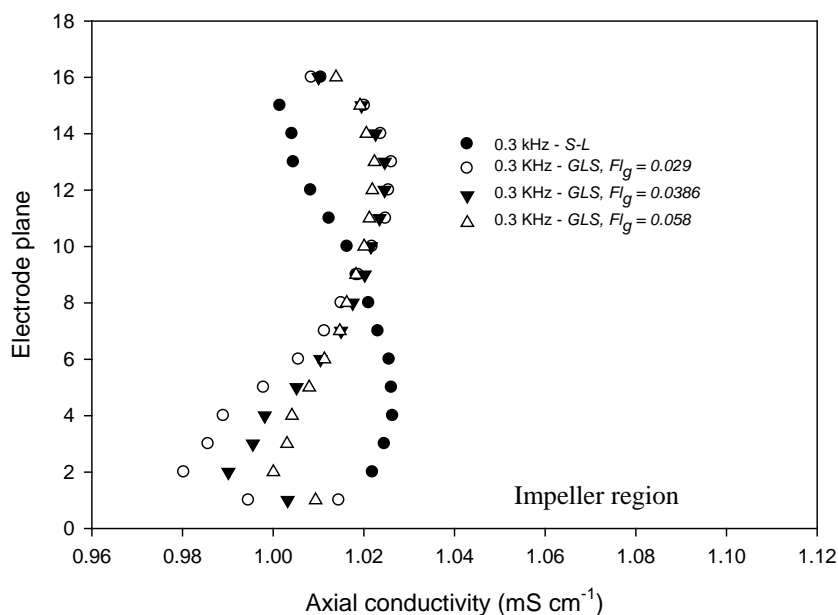


Figure 5.37. Collimated conductivity distributions at 0.3 kHz

5.5. Conclusion

Electrical Resistance spectroscopy has been investigated using a modified *ERT* approach to characterise an agitated *GLS* system. For the first time, it has been shown that by changing the frequency at a given current, the gas phase (air) in an agitated vessel can be isolated from conducting solids (stainless steel), allowing for measurements of the gas and solids phase without significant interference. This technique relies on an electric phenomenon observed when *AC* flows through a conducting solid. By increasing the frequency of an *AC*, the conductor's surface self-inducts and a measurable voltage is detected by *ERT* on the surface. When the frequency is decreased, the observation relapses.

Preliminary verification experiments were initially carried out using a stainless steel static phantom in a circular array *ERT* vessel for proof of concept. By changing the frequency from low to high values, it was shown that the phantom's effective resistance and subsequently its mean conductivity increased, whilst when the same was done to a plumed gas phase the conductivity remained unaltered. At low frequencies, the conductivity of the phantom decreased to values close to that of the bulk liquid phase.

This set precedence for the technique to be applied to agitated stainless steel particles in a *S-L* system and agitated *G-L* system. Measurements were carried out with a linear *ERT* probe. The objective was to show that the behaviour was not limited to phantoms and the circular array vessel but could also be applied to agitated systems and a linear *ERT* probe.

In the agitated system, it was shown that as the frequency changed from low to high values, the particles self-inducted and the mean conductivity of the agitated *S-L* system systems corresponded to the phantom system. The agitated *G-L* system also corresponded to the plumed gas system. The technique was then applied to a *GLS* system. The highest (9.6 kHz) and lowest frequencies (0.3 kHz) that did and did not isolate the gas phase were used.

It was shown via vessel images, mean axial conductivity plots, linear axial conductivity plots and conductivity tomograms that the solid and the gas phase could be detected simultaneously at 9.6 kHz, however at 0.3 kHz; the gas phase alone could be detected. By subtracting the conductivity of the solids and gas, the change in solids holdup was obtained. During the course of the study, a limit to the solid concentration that could be used was noted whilst energy dissipation to heat during agitation increased the conductivity of the system and consequently the conductivity readings. For

the latter, it was advised that upon use, the temperature of the system should be measured and compensated accordingly in the conductivity readings.

Chapter 6. Conclusions and future work

6.1. Conclusions

In Chapter 2, an agitated $L-L$ system for PGM extraction was investigated using a substitute Copper (Cu) – hydrochloric acid (HCl) aqueous solution dispersed in an organic phase comprised of kerosene and LIX84-A to assess mixer design for solvent extraction. The effects of agitation intensity (P/V), phase flow fraction ratio, ϕ_c/ϕ_d (where ϕ_d and ϕ_c are the dispersed and continuous phase flow fraction ratio) and the ratio of impeller diameter, D , to vessel diameter, T , on the droplet size distribution were investigated.

Within the range of operating conditions studied, it was shown that by altering P/V , the droplet size generated in the agitated $L-L$ system varied considerably as both ϕ_c/ϕ_d and D/T were changed. As expected, changing a smaller D/T impeller for a larger and midrange D/T impeller at a fixed P/V and ϕ_c/ϕ_d increased the arithmetic mean droplet size (d_{10}) and the Sauter mean droplet size (d_{32}). The droplet size distribution broadened and skewed towards large droplet sizes. This took place because of the subsequent increase in the ratio of pumping capacity (Q) with impeller tip speed (U_{tip}). It is of importance for mixer design because at the expense of smaller droplet sizes the larger D/T impeller can be used if circulation time (t_c) demonstrates a larger limiting effect to the rate of extraction. Stagnation and excessive short circuiting will also be averted. At a similar P/V and ϕ_c/ϕ_d the smaller D/T impeller should be used if droplet size and mass transfer are important limiting factors to the rate of extraction, since the interfacial area and rate constant will increase with respect to the droplet size.

At a fixed P/V and D/T , it was also shown that by changing a larger ϕ_c/ϕ_d for a midrange and smaller ϕ_c/ϕ_d , turbulence damping increased leading to the decrease in the maximum shear rate ($\dot{\gamma}_m$) and the increase in droplet size.

Theoretical relationships between We , $\overline{\varepsilon_T}$ and droplet size, were used to study the effects of P/V on droplet size. Certain operating conditions were shown to satisfy the specific theoretical constants associated with these relationships, which allows for satisfactory scale-up rules to be defined for mixer design.

In Chapter 3, the effect of the preceding factors in the mixer studies and the dispersed phase throughput, Q_d/A (where A is the horizontal cross sectional area of the settler) on the dispersion concentration (C_a) and phase separation in the settler were investigated in order to establish the requirements for the design of a settler.

C_a was shown to depend on P/V , settler depth, D/T and Q_c/Q_d , in the particular order, wherein increasing P/V and Q_c/Q_d increased C_a , whilst increasing settler depth and D/T decreased C_a . Their significance and contributions were also quantified with Minitab®. It was also shown that by varying Q_d/A at $P/V = 0.9 \text{ kW m}^{-3}$, a power law relationship between Q_d/A and C_a was obtained whilst at $P/V = 2.7 \text{ kW m}^{-3}$ a linear relationship was obtained. The power law relationship showed that Q_d/A increased in direct linear proportion whilst C_a varied the power law constants. The contribution by C_a was also less than the contribution by either Q_d or A . The settler was flooded at $P/V = 2.7 \text{ kW m}^{-3}$ due to dispersion carryover making the A required for the introduction of retrofits such as coalescence enhancers much greater than the necessary A at $P/V = 0.9 \text{ kW m}^{-3}$.

In Chapter 4, a model sponge nickel[®], sodium hypochlorite system was used to study particle hydrodynamic behaviour during gas emitting reactions under mixing conditions. Gas phase hold-up (φ_g) was demonstrated as not being dependent upon agitation speed over the range of operating conditions studied, since impeller flow dominated the bubble flow regime and the presence of gas was found to markedly increase the impeller speed (N) required to fulfill solids suspension performances for gas liquid solid (*GLS*) systems.

In Chapter 5, a novel characterisation technique called Electrical Resistance Spectroscopy was developed using Electrical Resistance Tomography (*ERT*) to observe gas (air) and solids distribution in an agitated *GLS* system. It was shown using a static stainless steel phantom and agitated stainless steel particles in ionic solutions that as the frequency of the alternating current (*AC*) on *ERT* was increased from low (0.3 kHz) to high (9.6 kHz) values at a constant current, the effective resistance of these objects increased due to self-inductance, whilst the conductivity of plume of gas and an agitated gas-liquid (*G-L*) system remained unchanged, since gas is a poor conductor of electricity.

Using the two frequencies an agitated *GLS* system made-up of the stainless steel particles and air was characterised. The difference between the conductivity distribution of the *GLS* system at 0.3 kHz and 9.6 kHz at various gas sparged regimes corresponded to the change in solid concentration, whilst the various gas sparged regimes were observed at 0.3 kW m^{-3} . During the course of the study, a limit to the solid concentration that could be used was observed whilst energy dissipation due to heat during agitation increased the conductivity of the system and consequently the conductivity readings. For the latter, it was advised that during use, the temperature of the system should be measured and compensated in the conductivity readings.

6.2. Future work

Time restrictions limited the application of the findings from the studies to the sponsoring company's processes. However a Development Engineer was employed from September 2011 to applying the findings from the mixer and settler studies to the company's solvent extraction processes.

In Chapter 2, the findings from the mixer studies will be extended to real Platinum Group Metal (*PGM*) systems, where mass transfer can become an important factor to droplet size distributions. In Chapter 3, a detailed settler design will accompany the findings. Internal modifications to the settler will be carried out to improve the effectiveness of the separation process. The dispersions' distribution process will be studied since it is the most successful means of improving settler performance. By ensuring that the feed is evenly distributed across the full settler width, most of the settler area will potentially be used. The use of picket fences to thin the emulsion bands and reduce entrainment will also be investigated.

In Chapter 4, additional experimental programs will need to be conducted using characterisation equipment such as Positron Emission Particle Tracking (*PEPT*) to obtain numerical information that supports the visual observations obtained from the gas evolving solid-liquid (*S-L*) studies. A limitation to the use of *PEPT* is the size of the nickel particles ($\leq 30 \mu\text{m}$), since the technique relies on particle labeling which suits particle sizes as large as $100 \mu\text{m}$. Extensions of the numerical study to a leaching system will require a well defined experimental plan, since the ideality of the nickel and sodium hypochlorite system simplifies reaction mechanism, the activation energy and may be amplifying the gas evolution rate and entrapment in the leach system. A detailed kinetic study of the nickel and sodium hypochlorite system will be needed.

In Chapter 5, the prerequisites of *ERT* spectroscopy and skin effect with stainless steel are well discussed. Extending the fundamentals to a leaching system with *PGM* alloys may require frequency sweep ranges and a current that falls outside that of stainless steel. A non-harmonised and chirped *ERT* hardware that allows a user to scan multiple frequencies to seek a suitable frequency range for *PGM* alloys should be developed and investigated. The chirp technology will speed up the sweep process. A pure *PGM* metal may not be a suitable choice since it is a perfect conductor and will not demonstrate skin effect.

References

- Abouelwafa, M.S.A., Kendall, E.J.M., 1980. The measurement of component ratios in multiphase systems using gamma-ray attenuation. *J. Phys. E: Sci. Instrum.* 13, p.341.
- Adams, L., Chiti, F., Guida, A., Jaffer, S., Nienow, A.W., Barigou, M., 2008. Positron emission particle tracking inside caverns formed during mixing of Industrial slurry. 6th *International Symposium on Mixing in Industrial Process Industries- ISMIP VI*, Niagara on the Lake, Niagara Falls, Ontario, Canada.
- Altobelli, S., Mondy, L., 2002. Hindered Flotation Functions from NMR Imaging. *J. Rheol.* 46, p.1341-52.
- Allan, R.S. and Mason, S.G., 1961. Effects of Electric Fields on coalescence in Liquid-Liquid Systems. *Trans.Faraday.Soc.* 57, p.2027.
- Artzen, R., 2001. *Gravity Separator Revamping*. PhD Thesis, Norwegian University of Science and Technology, Trondheim, Norway.
- Aubin, J., Mavros, P., Fletcher, D.F., Xuereb, C., Bertrand, J., 2001. Effect of axial agitator configuration (up-pumping, down-pumping, reverse rotation) on flow patterns generated in stirred vessels. In: *International Symposium on Mixing in Industrial Processes—ISMIP4*, Toulouse, France, 14–16 May.

- Bailes, P.J., Larkai, S.K.L., 1981. An experimental investigation into the use of high voltage d.c. fields for liquid phase separation. *Trans. IChemE.* 59, p.229–237.
- Bailes, P.J., Larkai, S.K.L., 1986. Electrostatic separation of liquid dispersions. UK Patent 217 1031A.
- Batchelor, G. K., 1952. The effect of homogeneous turbulence on material lines and surfaces. *Proc. Roy. Sci. London.* 213, p.349-366.
- Barnea, E., Mizrahi, J., 1975. Separation mechanism of liquid-liquid dispersions in a deep layer gravity settler: Part I – The structure of the dispersion band. *Trans. Inst. Chem. Eng.* 53a, p.61-69.
- Barnea, E., 1980. Liquid-liquid contacting – Art or science? Part II. Design methods for mixer-settlers. *Hydromet.* 5, p.127-147.
- Barnea, E., Mizrahi J., 1975. Separation Mechanism of Liquid-Liquid Dispersions in a Deep Layer Gravity Settler: Part IV - Continuous Settler Characteristics. *Trans. Instn. Chem. Eng.* 53, p.83-92.
- Behling, M., Mewes, D., 2006. Dual-Energy X-Ray Tomographic Measurement of Local Phase Fractions in 3-Phase Bubble Columns. *ASME Conference Proceedings.*
- Benac, J., O'Sullivan, J. A., Williamson, J. F., 2004. Alternating minimization algorithm for dual energy X-ray CT. *Proc. IEEE Int. Symp. Biomedical Imag.* p.579 ,

-
- Bieberle, M., Barthel, F., Menz, H-J., Mayer, H-G., and Hampel, U., 2011. Ultrafast three-dimensional x-ray computed tomography. *Appl. Phys. Lett.* 98.
- Bolton, G.T., Qiu, C.H., Wang, M., 2002. A novel electrical tomography sensor for monitoring the phase distribution in industrial reactors. *Fluid Mixing VII*. July 10-11.
- Boyer, C., Fanget, B., 2002. Measurement of liquid flow distribution in trickle bed reactor of large diameter with a new gamma-ray tomographic system. *Chem. Eng. Sci*, 57, pp. 1079–1089.
- Brennan, D. J., Lehrer, I. H., 1976. Impeller Mixing in Vessels Experimental Studies on the Influence of Some Parameters and Formulation of a General Mixing Time Equation. *Trans. Instn.Chem. Engrs.* 54, p.139.
- Brooks, B. W., 1979. Drop Size Distributions in Agitated Liquid/Liquid Dispersion. *Trans. Instn. Chem. Engrs.* 57, p.211.
- Brown, D. E., Pitt, K., 1972. Drop Size Distribution of Stirred Non-Coalescing Liquid-Liquid System. *Chem. Eng. Sci.* 27, p.577.
- Bruijn, W., Van't Riet, K. and Smith, J. M., Power consumption with aerated Rushton turbines. *Trans. Inst. Chem. Engrs.* Vol. 52, 1974, pp. 88-104

- Bolton, G.T., 2006. A review of linear electrical tomography probes for monitoring the behaviour of multiphase mixing processes. 12th European Conference on Mixing, Bologna, Italy.
- Buoyatiotis, B. A., Thornton, J. D., 1967. *Int. Chem. Eng. Symp. Ser.* No.26
- Bjørn Tore, H., Geir Anton, J., Stein-Arild, T., Erling A, H., 2005. Multimodality tomography for multiphase hydrocarbon flow measurements. *IEEE.Sens. J.* Vol.5 , Iss2 p.153-160.
- Calabrese, R. V., Chang, T. P. K., Dang, R.T., 1986. Drop Breakup in Turbulent Stirred-Tank Contactors Part I: Effect of Dispersed-Phase Viscosity. *AIChE J.* 32, p. 657.
- Calabrese, R. V., Chang, T. P. K., Dang, R.T., 1986. Drop Breakup in Turbulent Stirred-Tank Contactors Part II: Relative influence of viscosity and interfacial tension. *AIChE J.* 32, p. 667.
- Caulkin, R., Jia, X., Xu, C., Fairweather, M., Williams, R.A., Stitt, H., Nijemeisland, M., Aferka, S., Crine, M., Leonard, A., Toye, D., Marchot, P., 2009. Simulations of Structures in Packed Columns and Validation by X-ray Tomography. *Ind. Eng. Chem. Res.* 48, p.202-213.
- Cents, A. H. G., Brilman, D. W. F., Versteeg, G. F., 2004. Measuring Bubble, Drop and Particle Sizes in Multiphase Systems with Ultrasound. *AIChE J.* 50, No. 11.
- Chapman, C. M., Nienow, A. W, Cooke, M., Middleton, J. C., 1983. Particle-Gas-Liquid Mixing in Stirred Vessels Part III: Three Phase Mixing. *Chem. Eng. Res. Des.* 61,p.167

- Chen, H. T., Middleman, S., 1967. Drop Size Distribution in Agitated Liquid-Liquid Systems. *AIChE J.* 13, p.989.
- Collias, D.I., Prud'homme, R. K., 1992. Diagnostic Techniques of Mixing Effectiveness: The Effect of Shear and Elongation in Drop Production in Mixing Tanks. *Chem. Eng. Set.* 47, p.1401
- Coenen, J.G., Maas, J.G., 1994. Material classification by dual-energy computerized x-ray tomography. *International Symposium on Computerized Tomography for Industrial Applications, Berlin*, pp. 120-127.
- Cooper, R. C., Wolf, D., 1968. Velocity Profiles and Pumping Capacities for Turbine Type Impellers. *Can. J. of Chem. Eng.* 46, p.94.
- Cottrell, F.G., Speed, J.B., 1911. Separating and collecting particles of one liquid suspended in another liquid, US Patent 987 115.
- Coualoglou, C. A., Tavlarides, L., 1976. Drop Size Distributions and Coalescence Frequencies of Liquid- Liquid Dispersions in Flow Vessels. *AIChE J.* 22, p.289.
- Coualoglou, C. A., Tavlarides, L., 1977. Description of Interaction Processes in Agitated Liquid-Liquid Dispersions. *Chem. Eng. Sci.* 32, p.1289.
- Crowe, C., Sommerfeld, M., Tsuji, Y., 1997. Multiphase flows with droplets and particles. CRC Press.

- Dreher, T.M., Glass, J., O'Connor, A.J., Stevens, G.W., 1999. Effect of rheology on coalescence rates and emulsion stability. *AIChE J.* Vol.45, No.6, p.1182-1190.
- Doublier, L., 1991. The drainage and rupture of a non-foaming liquid film formed upon bubble impact with a free surface. *Int. J. Multiphase Flow.* 17, p.783–803.
- Duduković, M.P., 2003. Use of gamma Ray computed tomography (CT) and computer aided radioactive particle tracking (CARPT) in multiphase reactors. *Hemjska industrija.* 57(6), p.249-261
- Duineveld, P.C., 1994. *Bouncing and coalescence of two bubbles in water.* PhD Thesis, University of Twente, the Netherlands.
- Dukhin, A.S., Goetz, P.J., 2002. Ultrasound for characterizing colloids. *Elsevier.*
- Dutta, N. N., Pangarkar, V G., 1995. Critical Impeller Speed for Solid Suspension in Multi-Impeller Three Phase Agitated Contactors. *Can. J. of Chem. Eng.* 73, p.273
- Dyakowski T., Jeanmeure L.F.C., Jaworski A.J., 2000. Applications of electrical resistance tomography for gas-liquid and liquid-solids flows - a review. *Powder Tech.* 112, pp. 174-192.
- Dunscombe, P. B., Katz, D. E., Stacey, A. J., 1984. Some practical aspects of dual-energy CT scanning. *Brit. J. Radiol.* 57, p. 82–7.

- Eckert, N.L., Gormely, L.S., 1989. Phase separation in an experimental mixer-settler. *Chem.Eng.Res.Des.* Vol.67, p.175.
- Edwards, I., Axon, S.A., Barigou, M., and Stitt, E.H., 2009. Combined Use of PEPT and ERT in the Study of Aluminum Hydroxide Precipitation. *Ind. Eng. Chem. Res.* 48, p.1019–1028.
- Engler, P., Friedman, W.D., 1990. Review of Dual-Energy Computed Tomography Techniques. *Mat. Eval.* 48, pp. 623-629.
- Falkovich, G., Fouxon, A., Stepanov, M.G., 2002. Acceleration of rain initiation by cloud turbulence. *Nature*, 419, p.151-154.
- Ford, J.J., Heindel, T.J., Jensen, T.C., Drake, J.B., 2008. X-ray computed tomography of a gas-sparged stirred-tank reactor. *Chem. Eng. Sci.* 63, p.2075-2085.
- Frøystein, T., Kvandal, H., Aakre, H., 2005. Dual energy gamma tomography system for high pressure multiphase flow,” *Flow Meas. Instrum.* vol.16, no.2/3, p.99–112.
- Gabriele, A., Tsoligkas, A.N., Kings, I.N., Simmons, M.J.H., 2011. Use of PIV to measure turbulence modulation in a high throughput stirred vessel with the addition of high Stokes number particles for both up- and down-pumping configurations. *Chem. Eng. Sci.*, published online, doi:10.1016/j.ces.2011.08.007

- Gallego-Lizon, T., Perez de Ortiz, E. S., 2000. Drop sizes in liquid membrane dispersions, *Ind. Eng. Chem. Res.* 39, p.5020-5028.
- Gehrke, S., Wirth, K., 2005. Application of Conventional- and Dual-Energy X-Ray Tomography in Process Engineering. *IEEE. SEN. J.* Vol. 5, No. 2, p.183
- Gilberd, P. W., 1982. The anomalous skin effect and the optical properties of metals, *J. Phys. F: Met. Phys.*, vol. 12, no. 8.
- Gladden, L.F., Anadon, L.D., Dunckley, C.P., Mantle, M.D., Sederman, A.J., 2007. Insights into gas–liquid–solid reactors obtained by magnetic resonance imaging. *Chem.Eng.Sci.* 62, p.6969 – 6977.
- Gnanasundaram, S., Degaleesan, T. E., Laddha, G. S., 1979. Prediction of Mean Drop Size in Batch Agitated Vessels. *Can. J. of Chem.Eng.* 57, p.141.
- Godfrey, J.C. and Slater, M.J., eds., 1994. Liquid-liquid extraction equipment. Chichester: John Wiley & Sons.
- Gondo, S., Kusunoki, K., 1969. A New Look at Gravity settlers, *Hydrocarb.Process Petrol.Ref.* 48, p.209.
- Grassler, T., Wirth, K.E., 1999. X-ray Computed Tomography in Mechanical Engineering – A Non-intrusive Technique to Characterize Vertical Multiphase Flows. *Computerized Tomography*

for *Industrial Applications and Image Processing in Radiology*. Berlin, Germany, March 15 - 17, 1999.

- Grassler, T., Wirth, K.E., 2001. Dual-Energy X-ray Tomography in Process Engineering – A Non-Intrusive Technique to Characterise Vertical Multiphase Flows. *2nd World Congress on Industrial Process Tomography*. Hannover, Germany, 29th - 31st August 2001.
- Gray, D. J., Treybal, R. E., Barnett, S. M., 1982. Mixing of Single and Two Phase Systems: Power Consumption of impellers. *AIChE J.* 28, p.195.
- Greaves, M., Barigou, M., 1988. Estimation of Gas Hold-Up and Impeller Power in a Stirred Vessel Reactor. *ICHEME Symposium Series*. No. 108, p.235.
- Harnby, N., Edwards, M.F. and Nienow, A.W., *Mixing in the Process Industries*; 1985, *Butterworths*. London.
- Hanlon, A. D., Gibbs, S. J., Hall, L. D., Haycock, D. E., Frith, W. J., Ablett, S., 1998. Rapid MRI and Velocimetry of cylindrical coquette flow. *Mag.Reson.Imag.* 16 (8), p953.
- Hartland, S., Jeelani, S.A.K., 1994. Gravity settlers, In the book of *Liquid-liquid extraction equipment*, ed. Godfrey, J.C. and Slater, M.J., John Wiley & Sons, England. p.411-530.
- Howell, W.H., Golding, J.A., Ritcey, G.M., 1988. Bench-Scale Mixer-Settler Study of the Extraction and Stripping of Uranium from Solution. *Hydromet.* 19, p.11-30.

- Hinze, J.O., 1955. Fundamentals of the Hydrodynamic Mechanism of Splitting in Dispersion Processes. *AIChE J.* 1, p.291.
- Holden, P.J., Wang, M., Mann, R., Dickin, F.J., Edwards, R.B., 1998, Imaging stirred vessel macromixing using electrical resistance tomography, *AIChE J.* 44(4), p.780-790
- Holmes, J. T., Wilke, C. R., Olander, D. R., 1963. Convective Mass Transfer in a Diaphragm Diffusion Cell. *J. Phys. Chem.* 67, p.1469-1472.
- Hiraoka, S., Tada, Y., Suzuki, H., Mori, H., Aragaki, T., Yamada, I., 1990. Correlation of Mass Transfer Volumetric Coefficient with Power Input in Stirred Liquid-Liquid Dispersions. *J.Chem.Eng. Japan.* 23, p.468
- Hughmark, G. A., 1980. Power Requirements and Interfacial Area in Gas-Liquid Turbine Agitated Systems. *Ind. Eng. Chem. Process Des. Dev.* 19, p.638.
- Ivanov, I.B., Dimitrov, D.S., 1988. Thin film drainage, In the book of thin liquid films, Fundamental and applications. *Marcel Dekker, New York.* p.379-496.
- Jaworski, Z., Nienow A.W., Koutsakos, E., Dyster, K., Bujalski, W., 1991. An LDA Study of Turbulent Flow in a Baffled Vessel Agitated by a Pitched Blade Turbine. *Trans IChemE.* 69 A, p.313 - 320.

- Jeelani, S. A. K., Hartland, S., 1985. Prediction of steady state dispersion height from batch settling data. *AIChE J.* 31(5), p.711 - 720.
- Jeelani, S.A.K., Hartland, S., 1991. Collision of oscillating liquid drops. *Che.Eng.Sci.* Vol. 46, 7, p.1807-1814.
- Jeelani, S.A.K., Hartland, S., 1994. Effect of interfacial mobility on thin film drainage. *J. Colloid Int. Sci.* 164, p.296 - 308.
- Jeffreys, C.V. , Davies, CA., 1971. Coalescence of Liquid Droplets and Liquid Dispersion; In Recent Advances in Liquid - Liquid Extraction, C. Hanson, Ed., *Pergamon Press*, Oxford,
- Jeffreys, C, V., Hawksley, J.L., 1965a. Coalescence of Liquid Droplets in Two-Component-Two Phase Systems: Part I – Effect of Physical Properties on the Rate of Coalescence. *AIChE J.*, 11, p.413.
- Johansen, G, A., Jackson, P., 2000. Salinity independent measurement of gas volume fraction in oil/gas/water pipe flow. *Appl. Rad. Isotop.* 53, p. 595-601.
- Johansen, G.A., 2005. Nuclear tomography methods in industry. *Proceedings of the 22nd International Nuclear Physics Conference (Part 2). Nuclear Physics A.* Volume 752 , p.696-705
- Johansen, G.A., Frøystein, T., Hjertakery, B.T., Olsen, Ø., 1996. A dual sensor flow imaging tomographic system, *Meas. Sci. Technol.* 7, pp. 297–307.

- Johnson Matthey, Platinum 2011 interim Review, from http://www.platinum.matthey.com/uploaded_files/Int_2011/press-release-oz-final.pdf
- Kafarov, V. V., Babanov, B. M., 1959. Phase contact area of immiscible liquids during agitation by mechanical stirrers. *Zh. Prikl. Khim.* 32, p.789.
- Kankaanpaa, T., 2005. Studying Solvent Extraction Settler Process by Using CFD. *EPD Congress* (Ed Schlesinger ME), TMS.
- Kantzas, A. 1994. Computation of holdups in fluidized and trickle beds by computer-assisted tomography. *AIChE J.* 40, p.1254.
- Kissa, E., 1999. Dispersions. Characterization, Testing and Measurement. *Marcel Dekker, New York.*
- Hancock, F. E., King, F., 1996. *Catalysis Today.* 27, p203
- Kolmogoroff, A. N., 1941a. Local structure of turbulence in an incompressible fluid for very large Reynolds numbers. *Comptes Rendus (Doklady) de l'Academie des Sciences de l'URSS.* 31, p.301 - 305.
- Kraume, M., and Gabor, A., Schulze, K., 2004. Influence of physical properties on drop size distribution of stirred liquid-liquid dispersions. *Chem. Eng. Technol.* 27(3), p.330 - 334.

- Kourunen, J., Kayhko, R., Matula, J., Kayhko, J., Vauhkonen, M., Heikkinen, L.M., 2008. Imaging of mixing of two miscible liquids using electrical impedance tomography and linear impedance sensor. *Flow Meas. & Inst.* 19, p391-396.
- Kumar, S.B., Moslemiam, D., Dudukovic, M.P., 1995. A gamma-ray tomographic scanner for imaging voidage distribution in two-phase flow systems. *Flow Meas. Instrum.* 61, p.61–73.
- Lagisetty, J.S., Das. P.K., Kumar, R., and Gandhi, K.S., 1986. Breakage of viscous and non-Newtonian drops in stirred dispersions. *Chem. Eng. Sci.* 41 .p. 65 - 72.
- Lang, S.B., Wilke, CR., 1974a. A Hydrodynamic mechanism for the Coalescence of Liquid Drops: Part I - Theory of Coalescence at a Planar Interface. *Ind.Eng.Chem. Fundam.* 10, p.329.
- Lang, S.B., Wilke, CR., 1974b. A Hydrodynamic mechanism for the Coalescence of Liquid Drops: Part I – Experimental studies. *Ind.Eng.Chem. Fundam.* 10, p.341.
- Lawson, G.B., 1967. Coalescence processes. *Chem. Proc. Eng.* May: 45–60.
- Lehr, F., 2002. Bubble-size distributions and flowfields in bubble columns. *AIChE J.* 48, p.2426 - 2443.

- Lehr, F., Mewes, D., 1999. A transport equation for the interfacial area density applied to bubble columns. *Chem.Eng.Sci.* 56, p.1159 - 1166.
- Lemenand, T., Della Valle, D., Zellouf, Y., Peerhossaini, H., 2003. Droplets formation in turbulent mixing of two immiscible fluids in a new type of static mixer. *Int. J. Multiphase Flow.* 29(5), p.813 - 840.
- Leng, D.E., Calabrese, R.V., 2004. Immiscible liquid-liquid systems, In the book of Handbook of industrial mixing, science and practice, ed. Paul, E.L., Atiemo-Obeng, V.A., and Kresta, S.M. *John Wiley & Sons Inc., U.S.A.* p.639 - 753.
- LeVert, F. E. e Helminski E., 1973. A Dual-energy method for measuring void fractions in flowing medium. *Tuskegee Institute, School of Engineering, Alabama, Technical Note.*
- Li, Y., Yang, W., 2009. Measurement of multi-phase distribution using an integrated dual-modality sensor. In: *2009 IEEE International Workshop on Imaging Systems and Techniques, 1st 2009 – Proceedings*, Hong Kong, pp. 335–339.
- Lim, M.H.M., Sederman, A.J., Gladden, L.F., Stitt, E.H., 2004. New insights to trickle and pulse flow hydrodynamics in trickle-bed reactors using MRI. *Chem.Eng.Sci.* 59, p.5403 – 5410.
- Lister, M. W., 1956b. Decomposition of Sodium Hypochlorite: The Catalyzed Reaction. *Can. J. Chem.* 34, p.479-488.

- Liter, S., Gayton., T., John, R., Shollenberger, K.A., Ceccio, L. S., 2002. Electrical-Impedance Tomography for Opaque Multiphase Flows in Metallic (Electrically-Conducting) Vessels. Sandia Report: AND2002-3834. Nov.2002 http://www.fischer-tropsch.org/DOE/DOE_reports/sandia_bubble_col/2002-3834/liter%20sand2002-3834.pdf.
(Last accessed 19 Nov 2009).
- Liu, S., and Li, D., 1999. Drop coalescence in turbulent dispersions. *Che.Eng.Sci.* Vol. 54, p.5667-5675.
- Liu, Yue-Jin., Li, W., Han, Lu-Chang., Cao, Y., Luo, He-an, Al-Dahhan, M., Dudukovic, M.P., 2011. [gamma]-CT measurement and CFD simulation of cross section gas holdup distribution in a gas-liquid stirred standard Rushton tank. *Chem.Eng. Sci.*Vol. 66, No. 17.
- Lutran, P.G., Ng, K. M., Delikat, E. P. 1991. Liquid distribution in trickle beds. An experiment using computer-assisted tomography. *Ind. Eng. Chem. Res.* 30, p.1270.
- Macdonald, R, J., 1992. Impedance Spectroscopy. *Annals. Bio. Eng.* Vol. 20, p. 289-305.
- Madden A. J., and Damerell G. L., 1962. *Cleveland Meeting, Amer. Inst. Chem. Engrs.* 8, p.233.
- Madia, J. R., Fruh, S. M., Miller, C. A., Beerbower, A., 1976. Granular packed bed coalescer: influence of packing wettability on coalescence. *Envir.Sci & Technol.* vol. 10, no. 10, p.1044–1046.

- Magiera, R., Blass, E., Separation of liquid–liquid dispersions by flow through fiber beds. *Filtration/Separation*. May (1997), pp. 369–376.
- Manikowski, M., Bodemeier, S., Liibbert, A., Bujalski, W., Nienow, A. W., 1994. Measurement of Gas and Liquid Flows in Stirred Tank Reactors with Multiple Agitators. *Can. J. of Chem. Eng.* 72, p.769.
- Mann, R., Dickin, F.J., Wang, M., Dyakowski, T., Williams, R. A., Edwards, R. B., Forrest , A. E., Holden P. J., 1997. Application of electrical resistance tomography to interrogate mixing processes at plant scale. *Chem.Eng. Sci.* 52(13), p.2087-2097.
- Mantle, M. D., Sederman, A. J., Gladden, L. F., 2001. Single- and two-phase flow in fixed-bed reactors: MRI flow visualisation and lattice-Boltzmann simulations; *Chem.Eng.Sci.* 56, p.523-529.
- Mantle, M.D., Sederman, A.J., 2003. Dynamic MRI in chemical process and reaction engineering. *Prog. Nucl. Magn. Reson. Spectrosc.* 43(3).
- Marchot, P., Toye, D., Crine, M., L'Homme, G., Pelsser A. M., Olujic, Z., 2001. Liquid distribution images on structured packing by X-ray computed tomography. *AIChE J.* 47, p.1471-6.
- McCabe, W.L., 2001. *Unit Operations of Chemical Engineering* Singapore: McGraw-Hill Book Co. p.164.

- Metzner, A. B., Taylor, J. S., 1960. Flow Patterns in Agitated Vessels. *AIChE J.* 6 (1), p.109 - 114.
- Miller, R. S., Ralph, J. L., Curl, R. L., Towell, G. D., 1963. *AIChE J.* 9, p.196.
- Miller, G. M., 2001. Design Tools to Control Transients in Solvent Extraction Plants. SME Annual Meeting, Denver. February 2001.
- Mlynek, Y., Resnick, W., 1972. Drop Sizes in an Agitated Liquid-Liquid System; *AIChE J.* 18, p.122.
- Moser, K.W., Georgiadis, J.G., 2003. Synchronised EPI phase contrast Velocimetry in a mixing reactor. *Mag. Reson.Imag.* 21(1), p.127.
- Montante, G., Horn, D., Paglianti, A., 2008. Gas-liquid flow and bubble size distribution in stirred tanks. *Chem.Eng.Sci.* 63(8), p.2107-2118.
- Nadv, C., Semiat, R., 1995. Batch Settling of Liquid-Liquid Dispersion. *Ind.Eng.Chem. Res.* 34, p.2427-2435.
- Nahvi, M., Hoyle, B.S., 2008a. Spectro-tomography - an electrical sensing method for integrated estimation of component identification and distribution mapping in industrial processes – *IEEE SENSORS Conference*.

- Nahvi, M., Hoyle, B.S., 2008b. Wideband electrical impedance tomography. *Meas. Sci. Technol.* 19
- Narasimhan, S., Harpaz, N., Longmore, G., Carver, J. P., Grey, A. A., Schachter, H., (1980). *J. Biol. Chem.* 255, p.4876 - 4884.
- Nienow, A. W., 1975. "Agitated Vessel Particle-Liquid Mass Transfer, A Comparison Between Theories and Data. *Chem.Eng. J.* 9, p.153.
- Nienow, A.W., Warmoeskerken, M.M.C.G., Smith, J.M., Konno, M., 1985."On the Flooding/Loading Transition and the Complete Dispersal Condition in Aerated Vessels Agitated by a Rushton Turbine", in "Proc. 5th Eur. Conf. Mixing". Wurzburg, Germany, *BHRA Fluid Engineering*, Cranfield, UK. (Jun. 10–12,). pp. 143–153
- Nishikawa, M., Mori, E, Fujieda, S., Kayama, T., 1987. Scale-up of Liquid-Liquid Phase Mixing Vessel. *J. Chem. Eng. Japan.* 20, p.454.
- Oyama, Y., Endoh, K., 1955. Power Characteristics of Gas-Liquid Contacting Mixers. *Kagaku Kogaku.*19, p2
- Pacek, A.W., Moore, I.P.T., Nienow, A.W., Calabrese, R.V., 1994. Video technique for measuring dynamics of liquid–liquid dispersion during phase inversion. *AIChE J.* 40, p.1940 - 1949.

- Pacek, A. W., Nienow, A. W., 1995. Measurement of drop size distribution in concentrated liquid-liquid dispersions: Video and capillary techniques. *Trans IChemE Part A*. 73, p.512 - 518.
- Pacek, A.W., Man, C.C., Nienow, A.W., 1998. On the Sauter Mean Diameter and Size Distributions in Turbulent Liquid/Liquid Dispersions in a Stirred Vessel. *Chem. Eng. Sci.* 53, p.2005 - 2011.
- Parker, D. J., McNeil, P. A., 1996 Positron emission tomography for process applications *Meas. Sci. Technol.* 7 , p.287–96
- Perry, R. H., Green, D.W., 1984. Perry's Chemical Engineers Handbook, 6th ed. (Eds.), New York.
- Razzak, S, A., Barghi, S., Zhu, J, X., Mi , Y., 2009. Phase holdup measurement in a gas–liquid–solid circulating fluidized bed (GLSCFB) riser using electrical resistance tomography and optical fibre probe. *J. Chem. Eng. Data.* 147(15), p.210-218.
- Reeve, R.N., Godfrey, J.C., 2002. Phase inversion during liquid-liquid mixing in continuous flow, pump-mix, agitated tanks. 7th UK Conference on mixing, organised by the IChemE Fluid Mixing Subject Group.

- Ricard, F., Brechtelsbauer, C., Xu, X.Y., Lawrence, C.J., 2005. Monitoring of multiphase pharmaceutical Processes using electrical resistance tomography. *Chem.Eng.Res.Des.* 83(A7), p.794–805.
- Raghav Rao, K. S. M. S., Joshi, J. B., 1988. Liquid-Phase Mixing and Power Consumption in Mechanically Agitated Solid-Liquid Contactors. *Chem. Eng.J.*39, p.111.
- Richardson, L.F., 1926. Atmospheric diffusion shown on a distance – neighbour graph. *Proc. of the Royal Society A.* 110, p.709 - 737.
- Robert-Coutant, C., Moulin, V., Sauze, R., Rizo, P., Casagrande, J. M., 1999. Estimation of the matrix attenuation in heterogeneous radioactive waste drums using dual-energy computed tomography. *Nucl. Instr. Meth. Phys. Res. A.* 422, pp. 949–56.
- Roman, R. J., Benner, B. R., and Becker, G. W., Diffusion Model for Heap Leaching and Its Application to Scale-Up. *Trans. Soc. Min. Eng.* 256, 1974, p.247-256.
- Rushton, J. H., Costich, E.W., Everett, H. J., 1950. Power characteristics of mixing impellers. *Chem. Eng. Progr.* 46, p.395 - 404.
- Ruszkowski S., 1994. A rational method for measuring blending performance and comparison of different impeller types. *ICHEME Symposium Series.*136, pp. 283–291.

- Ryon, A.D., Daley, F.L., Lowrie, R.S., 1959. Scale up of Mixer-Settlers. *Che.Eng.Prog.* Vol.55, 10, p.70-75.
- Salgado, C. M., Brandão, L. E., Nascimento, C. M., Ramos, R., Silva, A. X. E Schirru, R., 2009. Prediction of volume fractions in three-phase flows using nuclear technique and artificial neural network. *App. Rad.Isot*, 67, p. 1812-1818.
- Sano, Y., Usui, H., 1985. Interrelations among Mixing Time, Power Number and Discharge Flow Rate Number in Baffled Mixing Vessels. *J. Chem. Eng. Japan*.18, p.47.
- Sareen, S.S., Rose, P.M., Gudesen, R.C., Kintner, R.C., 1966. Coalescence in Fibrous Beds. *AIChE J.* 12, p. 1045.
- Shinnar, R., Church, J., 1960. Prediction particle size in agitated dispersions. *Ind.& Eng. Chem.* 52, p.253 - 256.
- Simmons. M. J. H., Edwards. I., Hall.J. F., Fan.X., Parker.D. J., Stitt E. H., 2009. Techniques for visualisation of cavern boundaries in opaque industrial mixing systems. *AIChE J.* 55(11), p.2765-2772.
- Skelland, A.H.P., Ramsay, G. G ., 1987. Minimum Agitator Speeds for Complete Liquid-Liquid Dispersion. *Ind. Eng. Chem. Res.* 26 (1), 77-81.

- Smith, J. M., Katsanevakis, A. N., 1993. Impeller Power Demand in Mechanically Agitated Boiling Systems. *Trans. Instn. Chem. Engrs.* 71, Part A, p.145.
- Smith, T. N., 1974. Measurement of drop size in liquid-liquid dispersions. *Chem.Eng.Sci*, 29, p.583 - 587.
- Sprow, F. B., 1967. Drop Size Distributions in Strongly Coalescing Agitated Liquid-Liquid Systems. *AIChE J.* 13, p.995.
- Stamatoudis, M., Tavlarides, L., 1985. Effect of continuous phase viscosity on the drop liquid-liquid dispersions in agitated vessels. *Ind. Eng. Chem. Process. Des. Dev.* 24, p.1175 - 1181.
- Stanley, S.J., Mann, R., Primrose, K., 2002. Tomographic imaging of fluid mixing in three dimensions for single-feed semi-batch operation of a stirred vessel. *Trans.IChemE.* 80(A), p.831-844.
- Stanley, S. J., Bolton, Gary, T., 2008. A Review of Recent Electrical Resistance Tomography (ERT) Applications for Wet Particulate Processing. *Part.Syst.Charact.* 25, p.207–215.
- Stephenson, D. R., Rodgers, T.L., Mann, R., York, T.A., 2009. Application of three-dimensional electrical impedance tomography to investigate fluid mixing in a stirred vessel. *13th European Conference on Mixing, London.*
- Stitt, E.H., Hancock, F.E., Peeling, R.H., Scott, J. 2003. *Catalysis Today.* 79-80, pp125-138

- Tapp, H. S., Williams, R. A., 1999. Status and Applications of Microelectrical Resistance Tomography. *1st World Congress on Industrial Process Tomography, Buxton, Greater Manchester*, April 14-17.
- Tatterson, G. B., 1991. Circulation Times and Pumping Capacities, Fluid Mixing and Gas Dispersion in Agitated Tanks. *McGraw-Hill Inc, New York*. p.208 - 222.
- Toye, D., Marchot, P., Crine, M., Pelsser, A.M., L'Homme, G., 1998. Local measurements of void fraction and liquid holdup in packed columns using X-ray computed tomography, *Chem. Eng.Process.*, 37, p.511-20.
- Treybal, R.E., 1963. *Liquid Extraction*, McGraw Hill, New York. p.147.
- Thornton, J. D., 1956. Spray Liquid-Liquid Extraction Columns: Prediction of Limiting Holdup and Flooding Rates. *Chem.Eng. Sci.* 5, p.201-208.
- Unadkat, H., Rielly, C.D., Hargrave, G.K., Nagy, Z.K., 2009. Application of fluorescent PIV and digital image analysis to measure turbulence properties of solid-liquid stirred suspensions. *Chem.Eng.Res.Des.* 87 (4A), p.573-586.
- Varma, R., 2006. Simulation and Experimental Studies in Dual Source Gamma Ray Computer Tomography for Imaging Three Phase Systems. *Catalysis and Reaction Engineering Division. AIChE annual meeting*.

- Varma, R., O'Sullivan, J. A., Al-Dahhan, M., 2007. Dual Source Computed Tomography For Measuring Phase Holdup Distribution In Multiphase Systems. *Novel Computational and Experimental Methods in Multiphase Mixing. AIChE annual meeting.*
- Vermeulen, T., Williams, G. M., Langlois, G. E., 1955. Interfacial area in Liquid-Liquid and Gas-Liquid Agitation. *Chem. Eng. Prog.* 26 (1), 51 (2), p.85F-94F.
- Wadsworth, M. E., Pitt, C. H., 1980. An Assessment of Energy Requirements in Proven and Copper Processes, *Contract EM-78-S-07-1743, U.S. Department of Energy, University of Utah, Salt Lake City, UT.* Dec 31.
- Walter, G. J., 2002. Op Amp Applications, Analog Devices, ISBN 0-916550-26-5, Also available as Op Amp Applications Handbook, *Elsevier/Newnes*, 2005, ISBN 0-7506-7844-5. Chapter 1.
- Wang, M., Dorward, A., Vlaev, D., and Mann, R., 2000. Measurements of gas-liquid mixing in a stirred vessel using electrical resistance tomography (ERT). *Chem.Eng.J.* 77(1-2), p.93-98.
- Warmoeskerken, M. M. C. G., Smith, J. M., 1985. Flooding of disc turbines in gas-liquid dispersions, A new description of the phenomenon. *Chem. Eng. Sci.* Vol. 40, pp.2063-2071.
- Warmoeskerken, M.M.C.G., van, Houwelingen M.C., Frijlink, J.J., Smith, J.M., 1984. The role of cavity formation in stirred gas-liquid-solid reactors. *Chem. Eng. Res. Des.* 62, pp. 197-200.

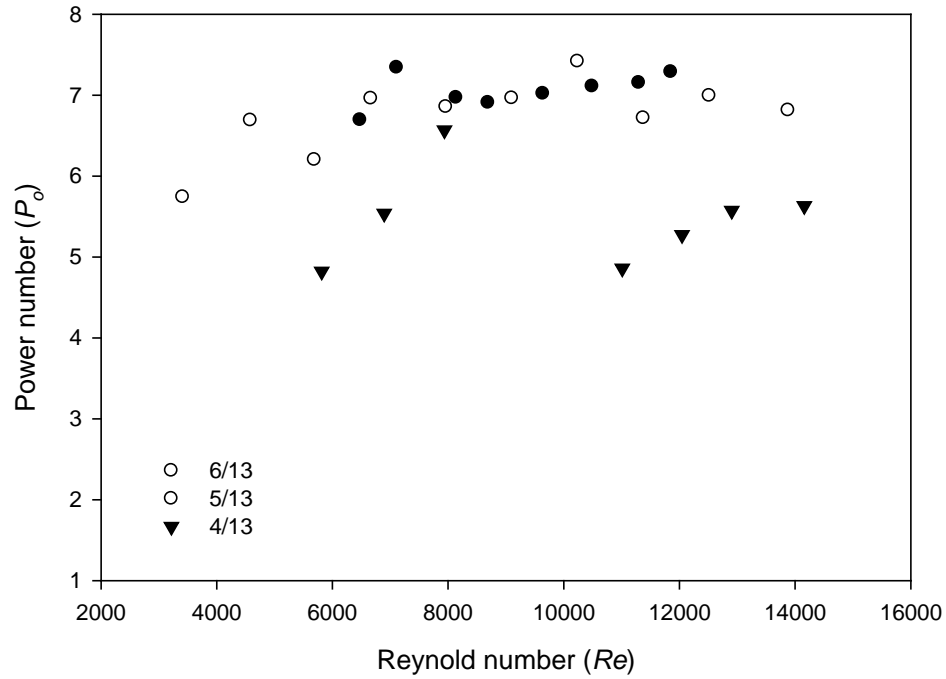
- Warsito, W., Fan, L, S., 2001. Measurement of real-time flow structures in gas–liquid and gas–liquid–solid flow systems using electrical capacitance tomography (ECT). *Chem.Eng.Sci.* 56, p.6455–6462.
- Watson, C. C., 1989. Optimal linear compression of X-ray transmission spectra. Schlumberger-Doll Research Note.
- Watt, J.S., Steffner, E.J., 1985. Dual energy gamma-ray transmission techniques applied to on-line analysis in the coal and mineral industries. *Int. J.Appl.Radiat.Isot.* 36 11, p.867.
- Weinstein, B., and Treybal, R. E., 1973. Liquid-Liquid Contacting in Unbaffled Agitated Vessels. *AIChE J.*19, p.304.
- Wellington. S. L., Vinegar,H. J., 1987. X-ray computerized tomography, *J. Petroleum Technology.* 39(8), p. 885–98,
- White, A.M., Brenner, E., 1934. Studies in agitation. *Trans. Am. Inst. Chem. Eng.* 30, p. 585.
- Wille, M., Langer, G., Werner U., 2001. The influence of macroscopic elongational flow on dispersion processes in agitated tanks. *Chem.Eng.Technol.* 24(2), 119–127.
- Yang, B., Takahashi, K., Takeishi, M., 2000b. “Styrene Drop Size and Size Distribution in an Aqueous Solution of Polyvinyl Alcohol“. *Ind. Eng. Chem. Res.* 39, p.2085–2090.

- Ying. Z., Naidu, R., Crawford, C. R., 2006. Dual energy computed tomography for explosive detection. *J. X-Ray.Sci & Tech.* 14 (2006), p.235–256.
- Yingxiang, Wu., 2007. Multiphase flow measurement by dual gamma ray tomography Source: *AIP conference proceedings.* Vol: 914. 1, p:31-36.
- Yoshida, M., Yamagiwa, K., Ohkawa, A., Tezura, S., 2011. Gas-Liquid Mass Transfer in an Unbaffled Vessel Agitated by Unsteadily Forward-Reverse Rotating Multiple Impellers; Mass Transfer in Multiphase Systems and its Applications. *Intech.*
- Young, D.F., Munson, B. R., Okiishi, T. H., 2003. A Brief Introduction to Fluid Mechanics (third Ed.). *Wiley*, New York.
- Zhou, G., Kresta, S. M., 1998b. Evolution of drop size distribution in liquid-liquid dispersions for various impellers. *Chem. Eng. Sci.* 53 (11), p.2099 – 2113
- Zwietering, T. N., 1958. Suspending of solid particles in liquid by agitators. *Chem. Eng. Sci.* Vol. 8, p. 244 – 253.

Appendix

Appendix A (i)

Plot of P_o versus Re



Appendix A (ii)

Droplet size percentage error

Q_c/Q_d	P/V	D/T		
		4/13	5/13	6/13
Droplet size percentage error				
1:1	0.3	6.4	8.8	11.4
	0.9	2.8	4.5	7.6
	2.7	2.5	3.3	4.3
3.5:2	0.3	12.8	13.3	16
	0.9	5	7.24	12
	2.7	2.5	4.32	7.3
3.5:1	0.3	6.4	9.4	10
	0.9	2.8	4.4	5
	2.7	2	6.	5.2

Appendix A (iii)

Statistical tests for d_{32} versus $\overline{\varepsilon_T}$

Statistical Tests: D/T = 4/13

Normality Test (Shapiro-Wilk)	Passed (P = 0.1263)
W Statistic= 0.8711	Significance Level = 0.0500
Constant Variance Test	Passed (P = 0.0769)

Data Set for O:A = 1:1

Number of Observations = 3

Rsqr = 0.9689

Residual Sum of Squares = 1.9186E-007

Parameter Estimates				
	Coefficient	Std. Error	t	P
a	0.48	0.4336	1.1030	0.3506
b	-0.63	0.1477	-5.3114	0.0130

Data Set for O:A = 3.5:1

Number of Observations = 3

Rsqr = 0.9659

Residual Sum of Squares = 1.2247E-007

Parameter Estimates				
	Coefficient	Std. Error	t	P
a	0.2998	0.3351	0.8946	0.4369
b	-0.6464	0.1815	-4.1127	0.0260

Data Set for O:A = 3.5:2

Number of Observations = 3

Rsqr = 0.9902

Residual Sum of Squares = 1.6397E-007

Parameter Estimates				
	Coefficient	Std. Error	t	P
a	2.4938	1.9064	1.3081	0.2820
b	-0.5514	0.1264	-7.9219	0.0042

Statistical Tests: D/T = 5/13

Normality Test (Shapiro-Wilk) Passed (P = 0.5801)
W Statistic= 0.9398 Significance Level = 0.0500
Constant Variance Test Passed (P = 0.4072)

Data Set for O:A = 1:1

Number of Observations = 3

Rsqr = 0.9831

Residual Sum of Squares = 7.2395E-008

Parameter Estimates				
	Coefficient	Std. Error	t	P
a	0.3431	0.3404	1.0080	0.3877
b	-0.7515	0.1648	-4.6221	0.0191

Data Set for O:A = 3.5:1

Number of Observations = 3

Rsqr = 0.9655

Residual Sum of Squares = 5.7831E-008

Parameter Estimates:				
	Coefficient	Std. Error	t	P
a	0.1030	0.1269	0.8120	0.4762
b	-0.4717	0.2022	-3.0248	0.0565

Data Set for O:A = 3.5:2

Number of Observations = 3

Rsqr = 0.9638

Residual Sum of Squares = 3.1282E-007

Parameter Estimates:				
	Coefficient	Std. Error	t	P
a	0.9284	0.7795	1.1910	0.3193
b	-0.6070	0.1406	-6.3111	0.0080

Statistical Tests: D/T = 6/13

Normality Test (Shapiro-Wilk) Passed (P = 0.4449)
W Statistic= 0.9261 Significance Level = 0.0500
Constant Variance Test Passed (P = 0.6116)

Data Set for O:A = 1:1

Number of Observations = 3

Rsqr = 0.9861

Residual Sum of Squares = 6.1068E-008

Parameter Estimates:				
	Coefficient	Std. Error	t	P
a	0.3084	0.3931	0.7843	0.4901
b	-0.7363	0.2115	-3.4813	0.0400

Data Set for O:A = 3.5:1

Number of Observations = 3

Rsqr = 0.9737

Residual Sum of Squares = 5.4947E-008

Parameter Estimates:				
	Coefficient	Std. Error	t	P
a	0.1179	0.1772	0.6653	0.5535
b	-0.4242	0.2470	-2.4862	0.0888

Data Set for O:A = 3.5:2

Number of Observations = 3

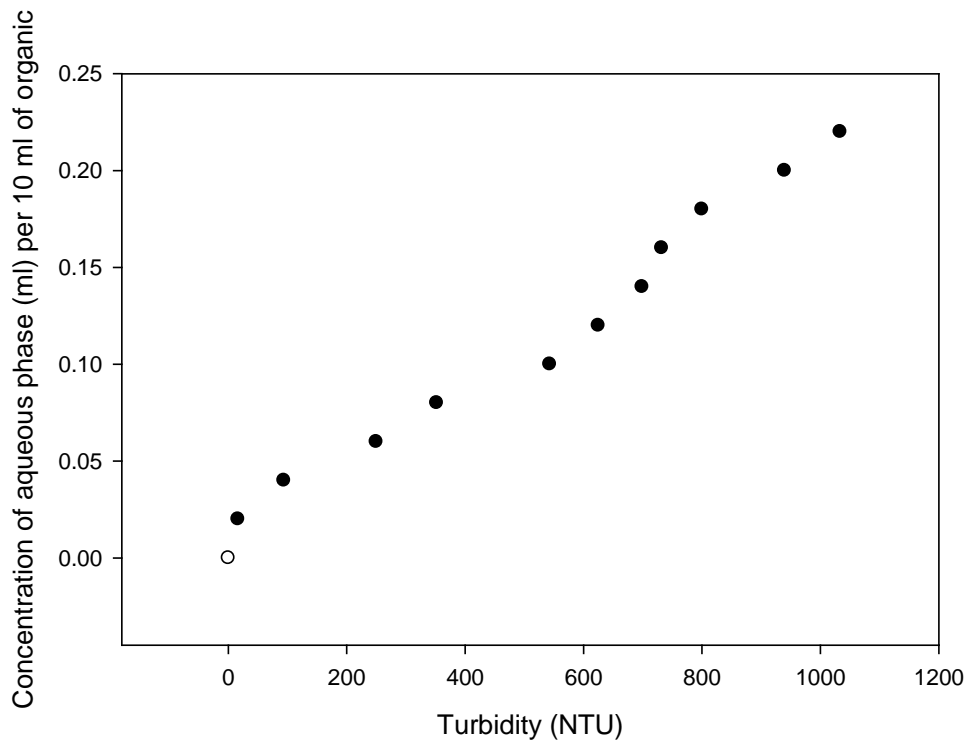
Rsqr = 0.7990

Residual Sum of Squares = 7.3482E-007

Parameter Estimates:				
	Coefficient	Std. Error	t	P
a	0.0512	0.0422	1.2141	0.3116
b	-0.6530	0.1327	-2.9609	0.0595

Appendix B

Turbidity meter calibrations



Appendix C

List of publications

Conferences:

Oguh U.I., Hall J.F., Bolton G.T., Castillo M., Stitt E.H

Gas-Liquid-Solid Characterisation by a Novel Frequency Sweep Spectroscopy Technique Using ERT, 8th World Congress of Chemical Engineering, Montreal, August 23 – 27, 2009, *Presentation*.

U. Oguh, J.F.Hall, M.J.H. Simmons, M. Barigou, S. Collard, E.H. Stitt

The Suspension of solids in Gas Evolving System, 13th European Conference on Mixing, London, 14-17 April 2009, *Poster*.

U. Oguh, J.F.Hall, M.J.H. Simmons, M. Barigou, S. Collard, E.H. Stitt

The Suspension of solids in Gas Evolving System, 9th UK Particle Technology Forum, Herriot Watt University, *Poster*.

Appendix D

13th European Conference on Mixing
London, 14-17 April 2009

A STUDY OF HYDRODYNAMICS IN GAS-EVOLVING REACTIONS

U. Oguh ^{a,b}, J.F. Hall ^{a,*}, M.J.H. Simmons ^{a,b}, M. Barigou ^b, S. Collard ^a, E.H. Stitt ^a

^a Johnson Matthey Technology Centre, PO Box 1, Belasis Avenue, Billingham, Teesside,
TS23 1LB, UK

^b School of Chemical Engineering, University of Birmingham, Edgbaston, Birmingham,
B15 2TT, UK

Abstract Three-phase gas-liquid-solid systems in which the gas phase is evolved from the liquid phase by reaction at the solid surface have received little prior attention despite their common occurrence in many industrial processes such as hydrometallurgical leaching or liquid-phase dehydrogenation. This study has examined the effect of reagent concentration and solid loading upon the gas evolution rate, gas-phase hold-up, and solids suspension behaviour for a model reactive system of sodium hypochlorite dissociation over porous nickel catalyst in a laboratory scale stirred vessel equipped with a Rushton Turbine impeller. Gas evolution rate was found to be directly proportional to both nickel loading and hypochlorite concentration. Gas-phase hold-up was found to positively correlate with gas evolution rate, as the gas-phase was fully dispersed at the operating conditions and impeller-driven flow dominated the bubble flow regime. Solid suspension performance was found to be affected severely by gas presence, even though the filling of the catalyst pores with evolved gas reduced the effective particle density.

Keywords: gas-liquid-solid, solid suspension, gas evolution, hold-up

1. Introduction

Mixing is a special feature of agitation, which has been established as very important in a vast range of chemical processes. The agitation of multi-component multiphase systems in industry is necessary to enhance mass and heat transfer between phases in systems. Typically, agitation is carried out for three distinct reasons, namely; the production of dynamic uniformity within multi-component multiphase systems, the facilitation of mass or energy transfer within a system not in equilibrium, and the promotion of phase change in multi-component systems with or without a change in composition. Mixing efficiency influences the yield and selectivity of chemical process being considered. Therefore, the design and the operation of mixing devices determine the profitability and acceptability of a given plant.

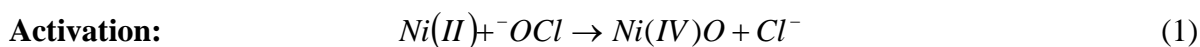
* Corresponding Author:
Dr Jonathan Hall
Tel: +44 (0)1642 522678
Fax: +44 (0)1642 522542
Email: jonathan.hall@matthey.com

In this study the interaction between mixing and gas evolving solid-liquid (three phase) reacting systems is investigated for stirred vessels operated under turbulent flow conditions. It is still considered a niche topic, due to the little attention that has been paid to it, despite its common occurrence within the industry. In the available literature of studies on three-phase mixing, previous research has focussed exclusively on systems concerning a pseudo-continuous solid-liquid phase and a sparged/bubbled gas phase. The findings of these studies have benefited processes such as catalytic hydrogenation, wastewater treatment and fermentation. However it cannot be ignored that there is a simplified aspect to them when it comes to gas evolving solid-liquid system.

Examples of gas evolving solid-liquid (three phase) reacting processes in the industry include the leaching and oxidation of ferrous ores, which leads to the production of leach residue (solid particulate matter) and evolved gas, as well as catalytic dehydrogenation reactions such as aromatisation, whereby the six-membered hydrocarbon ring of an alicyclic compound is aromatised in the presence of hydrogenation catalysts, leading to the loss of hydrogen [1].

Gas-sparged systems present a simplification of the hydrodynamic phenomena within processes such as these. This ideal has often been further exaggerated by the use of smooth spherical objects such as glass beads, whereas in real processes the objects could be highly porous. Furthermore, this approach also disregards the influence of trapped bubbles within the solids, which makes them buoyant, hampering solid-gas as well as solid-liquid mass transfer.

This work mimics a leaching process common to many industrial hydrometallurgical processes. Sponge Nickel[®] is used as the solid phase, which catalytically dissociates the liquid phase (sodium hypochlorite), liberating oxygen in the process. The chemical reaction governing this process is given below, as described by Hancock *et al* [2].



The catalytic action on sodium hypochlorite is a simple one, which has been applied previously in the literature by various authors, the main focus of their work being exclusively on the effective abatement and destruction of effluents containing sodium hypochlorite in the chlorine and other related industries [2,3].

Sodium hypochlorite dissociation chemistry is covered in the previous literature presented by Lister *et al.* [4] and Hancock *et al* [2]. Hancock showed that the mechanism behind Ni activity, which is generally considered to involve higher oxidation states of the metal, was true. Lister investigated the catalytic activity of various transition element oxides, including Ni, Cu, Co, Fe and Mn, suggesting that the mechanism of the catalysis is through the oxidation of the metal to a higher oxide, which loses oxygen (4) and is later re-oxidised. During Ni catalytic action, the rate was shown to be proportional to the amount of Ni added with little dependence on hypochlorite concentration. It was thus presumed that since the rate is vaguely dependent on hypochlorite concentration, Ni catalytic reaction to oxygen (4) must be the slow reaction step and the rate-

determining step, requiring much the same amount of hypochlorite adsorbed on the catalyst surface over a range of concentration.

Ni catalysis was also found to be a first order reaction. To satisfy this account, the entire Ni surface is required to be covered with adsorbed hypochlorite ions and this happens in concentrated as well as dilute solutions, therefore making the adsorption of hypochlorite proportional to hypochlorite concentration. If the catalyst surface is not completely covered, it is impossible to predict what the reaction kinetics would be without knowing the dependence of adsorption on concentration. They showed that Ni, at the concentrations they used, behaved as though the catalyst were essentially covered with adsorbed ions.

2. Experimental Method

2.1 Materials Characterisation

250g of Sponge Nickel[®] was obtained from Alfa Aesar and characterized to determine the particle size distribution (PSD) using a Mastersizer 2000 particle size analyzer. Diameters of 7.8, 29 and 67.4 μm were obtained for d_{10} , d_{50} and d_{90} respectively. The particles were also characterized for pore size analysis by nitrogen sorption using a Micromeritics 2020 physisorption analyser at 77K. BET surface area value of 55.3 m^2g^{-1} , pore volume of 0.99 (ads) mlg^{-1} and an average pore diameter of 86 \AA were obtained. 2 kg of 14% sodium hypochlorite was purchased from Alfa Aesar. The solution was titrated to confirm the percentage of sodium hypochlorite present within the bulk. The reagents and equipment used for titration were potassium iodide; acetic acid and a Metrohm 857 Titrand equipped with an iPt Titrode, a beaker and stirrer. Titration confirmed that 13.67% w/v sodium hypochlorite was present per unit volume of solution. The specific mass of hypochlorite in the concentrated solution was obtained as 2.231g and its concentration was determined as 0.4464g/ml. In order to minimise experimental hazards, the maximum solution strength used was diluted to 8% w/v sodium hypochlorite and further diluted volumes containing 7%, 6%, 4% and 2% (all w/v) sodium hypochlorite were also studied.

2.2 Gas evolution rate

The gas evolution rates due to the catalytic activity of Sponge Nickel[®] on the diluted volumes were initially investigated using 100ml volume of each dilute solution, subjected to five Sponge Nickel[®] concentrations: 0.09, 0.08, 0.07, 0.06 and 0.05g/cm³. The solutions were made-up and their densities were measured. An apparatus was setup for measuring gas evolution rate (Fig 1). It consisted of a gas bubble flowmeter, magnetic stirrer, stoppers, delivery tube, three-neck round bottom flask, flow control stopcock, delivery flask with equalising arm, retort stand, thermocouple and a stop clock.

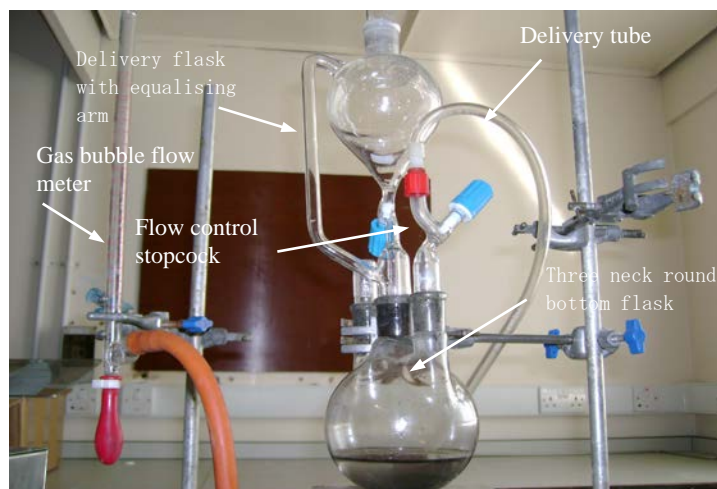


Fig.1 Gas evolution rate measuring apparatus

Sponge Nickel[®] was weighed accordingly. It was then fed to the three-necked flask with the magnetic stirrer in place. 100ml of the solution was transferred into the delivery vessel, which was subsequently stoppered. The fitted valve connected to the delivery tube was closed, and then the valve connected to the delivery vessel was opened, dropping the solution into the flask, and then shut. The rate of gas evolution was obtained by timing the bubble flow through the bubble flow meter. The temperature of reaction was also monitored with time. As per the literature by Lister *et al.* [4], the stirrer was operated at a moderately rapid speed to maintain suspension. The gas evolution rate obtained for each diluted solution and the corresponding concentration of Sponge Nickel[®] and sodium hypochlorite were plotted to observe behaviour and correlation.

2.3 Vessel Design, Configuration and impeller type

The vessel was a flat base Perspex vessel with internal diameter $T = 0.145\text{m}$; a height 0.33m and 4 equally spaced wall baffles with widths W_b of $14 \times 10^{-3}\text{ m}$ and thickness $2 \times 10^{-3}\text{ m}$. A 6 Blade Rushton Turbine (6BRT) with diameter $T/2.4 = 6 \times 10^{-2}\text{ m}$ and blade widths $W = 1.2 \times 10^{-2}\text{ m}$ was used to stir the medium. A clearance $T/4 = 3.6 \times 10^{-2}\text{ m}$ was maintained between the impeller and the vessel base. The shaft (with impeller) was mounted on an IKA Werke EUROSTAR POWER stirrer motor with a speed range of 0 to 2000rpm, controlled by a Labworldsoft program. The torque meter, IKA Werke VISCOKLICK VK 600, had a full torque range of 0 to 60Ncm. It was connected to the rotor, which had incorporated in it a strain gauge bridge, which was fixed to the shaft, and a stator, which communicated in frequency with the rotor. The output from the torque meter and stirrer motor, fed an amplifier whose output was directed to a computer via a converter. Labworldsoft program displayed the torque, actual and measured rotor speed.

2.4 Just-suspended speed, N_{js}

Different amounts of Sponge Nickel[®]; 0.130, 0.150, 0.190, 0.250 and 0.3 kg, were used to determine the effects of the slurry densities on the suspension of particles in the baffled vessel. In order to determine the effects of the gas phase on solids suspension, a non-gas evolving 2-phase system was evaluated using non-reactive brines of equal density to the various sodium hypochlorite solutions. These data were then compared directly with the equivalent reactive sodium hypochlorite system conditions to determine the effect of gas evolution on solids suspension.

The criterion for quantifying solids suspension was the just-suspended speed, N_{js} , as defined by Zwietering [5]. No characterisation or visualisation equipment was used to observe for N_{js} ; rather a

subjective approach of visually observing the vessel base using a see-through Perspex stand and a torch light was used to judge and justify Njs. Njs was deemed evident when no particle remained at the bottom of the vessel for longer than 1 or 2s. Njs values were obtained with an estimated error within $\pm 7\%$. Torque measurements to calculate power draw were also noted at Njs. This was carried out to determine the effects of the initial density of the dilute solutions on Njs (In actual fact the density of the solutions does change with time due to the loss of O_2 during catalytic dissociation).

3. Results and discussion

Observations and discussions based on 4.22, 4.3, 4.38, 4.55 and 4.74 weight percentages of Sponge Nickel[®] reactions with 2.5L of the varying concentrations of sodium hypochlorite are presented here.

3.1 Gas evolution rate

Gas evolution rate was evaluated on the basis of both Sponge Nickel[®] loading and sodium hypochlorite concentration. As expected, a direct relationship between oxygen evolution rate and concentrations of Sponge Nickel[®] (catalyst) and sodium hypochlorite (reagent) was observed.

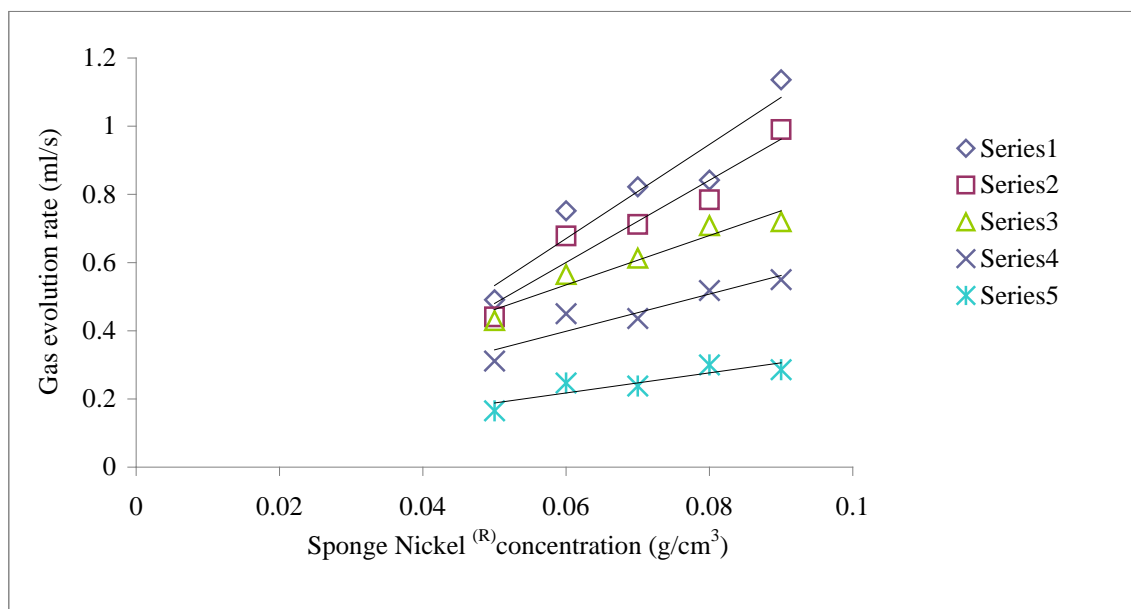


Fig.2 Oxygen evolution rate as a function of nickel loading

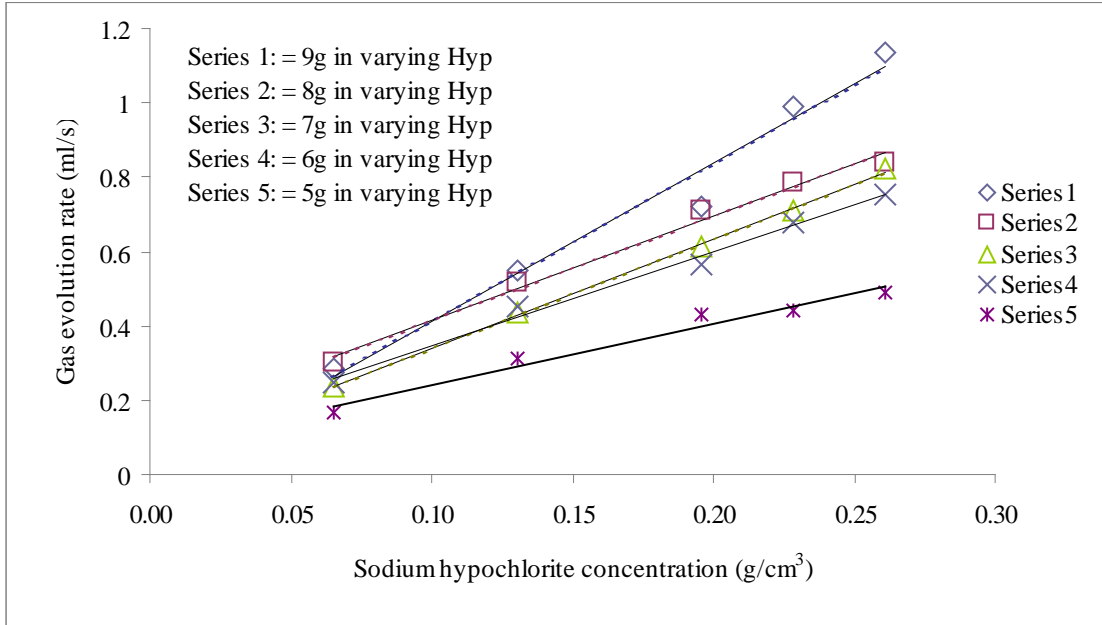


Fig 3. Gas evolution rate as function of hypochlorite ion concentration in solution

3.2 Gas Hold-up (ϕ_g)

Gas holdup was measured by the dynamic disengagement method. For all systems, irrespective of the solvent concentration or amount of Sponge Nickel[®], three liquid levels were observed when the impeller was stopped. ϕ_g was calculated from the gassed and ungassed liquid surface heights using Equation 4. Possible explanations governing these behavioural regimes are detailed below (with reference to the annotations in Fig 4).

$$\phi_g = \frac{H_2 - H_1}{H_2} \quad (4)$$

Regime 1: An initial liquid level (A) associated with the particles settling (H_1). This level was observed to be equal to the level when the solids were just added. At this point, negligible hypochlorite ions are absorbed to the catalyst surface. Sedimented particles were classified into three layers: upper (U), middle (M), and lower (L) particle beds.

Regime 2: Due to particle porosity, the entire Sponge Nickel[®] surface is covered with adsorbed hypochlorite ions. Acknowledging that the rate of reaction is proportional to the amount of Sponge Nickel[®], but independent of hypochlorite concentration, particles (B) beneath the uppermost layer of the particle bed still dissociate adsorbed hypochlorite ions at a rate comparable to particles in the upper layer that are exposed to the bulk hypochlorite solution until little or zero adsorbed species are left. Over this period, the liquid level due to gas expansion within the bulk liquid reaches a level (C) equal to that noted during impeller motion. This is described as the primary gas hold-up level (H_2).

Regime 3: At little or zero adsorbed hypochlorite ions by particles beneath the upper layer, the liquid level drops to a secondary gas hold-up level (D). This secondary gas hold-up level comes about primarily due to hypochlorite dissociation by particles (E) located at the upper particle bed.

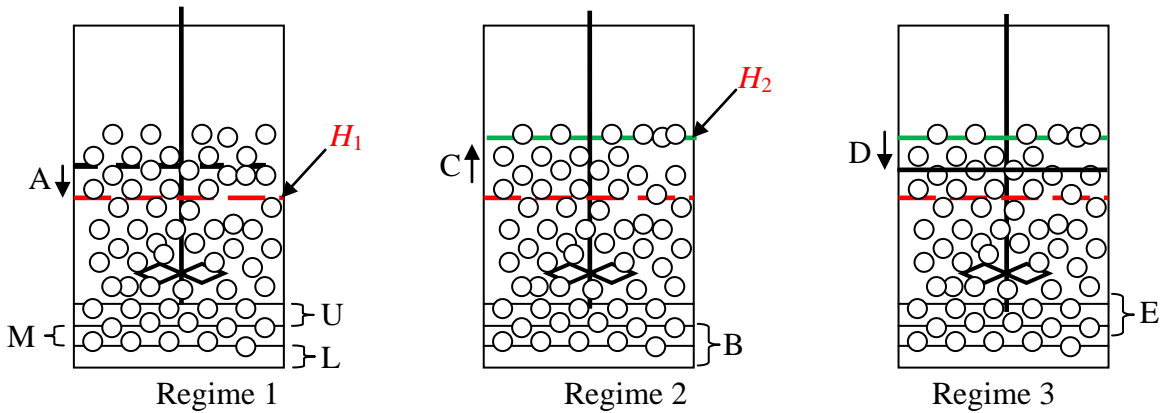


Fig.4 Gas hold-up and liquid levels associated with particle settling, gas expansion and contraction (see main body of text for explanation of annotations).

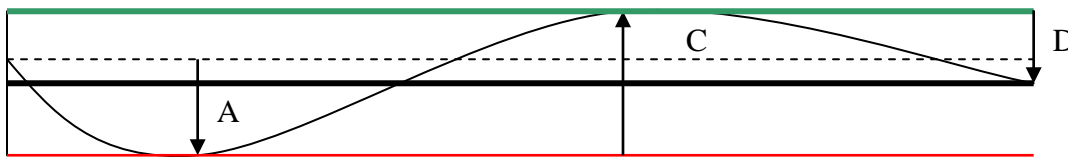


Fig.5 Telemetry of Gas hold-up and liquid levels associated with particle settling, gas expansion and contraction described above.

The change in ϕ_g with respect to gas evolution rate in the vessel is shown in Figure 6. ϕ_g can be seen to increase with gas evolution rate. For the range of gas evolution rates (Q_g), hold-ups (ϕ_g) and operating conditions used in this study the aeration number, N_A , takes values in the range $1.13 - 2.6 \times 10^{-4}$. At these values, the bubble flow regime in a sparged, stirred tank would generally be taken to lie within the fully dispersed regime [6]. Whilst there are undoubtedly differences in the bubble flow behaviour between sparged and gas-evolving two-phase systems, it is proposed that these differences are minimised towards the fully dispersed (low gas flow - high impeller speed) end of the regime spectrum. In the majority of literature covering sparged systems, gas discharge from spargers takes place beneath the turbine, which is classically central to the vessel.

Whereas, in gas evolving solid-liquid systems, the global gas discharge is spread across the vessel due to gas emission by catalytic action of the well distributed particles. Furthermore, the high ionic strength of the solution does not encourage any/significant bubble coalescence. Conversely, the differences are maximised at the high gas flow – low impeller speed end of the regime spectrum, as it is unlikely that impeller flooding or large trailing cavity formation could occur in a gas-evolving system. Over the full range of operating conditions studied in this work, the bubble flow regime is classified as fully dispersed. The impeller-driven flow is therefore dominant over the natural bubble convection behaviour, and gas hold-up is therefore a function of gas evolution rate alone.

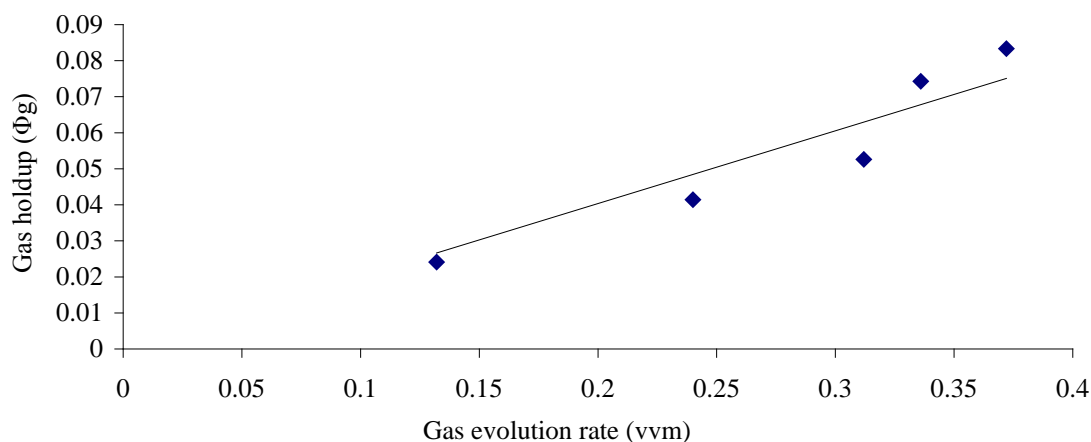


Fig.6 Gas hold-up as a function of gas evolution rate (for 4.22, 4.3, 4.38, 4.55 and 4.74 weight percentages of Sponge Nickel[®] in 8, 7, 6, 4 and 2% sodium hypochlorite solutions)

3.3 Solid phase suspension and settling behaviour

5 out of 25 possible combinations of Sponge Nickel[®] mass–hypochlorite concentrations were studied and the results are given in Table 1, including, N_{js} and power draw at just suspended speed (P_{js}) for the ungasged and gasged system, gas evolution rate (based on experimental trials), and gas hold-up values. From Table 1 it can clearly be seen that the introduction of the gas phase severely reduces the ease of suspension of the nickel particles. The data for the ungasged system were obtained from experiments performed using a non-reactive brine of equal density to the hypochlorite solution.

Table 1. Summary of just suspended speed results for gasged and ungasged systems using various Sponge Nickel[®] amounts

Mass (g)	Percentage Sodium hypochlorite in 2.5L (%)	Gas evolution rate (vvm)	N_{js} (Ungasged system) RPM	N_{js} (Gasged system) RPM	P_g/P_u (Ratio of gasged to ungasged power draw)	Gas hold-up (%)
250	8	0.70	430	670	2.34	7.36
250	4	0.36	430	550	2.98	3.21
190	6	0.378	410	604	4.05	3.82
130	8	0.372	400	665	4.24	9.04
130	4	0.24	380	570	4.55	3.21

For all operating conditions, the just suspended speed was greater for the three-phase system than for two-phases. This is indicative of high gas phase concentrations surrounding the particles. This gas phase acts as an energy sink via the action of compression and expansion in a fluctuating pressure field around the impeller region. Within incompressible turbulence, energy cascade

originates at the largest scale of turbulence (impeller region) where velocity fluctuations in the fluid are spatially correlated (integral scale of turbulence). The energy entering at the integral scale should be successively transferred to scales suitable for particle lift. The absorbance of energy by the bubbles limits this transfer and consequently the available energy in the fluid to lift the particles from the vessel base. This effect is slightly offset by the reduced effective density of the particles once their pores are filled with gas. The terminal falling velocity of a 75 μm diameter particle prior to pore filling (immediately upon addition to the hypochlorite solution and before full adsorption of hypochlorite ions to the nickel surface) was found to be 0.58 cm/s. Once gas generation commenced, the terminal falling velocity of the same particle was found to reduce to 0.40 cm/s. This equates to a reduction in fall velocity by 31% and a pore volume gas filling of 38%.

4. Conclusions

Gas evolution rate was characterised for a model nickel-sodium hypochlorite system over a range of operating conditions. Gas evolution rate was found to exhibit dependence on both parameters. Gas phase hold-up was found to lie in the range 3 – 7%, and was not dependent upon agitation speed over the range of operating conditions studied here, as the gas evolution rate was low enough to let impeller flow dominate the bubble flow regime.

The solids suspension performance for 2-phase liquid-solid and 3-phase gas-liquid-solid systems was quantified using Zwietering's just-suspended impeller speed condition. Although the presence of gas was found to markedly increase the impeller speed required to fulfil this criterion, a coherent pattern to the relationship between $N_{js}(u)$ and $N_{js}(g)$ could not be readily ascertained with respect to the concentrations of nickel and hypochlorite. An additional experimental programme is required to evaluate the significance of each variable and provide insight to which parameter controls solids suspension performance in gas-evolving systems.

References

1. Choudhary, V. R., Devadas, P. (1998) *Microporous and Mesoporous Mat*; **23**, p231
2. King, F., Hancock, F.E. (1996) *Catalysis Today*, 27, p203
3. Stitt, E.H., Hancock, F.E., Peeling, R.H., Scott, J. (2003) *Catalysis Today*, **79-80**, pp125-138
4. Lister, M.W. (1956) *Canadian Journal of Chemistry*. **34**
5. Zwietering, T. N. (1958) *Chem Eng Sci*, **8**, pp244-253
6. Middleton, J.C. (1992) "Gas-liquid dispersion and mixing", in *Mixing in the process industries* (N. Harnby, M.F. Edwards and A.W. Nienow, eds), Chapter 15, Butterworth-Heinemann, Oxford, pp 322-363

Appendix E

6th International Symposium on Process Tomography

Characterisation of Gas/Liquid/Solid Mixing Using Tomographic Electrical Resistance Spectroscopy

U.I. Oguh^{1,2}, J.F. Hall¹, G.T. Bolton^{3,4}, M.J.H. Simmons², M Barigou² & E.H. Stitt^{1*}
hugh.stitt@matthey.com

¹ Johnson Matthey Technology Centre, Billingham, TS23 4HS, UK

² School of Chemical Engineering, University of Birmingham, Edgbaston, B15 2TT, UK

³ Industrial Tomography Systems Ltd, Manchester, M3 2BA, UK

⁴ Present Address: National Nuclear Laboratory, Warrington, WA3 6AE, UK.

Keywords *A preliminary study of the potential of electrical resistance spectroscopic tomography to characterise multiphase stirred tank reactors is presented. A conductor has a frequency dependent effective resistance that is the sum of its static resistance and its self-inductance of which the latter is frequency dependent. Stirred tank reactors are extensively used in the chemical and related industries for carrying out catalytic reactions. These vessels feature a liquid continuum and discontinuous gas and solid phases; dispersed gas bubbles and suspended solid particles. As yet there is no single technique able to monitor both dispersed phases. Initial experiments employed phantoms in a 4-ring electrode cage system to demonstrate the electrical effects for the selected materials and to show the spatial capability. These were followed by two phase experiments in a standard configuration stirred tank using an ERT linear probe to demonstrate further that the principles could be applied also to dispersed systems. The linear probe was used in preference to the electrode cage because the main heterogeneity is expected to be in the azimuthal domain and the increased axial resolution of the probe is therefore beneficial. In addition to this, by using the probe the potential to apply this technique to industrial vessels is also demonstrated. Finally, a limited number of experiments were carried out in the stirred tank with a linear ERT probe for the full three phase system, with mixing conditions specifically selected to give different mixing regimes; thus widely different degrees of phase homogeneity. The tomograms and vertical average conductivity data are shown to correspond to expected and visual images of the resulting mixing homogeneity. This paper therefore presents a demonstration of the feasibility of employing spectroscopic ERT to monitor three phase industrial systems*

Keywords Stirred tanks, Gas-liquid-solid mixing, ERT, Electrical spectroscopy

1 INTRODUCTION

Multiphase mixing and contacting is an important requirement in the process industries, for example, in packed tower distillation, gas absorption and scrubbing towers as well as multi-phase catalytic reactors. Achieving good or adequate contacting and inter-dispersion of the individual phases is normally a prerequisite for efficient manufacturing plant operation. In the petroleum industry, the visualisation and characterisation of multiphase pipeline flow is also important for minimisation of transportation costs and to ensure safety.

Tomographic and velocimetric measurements of multiphase systems have been areas of significant effort for many years (Chaouki et al., 1997), with notable success in two phase systems and three phase systems, where one of the phases is immobile. Generally a single technique has allowed interrogation of only two distinct phases, or where three phases have been discriminated this has involved temporally separated data sets or the imposition of an *a priori* assumption in the data reconstruction. An alternative approach has been

* Corresponding author: email hugh.stitt@matthey.com, tel +44 1642 522704

to use an independent technique to resolve the third phase, referred to as multi-modal operation. The specific problem in the visualisation of agitated and pipe flow multiphase systems is that the gas and solid phases are both dispersed and mobile. This study reports on preliminary experiments to demonstrate the use of a tomographic electrical resistance spectroscopy technique for the simultaneous resolution of three phases in an agitated gas-liquid-solid (GLS) system.

2 Tomography of Multiphase Systems

In multiphase systems, the phase concentrations that are relevant to commercial applications lead to largely opaque mixtures and consequently optical based techniques are rarely applicable. Thus, electrical, magnetic resonance and hard field techniques have been used to visualise flows and phase distributions in multiphase systems.

2.1 Electrical Tomography Techniques

Circular array Electrical Resistance Tomography (ERT) has been widely employed as a visualisation tool in single and multiple plane designs for two-phase systems such as gas-liquid (G-L) distributions in bubble columns (Jin et al., 2007), stirred tanks (Wang et al., 2000), solid-liquid distribution in an agitated vessel (Ricard et al., 2005) and immiscible liquid-liquid (L-L) turbulent flow (Kourunen et al., 2008) with a conducting (commonly aqueous) continuous phase.

Electrical Capacitance Tomography (ECT) has been used to study the liquid phase distribution in trickle beds (Reinecke & Mewes, 1996) and in a cold flow monolith reactor (Mewes et al. 1999). Wang et al. (1998) used ECT to study spatial and temporal variations of solids hold up in a circulating gas-solid (G-S) fluidised bed. A 3D (or volumetric) ECT system has been used to study G-S fluidisation (Du et al., 2005) and G-L bubble columns (with a dielectric liquid phase) (Warsito & Fan, 2001).

For evaluating GLS systems, the same workers used a solid and liquid phase of similar electrical permittivity (Warsito & Fan, 2001), rendering the system in effect two-phase: gas and (solids + liquid). They measured the gas phase distribution using the ECT, but gained no information on the relative dispersion of the solid and liquid phase; implying an a priori assumption of a pseudo-homogeneous slurry phase.

Thus, using ECT or ERT alone, it has only been possible to resolve two phases. Some researchers have employed multi-modal approaches to study three phase systems. Multi-modal circular array ERT was recently used with a fibre optic probe to interrogate GLS systems (Razzak et al., 2009). Local conductivity measurements of the gas phase and non-conducting solid phase hold up were obtained. The average solids phase hold up was quantified using pressure gradient measurements in a riser whilst the fibre optic probe measured gas phase hold up independently. By combining these results, the gas and solid phase hold ups were discriminated.

Liter et al. (2002) used Gamma Densitometry Tomography (GDT) with circular array ERT to characterise a pilot-scale slurry bubble-column. ERT distinguished the conducting liquid phase from the gas and the solid phase, whilst GDT discriminated the non-attenuating gas phase from the liquid and the solid phases.

Multi-modal ECT has also been used with ERT to study oil-water-gas (LLG) distribution in pipelines (Li & Yang, 2009). The ECT mode was used to measure the oil-continuous whilst the ERT mode was used to measure water-continuous flows.

Bolton (2002) and Bolton et al. (2006) introduced a linear ERT probe that operates under the same measurement strategy as the circular array ERT but provides axial conductivity distribution information. They demonstrated its ability to effectively monitor homogeneous liquid phase mixing. This development, although intrusive, is especially useful for application into commercial vessels where incorporation of the "classic" electrode arrays and cage may not be practicable. Hitherto, there has been relatively little deployment of this approach for multiphase systems. Oguh (2012) showed its application to diagnosing poor solids suspension in a stirred tank. Ricard et al. (2005) also deployed the linear ERT probe into stirred tanks and compared on-line monitoring information and CFD modelling results of L-L dispersion and solids suspension in stirred tanks to the axial distribution information obtained with the probe.

2.2 Magnetic Resonance Imaging

Magnetic resonance imaging (MRI) has been used extensively to interrogate liquid and gas liquid flows in packed beds and structured reactors and its applicability to G-S fluidised beds has been demonstrated. Sederman & Gladden (2001) used MRI to measure the structure of packed beds of spheres and micro-porous extrudates. The H-NMR methodology required filling of the bed with water; a S-L phase distribution was thus interrogated. Subsequently Gladden et al. (2003) studied liquid trickle flow over a packed bed of porous extrudates. More recent developments in this technique allow dynamic monitoring of unstable G-L flows and the transition from stable (trickle flow) to unstable flows (pulsing regime) over a packed bed of particles (Gladden et al., 2005).

The determination of the distribution of liquid rivulets is however dependent on a detailed prior mapping of the distribution of the solid phase and/or arbitrary thresholding to discriminate the solid and liquid phases. Thus, although this appears to allow single modality discrimination of three phases, the reconstruction is dependent on an *a priori* assumption or difference in mapping with an independent measurement. While this is extremely effective for a small trickle bed reactor where the position of the solid particles is fixed in space, it does not allow for application to systems where the solid phase is mobile and where the solid particle size is lower than the voxel size; it would be unable to discriminate a G-L mixed voxel from a solid filled voxel.

MRI has also been applied to measuring gas distribution dynamically in a G-S bubbling fluidised bed (Muller et al., 2008). The phase resolution here is essentially between the dense fluidised phase and the bubbly (lean) phase, although some information on heterogeneity of the dense phase can be discerned.

2.3 Hard Field Techniques

X-ray and gamma-ray (γ -ray) tomography have been widely applied to the characterisation and measurement of multiphase systems (Chaouki et al, 1997, Johansen & Jackson, 2004). These are well-established techniques that provide a spatial density map as output. For systems where the dispersed phase characteristic length scale is longer than the characteristic pixel or voxel scale then the phases can be effectively discriminated by their relative densities. However, for systems where the phases have mobility and / or where the dispersed length scales are small, then voxels that contain more than one phase on a spatial or temporal basis cannot be resolved.

Kumar et al. (1995) developed a γ -ray tomography system for measuring spatially resolved gas hold up in a G-S bubble column. This system has also been deployed to interrogate the liquid phase distribution in a moderate diameter trickle bed (Boyer & Fanget, 2002) and monolith reactors (al-Dahhan et al., 2007), G-S fluid bed risers (Roy & Dudukovic, 2001) and gas hold up patterns in a stirred tank (Khopar et al., 2005 and Meuler & Dudukovic, 2010). A large-scale γ -tomography system has also been developed for commercial applications such as packed distillation towers and has been used on columns of up to 6 m in diameter (Darwood et al., 2003).

For slurry bubble column (GLS) systems, where both the gas and solids are dispersed and mobile, similar approaches have been used but in conjunction with the *a priori* assumption of a pseudo-homogeneous slurry phase; there is no independent interrogation of the particulate solid phase. To validate the assumption of slurry homogeneity injection of radioactive $^{56}\text{MnO}_2$ particles was used to give an independent measurement (Chen et al., 2006).

X-ray tomography (XRT) has also seen significant use for interrogation of multiphase flows and vessels. Liquid distributions in trickle beds were initially investigated by Lutran et al. (1991). Toye et al. (1998) used XRT to investigate void fractions and liquid hold up in packed columns. The same group (Marchot et al., 2001) investigated the sources and the nature of small-scale liquid and gas maldistributions in packed beds with an irrigated packing structure. Strong increases in dynamic liquid hold up at the interface between packing elements were clearly distinguished from flowing rivulets. Gas hold up distributions for fluidised beds has also been investigated using XRT by Kantzas *et al.* (1994). Ford et al (2008) used XRT to explore differences in gas dispersion regimes in stirred vessels. Recently, an ultrafast 3D XRT method based on electron beam scanning was introduced by Bieberle et al. (2011) and shown to be able to recover the structure of the phase boundaries found in G-S and G-L flows which undergo 3D structural changes.

The key feature of the above studies is that by using a single source and tomography as the only measurement technique it is only feasible to discriminate two phases, unless a priori assumptions or independent measurements are made. There are therefore examples of the use of hard field techniques in tandem with additional measurements to discriminate the third phase. For example, Johansen et al. (1996) and later Hjertaker et al. (2011) used combined capacitance and gamma ray tomographies to measure volume fractions in oil-water-gas (LLG) flows in pipes.

2.4 Dual-Source Single Modality Approaches

The use of dual energy sources for a single modality can be effectively used to resolve three phases, providing all three phases offer sufficient discrimination in the relevant physico-chemical property. This has mainly been exploited in hard field techniques.

Abouelwafa & Kendal (1980) used dual energy source γ -rays to interrogate oil-air-water systems. By using a number of discrete gamma energies, it was demonstrated that this method could be extended in theory to cover as many material types. Froystein et al. (2005) designed a fully automated dual energy γ -ray for use in a high pressure multiphase flow loop. The system facilitated the determination of phase distribution in multiphase systems. The system reconstructed the different fluid zones within a pipe cross section for different geometric configurations. Johansen & Jackson (2000) measured the gas volume fractions in oil-air-water pipe flows independent of the salinity of the water component. Temporal variations in the G-L distribution may disturb flow velocity measurements with this technique; with the major problem being the gas volume fraction. Li et al. (2005) and Wu et al. (2007) describe a dual energy γ -ray system, using ^{241}Am (59.5 keV) and ^{241}Cs (662 keV) sources to measure volume fractions for GLS pipe flow. Varma et al. (2004) used dual source γ -ray to map GLS phase distributions in an aerobic digester cold-flow mimic.

While the dual energy source γ -ray approach to GLS and LLG discrimination has seen a number of reports, with the primary application being oil flow monitoring, the equivalent XRT technique is much less prevalent. Grassler & Wirth (2001) showed the possibility of using dual-energy XRT in the determination of solids, liquid and gas distributions in a bubble column. By using static test objects composed of two different materials, they showed that it was possible to separate two different materials sufficiently with a maximum relative deviation of $\pm 20\%$. Gehrke & Wirth (2001, 2005) developed a dual energy XRT system to evaluate GLS systems, with specific application to slurry bubble columns and cold-flow mimic of the liquid feed section of an fluid catalytic cracking (FCC) bed riser reactor. Behling and Mewes (2006) distinguished 3 phases (air, water and PVC particles) in a bubble column with dual-energy XRT.

Nahvi & Hoyle (2008) described a spectro-tomography method with Electrical Impedance Tomography (EIT) to characterise complex multi-component systems. Spectro-tomography is a technique where a spectral range of the excitation signals is used to isolate materials by the difference in their response and electrical potential at fixed currents. Hoyle & Nahvi (2008) demonstrated the technique in a system composed of fruits (a banana and cucumber) in aqueous salt solution. By decreasing the frequency, they isolated the cucumber from the banana. They later demonstrated the technique in a crystallisation process (Nahvi & Hoyle, 2009).

The fundamental concept that governs Hoyle & Nahvi's (2008) technique is the difference in impedance or reactance of materials in the multi-component system with frequency. As dielectrics, one would expect the span of the impedance of each object to be well spaced apart for the technique to be successful. Generally, as the frequency of a sinusoidal alternating current (AC) through dielectrics is varied, the impedance to electrical charge comes about due to the alteration of molecular charges in the dielectric from their equilibrium positions by migration or orientation of permanent dipoles (Macdonald, 1992).

In conductors, the flow of an AC is seldom uniform due to skin and proximity effects. Conductors also demonstrate a frequency dependent effective resistance which is the sum of the static resistance and self-inductance. By increasing the frequency of the AC through the conductor, electrical charges saturate on their outer surface increasing the current per unit area and producing a measurable voltage on the conductor's surface. This phenomenon is called the skin effect (Gilberd, 1982). By decreasing the frequency, this behaviour is reversed and the AC will flow in a single direction across the entire cross-sectional area of the conductor; viz. it behaves as a direct current (DC).

Electrical spectroscopic tomography offers the prospect of equivalence in electrical tomography of the dual source hard field techniques; namely the ability to discriminate multiple dispersed and mobile phases using a single modality. It has not yet however been demonstrated for such an application

3 Materials and Methods

Two types of experiments were performed. The first used a circular ERT electrode array and radially disposed phantoms to quantitatively demonstrate the frequency dependence of the selected materials. The second was in an agitated vessel with the ERT electrodes presented as a vertical linear probe, thus generating axial conductivity profiles. The equipment and materials used will be described in turn.

3.1 Tomographic Equipment

In all cases the ERT electrode set was connected to a p2000 Data Acquisition System (DAS) hardware system (Industrial Tomography Systems, Manchester, UK). The sensors operate by injecting AC between sequential pairs of adjacent electrodes at a selected frequency. After each injection, the voltage difference between adjacent pairs of non-injecting electrodes is obtained from the relative change in voltage across the vessel. In this study a total of five frequencies were investigated: 9.6, 4.8, 2.4, 1.2, 0.6 and 0.3 kHz at a single injection current of 0.6 mA. Initial reference measurements of an undisturbed system are points of reference for comparison with a disturbed system. The selection of discrete frequencies was imposed by the frequency options available from the ITS hardware.

3.2 Preliminary Evaluation With Phantoms

The vessel used was unbaffled with a diameter (T) of 0.15 m. It incorporated 4 planes of 16 equally spaced electrodes on the vessel wall. The vessel, shown in Figure 1, is the same as that used by Edwards et al. (2009) and is described in more detail therein.



Figure 1. External and internal electrode arrangements of the circular array ERT vessel

The conducting solution was a 1.9 g L^{-1} nickel nitrate solution with a conductivity of 1.07 mS cm^{-1} at a temperature of 25°C . The phantom was a hollow stainless steel rod of length 0.290 m with outer and inner diameters of 0.035 m and 0.025 m respectively. It was aligned vertically and located axially in the vessel. A plume of air bubbles was generated using an aeration rate (Q) of $0.83 \times 10^{-4} \text{ m}^3 \text{ s}^{-1}$ (2 volume per volume per minute (vvm)). Air was delivered below the measurement plane by a rubber pipe with an upwards pointing outlet located axially within the vessel.

3.3 Experiments Using a Stirred Vessel

The mixing experiments were carried out using a Perspex vessel of $T = 0.014 \text{ m}$. It was equipped with 4 equally spaced baffles of width, $B = T/10$, a ringed sparger of diameter 0.04 m with $0.5 \times 10^{-3} \text{ m}$ diameter orifices. A standard six blade Rushton disc turbine (RDT6) with an impeller to vessel diameter ratio (D/T) of 3/7 was positioned at an impeller clearance to tank diameter ratio (C/T) of 4/14 from the vessel base. The

RDT6 was located below the last electrode plane close to the vessel bottom and was driven by a variable speed motor (Eurostar power control-visc, IKA Germany).

The linear ERT probe had 16 equally spaced and vertically aligned electrodes, described previously by Simmons et al (2009) and is shown in Figure 2. The probe was used to provide projected tomographic reconstructions and, more importantly axial conductivity profiles. The probe was placed adjacent to the vessel wall, tangentially behind a baffle (in the direction of impeller rotation) and turned to face towards the impeller shaft.



Figure 2. Linear ERT probe with electrode arrangements

Nickel nitrate solution of volume $2.6 \times 10^{-3} \text{ m}^3$ ($H/T=1.2$), temperature of 25°C and conductivity of 1.07 mS cm^{-1} was used again as the conducting liquid phase. Stainless steel particles nominal size of $250 \mu\text{m}$ and density (ρ) of 7800 kg m^{-3} were used as the dispersed solid phase at a loading of 6 g for every 100 g of slurry (6 % w/w).

In the G-L (no solids) control experiment an air flow rate, Q , of $0.83 \times 10^{-4} \text{ m}^3 \text{ s}^{-1}$ (2 v.v.m.) was used and introduced via the ring sparger described above. Three different experimental conditions were selected for the GLS mixing studies, corresponding two different regimes of G-L mixing, and the transition between them. These are given in Table 1.

N		Flg	Fr
(s^{-1})	(rpm)	-	-
13.3	800	0.029	1.08
10	600	0.0386	0.7
6.7	400	0.058	0.27

Table 1: Conditions for Three Phase Experiments

4 Preliminary Evaluation: Studies with Phantoms

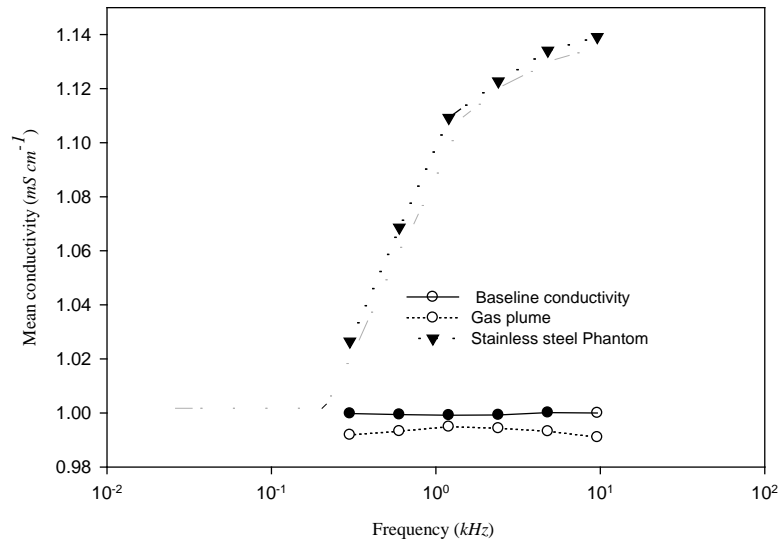


Figure 3. The effects of frequency on the mean conductivity of stainless steel phantom and air in nickel nitrate solution

5 Studies in Agitated Systems

Initially the responses of the dispersed two phase S-L and G-L systems were evaluated independently. The objective was to obtain independent frequency response data for the simplified systems prior to experiments with the full GLS system. *Note that the results of preliminary experiments only are reported here. Data from a far more comprehensive study are currently being collected. These, together with data analysis will be presented at the conference.*

5.1 Two Phase Studies (Calibration)

The just suspended impeller speed (N_{js}) for S-L mixing was measured by observing the base of the vessel and identifying the minimum impeller speed to ensure that particles did not remain on the bottom of the vessel for more than one to two seconds. The value of N_{js} for the ungasged system was approximately 13.3 s^{-1} (800 rpm) which corresponds to an impeller Reynolds number of $Re=55,280$ implying turbulent mixing ($Re > 10^4$). The multi-frequency tomographic experiment for (ungasged) S-L mixing was carried out using $N = N_{js}$.

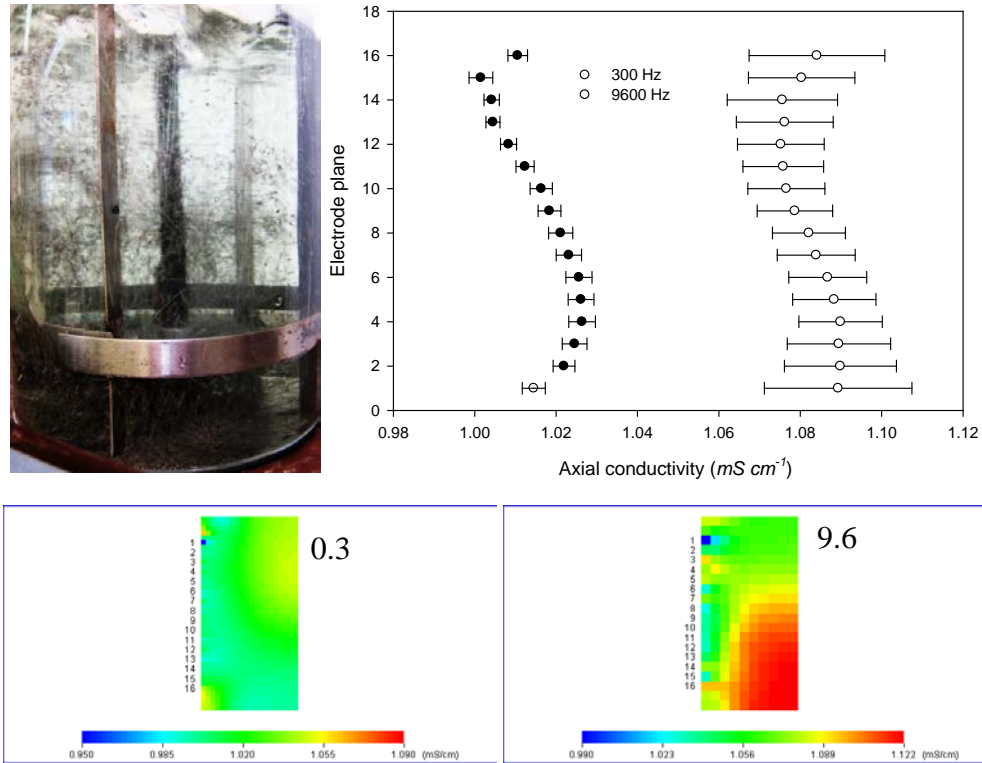


Figure 4 : Solid Liquid Mixing - image of the vessel under these conditions, along with the reconstructed tomograms and the conductivity profiles at both frequencies.

Figure 5 shows an image of the vessel under these conditions, along with the reconstructed tomograms and the conductivity profiles at both frequencies. The tomogram at 9.6 kHz shows clearly the skewed distribution of solids hold up towards the bottom of the vessel, which corresponds to the pictorial image and prediction from the mixing condition (impeller speed $N = N_{js}$). Considering the axial conductivity profiles, the 9.6 kHz profile is at a significantly higher conductivity than the 0.3 kHz, consistent with the increased response of the higher frequency to the suspended solids. The overall trends in the plotted averaged data do not however correspond entirely to the tomogram, showing a much reduced range of conductivities. This is believed to be due largely to the methods reconstruction and averaging used, and this is discussed later. Nonetheless, the ability of ERT spectroscopy to respond to a dispersed conducting phase is demonstrated. For solid-free G-L mixing a gassing rate was selected that provided full gas dispersion. This was done based on well-established design methods for standard configuration vessels with a Rushton turbine impeller. Figure 6 shows a Froude Number vs Gas Flow Number plot for a RDT6, redrawn from Middleton (1992).

$$\text{Froude No. } Fr = N^2 D / g \text{ and Gas flow Number } F_{lg} = Q / ND^3$$

Where N is impeller speed (s^{-1}), D is impeller diameter (m), g is gravitational acceleration (9.81 m s^{-2}) and Q is the gas flow rate ($\text{m}^3 \text{ s}^{-1}$). Both Fr and F_{lg} are dimensionless numbers.

This plot is useful in gas-liquid mixing system design because it conveniently displays the correlations for the transitions between gas-liquid mixing regimes: "Full Recirculation" of the gas (where the gas is reasonably uniformly dispersed throughout the vessel), "Limited Recirculation" (where the gas dispersion is substantially above the impeller only) and Flooding (where the impeller is swamped by gas and the bubbles rise as a largely undisturbed axial bubble plume with little dispersion of the gas). For the gas-liquid only experiment a condition that would result in a full dispersion of the gas is marked with a square denoted "GL" in Figure 6. This condition is an impeller speed $N = N_{js} = 13.3 \text{ s}^{-1} = 800 \text{ rpm}$. The gas phase hold up, measured using the dynamic disengagement method (Chapman *et al.*, 1983) was $\phi_g \approx 6 \text{ vol.}\%$.

The effects of altering the frequency on the conductivity of the stainless steel phantom in the nickel nitrate solution using the circular array ERT vessel are shown in Figure 3. Measurements were taken relative to a base plane measurement of 1. The blue regions correspond to the reference conductivity of solution. As the frequency is reduced from 9.6 kHz to 0.3 kHz the discrimination of the phantom significantly reduces; viz. the conductivity of the stainless steel phantom is reduced at lower frequencies.

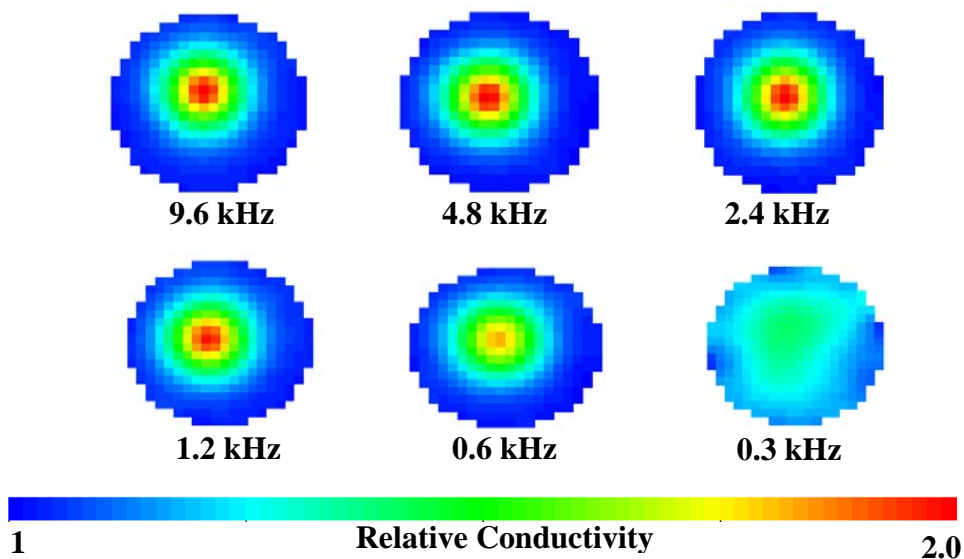


Figure 5. The effects of changing frequency on self inductance of the stainless steel phantom

Figure 4 shows the change in mean conductivity of the stainless steel phantom and of the bubble plume with frequency. Each data point had an error of $\sim \pm 0.005\%$ which is very low since the system was practically undisturbed. As previously demonstrated, by decreasing the frequency, the mean conductivity of the phantom decreased by $\sim 90\%$. It was unfortunately impossible to obtain reliable data at a frequency below 0.3 kHz where the influence of the solid should have been negligible due to unacceptably poor signal to noise ratios. As would be expected for an insulating material, there was also negligible change in the conductivity of the bubble plume.

When the frequency was increased, the conductivity of the phantom increased due to the skin effect phenomenon. As the frequency through a conductor increases, self-inductance takes place, causing an increase in the effective resistance on the conductor's surface. This increases the resistance to the flow of current and thus increases the current per unit area over the conductor's surface leading to the detection of a measurable voltage by ERT. As the frequency was decreased, this phenomenon relapsed and the AC flowed in a manner analogous to a DC, thereby decreasing the current per unit area on the conductor's surface. The validation with the phantom and circular array ERT vessel set a platform for work to be carried out on agitated S-L and G-L systems in a stirred vessel equipped with a linear ERT probe.

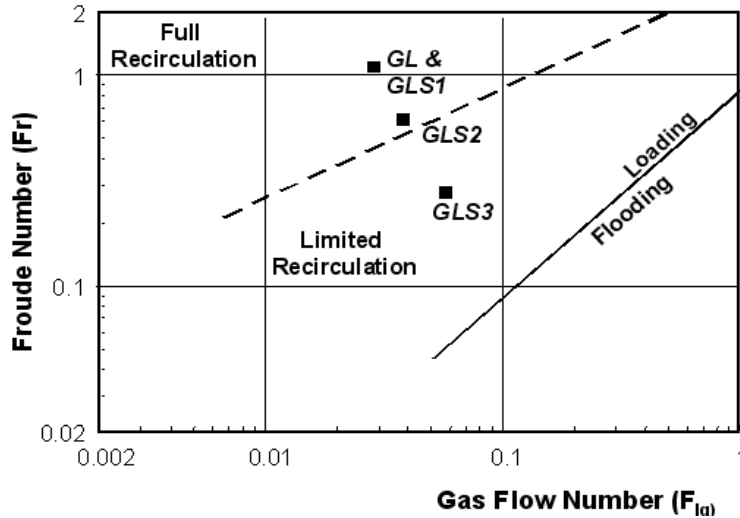


Figure 6: Selection of Conditions for G-L and G-L-S Experiments (G-L flow regime chart redrawn from Middleton (1992))

The mean conductivity data across the full range of frequencies for the liquid only, liquid-solid and gas-liquid experiments are given in Figure 7. The results are essentially consistent with those from the phantom study (Figure 4). The presence of gas shows negligible response to frequency, just small reduction in mean conductivity due to the gas hold up. The dispersed metal particles by contrast show a significant frequency effect.

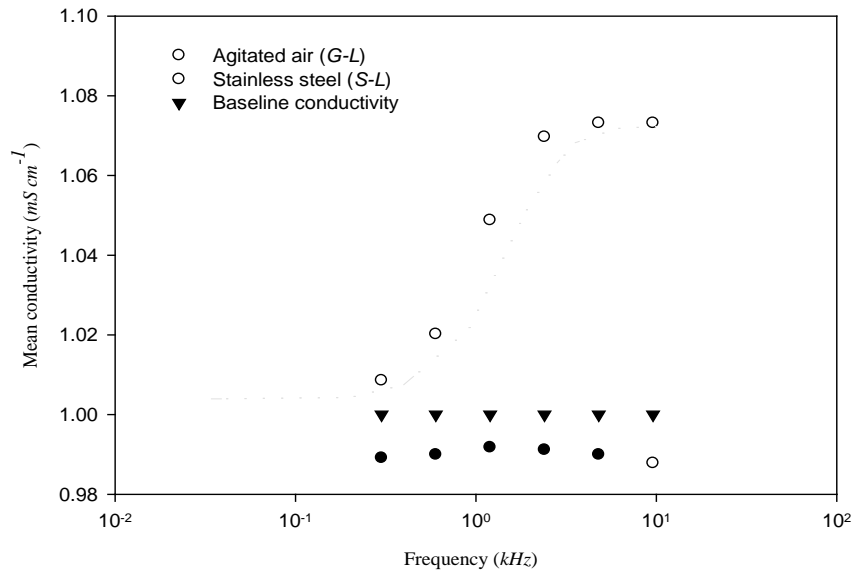
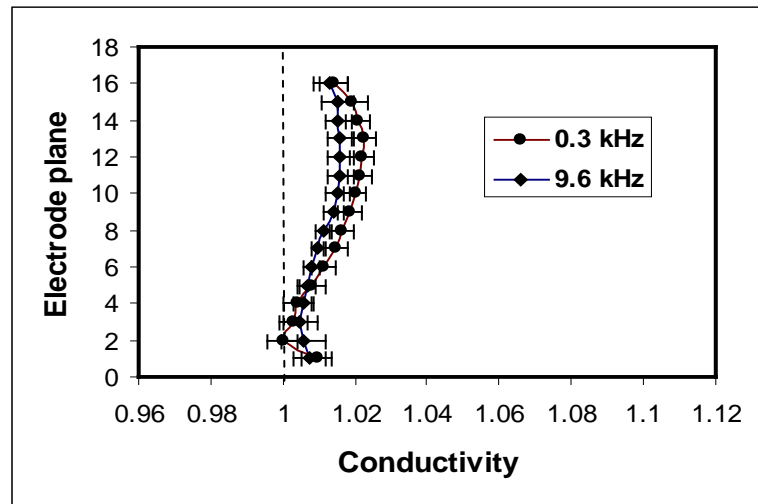


Figure 7. The effects of frequency on the mean conductivity of dispersed S-L and G-L systems

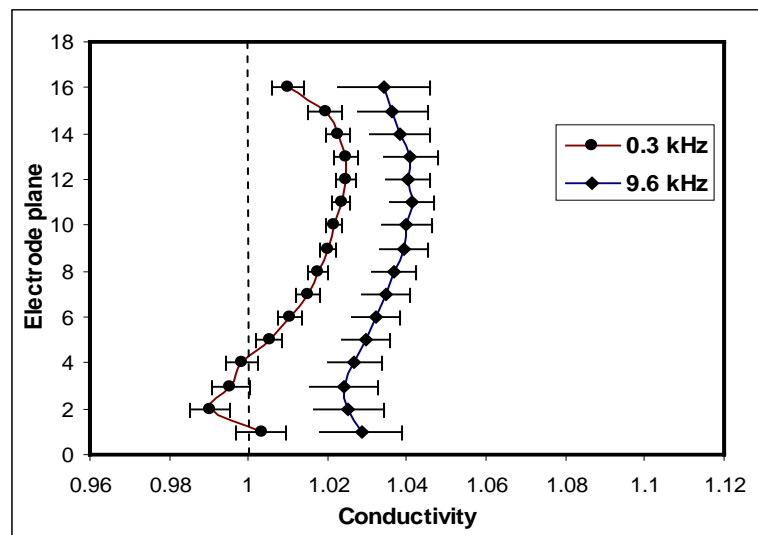
5.2 Three Phase Mixing Studies

Three experiments are reported here that demonstrate the ability of the ERT spectroscopy to detect at least semi-quantitatively different degrees of suspension and dispersion. The three experiments are denoted graphically in Figure 6, and the key parameters given in Table 1. The three conditions were deliberately selected to give gas-liquid mixing under three different regimes, two at partial gas dispersion and the most vigorous at full gas dispersion. The volumetric gas holds up values (measured by the gas disengagement method) were 2%, 4% and 6% respectively. Pictorial images of the three runs are shown along with the axial conductivity profiles, in Figure 8. Note that all axial profile graphs in Figures 5 and 8 are plotted on the same X-axis scale for ease of comparison.

GLS - Fr=0.3



GLS - Fr=0.7



GLS - Fr=1.1

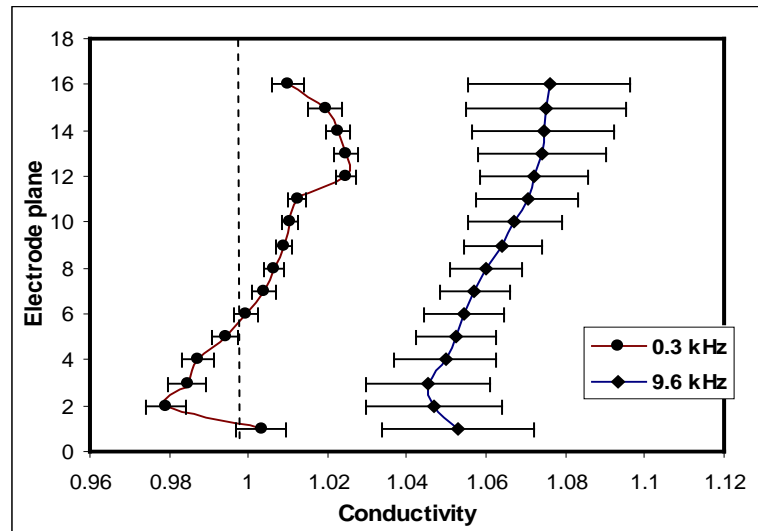


Figure 8: Gas-Liquid-Solid Mixing - image of the vessel under the three conditions along with the axial conductivity profiles at both frequencies obtained using a linear ERT probe.

Significant differences are observable with respect to the solids suspension. Compare for example the top image ($Fr = 0.3$, GLS3 on Figure 6) with that for gas-free solid liquid mixing in Figure 5. It is evident that the solids dispersion is markedly poorer for this particular gas sparged example. This is because the impeller is substantially "flooded" by the gas and the energy is not efficiently imparted to the liquid phase; so the solids suspension is much reduced. The effect of this on the axial profiles is also marked, with the profiles at 0.3 and 9.6 kHz, in contrast to Figure 5, now nearly co-incident. Comparing the 0.3 kHz profiles for the gassed and un-gassed cases, these are largely similar, indicating that the axial column of bubbles has relatively little impact on the voltages measured by the near-wall ERT probe electrodes

Increasing the impeller speed leads to an increase in both gas dispersion and in solids suspension. The former is evident obvious from the pictures in Figure 8 with the bottom image showing substantially complete gas dispersion. Closer examination of the images shows the latter also to be true. The increasing impact of the gas phase on the ERT is indicated by the decreasing conductivity in the lower planes of the profiles gas phase. The increasing solids suspension evidenced by the increasing average conductivity at the higher frequency.

6 Discussion

While the simple observations given in this paper are demonstration of the ability of multiple and dual frequency ERT to allow discrimination the gas and solid phases, the axial profiles are at present not entirely satisfactory. We are currently in the process of re-examining the data extraction and averaging protocols to try and improve this. The re-evaluation of the data processing will be reported at the conference. One key aspect is that the presented images and the method of conductivity averaging are all based on the conventional Linear Back Projection algorithm which is know to have has some uncertainties in regions further away from the probe. This method of image reconstruction may not be ideal.

There are hardware issues that need to be addressed as well. Currently available ERT equipment is not able to easily perform a frequency sweep and is thus not ideally suited to this type of work. More examples of this type of application may provide the necessary pull to move the hardware and software in this direction, possibly towards being able to identify optimal frequencies for discrimination.

Finally, this technique and other applications will require validation against conventional measurement techniques. This will require significant effort, and will of course be complicated by the fact that existing techniques can generally not measure reliably at the commercially relevant phase hold up values where this technique has most promise

7 Conclusions

The monitoring of three phase dispersed systems using tomographic techniques has largely been limited to date and largely only two phases have been mapped, except where multi-modal approaches have been employed or where, for X-ray and gamma-ray tomographies where dual energy source approaches have been successfully exploited in small number of cases. This paper has reported a preliminary experimental study to explore the potential of multiple frequency electrical resistance tomography to resolve using a single technique both gas and solid phases dispersed in a conducting liquid continuum, exemplified by a stirred reactor.

Initial experiments using phantoms demonstrated that at low frequency, the impact of the selected solid material was significantly reduced, while at higher frequency the solids dominated the response. The insulating gas phase had no frequency effect of course and its distribution can only be ascertained by variation in the measured conductivity; the approach normally used in ERT. Thus, to a first approximation the solid distribution could be discerned substantially using the high frequency and the distribution of the gas largely established by the spatial variation in conductivity at a lower frequency. A second set of experiments using dispersed metal particles showed that these effects were in evidence for dispersed systems as well as the discrete continuum presented in the phantom experiments.

The results of a limited number of experiments using a stirred tank with three phases (liquid continuum with particles and dispersed gas) have also been carried out for different mixing regimes; corresponding to significantly different axial distribution of the gas and solid phases. These initial results show that the system is able to provide information on the distribution of both dispersed phases, with evident differences in the conductivity results for the three conditions.

A significant amount of work remains to be done. There is as yet no quantitative validation of the results. There are certain aspects of data acquisition and data processing that require further development. A more complete set of results will be presented at the conference that will explore these last points and assess in more detail the technique. The data presented herein do however highlight the potential of the technique for multi-phase system measurement and monitoring.

8 REFERENCES

- ABOUELWafa, M.S.A., KENDALL, E.J.M., 1980. The measurement of component ratios in multiphase systems using gamma-ray attenuation. *J. Phys. E: Sci. Instrum.* 13, p.341.
- AL-DAHMAN M.H., KEMOUN A., CARTOLANO A.R., ROY S., DOBSON R., WILLIAMS J., (2007), Measuring gas-liquid distribution in a pilot scale monolith reactor via an Industrial Tomography Scanner (ITS), *Chem. Eng. Journal*, 130 (7) 147-152
- BEHLING M., MEWES D., 2006. Dual-Energy X-Ray Tomographic Measurement of Local Phase Fractions in 3-Phase Bubble Columns. *ASME Conference Proceedings*.
- BIEBERLE, M., BARTHEL, F., MENZ, H-J., MAYER, H-G., and HAMPEL, U., 2011. Ultrafast three-dimensional x-ray computed tomography. *Appl. Phys. Lett.* 98. 034101
- BOLTON G.T., QUI C.H., WANG M., (2002) A Novel Electrical Tomography Sensor for Monitoring the Phase Distribution in Industrial Reactors, [7th UK Conference on Mixing, Bradford](#)
- BOLTON, G.T., (2006). A review of linear electrical tomography probes for monitoring the behaviour of multiphase mixing processes. Proc. 12th Euro. Conf. Mixing, Bologna, Italy.
- BOYER C, FANGET B, (2002), Measurement of liquid flow distribution in trickle bed reactor of largediameter with a new gamma-ray tomographic system, *Chem. Eng. Sci.*, 57 1079-1089.
- CHAOUKI J., LARACHI F. DUDUKOVIC M.P., (1997), Non-Invasive monitoring of Multiphase Flows, Elsevier, Amsterdam.
- CHAPMAN, C.M., NIENOW, A.W, COOKE, M., MIDDLETON, J.C., (1983). Particle-Gas-Liquid Mixing in Stirred Vessels Part III: Three Phase Mixing. *Chem. Eng. Res. Des.* 61, 167
- CHEN P., GUPTA P., DUDUKOVIC M.P., TOSELAND B.A. (2006). Hydrodynamics of slurry bubble column during dimethyl ether (DME) synthesis: Gas-liquid recirculation model and radioactive tracer studies, *Chem. Eng. Sci.*, 61 (19), 6553-6570.
- DARWOOD M., DAVIES M., GODDEN D., JACKSON P., JAMES K., STITT E.H., (2003), Development and Implementation of Gamma-ray Tomography for Field Applications, 3rd World Congress on Industrial Process Tomography, Banff, Canada, 2-5 Sept 2003, pp 207-212.
- DU B., WARSITO W., FAN L.-S., (2005), ECT Studies of Gas-Solid Fluidized Beds of Different Diameters, *Ind. Eng. Chem. Res.*, 44 (14), pp 5020-5030.
- EDWARDS I., AXON S.A., BARIGOU M., STITT E.H., (2009) *The Combined Use of PEPT and ERT in the Study of Aluminium Hydroxide Precipitation*, I.E.C.Research 48, 1019-1028.

- FORD, J.J., HEINDEL, T.J., JENSEN, T.C., DRAKE, J.B., (2008). X-ray computed tomography of a gas-sparged stirred-tank reactor. *Chem. Eng. Sci.* 63, 2075-2085.
- FRØYSTEIN T., KVANDAL H., AAKRE H., (2005), Dual Energy Gamma Tomography System for High Pressure Multiphase Flow, *Flow Meas. Instr.*, 16, 99-112
- GEHRKE S., WIRTH K.-E., (2001) Dual Energy X-Ray Tomography in Process Engineering – A Non-Intrusive Technique to Characterise Vertical Multiphase Flows, Proc 2nd World Congr. Industrial Proc. Tomog. (WC IPT2), Hannover, Aug 2001, pp 90-97
- GEHRKE S., WIRTH K.-E., (2005), Application of Conventional and Dual Energy X-ray Tomography in Process Engineering, *IEEE Sensors J.*, 5, 183-187
- GILBERD P.W., (1982), The anomalous skin effect and the optical properties of metals, *J. Phys. F: Met. Phys.* 12 1845
- GLADDEN L.F., ANADON L.D., LIM M.H., SEDERMAN A.J., STITT E.H. (2005) Insights into the Mechanism of the Trickle-to-Pulse Transition in Trickle-Bed Reactors, *Ind.Eng.Chem.Res.*, 44, 6320-6331.
- GLADDEN L.F., LIM M.H.M., MANTLE M.D., SEDERMAN A.J., STITT E.H., (2003), MRI visualisation of two-phase flow in structured supports and trickle-bed reactors, *Catalysis Today* 79–80 203–210
- GRASSLER, T., WIRTH, K.E., 1999. X-ray Computed Tomography in Mechanical Engineering – A Non-intrusive Technique to Characterize Vertical Multiphase Flows. *Computerized Tomography for Industrial Applications and Image Processing in Radiology*. Berlin, Germany, March 15 - 17, 1999.
- HJERTAKER B.T., MAAD R., JOHANSEN G.A., (2011) Dual Mode Capacitance and Gamma Ray Tomography using the Landweber Reconstruction Algorithm, *Meas. Sci. Technol.*, 22, 104002
- HOYLE B.S., NAHVI M., (2008), Spectro-tomography - an electrical sensing method for integrated estimation of component identification and distribution mapping in industrial processes, *IEEE Sensors*, 8, 807-810
- JIN H., WANG M., WILLIAMS R.A., (2007), Analysis of bubble behaviors in bubble columns using electrical resistance tomography, *Chem. Eng. Journal*, 130 179-185.
- JOHANSEN, G.A., FRØYSTEIN, T., HJERTAKER, B.T., OLSEN, Ø., (1996). A dual sensor flow imaging tomographic system, *Meas. Sci. Technol.* 7, pp. 297–307
- JOHANSEN, G. A., JACKSON, P., 2000. Salinity independent measurement of gas volume fraction in oil/gas/water pipe flow. *Appl. Rad. Isotop.* 53, 595-601.
- JOHANSEN G.A., JACKSON P., (2004) Radioisotope Gauges for Industrial Process Measurement, John Wiley & Sons.
- KANTZAS, A. (1994). Computation of hold ups in fluidized and trickle beds by computer-assisted tomography. *AIChE J.* 40, 1254.
- KHOPAR A.R., RAMMOHAN A.R., V.V. RANADE V.V., DUDUKOVIC M.P. (2005), Gas-Liquid Flow Generated by a Rushton Turbine in Stirred Vessel: CARPT/CT Measurements and CFD Simulation, *Chem. Eng. Sci.*, 60, 2215-2229.
- KOURUNEN, J., KAYHKO, R., MATULA, J., KAYHKO, J., VAUHKONEN, M., HEIKKINEN, L.M., (2008). Imaging of mixing of two miscible liquids using electrical impedance tomography and linear impedance sensor. *Flow Meas. & Inst.* 19, 391-396.
- KUMAR, S.B., MOSLEMIAN, D., DUDUKOVIC, M.P., (1995) A gamma ray tomographic scanner for imaging void fraction distribution in bubble columns', *Flow Meas. Instr.*, 6(1), pp. 61-73.

- LI D., WU Y., LI Z., ZHONG X., (2005), Volumetric Fraction Measurement in Oil-Water-Gas Multiphase Flow with Dual Energy Gamma-ray System, *J. Zhejiang Univ. Science*, 6A, 1405-1411
- LI, Y., YANG, W., (2009). Measurement of multi-phase distribution using an integrated dual-modality sensor, *Proc. 1st IEEE International Workshop on Imaging Systems and Techniques*, Hong Kong, pp. 335–339.
- LITER S., GATRON T., JOHN R., SHOLLENBERGER K.A., CECCIO L.S., (2002). Electrical-Impedance Tomography for Opaque Multiphase Flows in Metallic (Electrically-Conducting) Vessels. Sandia Report: AND2002-3834. Nov.2002.
- LUTRAN, P.G., NG, K. M., DELIKAT, E. P. (1991). Liquid distribution in trickle beds. An experiment using computer-assisted tomography. *Ind. Eng. Chem. Res.* 30, 1270
- MARCHOT, P., TOYE, D., CRINE, M., L'HOMME, G., PELSSER A. M., OLUJIC, Z., 2001. Liquid distribution images on structured packing by X-ray computed tomography. *AIChE J.* 47, 1471-6.
- MACDONALD R. J., (1992). Impedance Spectroscopy. *Annals. Bio. Eng.* 20, 289-305.
- MEULER S.G., DUDUKOVIC M.P.(2010) Gas Hold up in Gas-Liquid Stirred Tanks, *Ind. Eng. Chem. Res.*, 49, 10744–10750.
- MEWES D, LOSER T, MILLIES M (1999) Modelling of two-phase flow in packings and monoliths, *Chem. Eng. Sci.*, 54, 4729-4747.
- MIDDLETON J.C., (1992) Gas-Liquid Dispersion and Mixing, pp322-363 in HARNBY N., EDWARDS M.F., NIENOW A.W. (1992) *Mixing in the Process Industries* (2nd Ed), Butterworth Heineman
- MULLER C.R., HOLLAND D.J., SEDERMAN A.J., MANTLE M.D., GLADDEN L.F., DAVIDSON J.F. (2008) Magnetic Resonance Imaging of fluidized beds, *Powder Technology*, 183 (1) 53-62
- NAHVI M., HOYLE B.S., (2008) Wideband Electrical Impedance Tomography, *Meas. Sci. Technol.* 19, 094011.
- NAHVI M., HOYLE B.S., (2009) Electrical Impedance Spectroscopy Sensing for Industrial Processes, *IEEE Sensors J.*, 9, 1808-1816.
- OGUH U.I., (2012) Eng.D. Thesis, University of Birmingham, UK.
- RAZZAK S.A., BARGHI S., ZHU J.-X., MI Y., (2009), Phase Hold up Measurement in a Gas-Liquid-Solid Circulating Fluidised Bed (GLSVFB) Riser Using Electrical Resistance Tomography and Optical Fibre Probe, *Chem. Eng. Journal*, 147, 210-218
- REINECKE N, MEWES D, (1996), Tomographic imaging of trickle-bed reactors, *Chem. Eng. Sci.*, 51,2131-2138
- RICARD, F., BRECHTELSBAUER, C., XU, X.Y., LAWRENCE, C.J., (2005). Monitoring of multiphase pharmaceutical Processes using electrical resistance tomography. *Chem.Eng.Res.Des.* 83(A7), p.794–805.
- ROY S., DUDUKOVIC M.P., (2001), Flow Mapping and Modeling of Liquid-Solid Risers, *Ind. Eng. Chem. Res.*, 40 5440–5454
- SEDERMAN AJ, GLADDEN LF, (2001), Magnetic resonance imaging as a quantitative probe of gas liquid distribution and wetting efficiency in trickle bed reactors, *Chem. Eng. Sci.*, 56, 2615-26.
- SIMMONS M.J.H., EDWARDS I., HALL J.F., FAN X., PARKER D.J., STITT E.H., (2009) *Techniques for Visualisation of Cavern Boundaries in Opaque Industrial Mixing Systems*, *AIChE Journal*, 55, 2765-2772.

TOYE, D., MARCHOT, P., CRINE, M., PELSSER, A.M., L'HOMME, G., (1998). Local measurements of void fraction and liquid hold up in packed columns using X-ray computed tomography, *Chem. Eng. Process.*, 37, 511-20.

VARMA, R., O'SULLIVAN, J. A., AL-DAHMAN, M., 2007. Dual Source Computed Tomography For Measuring Phase Hold up Distribution In Multiphase Systems, AIChE Annual Meeting, Nov 2007

WANG, M., DORWARD, A., VLASEV D., MANN, R., (2000). Measurements of gas-liquid mixing in a stirred vessel using electrical resistance tomography (ERT). *Chem.Eng.J.* 77, 93-98.

WANG, S. DYAKOWSKI, T., GELDART D., BECK M., (1998) Application of Electrical Capacitance Tomography to Flow Modelling within a Circulating Fluidized Bed, *Particle & Particle Systems Characterization*, 15 (1) 51-55.

WARBITO W., FAN L.-S., (2001) Measurements of Real Time Flow Structure in Gas-Liquid and Gas-Liquid-Solid Flow Systems Using Electrical Capacitance Tomography (ECT)," *Chem. Eng. Sci.*, 56, 6455-6462.

WU Y., CUI B., LI D., SCHALBERG H.I., ZHENG Z., ZHONG X., (2007), Multiphase Flow Measurement by Dual Gamma Ray Tomography, *Proc 5th Int.Symp.Meas.Techniques for Multiphase Flows*, Macau, 5 June 2007, Publ AIP

Appendix F

Minitab is statistical analysis software. It can be used for learning about statistics as well as statistical research. Statistical analysis computer applications have the advantage of being accurate, reliable, and generally faster than computing statistics and drawing graphs by hand. Minitab is relatively easy to use once you know a few fundamentals.